

AD-A118 744

SYSTEMS AND APPLIED SCIENCES CORP RIVERDALE MD
TECHNIQUE DEVELOPMENT FOR WEATHER FORECASTING.(U)
NOV 81 A M GERLACH

F/G 4/2

F19628-81-C-0039

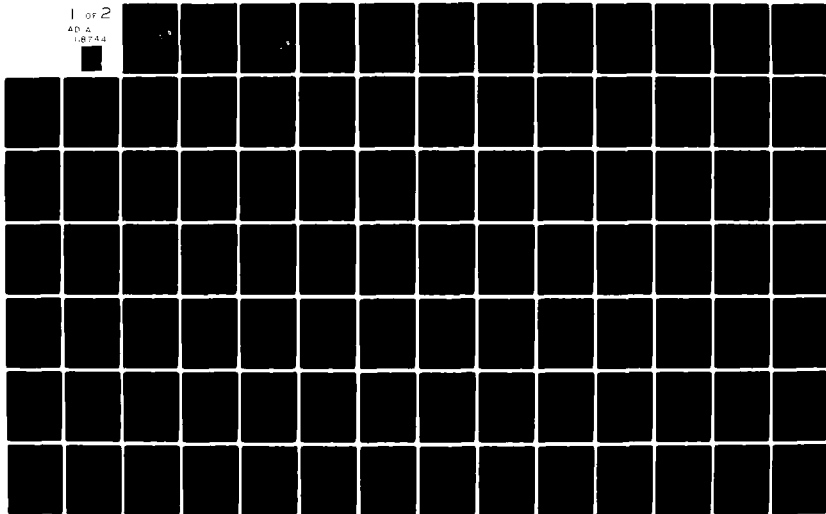
UNCLASSIFIED

AFGL-TR-82-0020

NL

1 OF 2

AD-A
1-8744



AFGL-TR-82-0020

12

AD A118744

TECHNIQUE DEVELOPMENT FOR WEATHER FORECASTING

Alan M. Gerlach (ed.)

Systems and Applied Sciences Corporation
6811 Kenilworth Avenue
P. O. Box 308
Riverdale, MD 20737

DTIC
ELECTE
AUG 31 1982
S D H

30 November 1981

Final Report for Period 1 December 1980 - 30 November 1981

Approved for public release; distribution unlimited

AIR FORCE GEOPHYSICS LABORATORY
AIR FORCE SYSTEMS COMMAND
UNITED STATES AIR FORCE
HANSCOM AFB, MASSACHUSETTS 01731

DTIC FILE COPY

82 08 30 081

Qualified requestors may obtain additional copies from the Defense Technical Information Center. All others should apply to the National Technical Information Service.

UNCLASSIFIED

SECURITY CLASSIFICATION OF THIS PAGE (When Data Entered)

REPORT DOCUMENTATION PAGE		READ INSTRUCTIONS BEFORE COMPLETING FORM
1. REPORT NUMBER AFGL-TR-82-0020	2. GOVT ACCESSION NO. AD-A118744	3. RECIPIENT'S CATALOG NUMBER
4. TITLE (and Subtitle) TECHNIQUE DEVELOPMENT FOR WEATHER FORECASTING		5. TYPE OF REPORT & PERIOD COVERED Final Report 1 Dec 80 - 30 Nov 81
7. AUTHOR(s) Alan M. Gerlach (ed.)		6. PERFORMING ORG. REPORT NUMBER
9. PERFORMING ORGANIZATION NAME AND ADDRESS Systems and Applied Sciences Corporation 6811 Kenilworth Avenue, P. O. Box 308 Riverdale, MD 20737		8. CONTRACT OR GRANT NUMBER(s) F19628-81-C-0039
11. CONTROLLING OFFICE NAME AND ADDRESS Air Force Geophysics Laboratory Hanscom AFB, MA 01731 Charles Burger/Manager/LY		10. PROGRAM ELEMENT, PROJECT, TASK AREA & WORK UNIT NUMBERS 61102F, 62101F 667000AB
14. MONITORING AGENCY NAME & ADDRESS (if different from Controlling Office)		12. REPORT DATE 30 November 1981
		13. NUMBER OF PAGES 187
		15. SECURITY CLASS. (of this report) UNCLASSIFIED
		15a. DECLASSIFICATION/DOWNGRADING SCHEDULE
16. DISTRIBUTION STATEMENT (of this Report) Approved for public release; distribution unlimited		
17. DISTRIBUTION STATEMENT (of the abstract entered in Block 20, if different from Report)		
18. SUPPLEMENTARY NOTES		
19. KEY WORDS (Continue on reverse side if necessary and identify by block number)		
GLOBAL MOISTURE DISTRIBUTION SATELLITE IMAGERY ANALYSIS INITIALIZATION CLUSTERING MESOSCALE FORECASTING CLOUD BRIGHTNESS INTERACTIVE FORECASTING (McIDAS) DOPPLER RADAR WIND RETRIEVAL		
20. ABSTRACT (Continue on reverse side if necessary and identify by block number)		
<p>This report summarizes weather research conducted by SASC in several technical areas: in numerical weather prediction, investigation of the physical and spectral characteristics of global moisture distribution, and examination of the generation of harmonics for analysis of meteorological data in the vertical and horizontal; development of McIDAS-based interactive aids for formulating mesoscale forecasts; development of specialized computer programs for sensor and technique evaluation; in satellite meteorology, interactive</p>		

DD FORM 1 JAN 73 1473

EDITION OF 1 NOV 65 IS OBSOLETE

UNCLASSIFIED


SECURITY CLASSIFICATION OF THIS PAGE (When Data Entered)

DTIC
ELECTED
SEP 1 1982
H

UNCLASSIFIED

SECURITY CLASSIFICATION OF THIS PAGE(When Data Entered)

adaptation of a clustering technique for image analysis, and test of curves relating cloud cover and average reflectivity; in weather radar, development of a single-Doppler wind retrieval technique, real-time conversion of a storm cell detection and tracking technique, and studies of turbulence structures. In addition, the maintenance, enhancement, and use of McIDAS are described.

Accession For		<input checked="checked" type="checkbox"/>
NTIS GRA&I		<input type="checkbox"/>
DTIC TAB		<input type="checkbox"/>
Unannounced		<input type="checkbox"/>
Justification		
By _____		
Distribution/		
Availability Codes		
Dist	Avail and/or	Special
		

UNCLASSIFIED

SECURITY CLASSIFICATION OF THIS PAGE(When Data Entered)

FOREWORD

This is the Final Report under Contract F19628-81-C-0039 with the Meteorology Division, Air Force Geophysics Laboratory. The contract extended from December 1, 1980 to November 30, 1981.

The report consists of narrative descriptions of work accomplished during the contract period and two technical papers reporting research achievements. Work which was reported on previously (in Scientific Report No. 1) is referenced in the appropriate place but is not repeated.

The contract called for effort in five discrete areas, reported upon in the monthly R&D Status Reports under these headings:

Numerical Weather Prediction
Mesoscale Forecasting
Satellite Meteorology
McIDAS Operation and Enhancement
Radar Meteorology

This Final Report is organized similarly.

Personnel associated with these areas at any time during the contract were:

Numerical Weather Prediction	-	Donald C. Norquist, M.S. Isidore M. Halberstam, Ph.D. Shu-Lin Tung, M.S. Chris Johnson, B.S. Joan-Marie Freni, B.A.
Mesoscale Forecasting	-	Joan M. Ward, A.B. Maureen F. Hampton, B.A. Russell C. Dengel, B.S. Gail A. Dengel, M.S. Randy Schechter, M.S. Charles F. Ivaldi, Jr., B.S. Michael E. Niedzielski, B.S. Scott D. Hamilton
Satellite Meteorology	-	Gail A. Dengel, M.S. Robert P. d'Entremont, B.S. Michael E. Niedzielski, B.S.

McIDAS Operation and Enhancement	-	John M. Powers, B.A. Barry A. Mareiro Gail A. Dengel, M.S.
Radar Meteorology	-	F. Ian Harris, Ph.D. Chen-Hung Chang, M.S. Glenn R. Smythe, M.S.

Principal Investigator was Alan M. Gerlach, Ph.D.

Subcontracts with Harris Corporation Computer Systems Division and Perkin-Elmer Customer Service Division provided on-site maintenance services for the McIDAS and Weather Radar Data Processing System respectively.

Reports were prepared by the scientists, engineers, and mathematicians identified in the Table of Contents with their technical reports.

TABLE OF CONTENTS

REPORT DOCUMENTATION PAGE.	1
FOREWARD.	3
TECHNICAL REPORTS	
SECTION 1: NUMERICAL WEATHER PREDICTION.	7
A. A STUDY OF THE PHYSICAL AND SPECTRAL CHARACTERISTICS OF GLOBAL MOISTURE DISTRIBUTION - Donald C. Norquist.	8
I. Introduction.	8
II. Construction and Comparison of Observed Fields.	9
III. Construction and Comparison of Analyzed Fields.	24
IV. Summary and Conclusions.	91
B. THE GENERATION OF HARMONICS FOR ANALYSIS OF METEOROLOG- ICAL DATA IN THE VERTICAL AND HORIZONTAL - Isidore M. Halberstam.	93
SECTION 2: MESOSCALE FORECASTING.	110
A. MESOSCALE FORECAST EXPERIMENT - Michael E. Niedzielski.	111
I. Introduction.	111
II. Software Modifications.	111
III. Forecast Procedure.	112
IV. Resulting Improvements.	115
a. Satellite Imagery Utilization.	115
b. Increased McIDAS Data Base.	116
(1) FOUS Bulletins.	116
(2) Manually Digitized Radar (MDR) Data.	124
c. Improvements in Conventional Data Displays.	130
d. Interactive Forecast Aids.	138
e. Automated Analysis and Forecast Routines.	145
V. Conclusion.	146
B. AFGL WEATHER TEST FACILITY SUPPORT - Joan M. Ward.	146
I. Introduction.	146
II. Data for Sensor Evaluation.	147
III. Verification of Prediction Techniques.	147
IV. Fog Model Display.	148
SECTION 3: SATELLITE METEOROLOGY.	151
A. CLUSTERING TECHNIQUE FOR SATELLITE IMAGERY ANALYSIS - Gail A. Dengel.	152

B. BRIGHTNESS VARIATION ANALYSIS - Michael E. Niedzielski. . .	.158
APPENDIX A.163
APPENDIX B.164
SECTION 4: McIDAS OPERATION AND ENHANCEMENT.166
A. SUPPORT TO RESEARCH PROJECTS - John M. Powers.167
B. HARDWARE ACQUISITION AND ENHANCEMENT - Barry A. Mareiro. . .	.173
C. SOFTWARE DOCUMENTATION - Gail A. Dengel.174
SECTION 5: RADAR METEOROLOGY.176
A. WIND RETRIEVAL - Glenn R. Smythe.177
I. Introduction.177
II. Discussion.177
B. REAL-TIME STORM CELL DETECTION AND TRACKING - Chen-Hung Chang.183
C. TURBULENCE MEASUREMENTS - Glenn R. Smythe.187

SECTION 1.

NUMERICAL WEATHER PREDICTION

A. A STUDY OF THE PHYSICAL AND SPECTRAL CHARACTERISTICS OF GLOBAL MOISTURE DISTRIBUTION

I. Introduction

Forecasting atmospheric moisture distributions and regions and intensities of precipitation remains one of the leading problems in numerical weather prediction. While parameterizations of large-scale and cumulus-scale precipitation within the models have received much of the blame for forecast inadequacies, a factor which cannot be overlooked but which has received too little attention is the preparation of the initial moisture fields.

Most of the current moisture analysis schemes used to support operational models are simply univariate offshoots of the analysis procedures for the other mass field parameters. Little attention is given to the similarities or differences that may exist between moisture and other mass field distributions. That the moisture analysis is as important to the forecast as the model itself has been shown by Phillips (1978)¹ among others. He interchanged moisture analyses in the same model with substantially different precipitation forecast results.

Another potential area for problems is the use of relative humidity instead of absolute humidity (the variable carried in most models) as the analyzed quantity. In this study we have taken a first step toward addressing the particular problem of moisture analyses. Taking both a summer and a winter synoptic case, we have studied the global distribution of moisture from two perspectives. First, using observed data from the First GARP Global Experiment (FGGE)² of the Global Atmospheric Research Program (GARP), global plots were subjectively analyzed to facilitate an examination of the fields in physical space. Second, using Hough analyses from FGGE as first-guess fields and performing successive corrections on them using the observations, representations of the observed fields at grid points were constructed for spectral analyses of the fields. This report compares the results of the mass and motion fields with the moisture

1. Phillips, N. A., 1978: A test of finer resolution. Office Note 171, National Meteorological Center, National Weather Service, NOAA.
2. Obtained from Department of the Air Force, OL-A, USAF Environmental Technical Applications Center (MAC), Federal Building, Asheville, NC 28801.

field, identifying similarities and differences, to determine the need for a separate analysis scheme for moisture.

II. Construction and Comparison of Observed Fields

Two synoptic times were chosen for the extraction of data from FGGE data tapes: January 15, 1978 at 00GMT (referred to as JAN), and July 20, 1978 at 00GMT (JUL). These dates were chosen only because they allowed the greatest ease in extracting data from available tapes. Synoptic cases were chosen rather than a time-average of a longer period of observations because of the objective to improve analyses for instantaneous forecast models, not climate prediction models. However, it is obviously desirable to identify typical similarities and differences between the fields for an analysis scheme usable for all synoptic situations. The preferred method would be to analyze many synoptic events separately and then average the statistics, especially in the spectral analyses. Since this is only a preliminary study, it is not claimed that the relationships discovered are totally representative of typical relationships between the various meteorological fields. However, many of the relationships discovered in this study would be expected to hold up in such an expanded study.

In extracting the data from the FGGE tapes a cutoff time of \pm two hours was used. Only upper-air (radiosonde) data were used for this study. In addition, only observations which satisfied the horizontal and vertical quality control checks were used. Once each data set was extracted, individual observations which were clearly erroneous were removed — an average of about two observations for each parameter per mandatory pressure level. The resulting data values were plotted on large mercator projection maps and were hand-analyzed. Examples of these maps are shown in Figs. 1a-1. Such maps were prepared for both JUL and JAN cases and for the parameters T (temperature, $^{\circ}$ K) and q (specific humidity, g/kg) for all mandatory levels between the surface and 300 mb, for Z (geopotential height, gpm) at 500 mb, and mean sea level (MSL) pressure. While all of the resulting maps were studied, further discussions in this report will concentrate on the 850 mb and 500 mb levels.

Because of the relative sparsity of data in the Southern Hemisphere and over all oceans except possibly the North Atlantic, no strong arguments can be made for the accuracy of the contours drawn in these regions.



Fig. 1a. Subjective analysis of mean sea level pressure (mb) for JAN at 00GMT. Only rawinsonde and surface land/marine observations were used and only observations made within two hours of 00GMT (before and after) were included. Contours drawn over the oceans and Southern Hemisphere are not necessarily accurate.

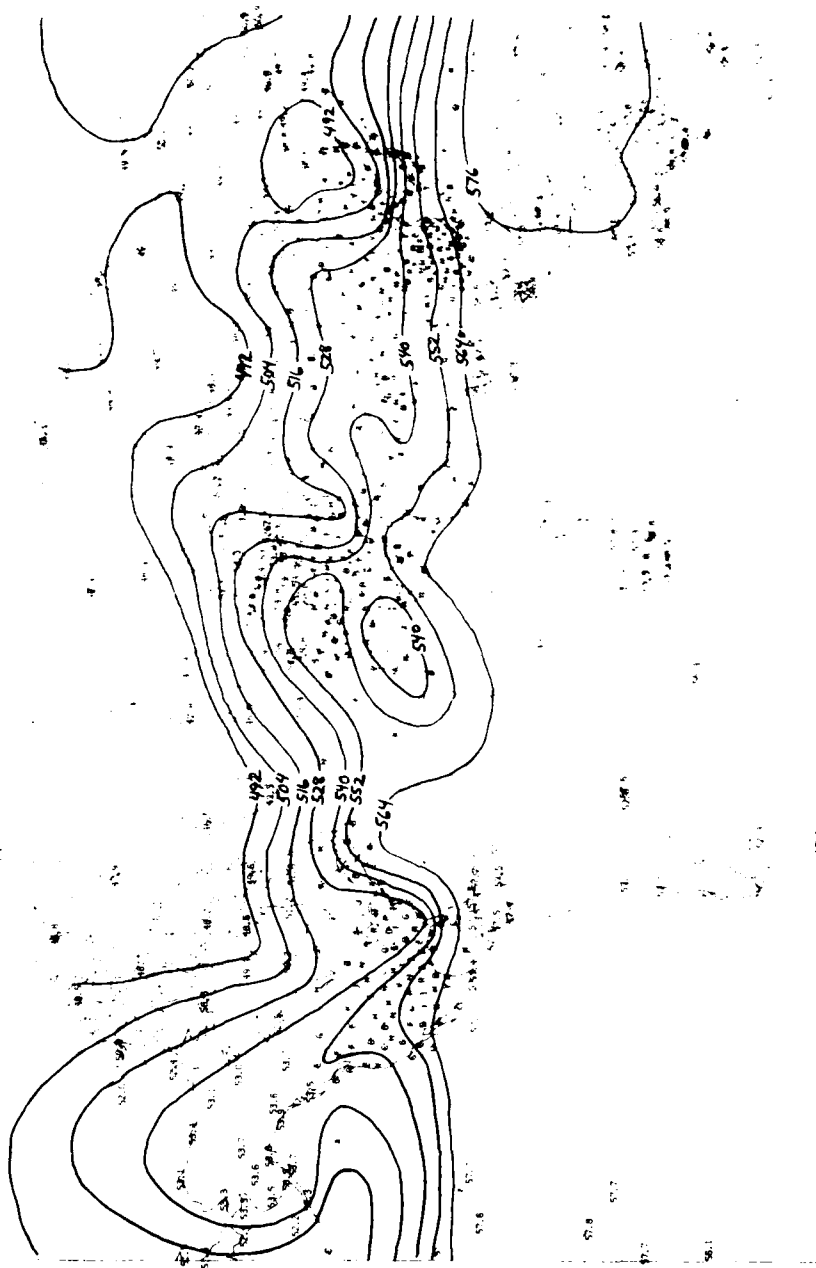


Fig. 1b. Subjective analysis of 500 mb geopotential height (dam) for JAN at 00MT. Only rawinsonde and surface land/marine observations were used and only observations made within two hours of 00MT (before and after) were included. Contours drawn over the oceans and Southern Hemisphere are not necessarily accurate.

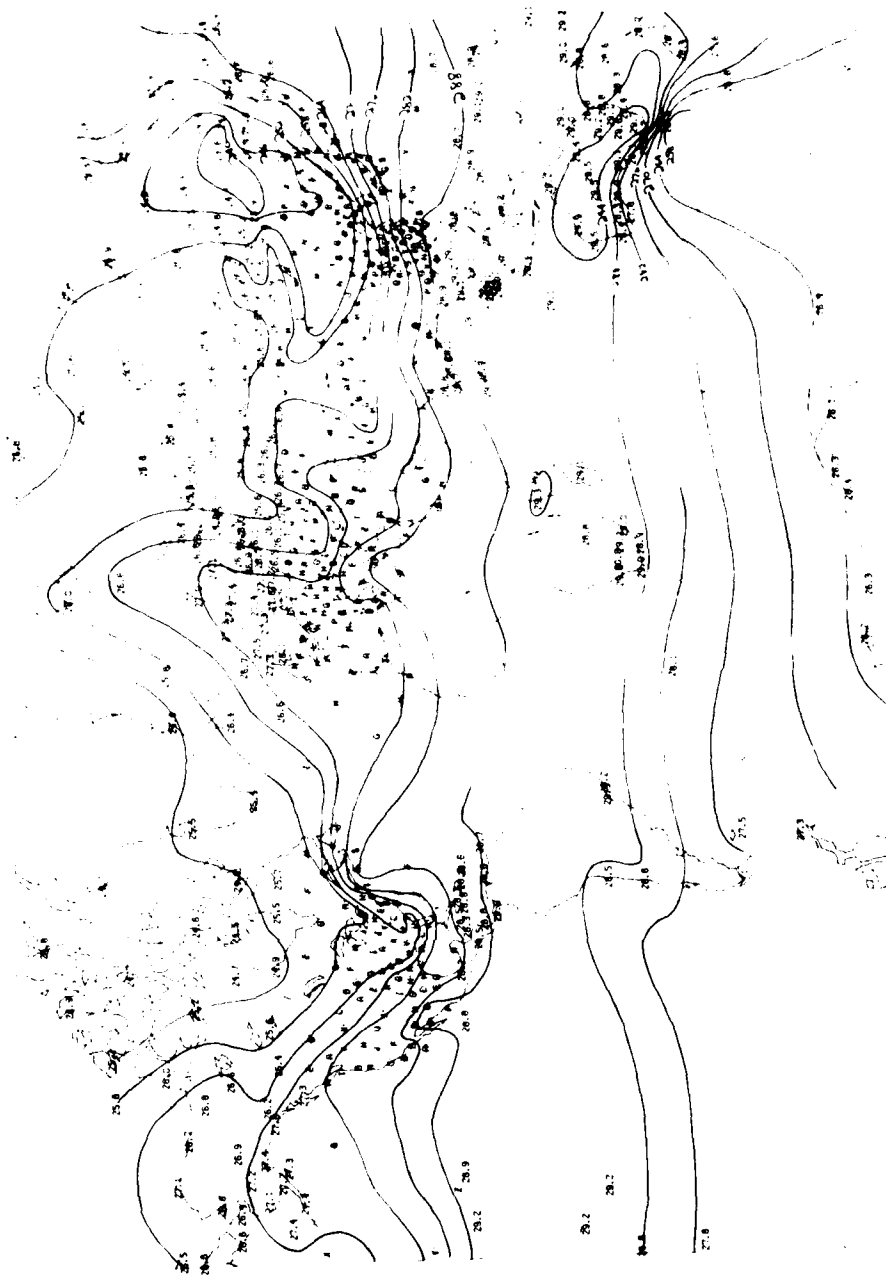


Fig. 1c. Subjective analysis of 850 mb temperature ($^{\circ}\text{K}$) for JAN at 00GMT. Only rawinsonde and surface land/marine observations were used and only observations made within two hours of 00GMT (before and after) were included. Contours drawn over the oceans and Southern Hemisphere are not necessarily accurate.

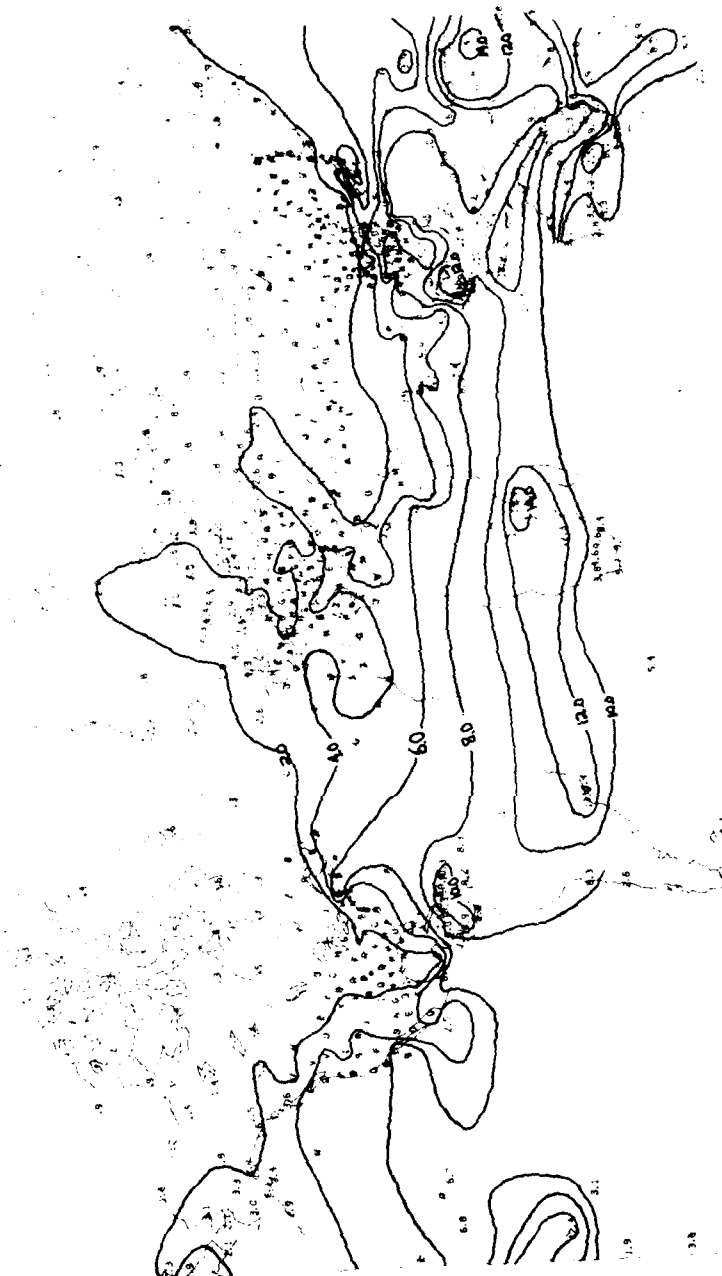


Fig. 1d. Subjective analysis of 850 mb specific humidity ($q \text{ kg}^{-1}$) for JAN at 00GMT. Only rawinsonde and surface land/marine observations were used and only observations made within two hours of 00GMT (before and after) were included. Contours drawn over the oceans and Southern Hemisphere are not necessarily accurate.

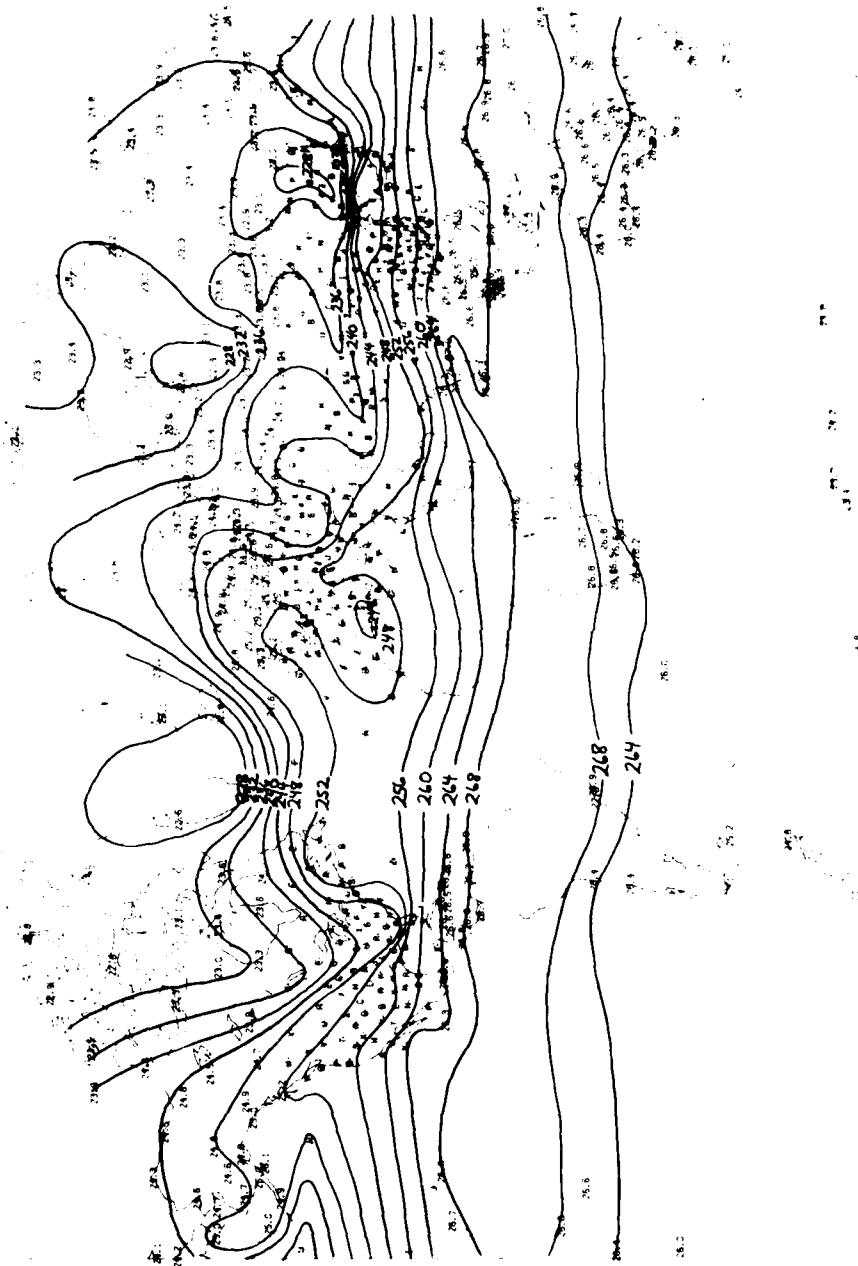


Fig. 1e. Subjective analysis of 500 mb temperature ($^{\circ}\text{K}$) for JAN at 00GMT. Only rawinsonde and surface land/marine observations were used and only observations made within two hours of 00GMT (before and after) were included. (Contours drawn over the oceans and Southern Hemisphere are not necessarily accurate.)



Fig. 1f. Subjective analysis of 500 mb specific humidity (g kg^{-1}) for JAN at 00GMT. Only rawinsonde and surface land/marine observations were used and only observations made within two hours of 00GMT (before and after) were included. Contours drawn over the oceans and Southern Hemisphere are not necessarily accurate.

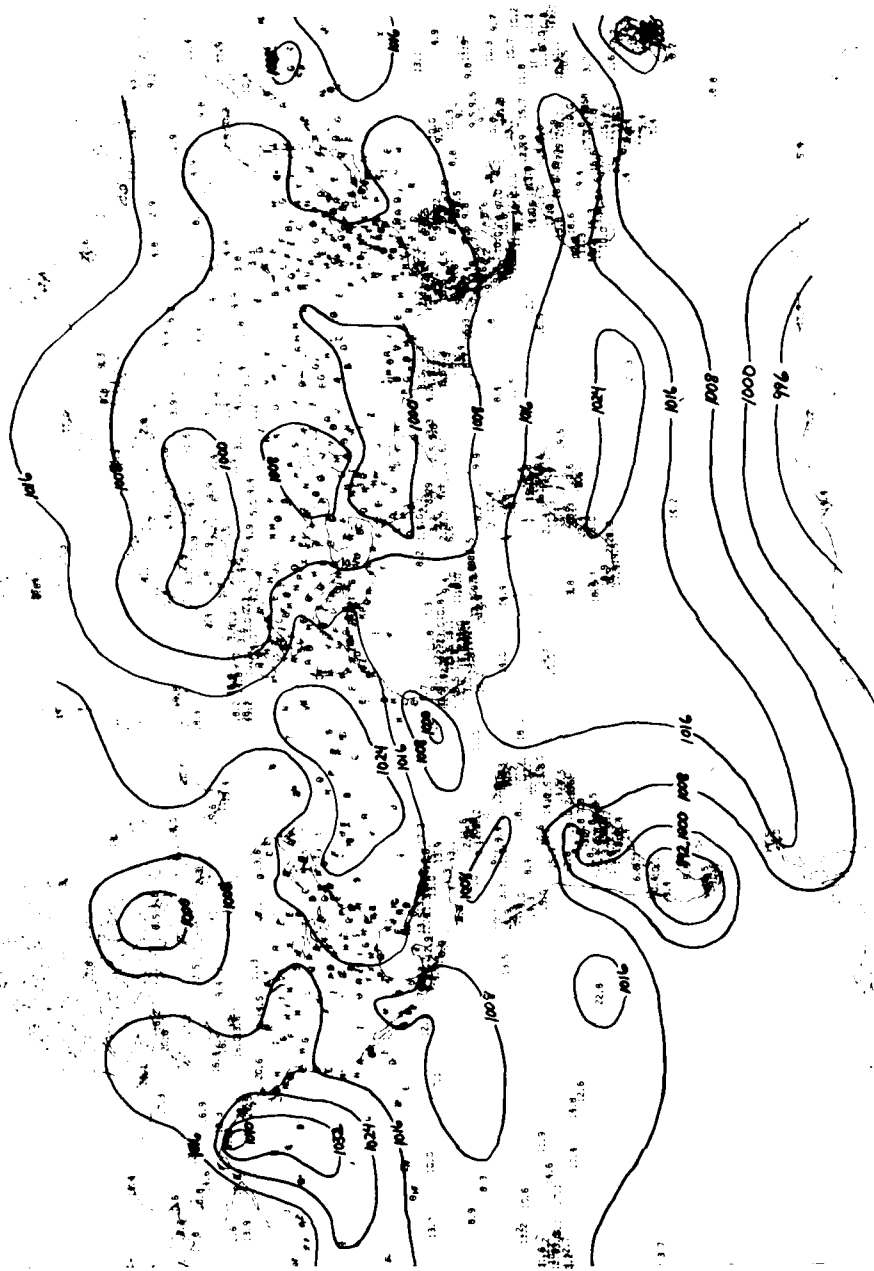


Fig. 19. Subjective analysis of mean sea level pressure (mb) for JUL at 00GMT. Only rawinsonde and surface land/marine observations were used and only observations made within two hours of 00GMT (before and after) were included. Contours drawn over the oceans and Southern Hemisphere are not necessarily accurate.

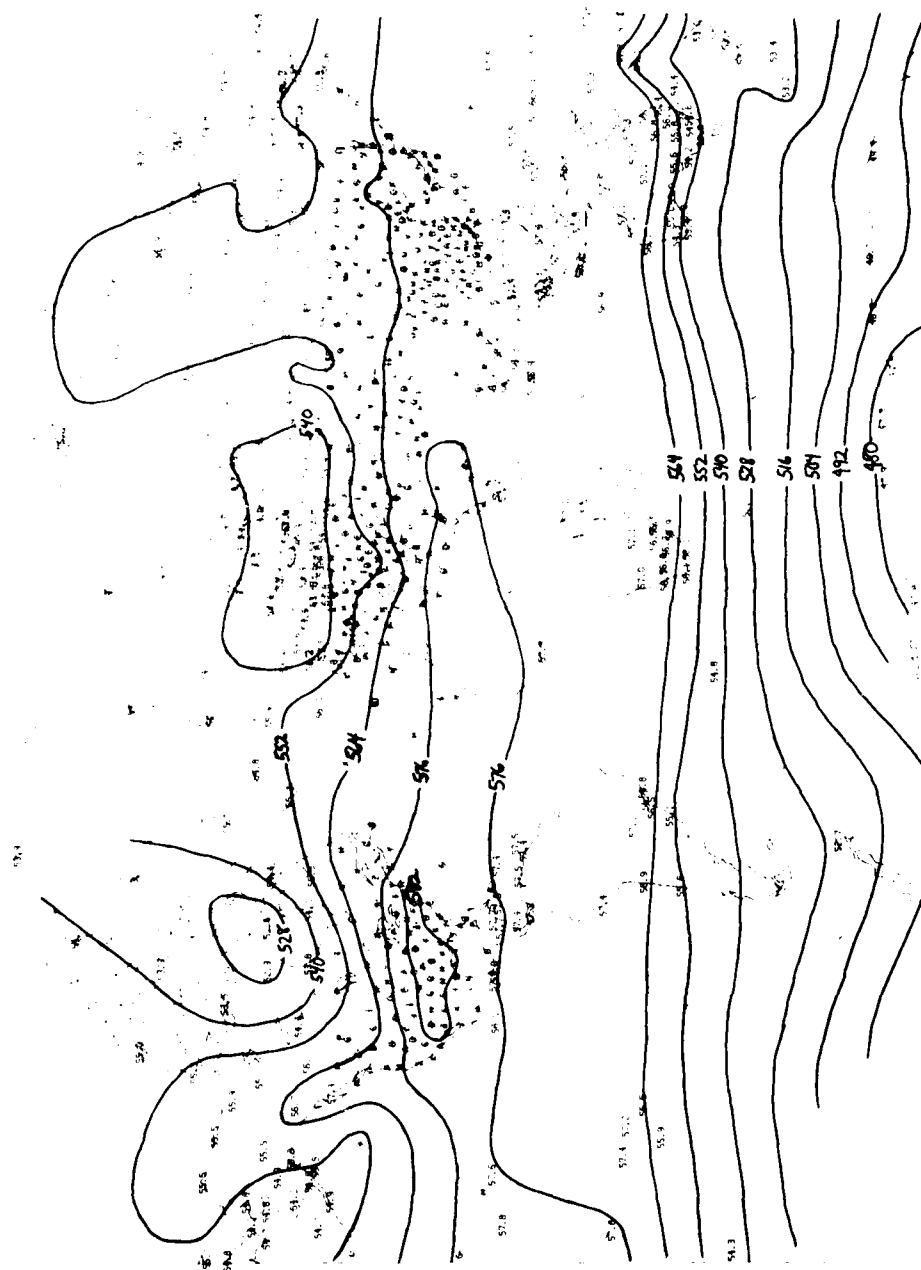


Fig. 1h. Subjective analysis of 500 mb geopotential height (dam) for JUL at 00GMT. Only rawinsonde and surface land/marine observations were used and only observations made within two hours of 00GMT (before and after) were included. Contours drawn over the oceans and Southern Hemisphere are not necessarily accurate.

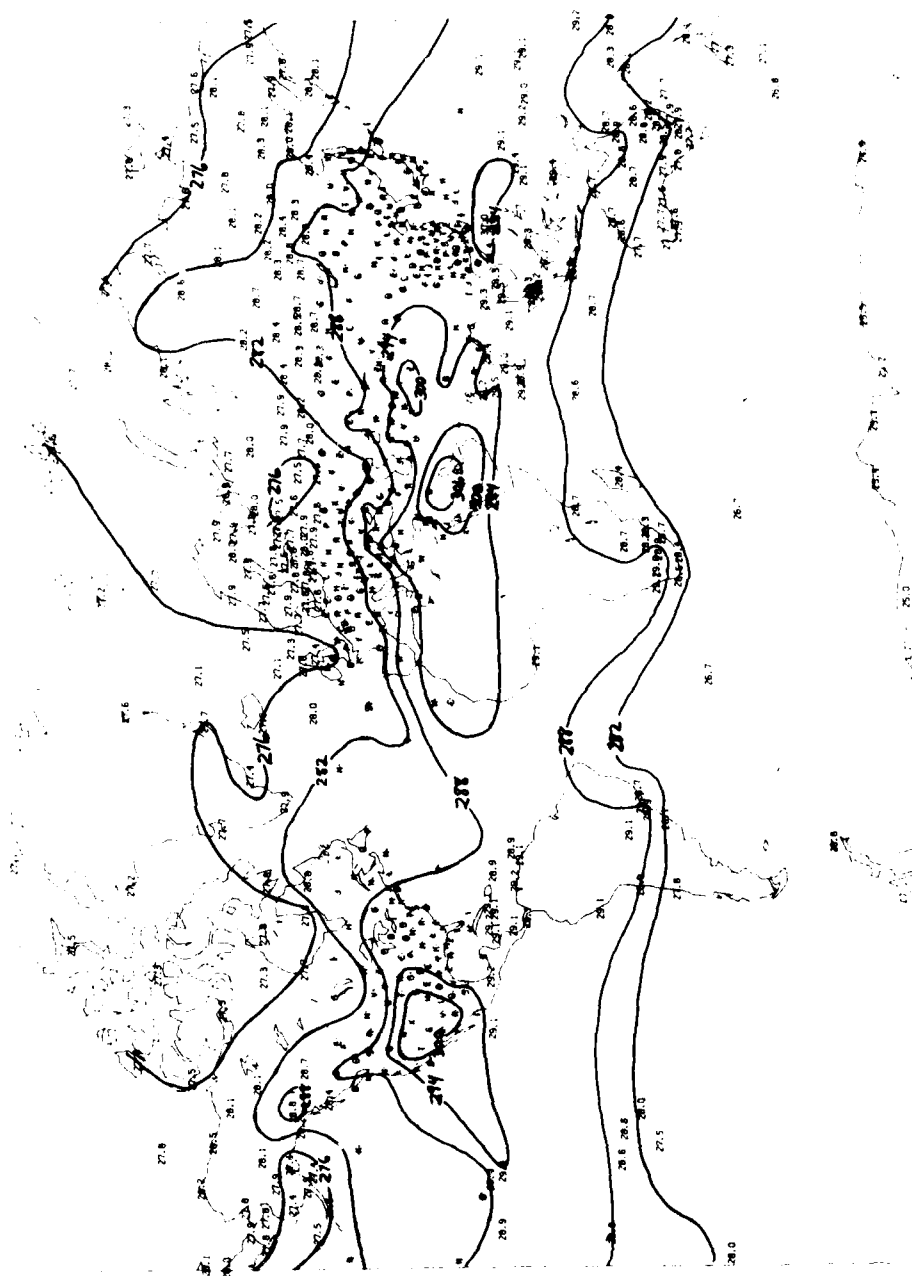


Fig. 11. Subjective analysis of 850 mb temperature ($^{\circ}\text{K}$) for JUL at 00GMT. Only rawinsonde and surface land/marine observations were used and only observations made within two hours of 00GMT (before and after) were included. Contours drawn over the oceans and Southern Hemisphere are not necessarily accurate.

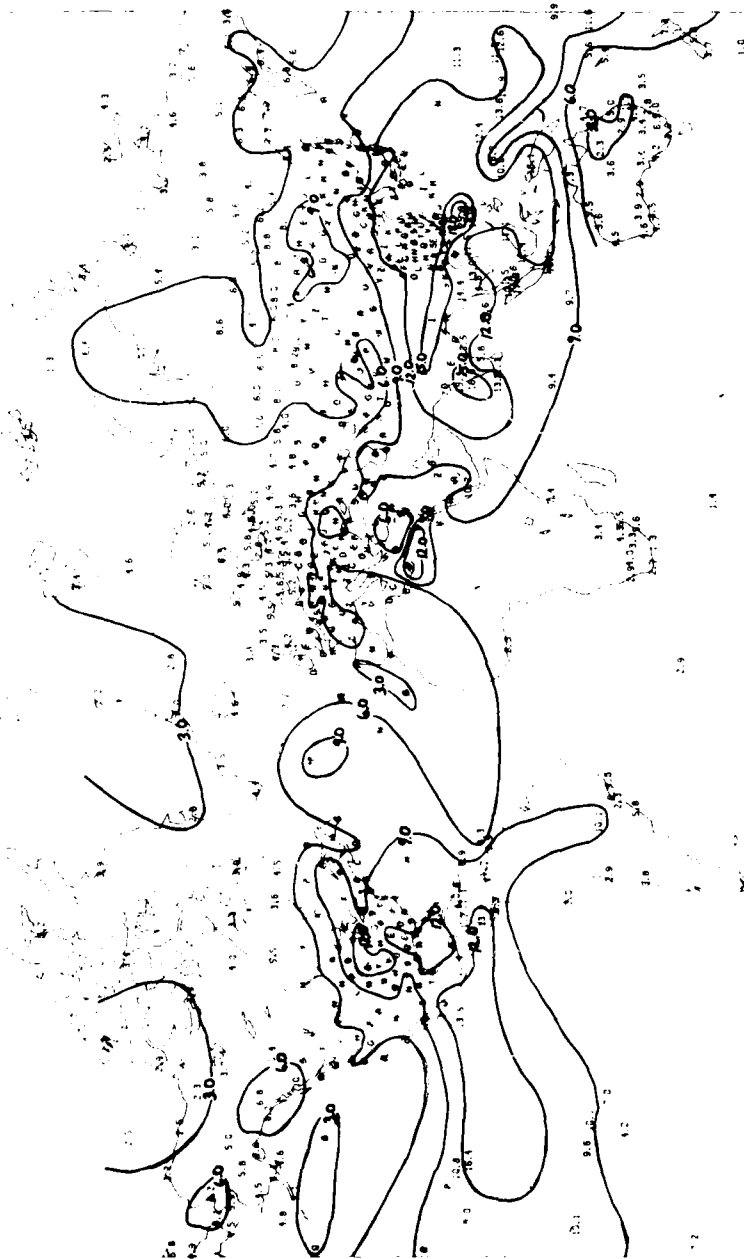


Fig. 1j. Subjective analysis of 850 mb specific humidity (g kg^{-1}) for JUL at 00GMT. Only rawinsonde and surface land/marine observations were used and only observations made within two hours of 00GMT (before and after) were included. Contours drawn over the oceans and Southern Hemisphere are not necessarily accurate.



Fig. 1k. Subjective analysis of 500 mb temperature ($^{\circ}$ K) for JUL at 00GMT. Only rawinsonde and surface land/marine observations were used and only observations made within two hours of 00GMT (before and after) were included. Contours drawn over the oceans and Southern Hemisphere are not necessarily accurate.

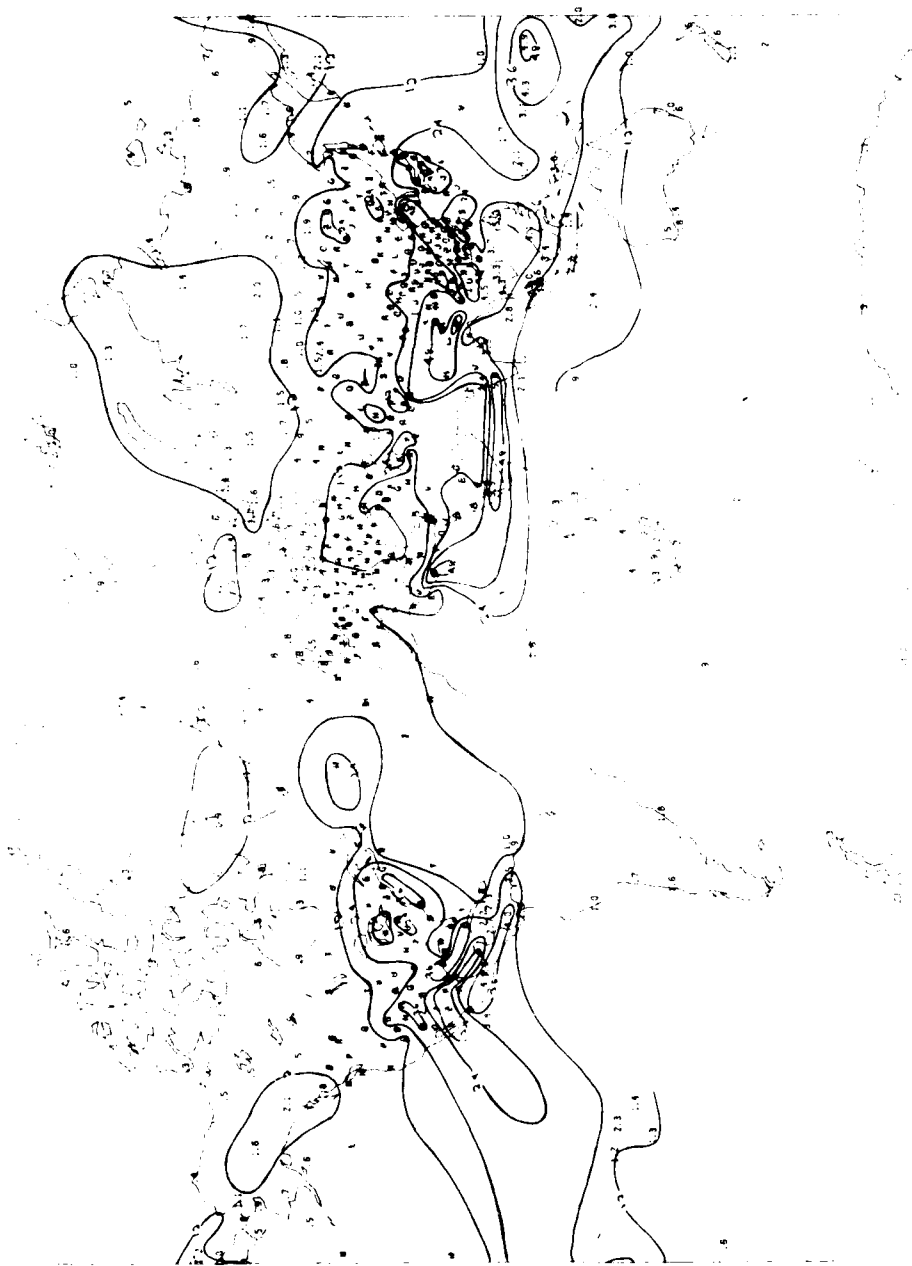


Fig. 11. Subjective analysis of 500 mb specific humidity (g kg^{-1}) for JUL at 00GMT. Only rawinsonde and surface land/marine observations were used and only observations made within two hours of 00GMT (before and after) were included. Contours drawn over the oceans and Southern Hemisphere are not necessarily accurate.

(Contours were not drawn to fit data values which appeared suspect when compared with surrounding values.) Therefore, our discussions of physical fields will focus on the Northern Hemisphere and primarily over and near the continents. Because of the low spatial resolution inherent in such a representation, only comparisons in the average and large-scale eddy domains can be made. No attempt is made to identify small-scale similarities or differences in these physical space representations.

Climatologically, the zonally averaged moisture is a maximum at the equator and decreases monotonically toward the poles (Oort and Rasmusson, 1971).³ This is reflected in the cases represented here. Of greater interest, however, are the departures from the zonal mean which may result from (1) land masses and (2) disturbances in the zonal mean flow. The former can be accounted for by climatological studies of moisture distribution. A product of one such study is shown, in Fig. 2, where Peixoto (1970)⁴ plots the time-averaged vertically integrated precipitable water \hat{w} defined in terms of the time-averaged specific humidity \hat{q} as

$$\hat{w} = \hat{q}^{-1} \int_{\text{sfc}}^{300 \text{ mb}} \hat{q} \, dp \quad (1)$$

where q is the acceleration due to gravity and p is pressure. By removing the zonal mean at each latitude from both the time-averaged field and any synoptic field, one can compare the magnitude of the departure from the zonal mean due entirely to the land masses with that due to eddies which appear in the chosen synoptic case. For example, when the JAN q field was used for the synoptic field, the two sources of departures from the zonal mean were found to be of the same order of magnitude. Calculations using q data for a station at 43.72° N and 65.25° W (near the moisture maximum associated with the northwest Atlantic storm) indicated a departure of $2.3 \times 10 \text{ kg m}^{-2}$ in precipitable water from the zonal average for JAN at 45° N computed from Cressman corrected q fields (explained in Section III). This largest eddy departure is compared to the largest

3. Oort, A. H., and E. M. Rasmusson, 1971: Atmospheric Circulation Statistics. NOAA Prof. Pap. No. 5 (NTIS-72-50295). 323 pp.
4. Peixoto, J. P., 1970: Water vapor balance of the atmosphere from five years of hemispheric data. Nordic Hydrol., 2, 120-138.

departure from the zonal mean of the time-averaged values on Fig. 2 (over the Sahara) of $-1.8 \times 10 \text{ kg m}^{-2}$ (where the time-averaged zonal mean was computed from Oort and Rasmusson for 30° N , yearly average).

Considering both contributions, we see perturbations in the zonally averaged moisture field for both dates. Identifying cyclonic systems from the MSL pressure map, we see disturbances over the west and east coasts of the U.S., eastern Europe, and off the east coast of Asia for JAN. In all four cases the moisture contours on the 850 mb diagram are

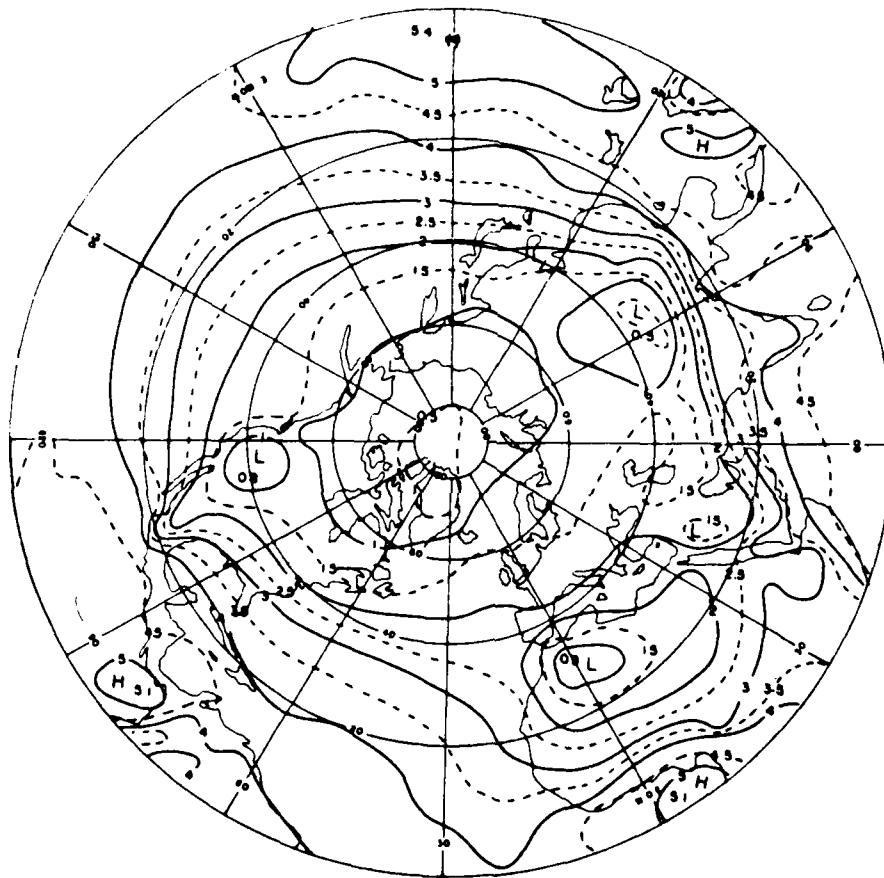


Fig. 2. Polar stereographic map of vertically integrated time mean precipitable water \bar{W} for the period May 1, 1958 - April 30, 1963. Units for \bar{W} are $\times 10 \text{ kg m}^{-2}$ (from Rosen et al., 1979⁵; taken originally from Peixoto, 1970).

5. Rosen, R. D., O. A. Salstein, and J. F. Peixoto, 1979: Variability in the annual fields of large-scale atmospheric water vapor transport. *Mon. Wea. Rev.*, 107, 26-37.

pushed northward ahead of the surface low and southward behind it. This is also true of the major circulations which appear on the JUL MSL pressure map. The "Bermuda High" centered in the Atlantic is pushing moisture into the central U.S., while the somewhat weaker cyclonic circulation over the Persian Gulf area is advecting moist air into central China and dry air into the eastern Mediterranean. This correlation between flow perturbations and moisture perturbations is also evident at 500 mb, although less so because of the smaller moisture values at this level.

The temperature advection patterns are at least as clearly seen as those of moisture. Positive departures from the zonal mean exist where southerly flow occurs and negative departures exist in regions of northerly flow. This is the nature of the eddies, as they act to offset the pole-equator temperature gradient which is primarily responsible for their origin and maintenance. Thus the large scale eddies bring cold, dry air equatorward and warm, moist air poleward. The correlation between warm and moist areas and dry and cold areas in the midlatitudes is clear in the figures.

An explanation should be given as to why specific humidity was used in the study rather than relative humidity. Initially, maps such as those in Fig. 1 were prepared for relative humidity in the same manner as for the other parameters. It was seen immediately that relative humidity observations showed a high degree of spatial irregularity - pockets of high humidity were often located next to pockets of low humidity at all levels. Such a discontinuous field is very difficult to analyze subjectively, and the ability of any objective analysis scheme to replicate such a highly irregular field is questionable. The specific humidity was somewhat more irregular than other fields but was more continuous spatially than relative humidity and therefore was used in this study.

III. Construction and Comparison of Analyzed Fields

To compare more closely the scales of variation in the moisture fields with those of the other parameters, it was necessary to obtain representations of the observed values on a regular grid. This could be done through a direct interpolation of the observations onto grid points, but any choice of interpolation would act to modify the spectral character of the field. Because this study concentrates on characteristics of observed fields, it is important to construct an analysis field which is most representative

of the observations. The Flattery analyses in the Level III FGGE data set² include the biases of this particular analysis scheme (e.g., a truncation at 15° longitude wavelength) and cannot be said to be the most representative of the data. This fact was demonstrated by Chu and Parrish (1977)⁶ when they showed that a simple scheme that transfers data to grid points resulted in a humidity field that better represented observations than the Flattery analysis (described by Cooley, 1974⁷) for a case over the eastern U.S. The method chosen for this study used the Flattery analyses as first-guess fields, then observations were used to correct the field in successive scans following directly (in a univariate manner) the well-known scheme developed by Cressman (1959)⁸. The same number of scans, scan radii, and distance weighting function given by Cressman were used in this study.

Upon completion of the Cressman correction fields, both the original field (FG) and the corrected field (CFG) were interpolated bilinearly to the observation locations for comparison with the observed values (OB). The following root mean square error quantities were then calculated for each field:

$$R_{CFG} = \left[\frac{\sum_{i=1}^N (CFG_i - OB_i)^2}{N} \right]^{1/2}, \quad R_{FG} = \left[\frac{\sum_{i=1}^N (FG_i - OB_i)^2}{N} \right]^{1/2}$$

where N is the number of observations used in each field for correction of the first guess. The quantity $1 - (R_{CFG}/R_{FG})$ can then be used as a measure of how much impact the observations had in correcting the first guess field; the closer to unity, the more the corrected field is like the observed field. Values for this quantity are given in Table 1.

After their construction, the corrected fields were plotted on a mercator projection map in order to compare their gross features with the subjective analysis maps. The figures for q' and v', departures from

6. Chu, R., and D. Parrish, 1977: Humidity analyses for operational prediction models at the National Meteorological Center. Office Note 140, National Meteorological Center, NWS, NOAA.
7. Cooley, D. S., 1974: A description of the Flattery global analysis method - No. 1. Tech. Proc. Bul. No. 105, NWS, NOAA.
8. Cressman, G., 1959: An operational objective analysis system. Mon. Wea. Rev., 87, 367-374.

zonal averages, are included in Figs. 3a-d. The areas of moisture perturbation mentioned earlier are seen, and a correlation with v' is clear for those areas from the maps.

TABLE 1. FORMULATION OF CRESSMAN-CORRECTED FIELDS.

Quantity	No. of Obs.	1/15, 78	No. of Obs.	1/29, 78
		$1 - (R_{CPG} / R_{PG})$		$1 - (R_{CPG} / R_{PG})$
T SFC	2079	.22106	2258	.29298
T 1000	354	.54706	296	.57463
T 850	601	.28393	619	.36135
T 700	559	.40271	564	.38666
T 500	621	.20505	644	.25932
T 400	508	.35490	533	.36533
T 300	571	.39409	624	.39354
T 1000	348	.50520	290	.59354
T 850	584	.45768	606	.50569
T 700	506	.38845	526	.30987
T 500	541	.48644	554	.46568
T 400	492	.60817	434	.41448
T 300	324	.71423	426	.41211
P MSL	2079	.22058	2258	.23681
Z 500	615	.24860	639	.32142
U 850	764	.31467	831	.32220
U 500	678	.21041	742	.12747
V 850	764	.33704	831	.34187
V 500	678	.25073	742	.24275

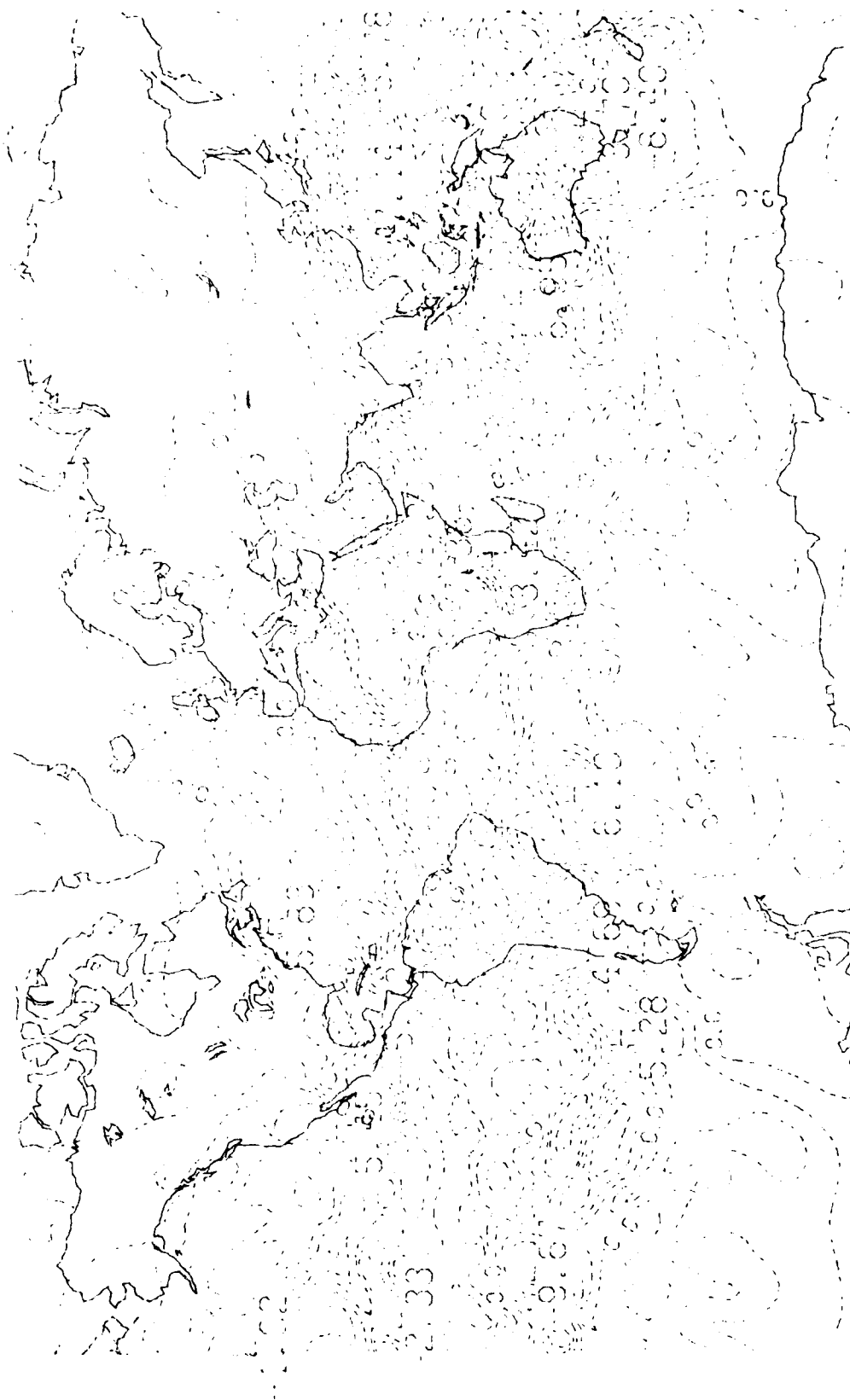
The corrected fields were analyzed spectrally using both zonal and spherical harmonic expansions. The departure from the zonal average A' was calculated for each 2.5° latitude and a fast Fourier transform (FFT) algorithm was used to obtain the coefficients a_m , b_m of the expansion of each quantity A :

$$A'(\phi, \lambda) = \sum_{m=1}^M \left(a_m(\phi) \cos m\lambda + b_m(\phi) \sin m\lambda \right) \quad (2)$$

where ϕ is latitude, λ longitude, m is the zonal wave number out to $m = 72$ in this case (note that $m = 0$ is identically zero because the zonal mean was removed). Next, the normalized zonal power $F_m(\phi)$ was calculated from

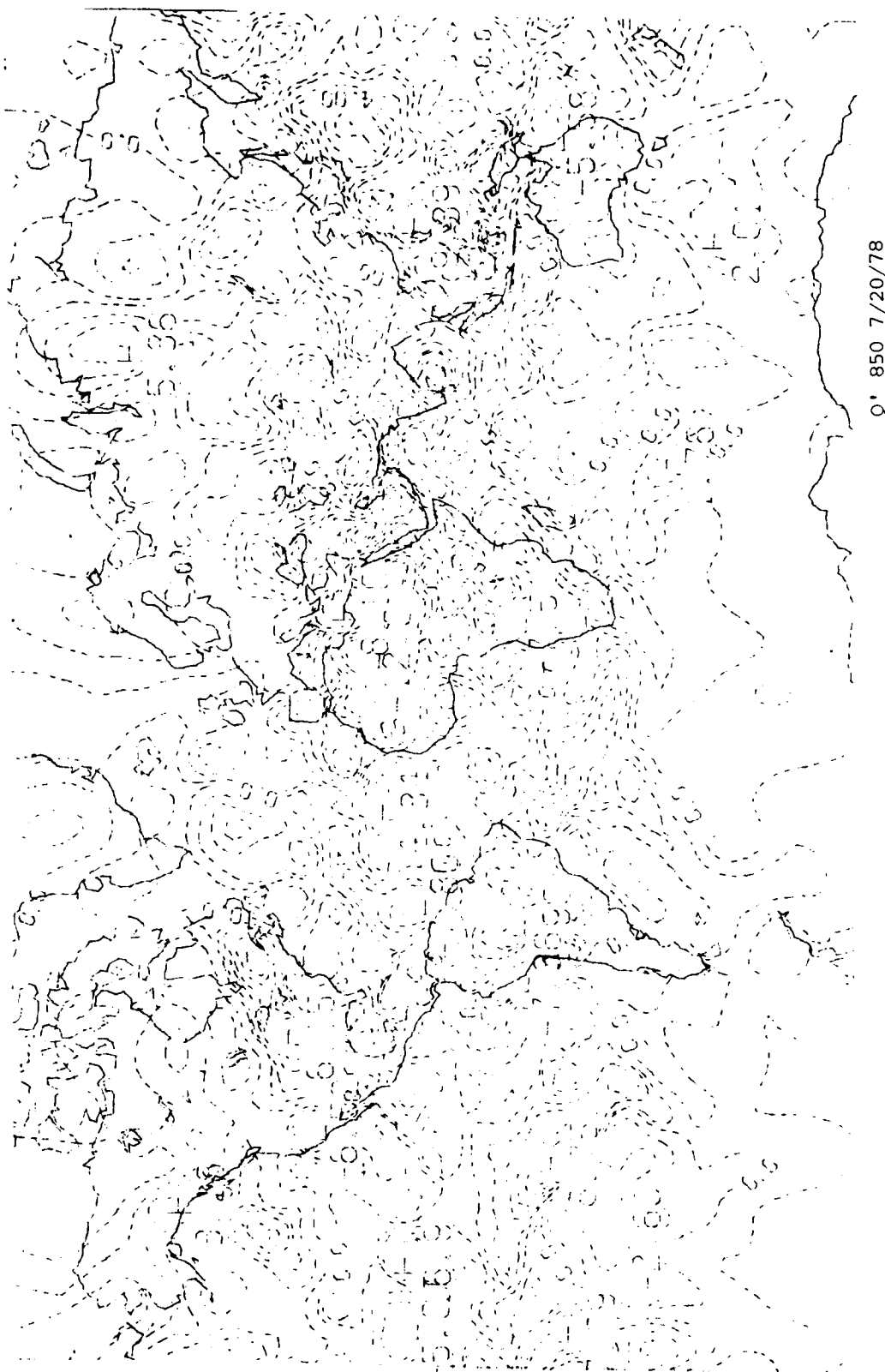
$$F_m(\phi) = \frac{a_m^2 + b_m^2}{\sum_{m=1}^M (a_m^2 + b_m^2)} \quad (3)$$

Thus the fractional contributions F_m over all wave numbers for a particular latitude should add up to unity. Figs. 4a-d show the normalized



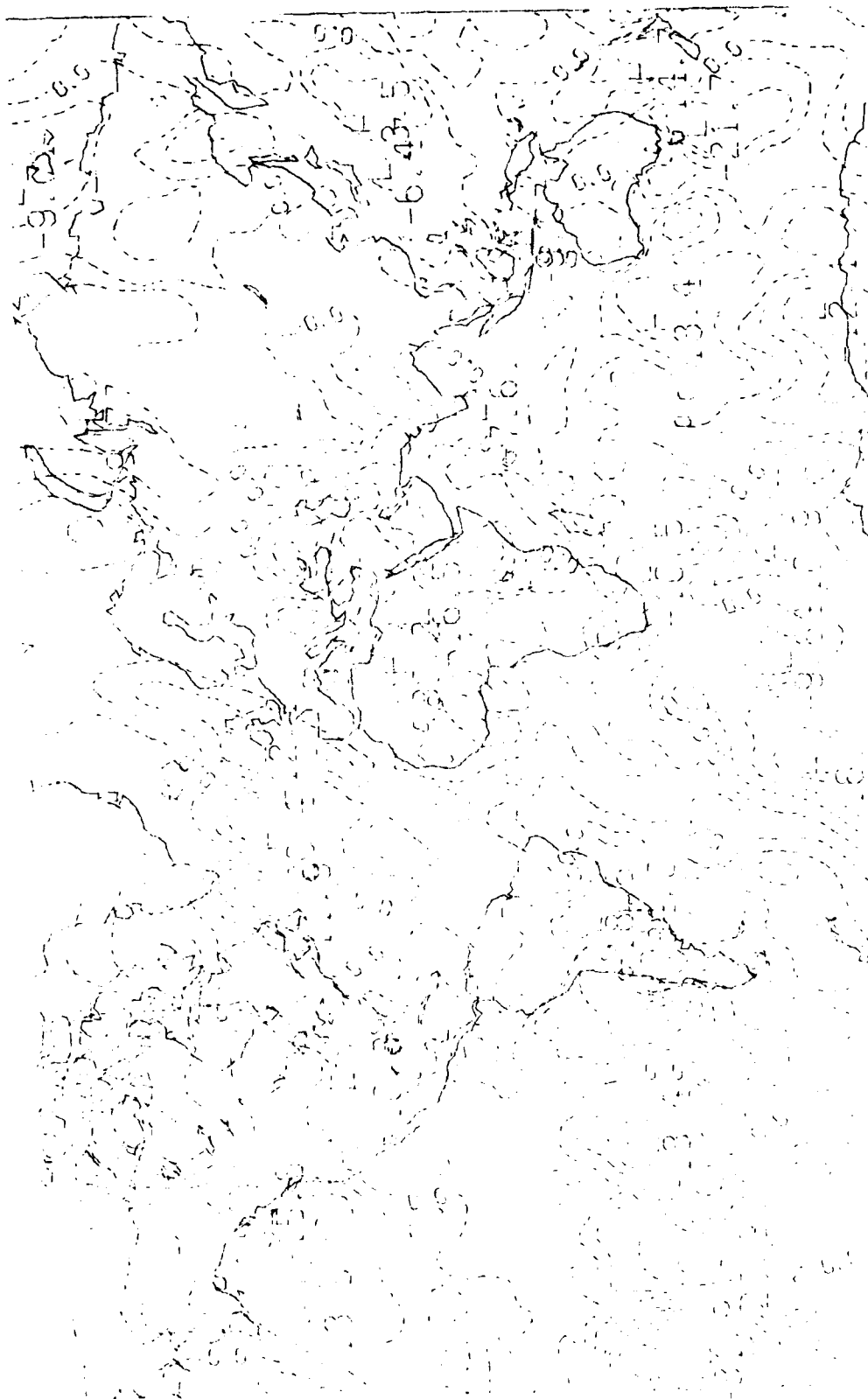
Q' 850 1/15/78

Fig. 3a. Departures from zonal averages for corrected fields. Units are $g\ kg^{-1}$, contour interval is $1\ g\ kg^{-1}$.



Q' 850 7/20/78

Fig. 3c. -1 Departures from zonal averages for corrected fields. Units are $g\ kg^{-1}$, contour interval is $1\ g\ kg^{-1}$.



V: 850 7/20/78

Fig. 3d. Departures from zonal averages for corrected fields. Units are $m s^{-1}$, contour interval is $5 m s^{-1}$.

power plotted vs. wave number for both the Flattery analysis (LVL3) fields and the observation-corrected fields for temperature and specific humidity for JUL. This spectrum was calculated using the average of the 47.5°, 50.0°, and 52.5° N latitude values, from which the departure from the zonal average was calculated and a_m and b_m were obtained. This latitude band was chosen because it consistently contained the greatest number of observations, and therefore should be the region of greatest difference between the LVL3 field and the corrected field. As expected, the greatest difference appears at wave numbers 25 and greater especially in the temperature, because of the truncation of the Flattery analysis at wave number 24. The successive correction procedure puts much of the higher wave number variation back into the spectra without making much of a change at lower wave numbers.

Figs. 5a-f illustrate the normalized power of q plotted with that of T , u , and v for comparison at this same latitude band for JAN. All of the plots are highly oscillatory, and some smoothing of this phenomenon would no doubt result from an average of such statistics calculated for a group of observations. The linear correlation coefficient value r is defined by

$$r = \frac{\overline{X_1 X_2} - \bar{X}_1 \bar{X}_2}{\left[(\overline{X_1^2} - \bar{X}_1^2) (\overline{X_2^2} - \bar{X}_2^2) \right]^{1/2}} \quad (4)$$

where X_1 and X_2 are the parameter values being compared (Panofsky and Brier, 1968⁹). It was computed using the normalized power for the two parameters plotted using only wave numbers one through 32, since values for greater wave numbers approach the noise level. Such a value gives some basis for quantitative comparison between T , u , and v as to which might represent the best approximation to the spectral composition of q . A comparison of the r values in Table 2 shows that T has a much better correlation with q than do u and v in all cases. Apparently, another quantity that is advected, in this case temperature, is more closely correlated to specific humidity than is the agent responsible for the advection, namely u and v . Perhaps the greatest contributing factor to this relationship is the tendency of both T and q to have the greatest power

9. Panofsky, H. A., and G. W. Brier, 1968: Some Applications of Statistics to Meteorology. The Pennsylvania State University, University Park, PA. 224 pp.

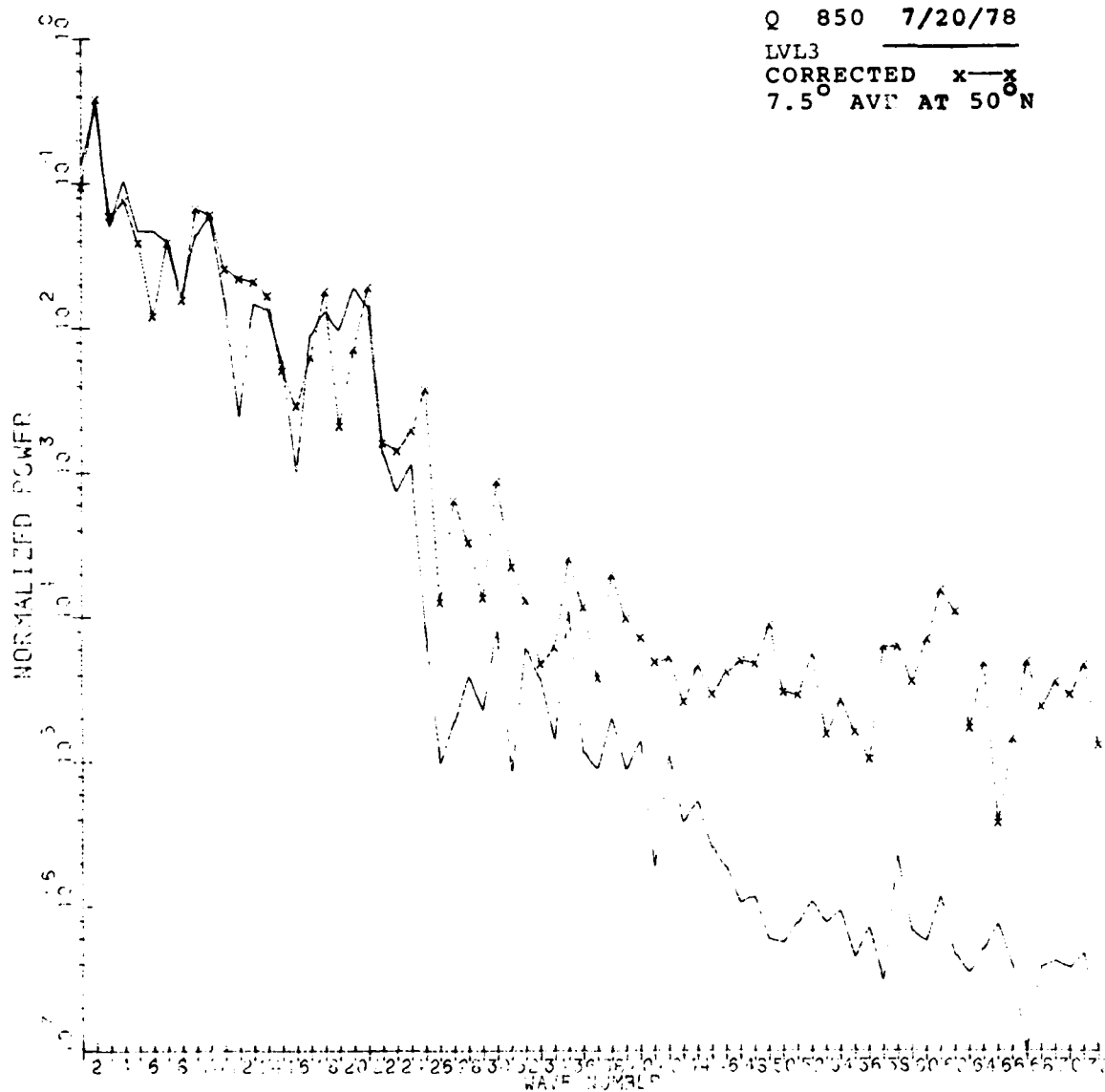


Fig. 4a. Normalized power for departures from zonal mean plotted as a function of wave number for an average of three latitude values centered at 50° N. Both LVL3 and corrected field results are plotted.

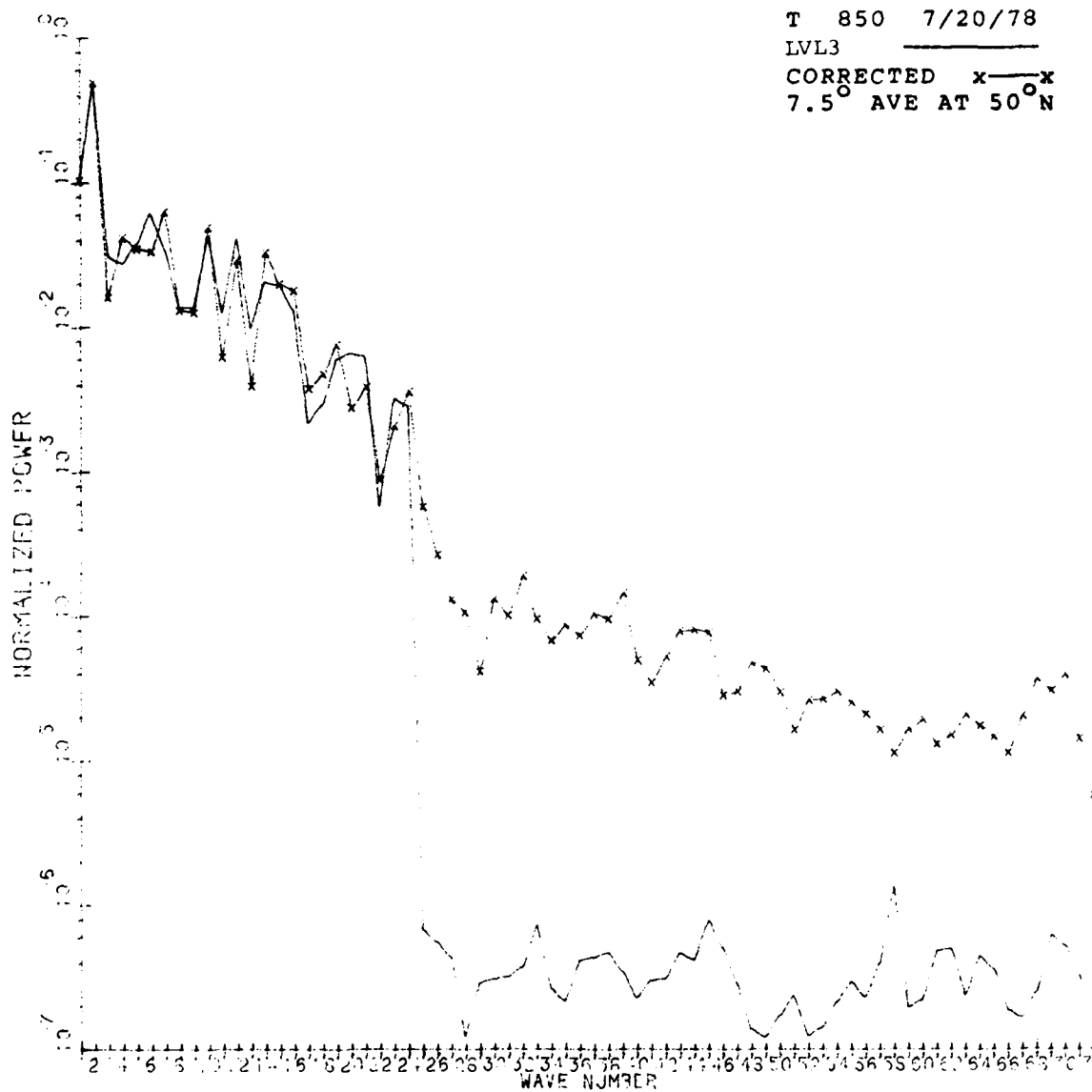


Fig. 4b. Normalized power for departures from zonal mean plotted as a function of wave number for an average of three latitude values centered at 50° N. Both LVL3 and corrected field results are plotted.

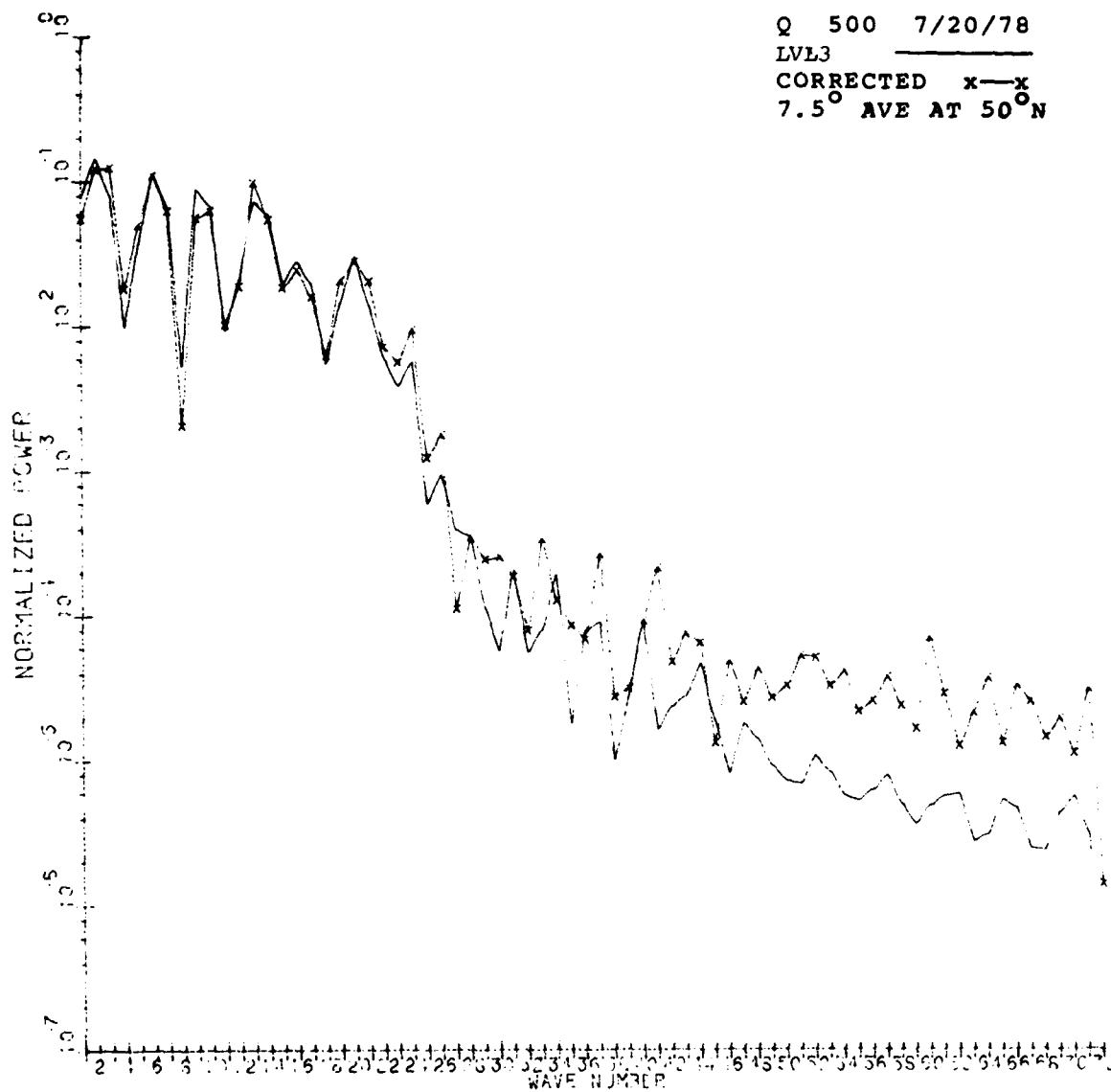


Fig. 4c. Normalized power for departures from zonal mean plotted as a function of wave number for an average of three latitude values centered at 50° N. Both LVL3 and corrected field results are plotted.

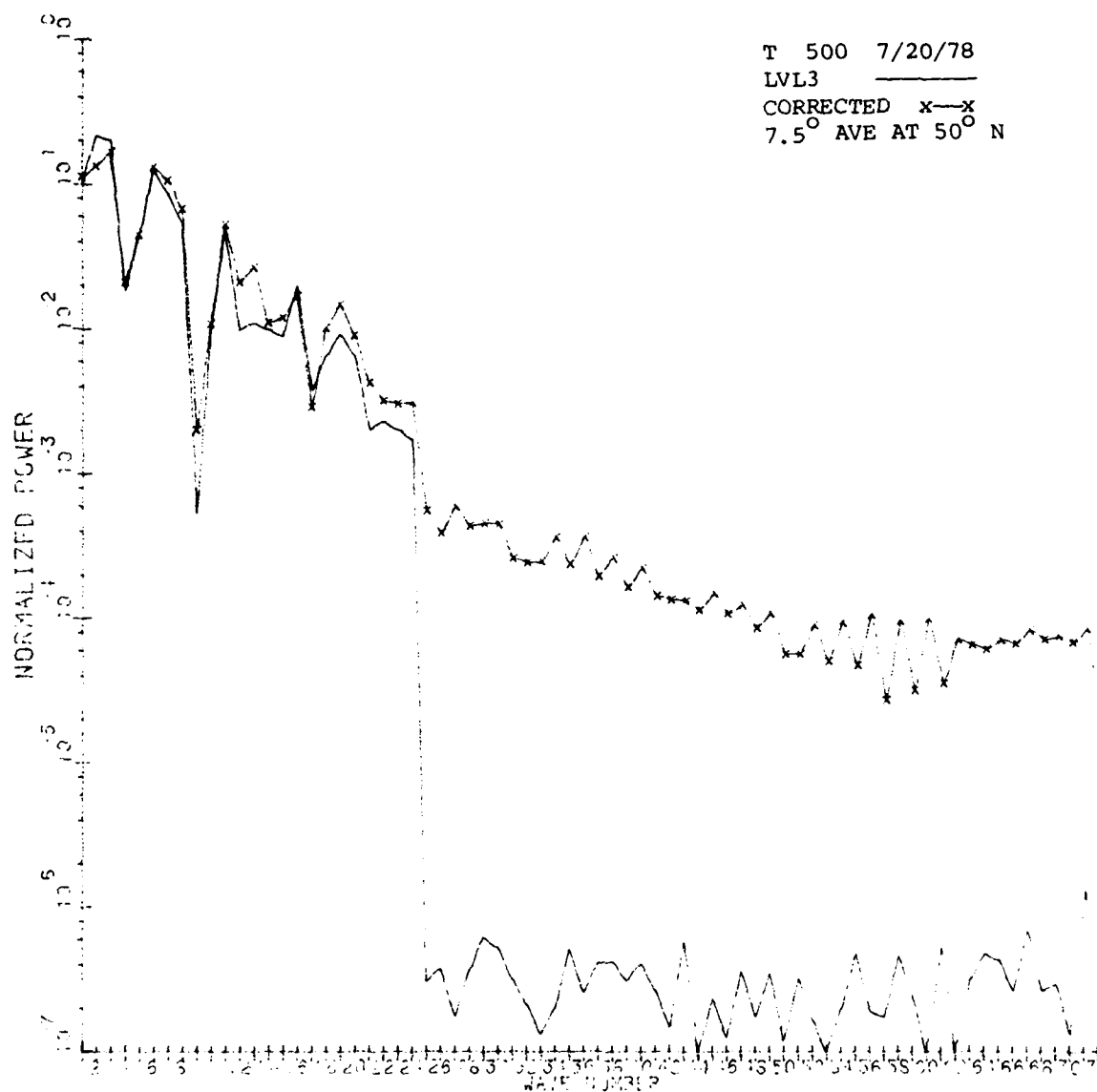


Fig. 4d. Normalized power for departures from zonal mean plotted as a function of wave number for an average of three latitude values centered at 50° N. Both LVL3 and corrected field results are plotted.

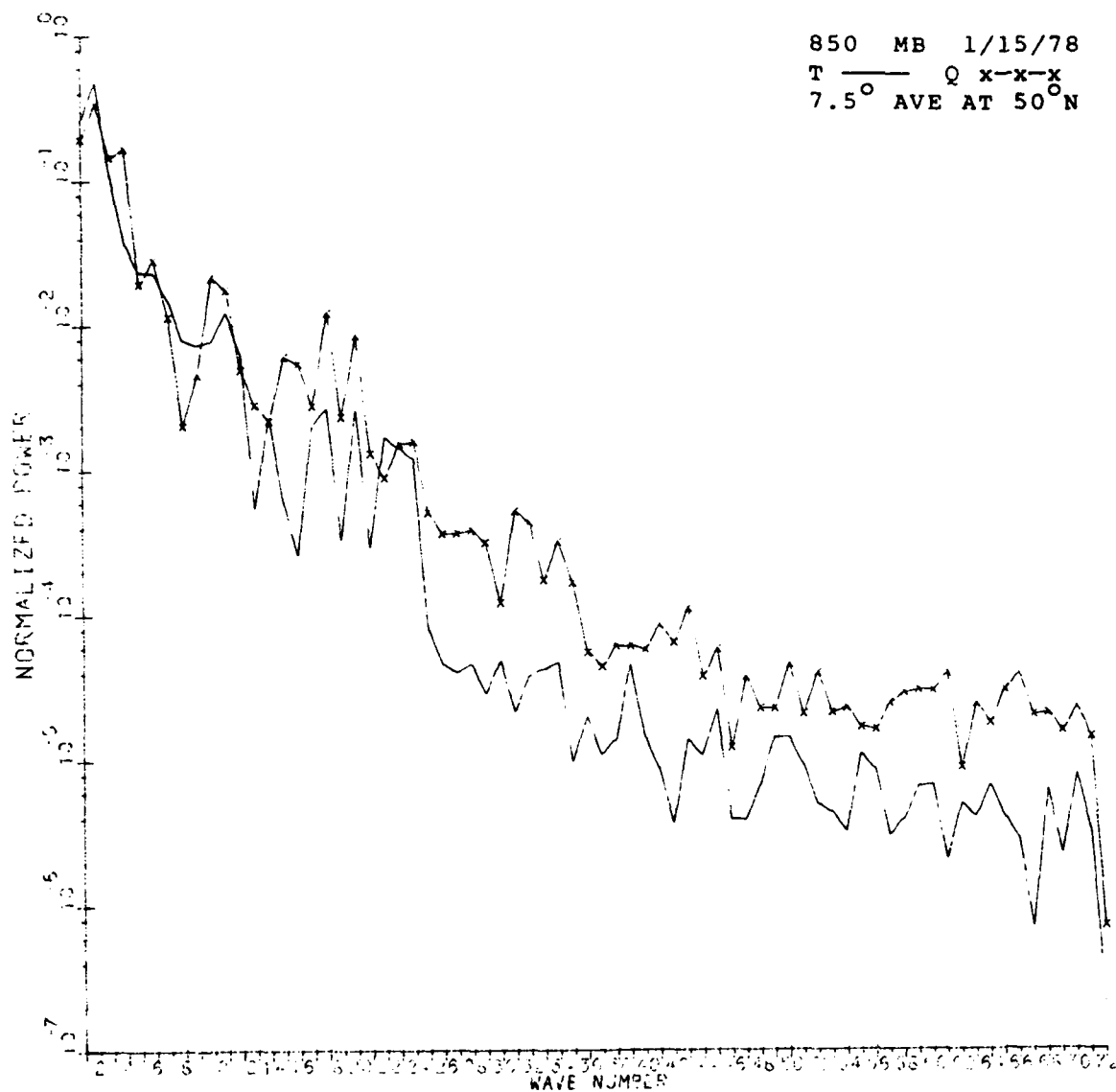


Fig. 5a. Normalized power for departures from zonal mean for a three latitude average centered at 50° N. Values for corrected fields only are plotted.

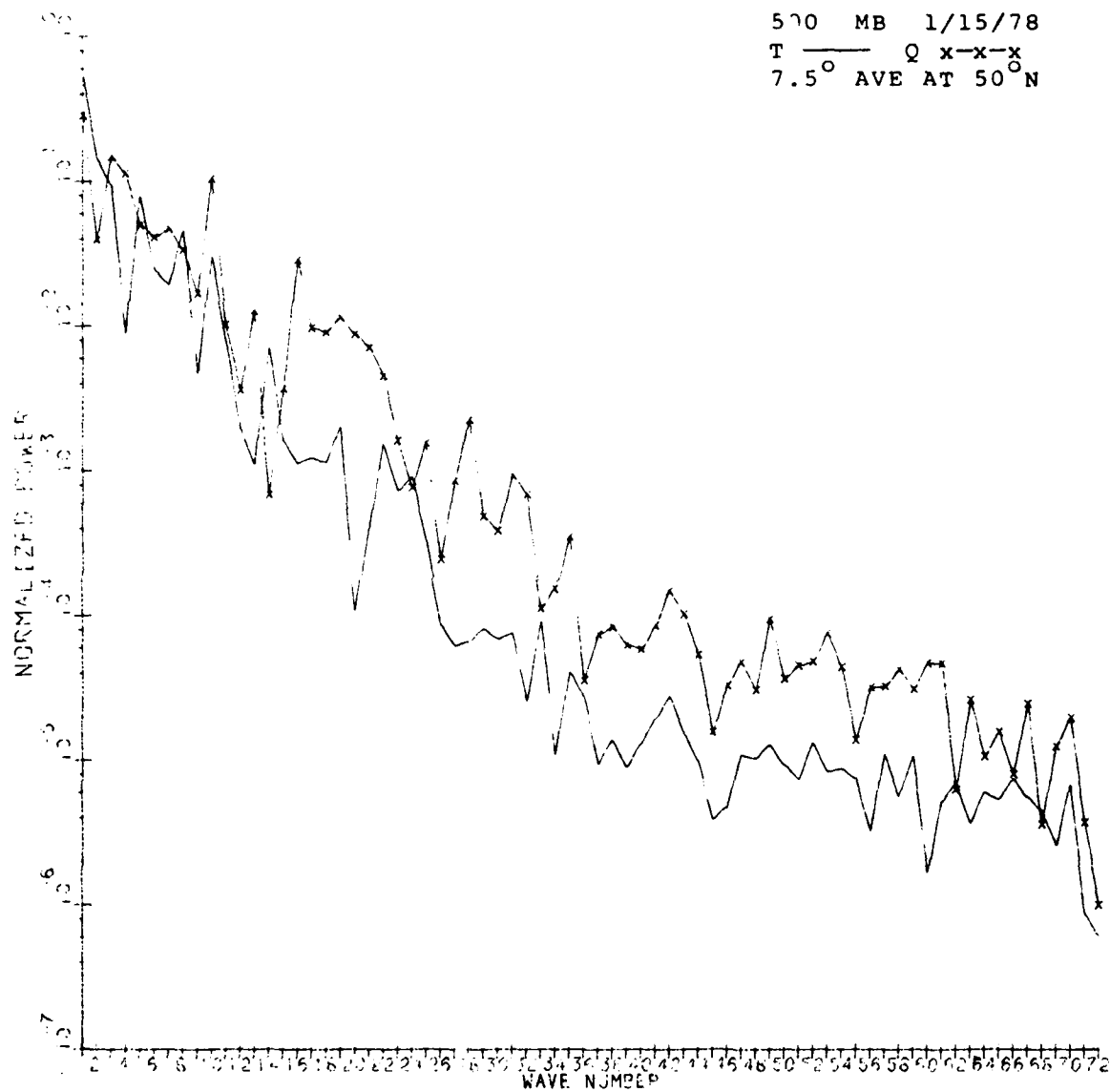


Fig. 5b. Normalized power for departures from zonal mean for a three latitude average centered at 50° N. Values for corrected fields only are plotted.

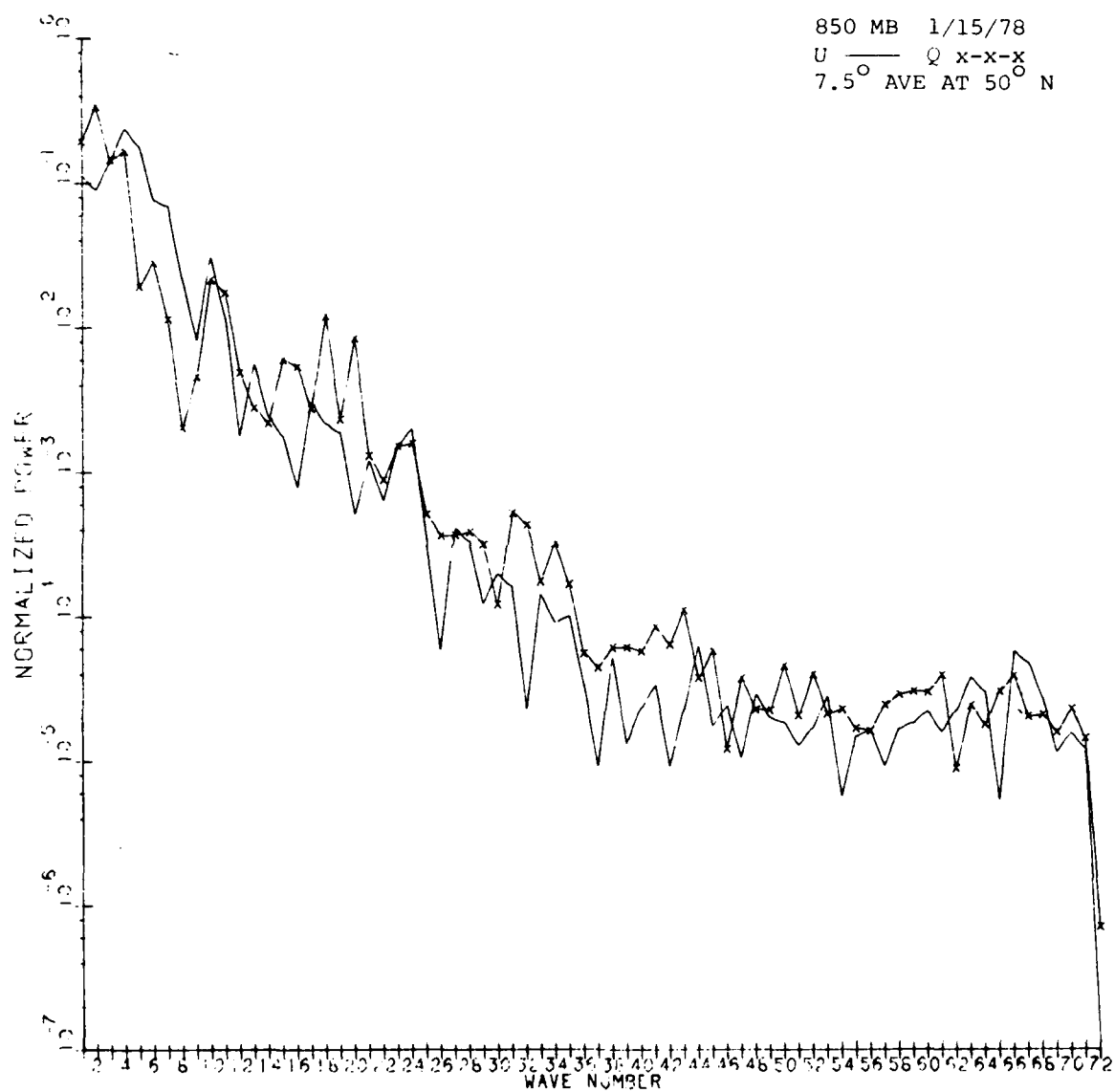


Fig. 5c. Normalized power for departures from zonal mean for a three latitude average centered at 50° N. Values for corrected fields only are plotted.

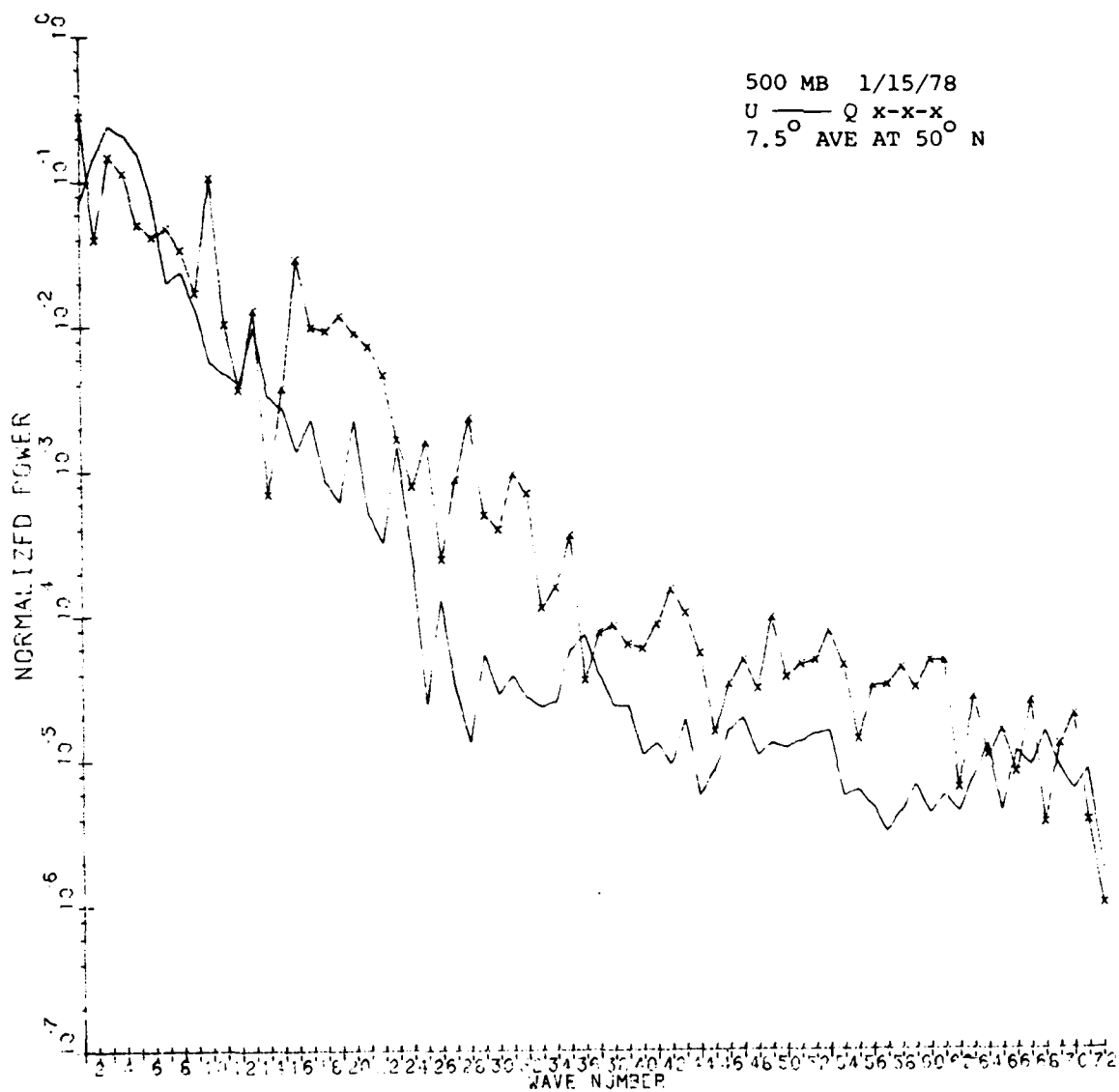


Fig. 5d. Normalized power for departures from zonal mean for a three latitude average centered at 50° N. Values for corrected fields only are plotted.

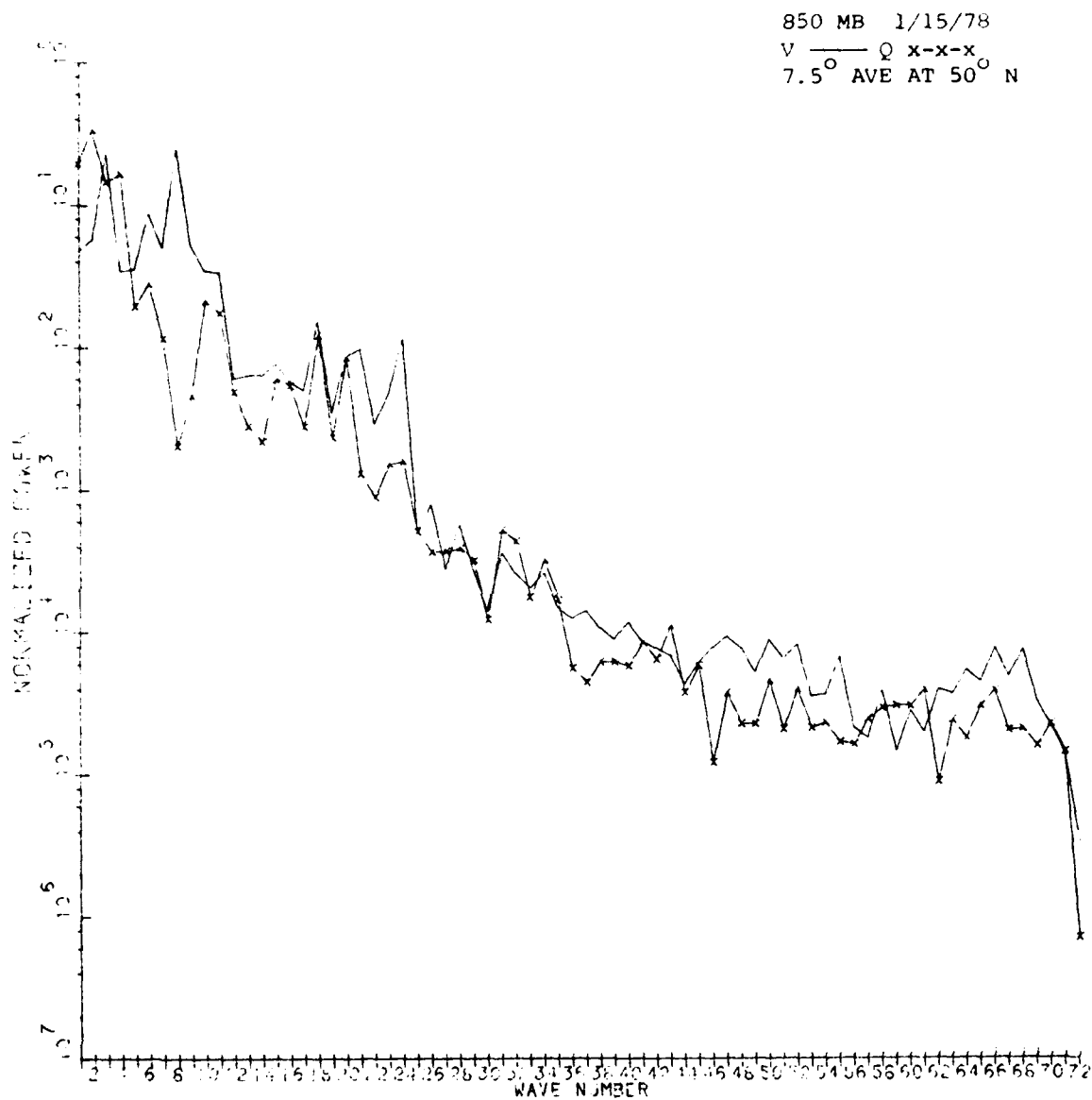


Fig. 5e. Normalized power for departures from zonal mean for a three latitude average centered at 50° N. Values for corrected fields only are plotted.

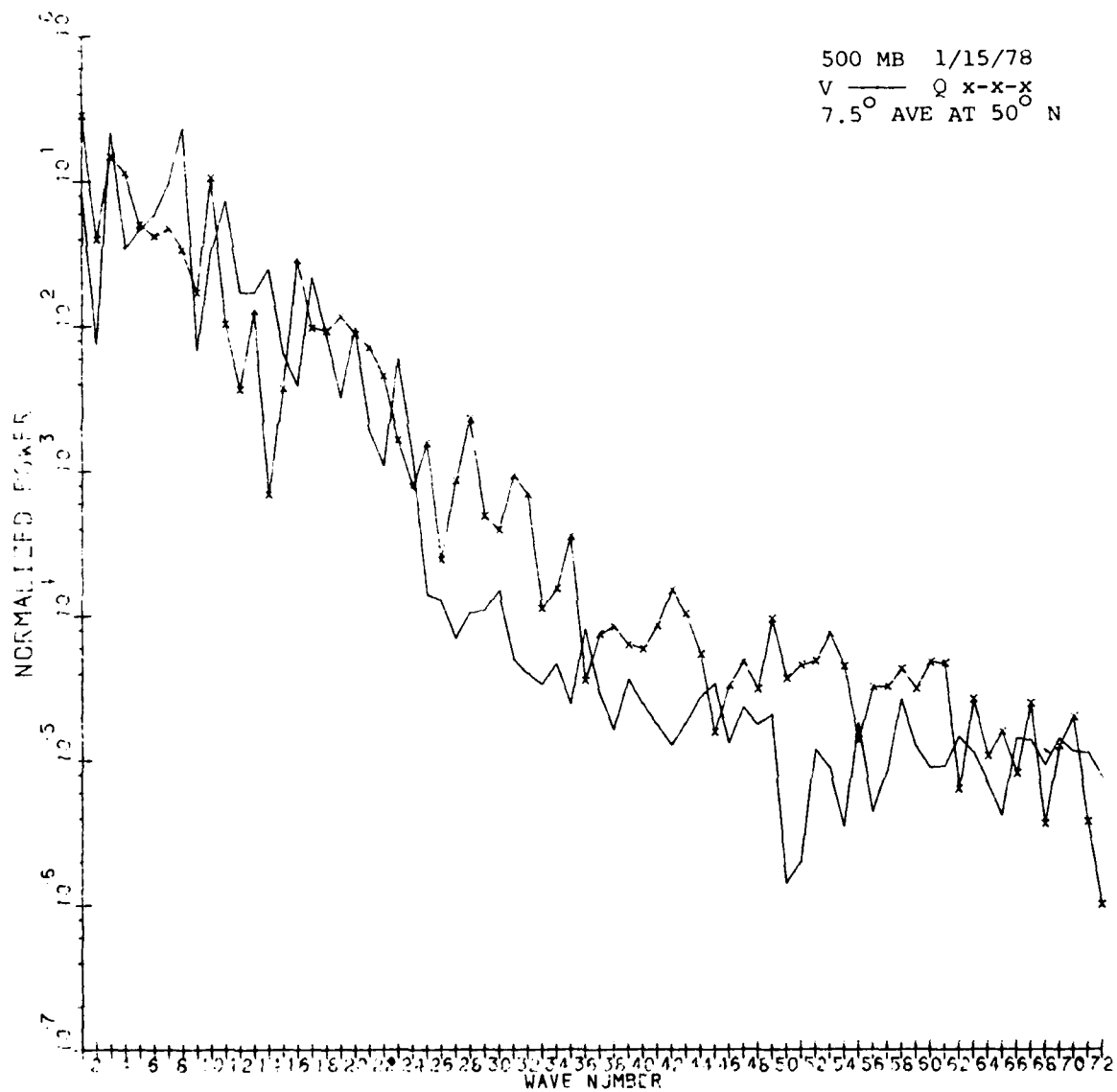


Fig. 5f. Normalized power for departures from zonal mean for a three latitude average centered at 50° N. Values for corrected fields only are plotted.

at wave number 2 and then decline more or less steadily with increasing wave number. The greatest amplitudes in the u and v spectra tended to be at somewhat larger wave numbers or were distributed over several wave numbers. This seems to be especially true for v.

TABLE 2. CORRELATION COEFFICIENT VALUES FOR ZONAL SPECTRA.

<u>Pressure Level</u>	<u>Date</u>	<u>q, T</u>	<u>q, u</u>	<u>q, v</u>
850	1/15/78	.93	.64	.31
	7/20/78	.97	.42	.12
500	1/15/78	.86	.59	.49
	7/20/78	.78	.60	.57

The normalized zonal power spectrum was calculated for all latitudes and plotted in \log_{10} form on latitude vs. wave number diagrams as seen in Figs. 6a-i. The contours represent the fractional contribution of each wave number to the total power at each latitude. For example, a point lying to the left of the -2 contour indicates that that wave number contributes at least 1% of the total power at a particular latitude. In these diagrams, the wave numbers correspond to the number of waves around each latitude circle irrespective of convergence of the meridians near the poles. Therefore, a particular wave number at high latitudes will correspond to a wave of shorter length than the same wave number at the equator by a factor of $\cos \phi$. This is reflected in the fact that in all diagrams the rate at which the power falls off with wave number increases toward the poles. The point of comparison should be between diagrams at particular choices of latitude, and not between latitudes (except for large departures from the $\cos \phi$ variation) on any one diagram.

In comparing the four q diagrams, we see no appreciable variation of the zonal spectra with height; similarly, no significant variation with season was observed from the JUL plots (not shown). Aside from the differences in latitudinal location of the spikes in the -4 contour, the q and T diagrams even look quite similar. The spikes indicate latitude bands where the variation of the quantity is spread out over a greater range of wave numbers and not concentrated so heavily in the long waves. The spike on the T diagram has its center on latitudes between 0° and 20° N, while the q diagram shows two lesser spikes, one in each hemisphere and both of which seem to change latitude slightly with time and height. The dia-

Q 850 1/15/78

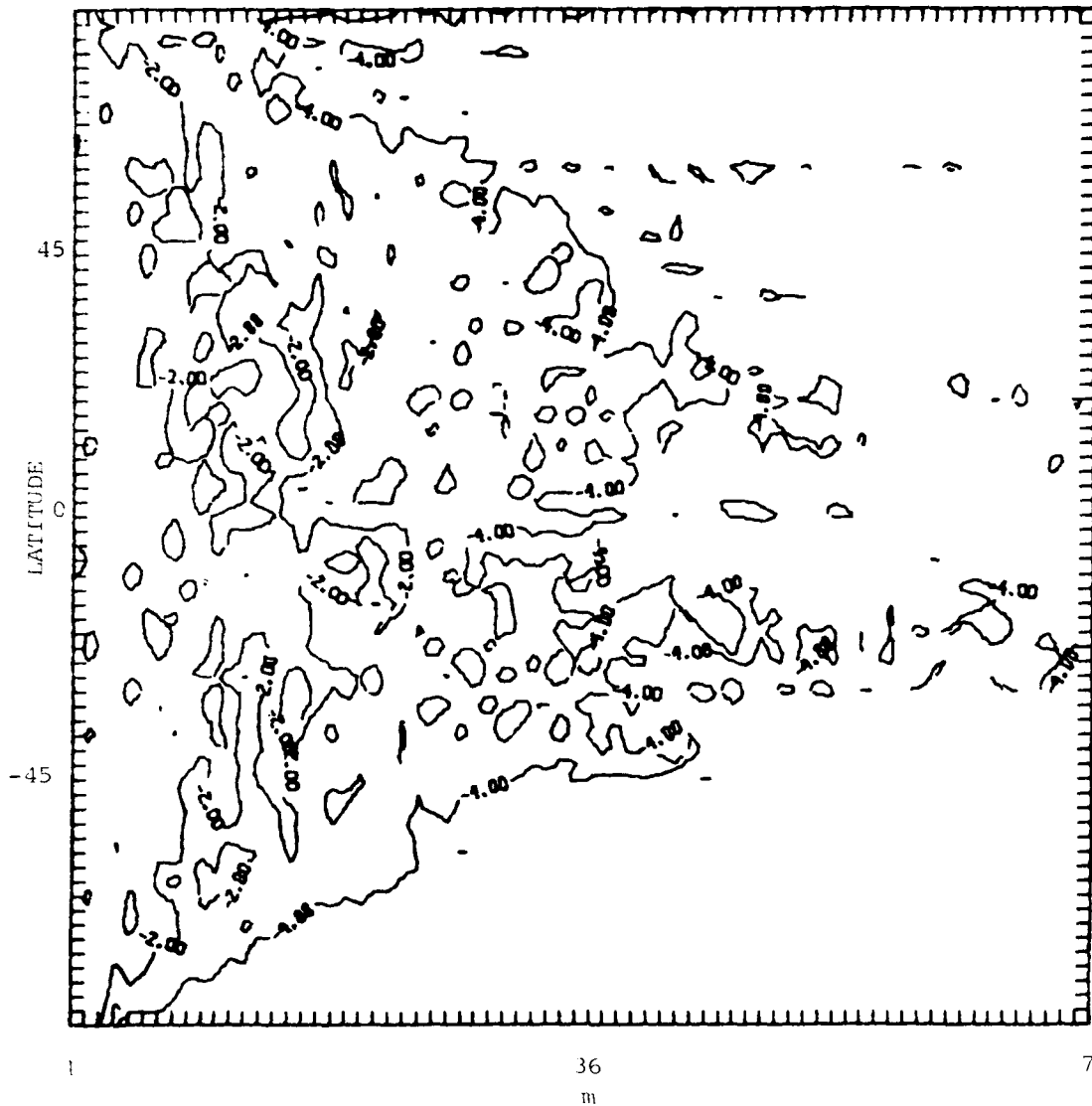


Fig. 6a. Zonal power spectra in powers of 10 for departures from zonal mean for 850 mb specific humidity. The fractional contribution summed over m for each latitude should equal unity.

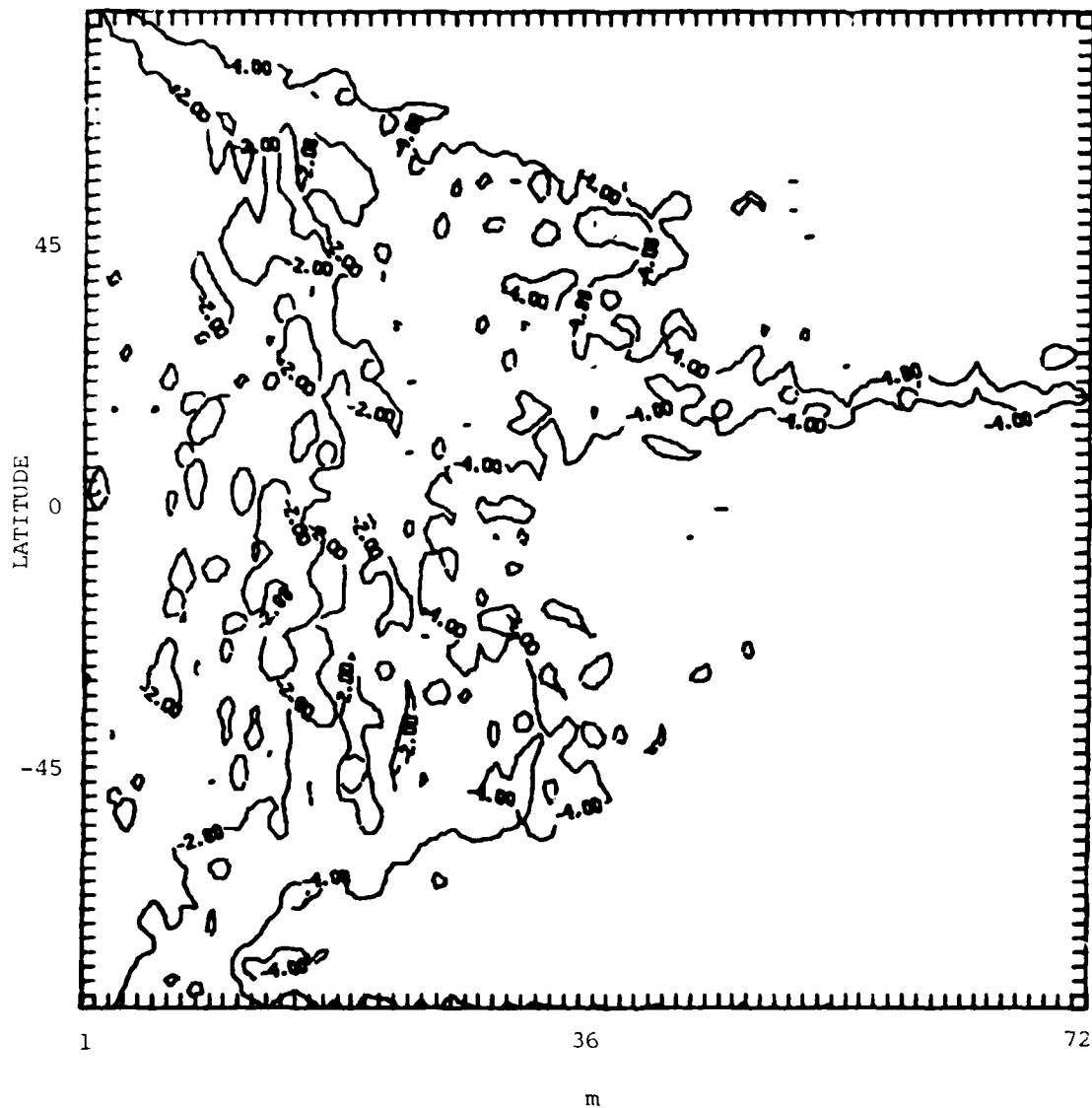


Fig. 6b. Zonal power spectra in powers of 10 for departures from zonal mean for 500 mb specific humidity. The fractional contribution summed over m for each latitude should equal unity.

T 850 1/15/78

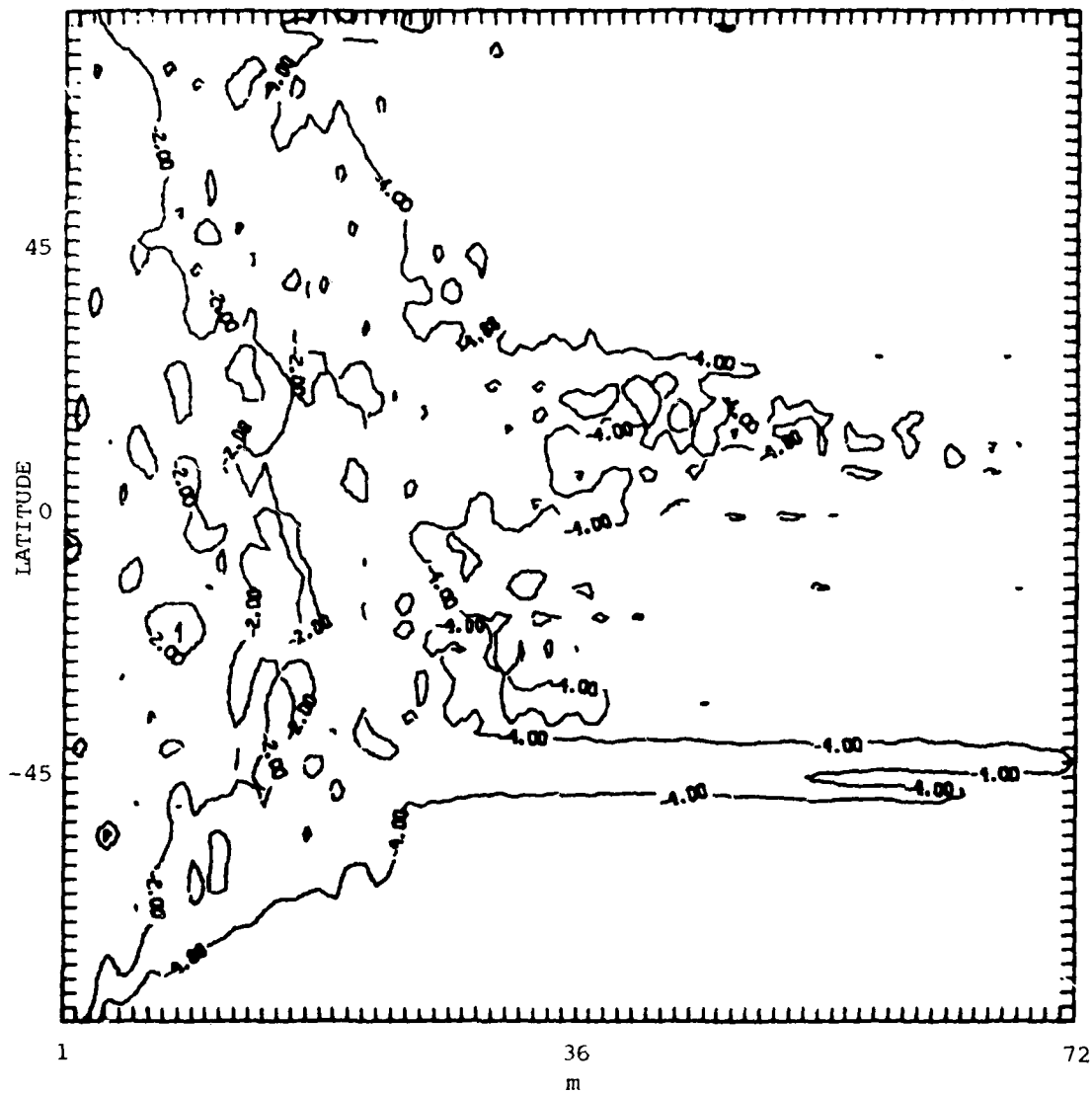


Fig. 6c. Zonal power spectra in powers of 10 for departures from zonal mean for 850 mb temperature. The fractional contribution summed over m for each latitude should equal unity.

T 500 1/15/78

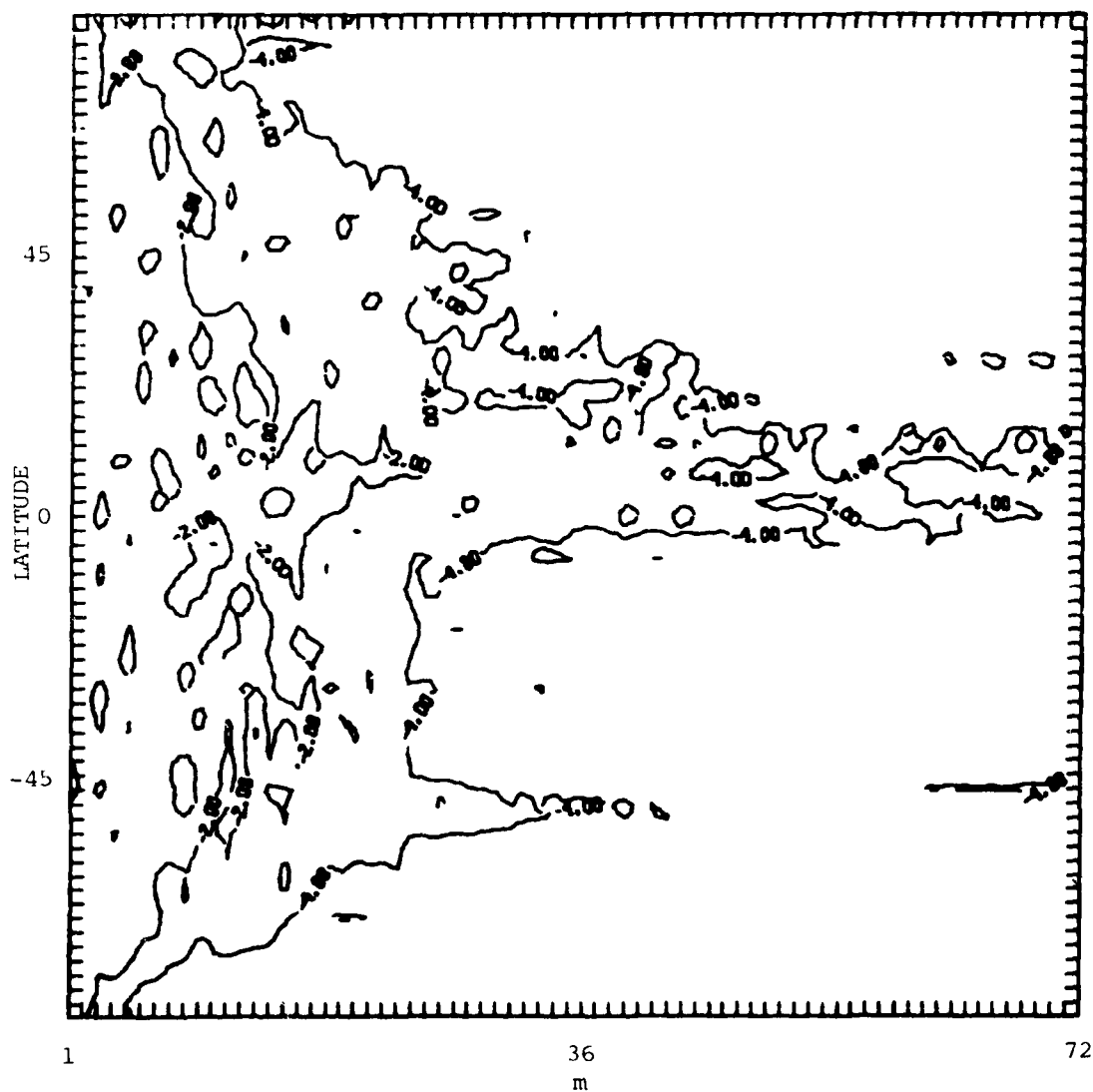


Fig. 6d. Zonal power spectra in powers of 10 for departures from zonal mean for 500 mb temperature. The fractional contribution summed over m for each latitude should equal unity.

Z 500 1/15/78

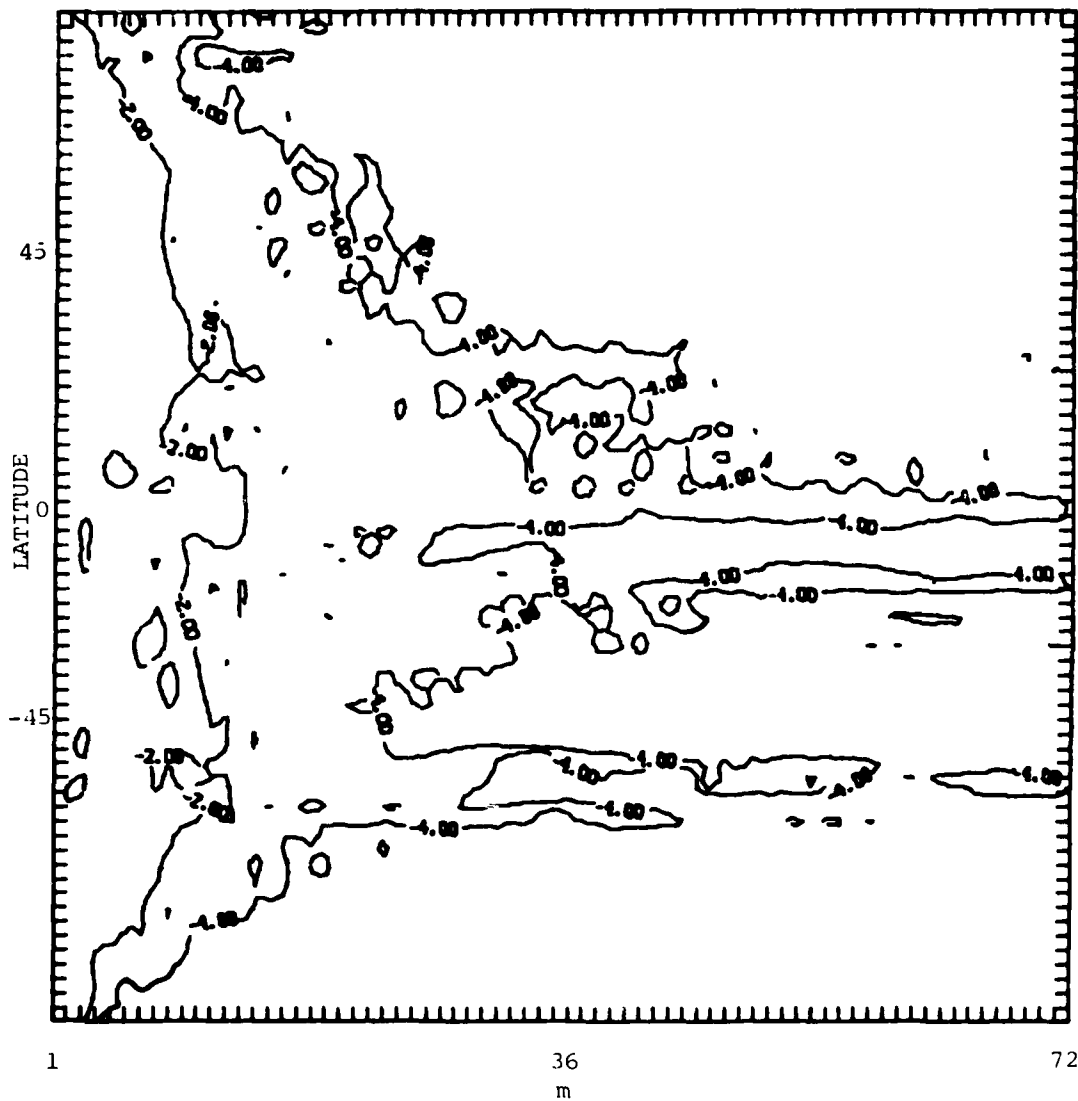


Fig. 6e. Zonal power spectra in powers of 10 for departures from zonal mean for 500 geopotential height. The fractional contribution summed over m for each latitude should equal unity.

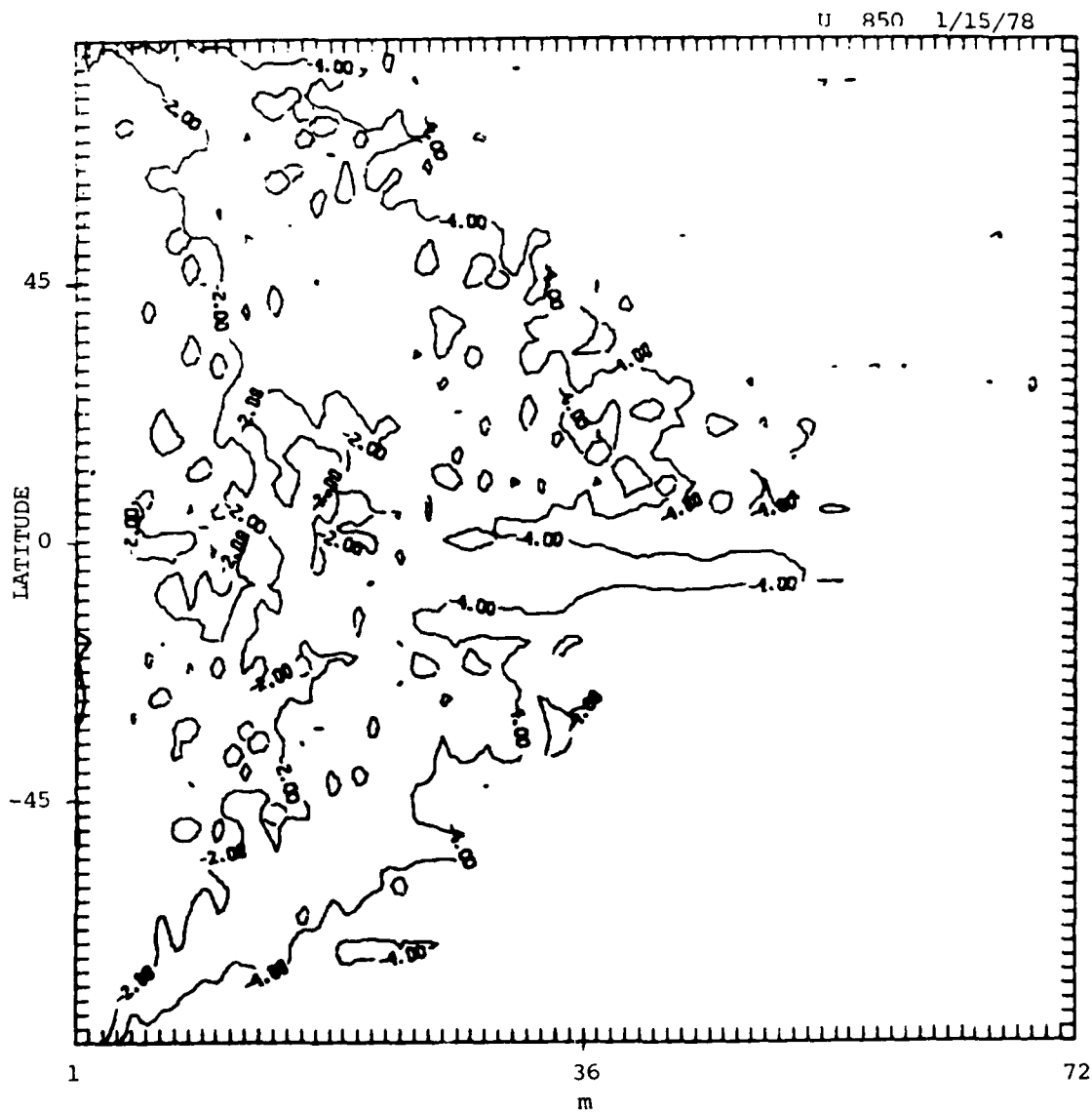


Fig. 6f. Zonal power spectra in powers of 10 for departures from zonal mean for 850 mb zonal velocity. The fractional contribution summed over m for each latitude should equal unity.

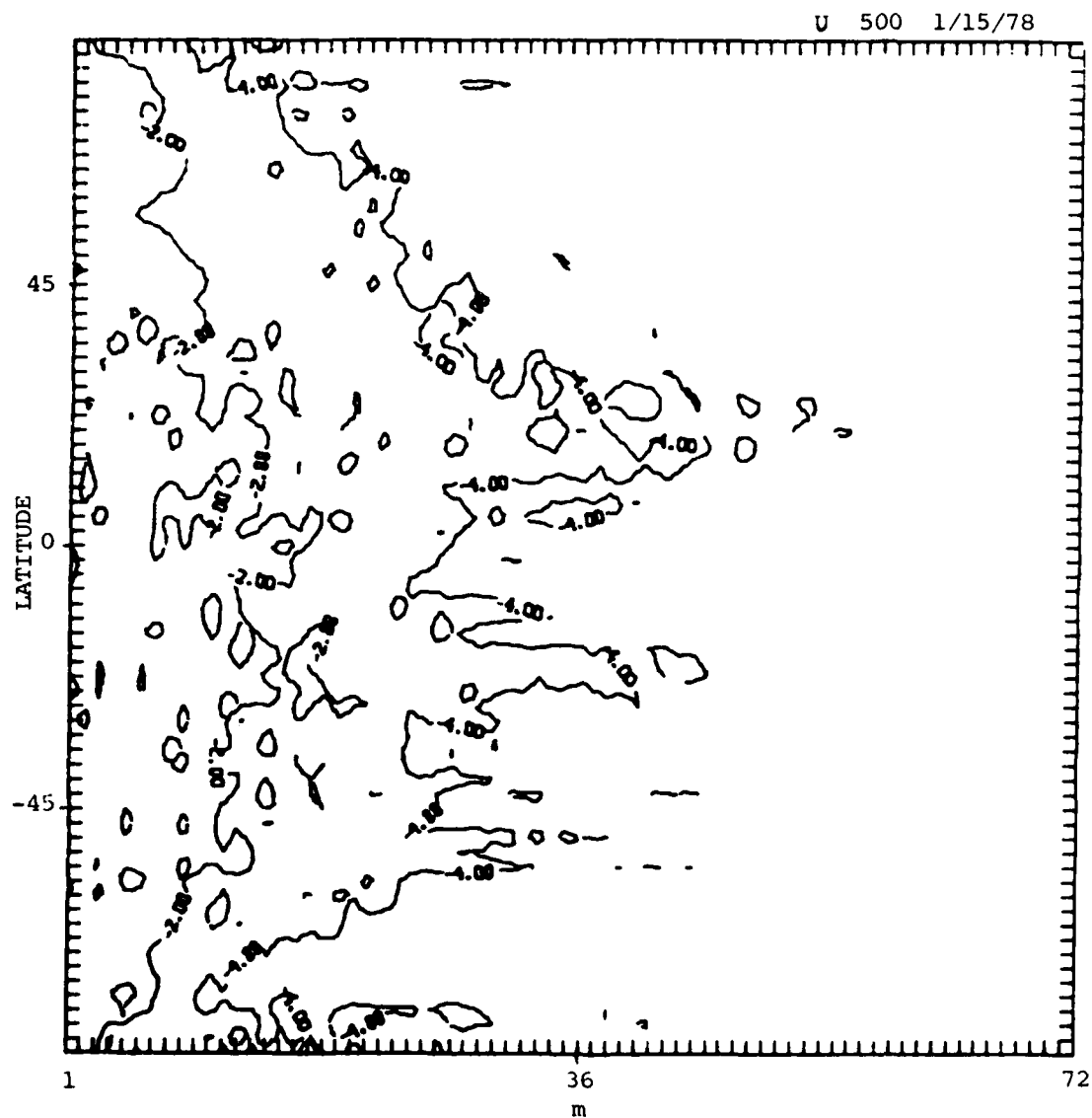


Fig. 6g. Zonal power spectra in powers of 10 for departures from zonal mean for 500 mb zonal velocity. The fractional contribution summed over m for each latitude should equal unity.

V 850 1/15/78

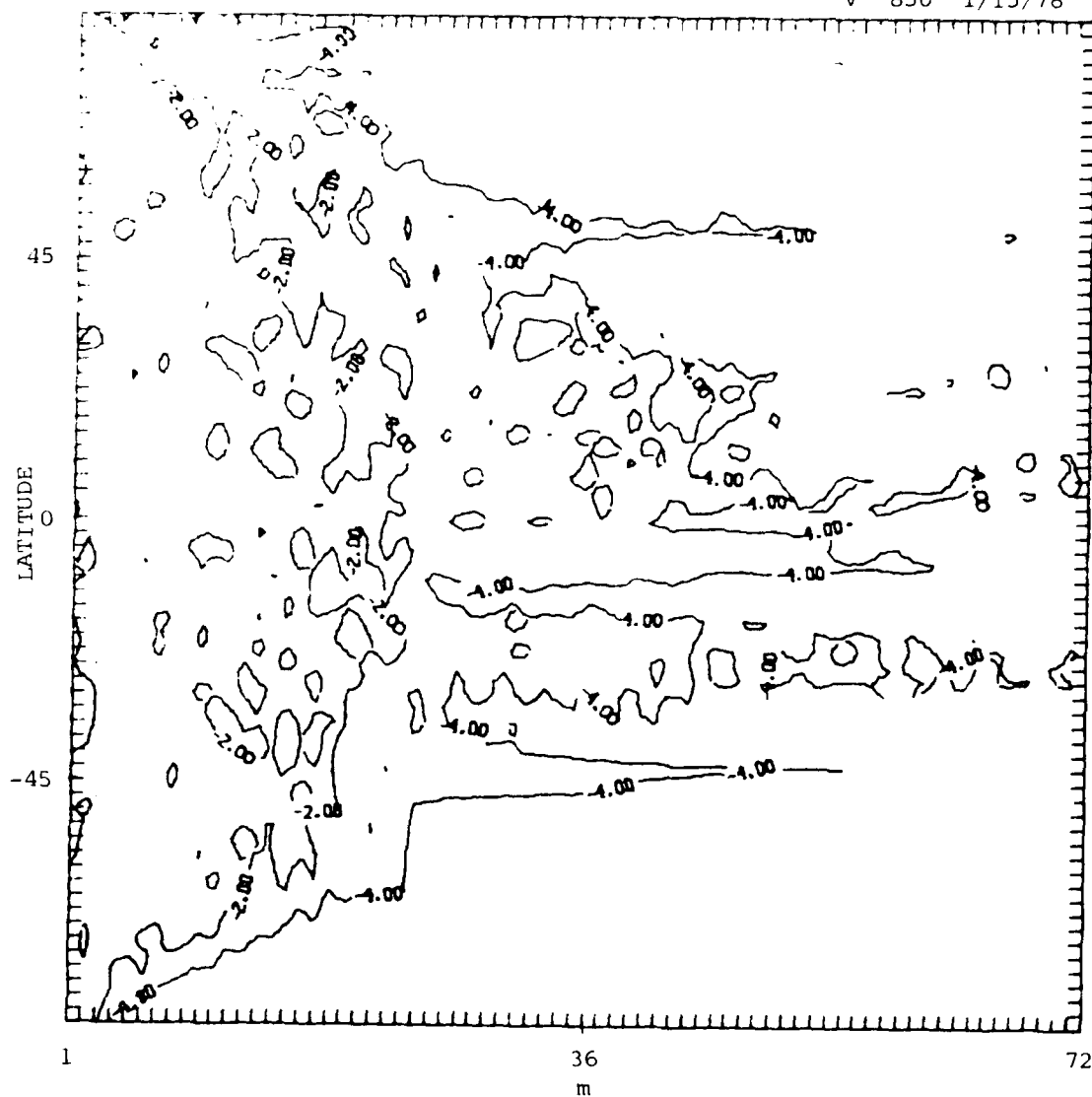


Fig. 6h. Zonal power spectra in powers of 10 for departures from zonal mean for 850 mb meridional velocity. The fractional contribution summed over m for each latitude should equal unity.

V 500 1/15/78

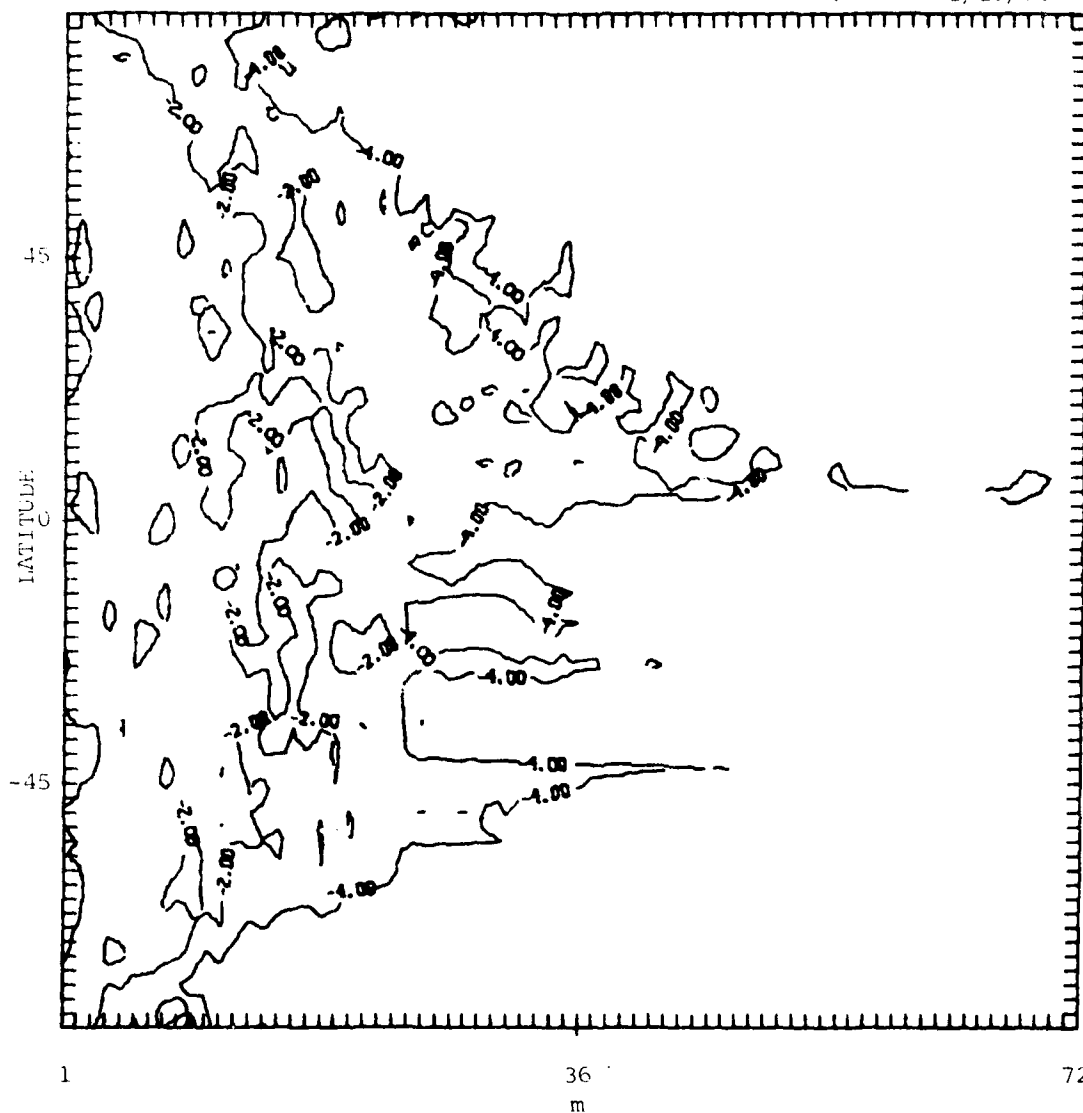


Fig. 6i. Zonal power spectra in powers of 10 for departures from zonal mean for 500 mb meridional velocity. The fractional contribution summed over m for each latitude should equal unity.

grams for Z (500 mb only) show a greater concentration of power in low wave numbers than do q and T. A comparison of the u diagrams with q shows a tendency of the -2 contour on the u diagram to lie somewhat to the left of that of the q diagram, especially at middle latitudes in both hemispheres. This is clearly not the case with the v spectra, which in some cases show even more wave numbers included in the 1% contribution category than for q. From these qualitative comparisons it can be tentatively concluded that temperature seems to have a zonal spectrum most like that of q, where u tends to show slightly more concentration of power in low wave numbers and v a tendency towards greater contributions from higher zonal wave numbers.

The total power of the zonal eddies, which is the denominator in Eq. (3), is plotted along with zonal mean power on a \log_{10} axis as a function of latitude in Figs. 7a-j. The fields used to obtain these power plots were the departures from the global mean as defined in Eqs. (6) and (7). Total eddy power for q^* is clearly unique in its latitudinal variation when compared to that of the other parameters. The power remains high in a broad band of latitudes and falls off at both poles. The width of this band of high power is greater at 850 mb than at 500 mb for both dates. At both levels, the total eddy power is greater in the summer hemisphere than it is in the winter hemisphere. The fact that this power difference between the seasons is greater in the Northern Hemisphere for both levels is probably due to the greater number of observations in the Northern Hemisphere.

The total eddy power - latitude curves for T^* and Z^* both show a bimodal structure with relative minima at the equator and poles and relative maxima at mid-latitudes. Power due to zonal eddies is greater in the winter hemisphere, as one would expect from looking at weather maps, but as such it is just opposite from the moisture variance. As in the case of the total eddy power for moisture, the winter hemisphere-summer hemisphere difference is greater in the Northern Hemisphere. As expected, the total power curves for Z^* 500 show the same characteristics as the T^* curves.

The fact that the total power of the zonal eddy specific humidity appears to be greater in the summer hemisphere in contrast to the other quantities may possibly be explained by the limiting factor of saturation.

Q 850 1/15/78
 ——— TOTAL EDDY POWER
 x-x-x ZONAL MEAN POWER

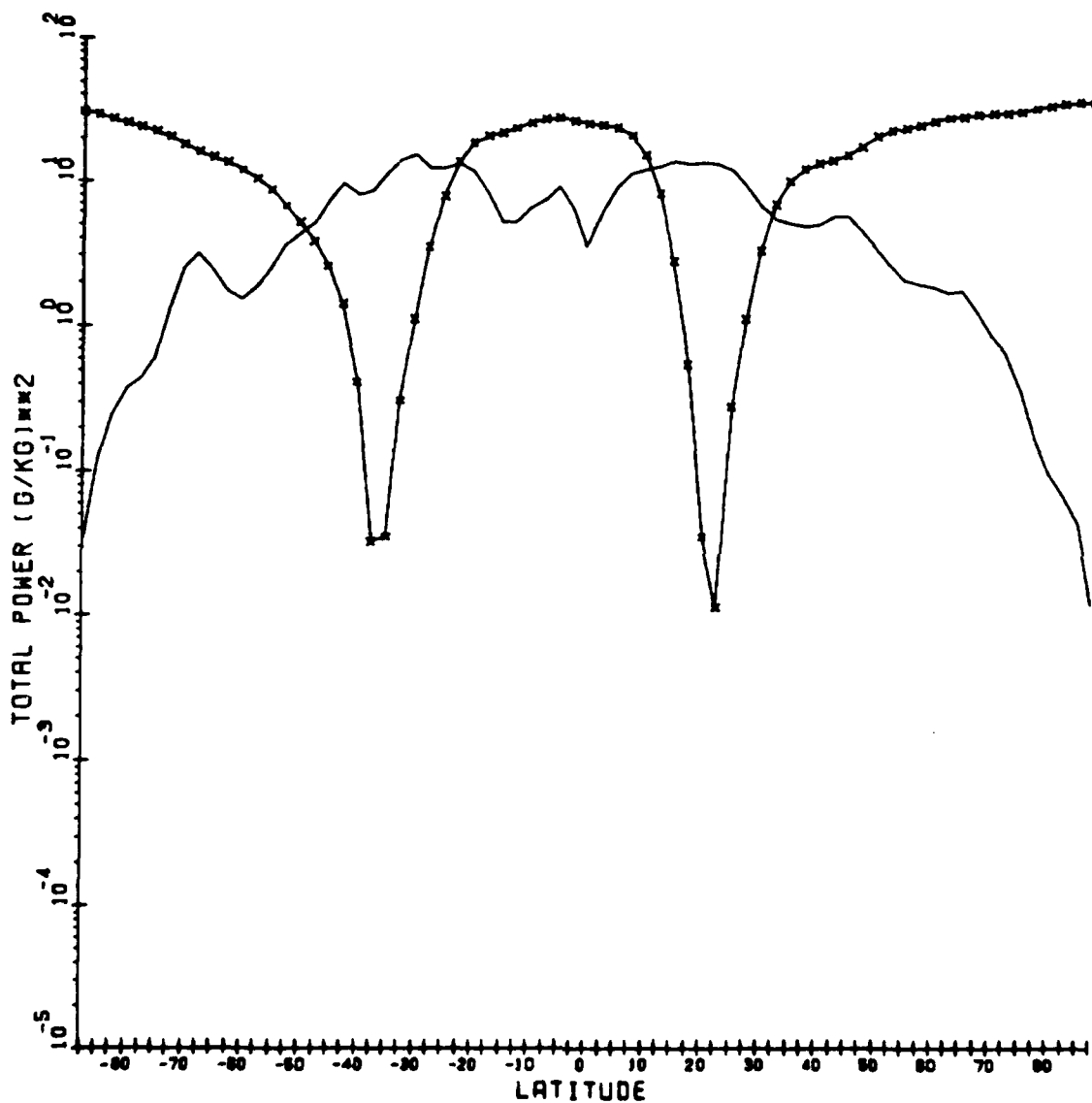


Fig. 7a. Total power due to the departures from the zonal mean (denominator in Eq. (3)) and power due to the zonal mean ($a_0^2(\phi)$) for 850 mb specific humidity for JAN. Quantities are calculated from the departures from the global mean.

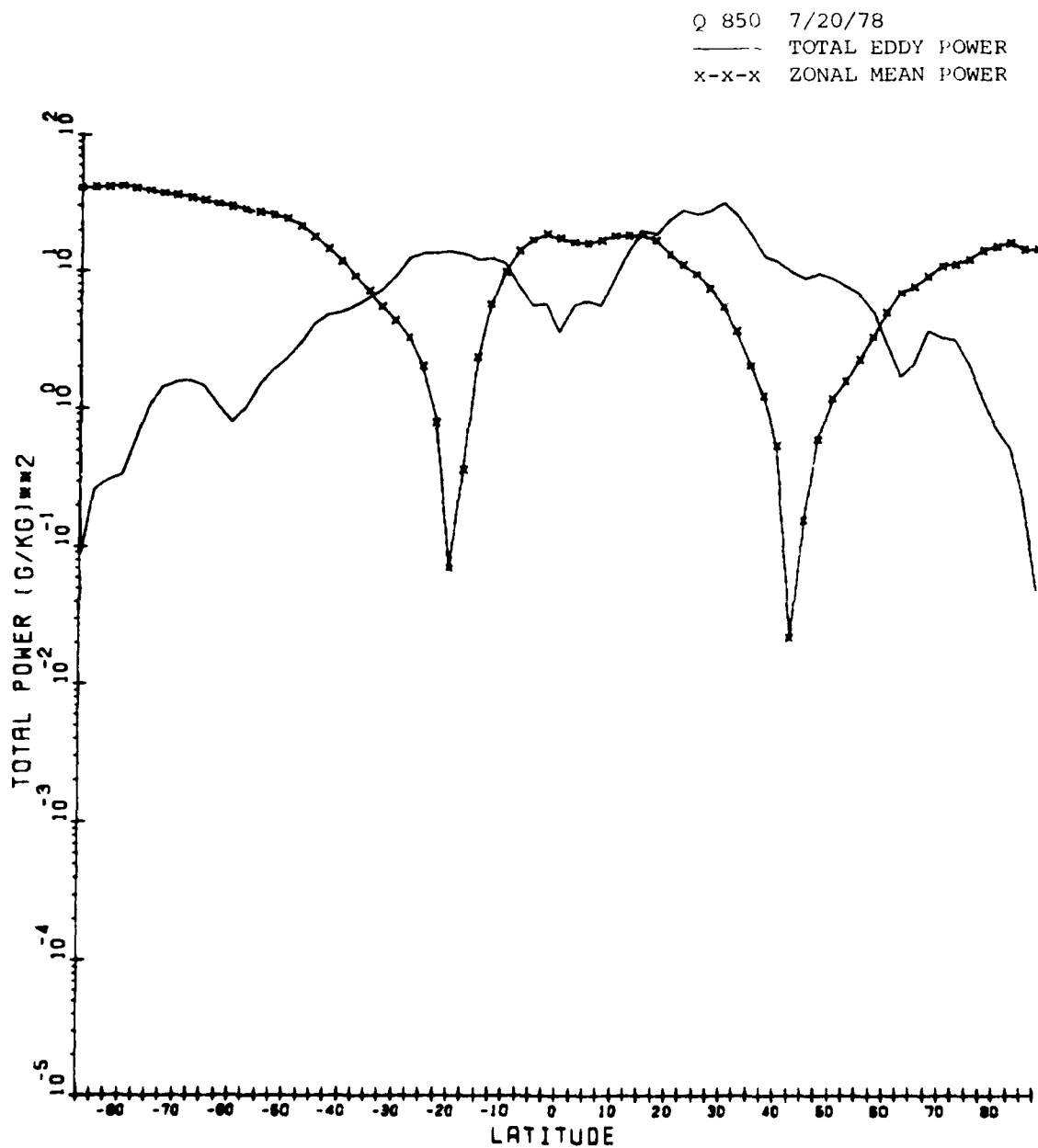


Fig. 7b. Total power due to the departures from the zonal mean (denominator in Eq. (3)) and power due to the zonal mean ($a_0^2(\phi)$) for 850 mb specific humidity for JUL. Quantities are calculated from the departures from the global mean.

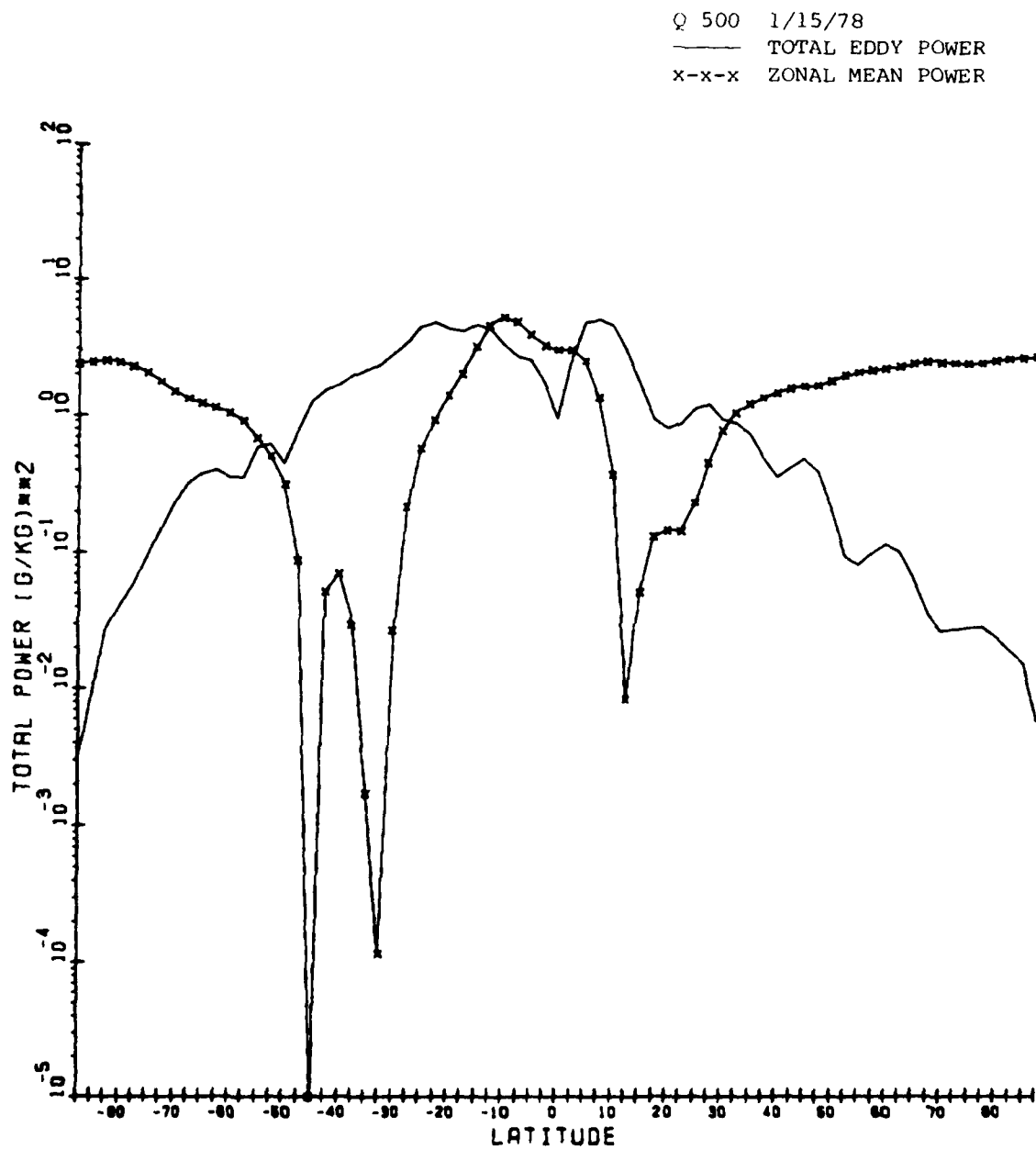


Fig. 7c. Total power due to the departures from the zonal mean (denominator in Eq. (3)) and power due to the zonal mean ($a_0^2(\phi)$) for 500 mb specific humidity for JAN. Quantities are calculated from the departures from the global mean.

Q 500 7/20/78
 ——— TOTAL EDDY POWER
 x-x-x ZONAL MEAN POWER

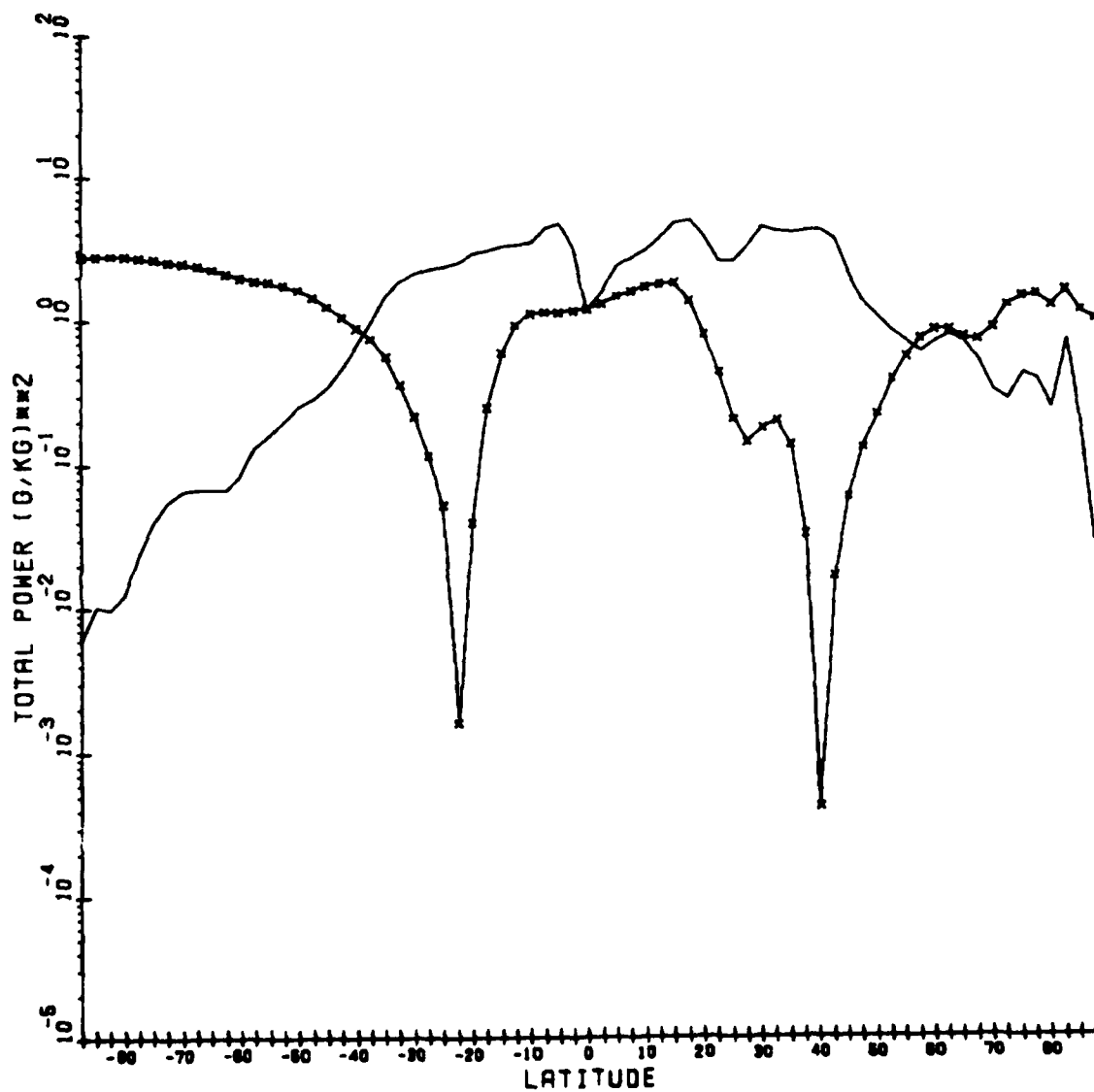


Fig. 7d. Total power due to the departures from the zonal mean (denominator in Eq. (3)) and power due to the zonal mean ($a_0^2(\phi)$) for 500 mb specific humidity for JUL. Quantities are calculated from the departures from the global mean.

T 850 1/15/78

— TOTAL EDDY POWER

x-x-x ZONAL MEAN POWER

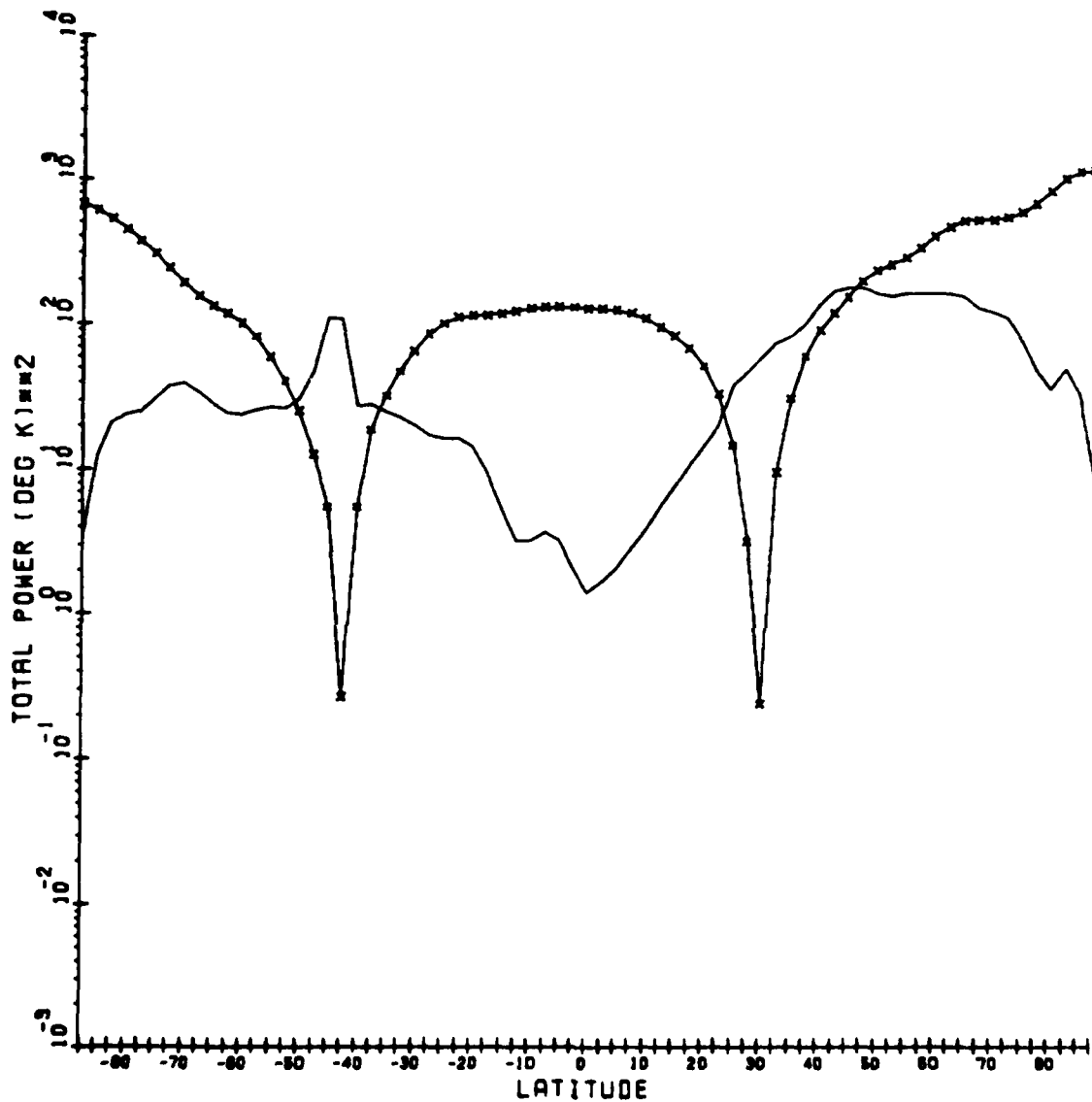


Fig. 7e. Total power due to the departures from the zonal mean (denominator in Eq. (3)) and power due to the zonal mean ($a_0^2(\phi)$) for 850 mb temperature for JAN. Quantities are calculated from the departures from the global mean.

T 850 7/20/78

— TOTAL EDDY POWER

x-x-x ZONAL MEAN POWER

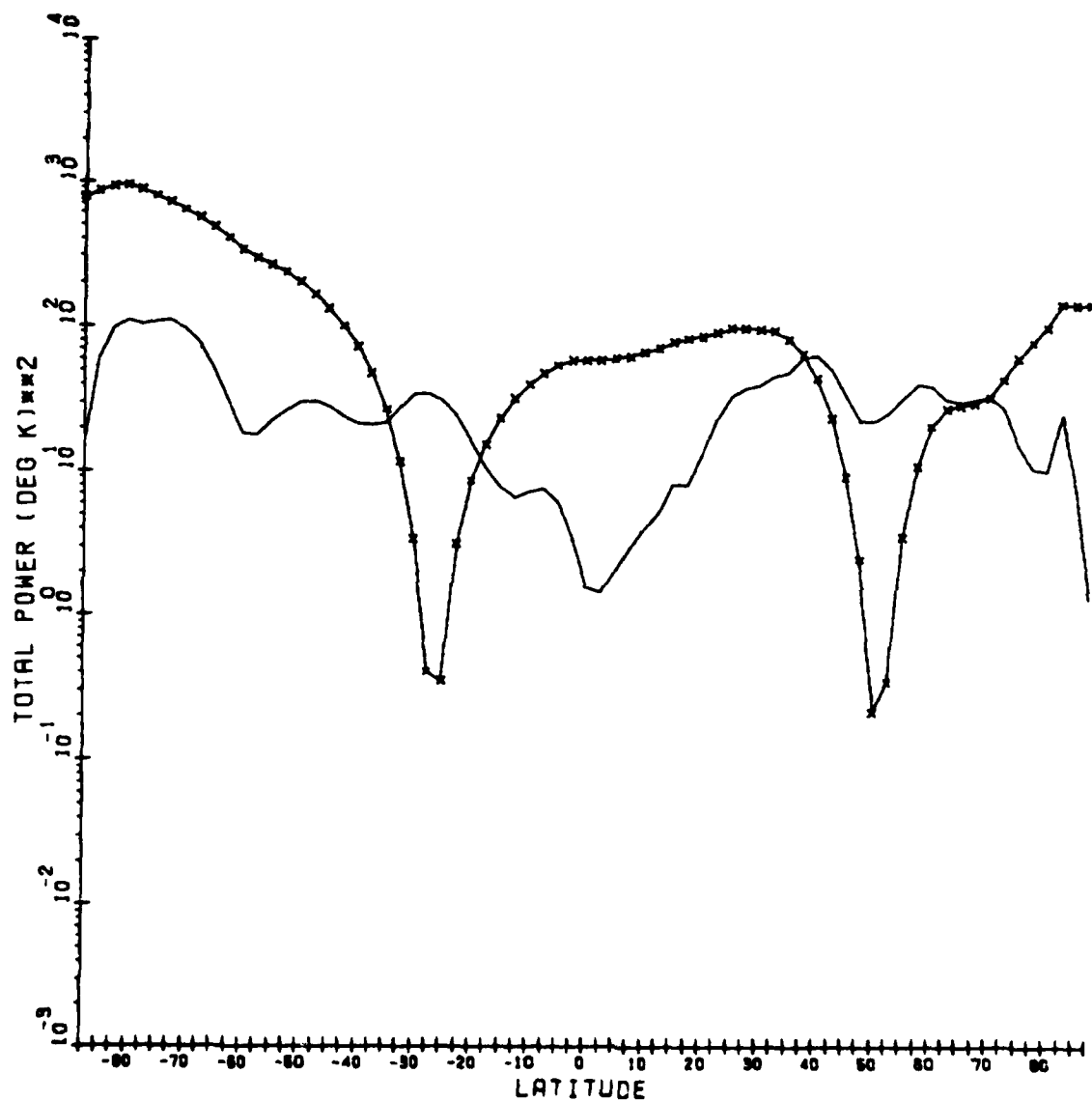


Fig. 7f. Total power due to the departures from the zonal mean (denominator in Eq. (3)) and power due to the zonal mean ($a_0(\phi)$) for 850 mb temperature for JUL. Quantities are calculated from the departures from the global mean.

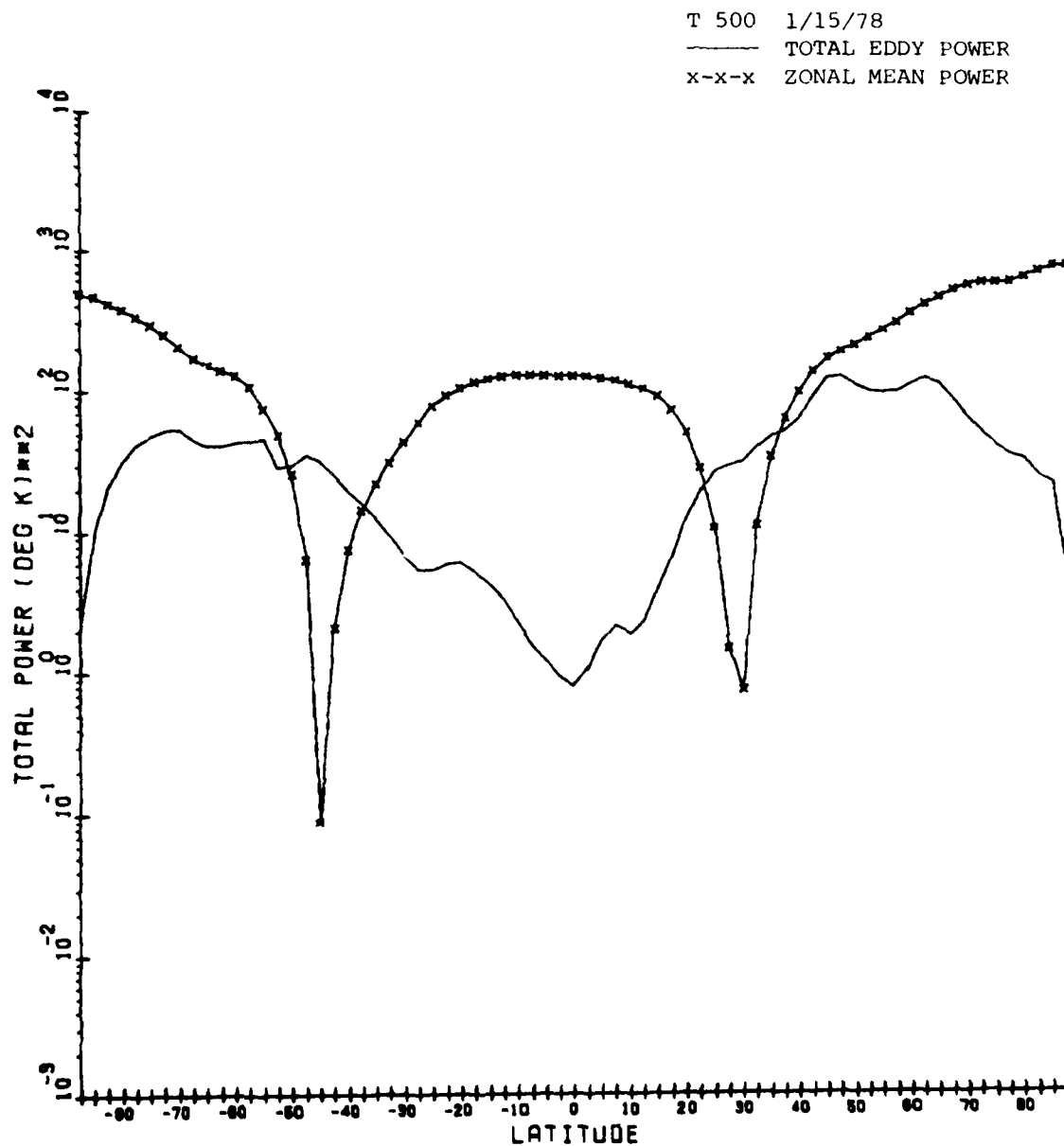


Fig. 7g. Total power due to the departures from the zonal mean (denominator in Eq. (3)) and power due to the zonal mean ($a_0^2(\phi)$) for 500 mb temperature for JAN. Quantities are calculated from the departures from the global mean.

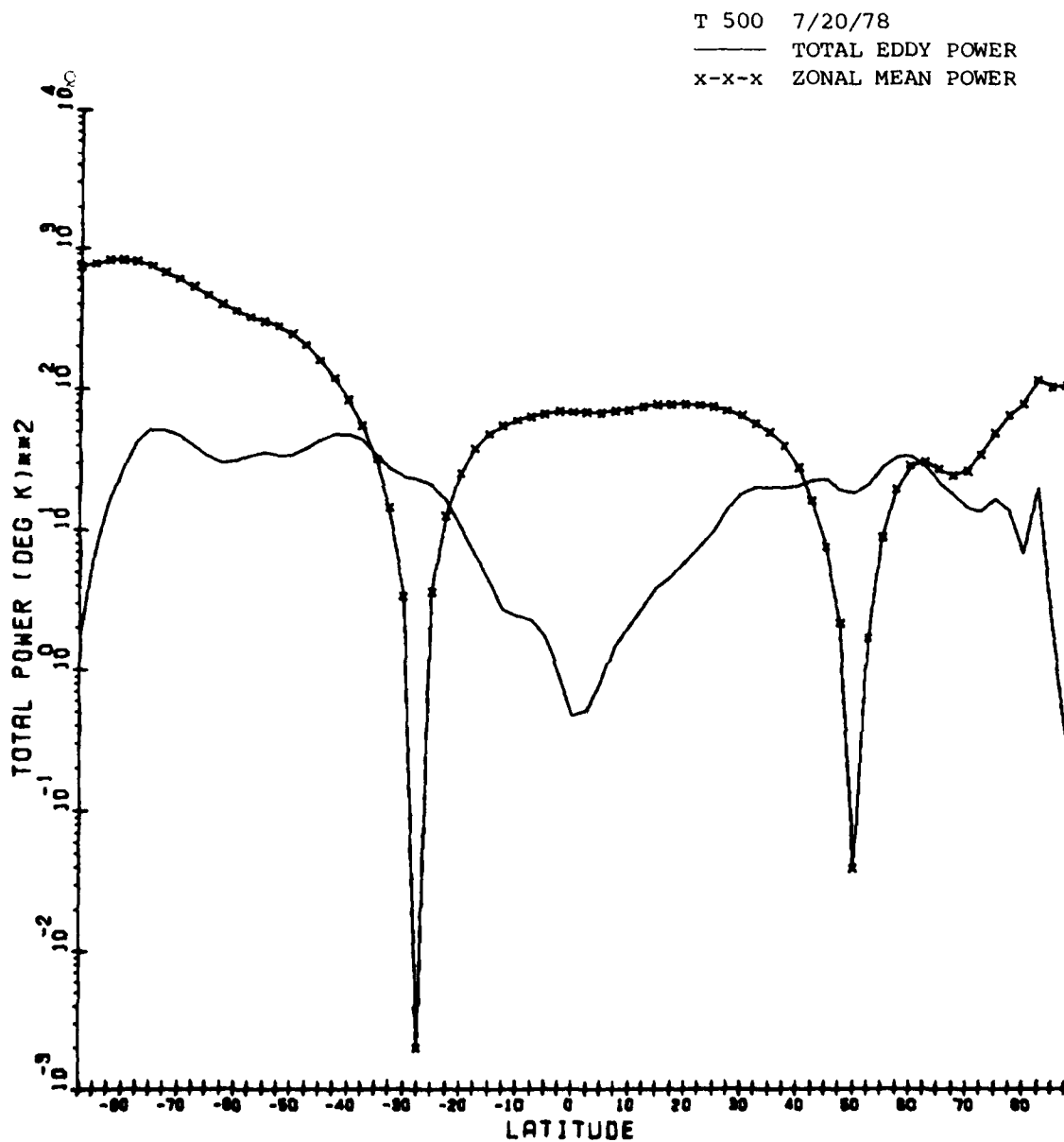


Fig. 7h. Total power due to the departures from the zonal mean (denominator in Eq. (3)) and power due to the zonal mean ($a_0^2(\phi)$) for 500 mb temperature for JUL. Quantities are calculated from the departures from the global mean.

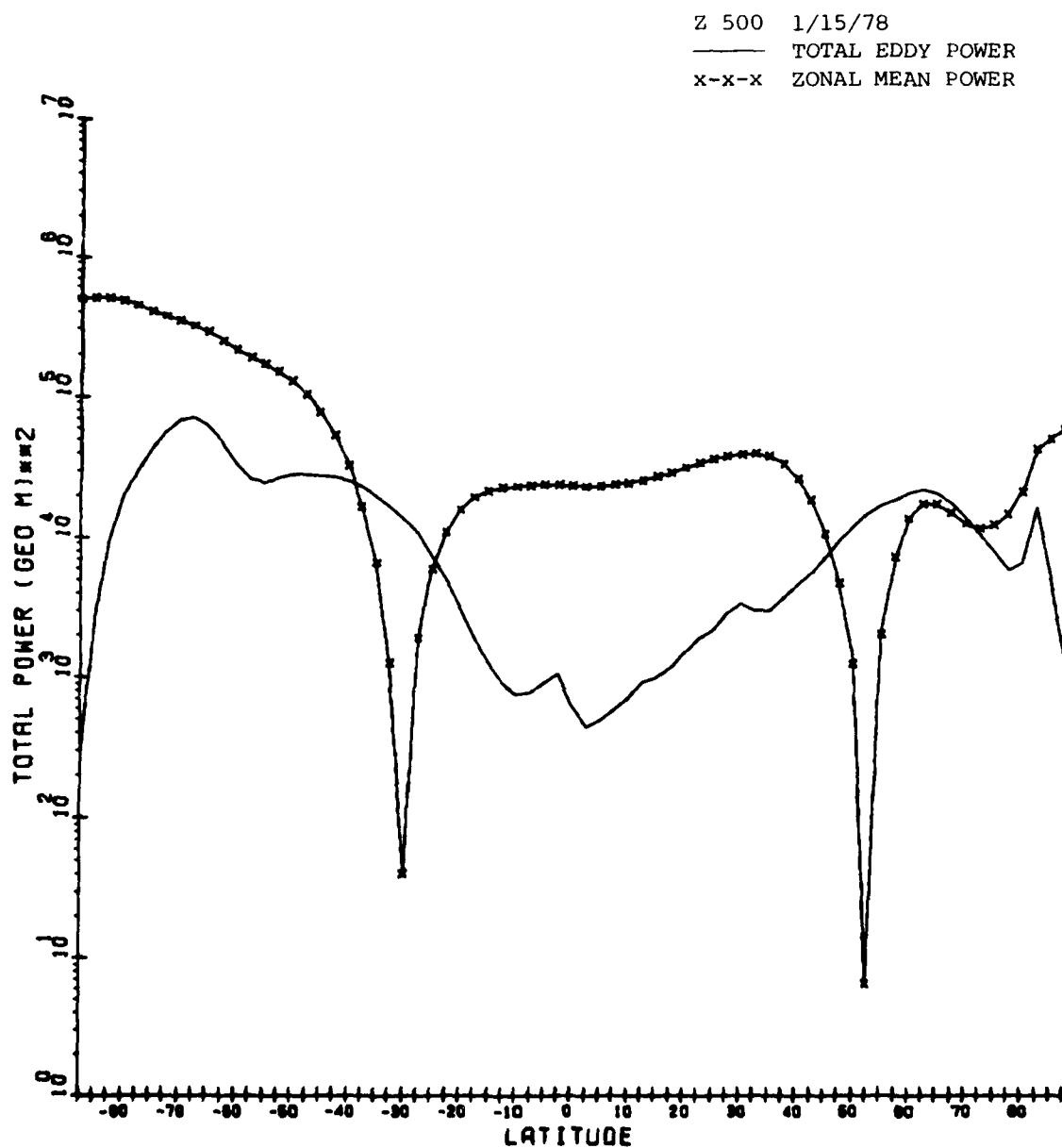


Fig. 7i. Total power due to the departures from the zonal mean (denominator in Eq. (3)) and power due to the zonal mean ($a_0^2(\phi)$) for 500 mb geopotential height in JAN. Quantities are calculated from the departures from the global mean.

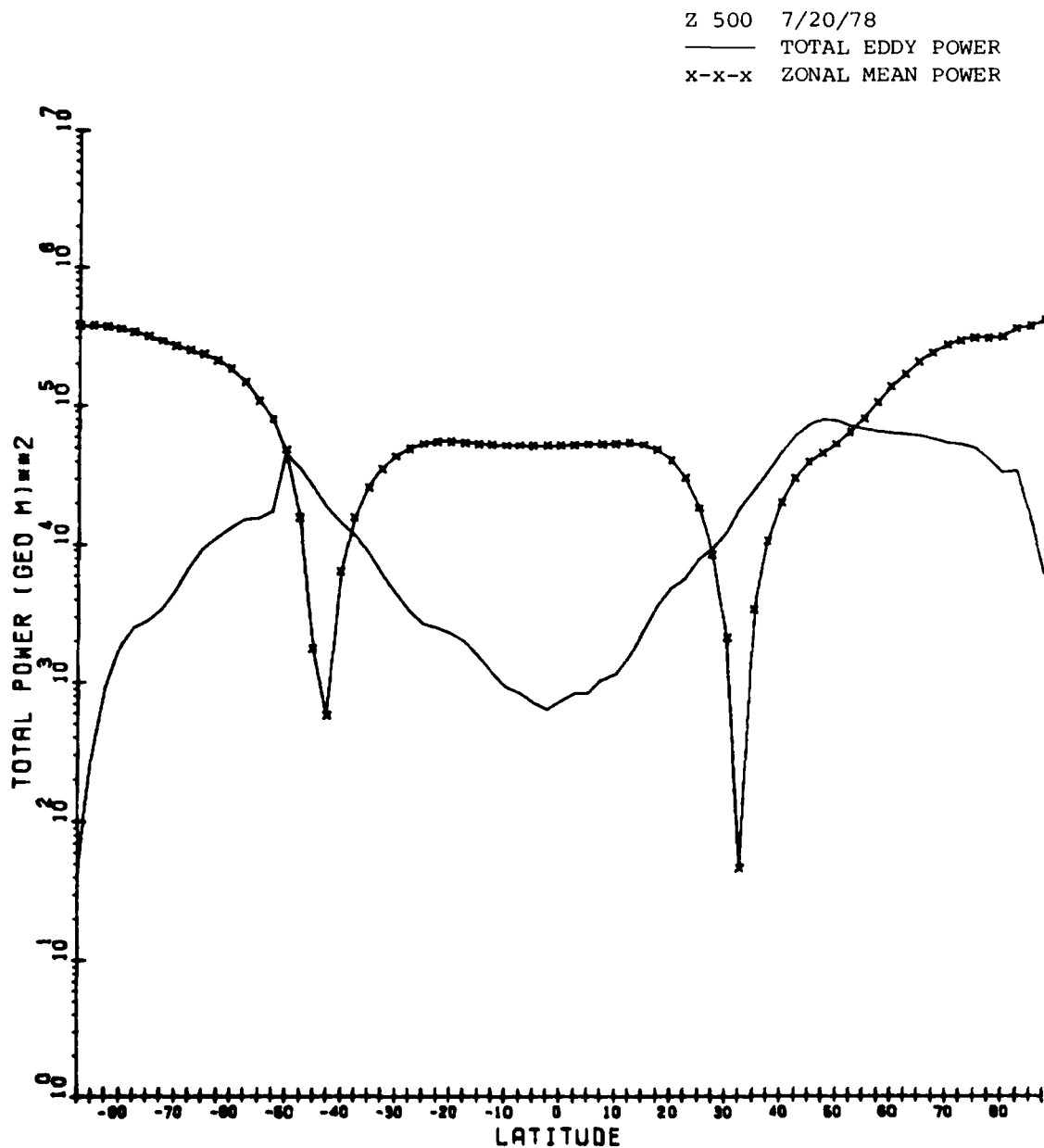


Fig. 7j. Total power due to the departures from the zonal mean (denominator in Eq. (3)) and power due to the zonal mean ($a_0^2(\phi)$) for 500 mb geopotential height in JUL. Quantities are calculated from the departures from the global mean.

Northern Hemisphere average values, given in Table 3, show that while temperature increases by only about 4 percent between winter and summer, the saturation specific humidity q_s (which acts as the upper limit for q) increases by 73 percent at 850 mb and 59 percent at 500 mb. Thus, the maximum allowable departure from the average is about 2.6 g/kg in the winter compared to 4.9 g/kg in the summer at 850 mb. The hemispheric average relative humidity, however, for the two cases is about the same, suggesting that this quantity might act as a less severe limit to the departure from the mean in the winter time. To investigate this, the total eddy power curves for RH based on the ratio of q to q_s were generated and appear in Figs. 8a-d. The fact that the winter-summer hemisphere difference is lessened for RH may indicate that lower temperatures tend to reduce the total variance about the zonal mean more for specific humidity than for relative humidity, which would appear to explain the lower variance for q in the winter hemisphere.

TABLE 3. NORTHERN HEMISPHERE AVERAGES.

<u>Level</u>	<u>Date</u>	<u>q (g kg⁻¹)</u>	<u>T (°K)</u>	<u>q_s (g kg⁻¹)</u>	<u>RH</u>
850	1/15/78	5.35952	276.49600	8.00103	.66985
850	7/20/78	8.95516	288.18456	13.83457	.64730
500	1/15/78	1.23598	254.71750	2.67001	.46291
500	7/20/78	2.13636	267.28384	4.25537	.50204

Following the zonal harmonic analysis, a surface spherical harmonic analysis was performed on the fields. This was carried out as an expansion of the departure from the global mean given by

$$A^*(\phi, \lambda) = \sum_{n=|m|}^N \sum_{m=0}^M (\alpha_n^m \cos m\lambda + \beta_n^m \sin m\lambda) P_n^m(\sin \phi) \quad (5)$$

where

$$A^*(\phi, \lambda) = A(\phi, \lambda) - [A] \quad (6)$$

$$[A] = \frac{1}{2} \int_{-\pi/2}^{\pi/2} \bar{A}(\phi) \cos \phi \, d\phi \quad (7)$$

$$N = |m| + N \quad (8)$$

RH 850 1/15/78

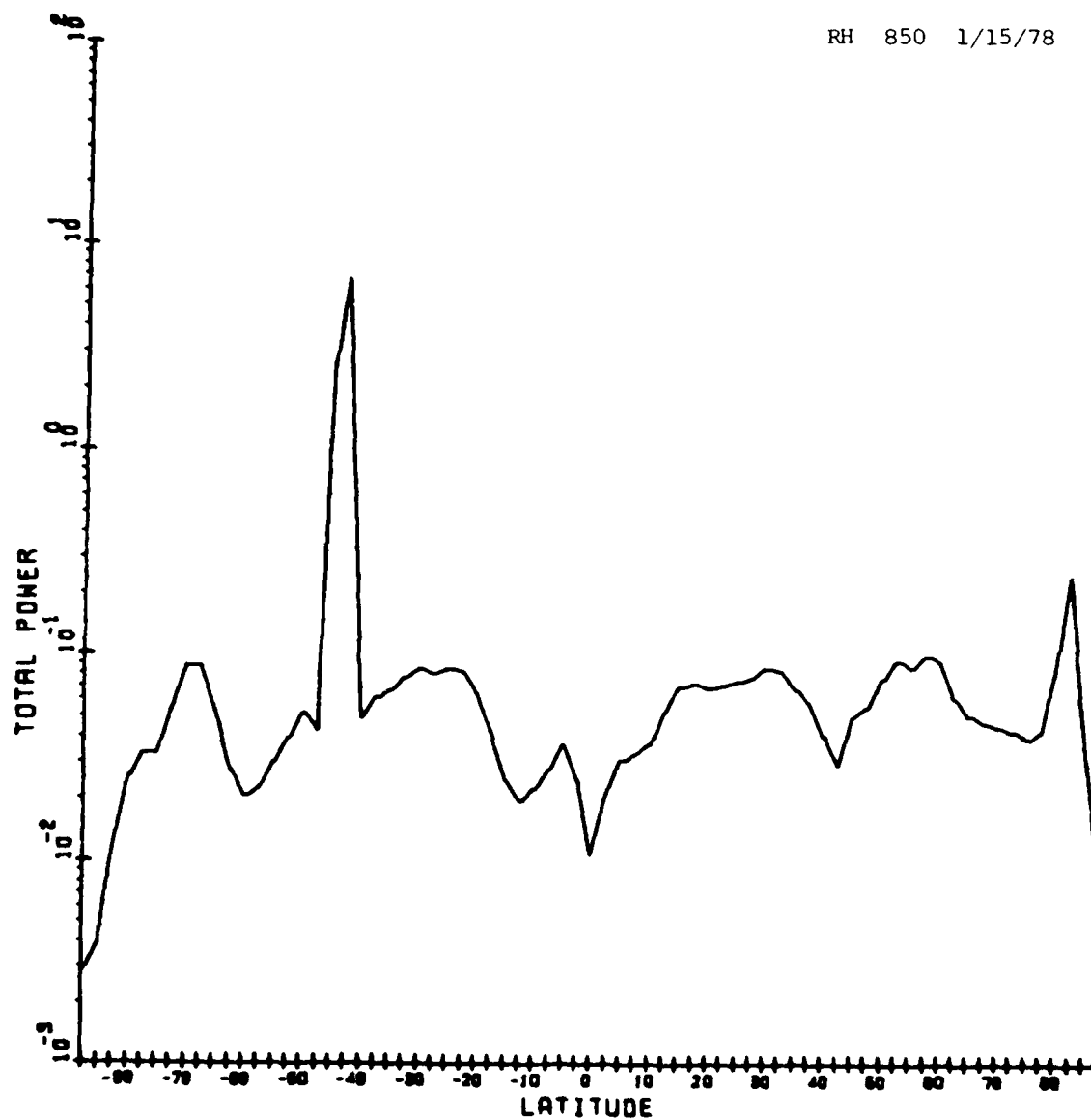


Fig. 8a. Total zonal power for the departures from the zonal average for the ratio q/q_s . Both q and T used in the calculations are the corrected field values.

RH 500 1/15/78

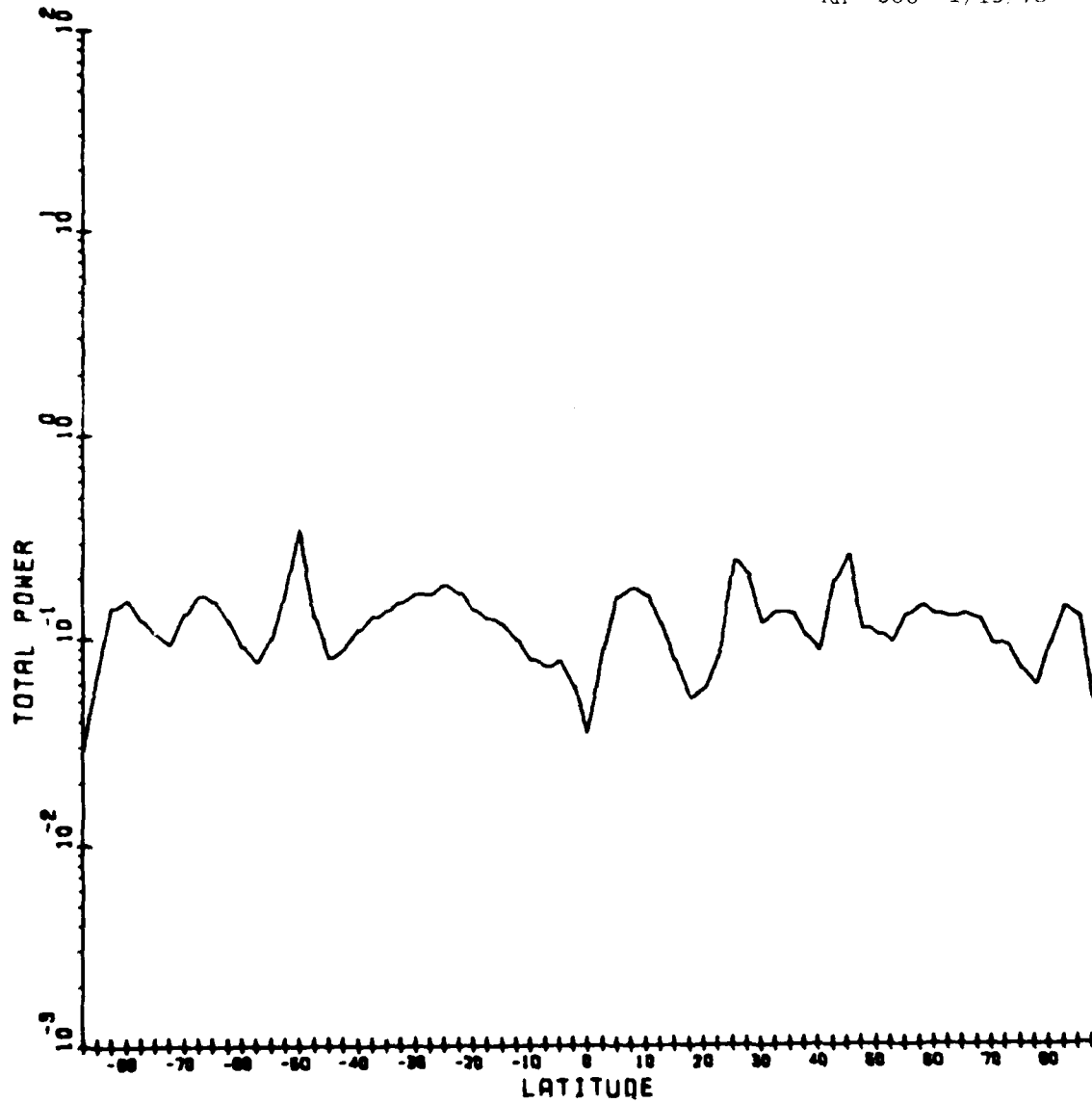


Fig. 8b. Total zonal power for the departures from the zonal average for the ratio q/q_s . Both q and T used in the calculations are the corrected field values.

RH 850 7/20/78

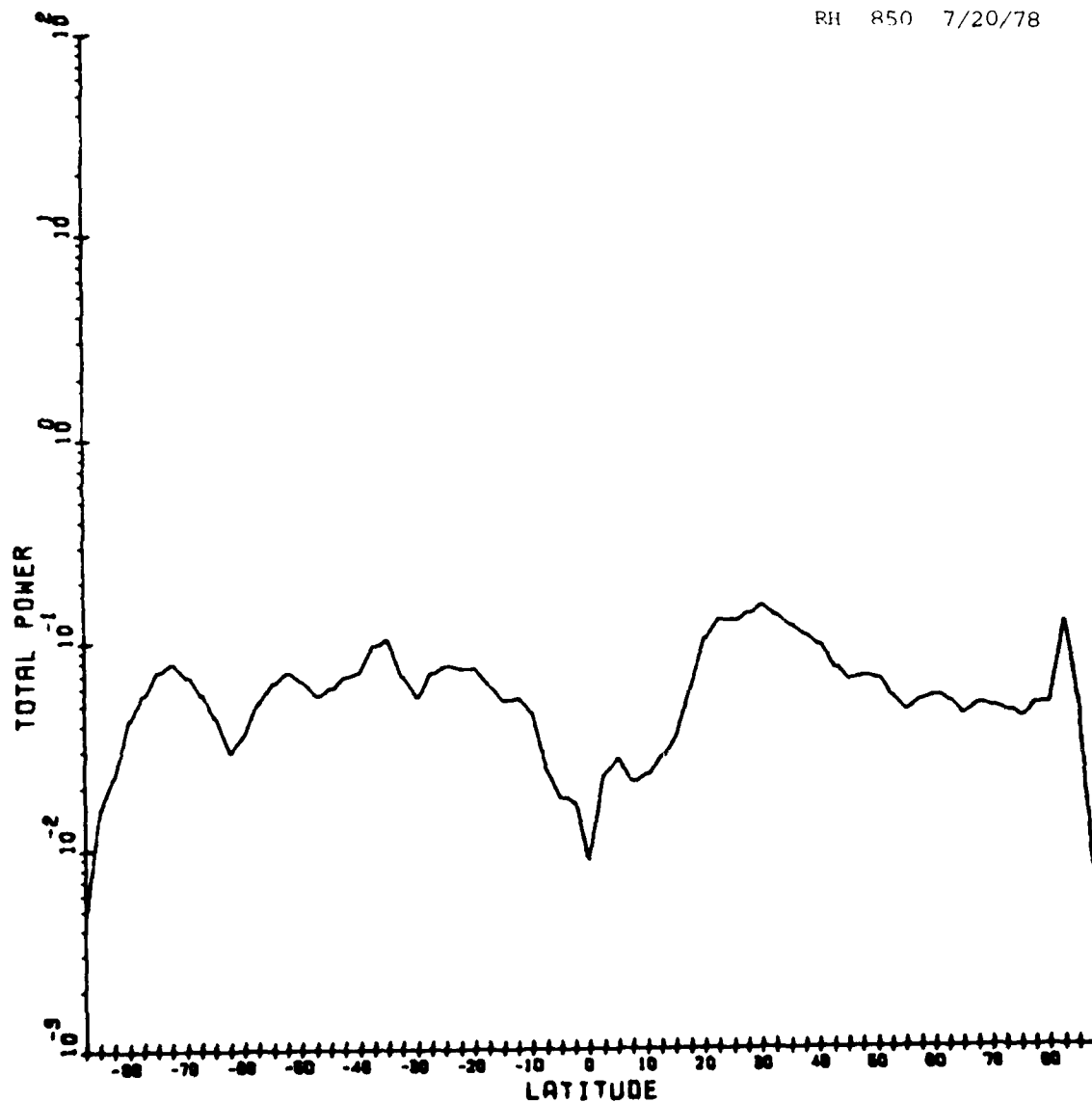


Fig. 8c. Total zonal power for the departures from the zonal average for the ratio q/q_s . Both q and T used in the calculations are the corrected field values.

RH 500 7/20/78

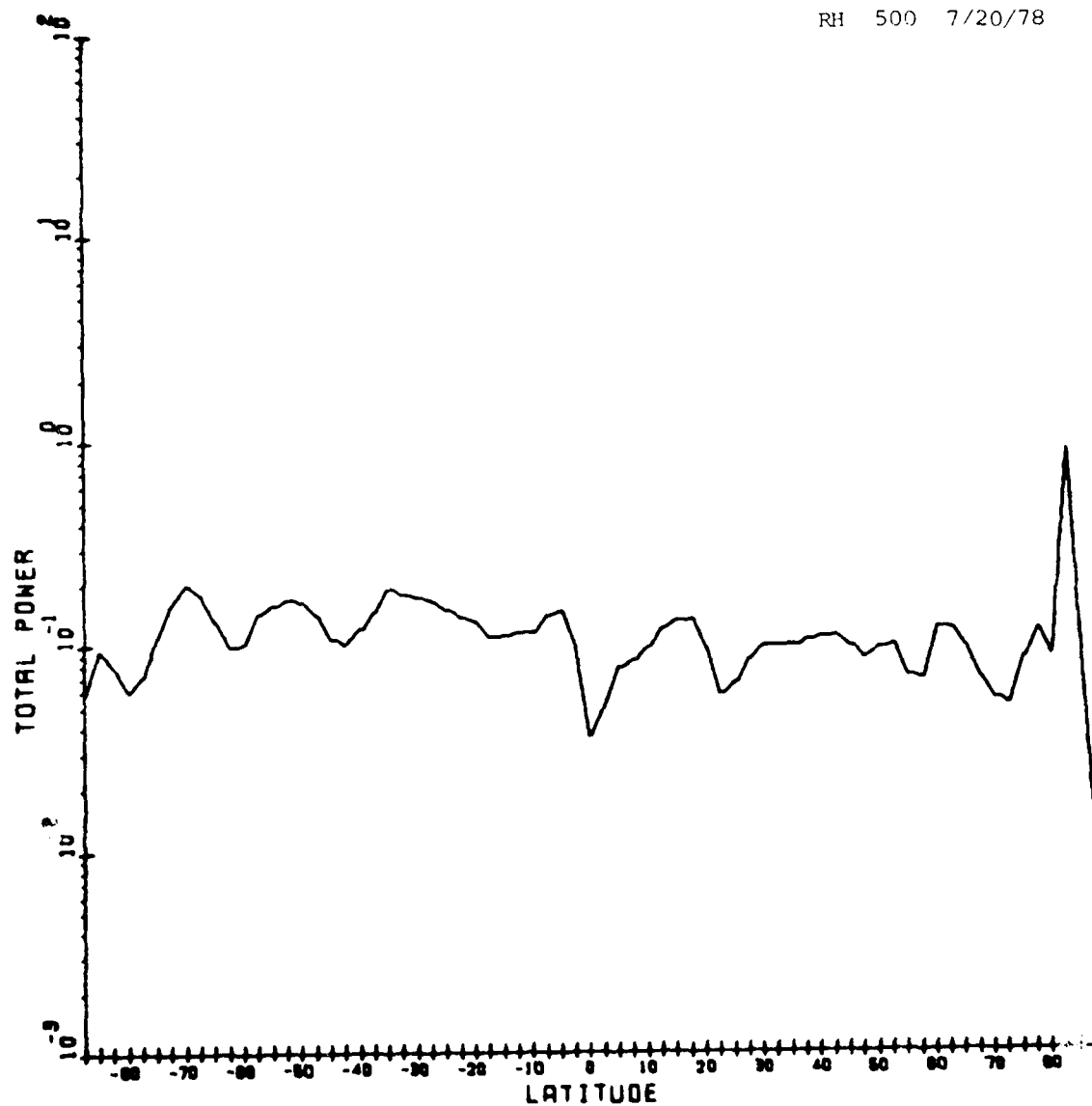


Fig. 8d. Total zonal power for the departures from the zonal average for the ratio q/q_s . Both q and T used in the calculations are the corrected field values.

where N represents the number of n modes and is a constant for a particular truncation, P_n^m is the associated Legendre function, and \bar{A} is the zonal mean. The expansion in Eq. (5) becomes exact for $M, N \rightarrow \infty$, but the number of grid points around latitude and longitude circles sets a maximum limit of 72. From the preceding zonal harmonic analyses, it is clear that amplitude approaches the noise level at $m = 32$; so a truncation limit of $M = 32$ was chosen. To evaluate the integral in Eq. (7), the global mean of the quantity, a Gaussian quadrature integration in the form

$$[A] \approx \sum_{k=1}^{64} \bar{A}_k w_k \quad (9)$$

was used, where w_k are the corresponding Gaussian weights. The 2.5° latitude values were interpolated linearly to the Gaussian latitudes, the quadrature was performed, then the values A^* were obtained at the Gaussian latitudes using Eq. (6). Once the departure values A^* were obtained, a Fast Fourier transform was used to evaluate the coefficients γ_{m_k} and δ_{m_k} of the expansion

$$A^*(\phi_k, \lambda) = \sum_{m=0}^M \gamma_{m_k} \cos m\lambda + \delta_{m_k} \sin m\lambda \quad (10)$$

where k represents the indices of the Gaussian latitudes, and $\gamma_{m_k}, \delta_{m_k}$ are given by

$$\gamma_{m_k} = \sum_{n=|m|}^N \alpha_n^m P_n^m(\mu_k) \quad (11)$$

$$\delta_{m_k} = \sum_{n=|m|}^N \beta_n^m P_n^m(\mu_k)$$

where $\mu_k = \sin \phi_k$. Using the orthonormality of P_n^m , we have

$$\begin{aligned} \alpha_n^m &= \int_{-1}^1 \gamma_{m_k} P_n^m(\mu_k) d\mu \\ \beta_n^m &= \int_{-1}^1 \delta_{m_k} P_n^m(\mu_k) d\mu. \end{aligned} \quad (12)$$

These integrals were also evaluated using the Gaussian quadrature technique. For $M = 32$ and 64 Gaussian latitudes, the highest order P_n^m that can be integrated exactly is P_{63}^{32} . Therefore $N = 63$ and $N = 31$ were chosen to complete the rhomboidal truncation of the expansion in Eq. (5). The forms of the quadrature for Eqs. (12) are

$$\alpha_n^m = \sum_{k=1}^{64} \gamma_{m_k} P_n^m(\mu_k) w_k \quad (13)$$

$$\beta_n^m = \sum_{k=1}^{64} \delta_{m_k} P_n^m(\mu_k) w_k.$$

The normalized power Δ_n^m was then evaluated in the form

$$\Delta_n^m = \frac{(\alpha_n^m)^2 + (\beta_n^m)^2}{\sum_{n=|m|}^{|m|+N} \sum_{m=0}^M [(\alpha_n^m)^2 + (\beta_n^m)^2]}. \quad (14)$$

Figs. 9a-i display the results of the spherical harmonic analyses for JAN. The quantity $n-m$ represents the number of times a particular harmonic passes through zero between the two poles; it can thus be thought of as a sort of meridional wave number. For this reason the logarithm of Δ_n^m was plotted on $n-m$ vs. m diagrams. As in the zonal spectrum figures, the \log_{10} values are plotted, so that the -3 contour refers to 0.1 percent contribution to the total power. As in the case of the zonal spectra, there is very little variation in the spherical spectra with season or height. However, when compared to the q figures, the temperature spectra show a greater concentration of power in low wave numbers both zonally and meridionally. More of the total power is contributed by higher wave numbers in q , so that short wave length variations are more important in the moisture variation than in the temperature variation. This difference in power distribution is even more evident in the Z 500 figure, especially in the concentration of power in the low zonal wave numbers which was seen in the zonal spectra. The power distribution for u is characterized by a marked spreading of the power toward higher meridional

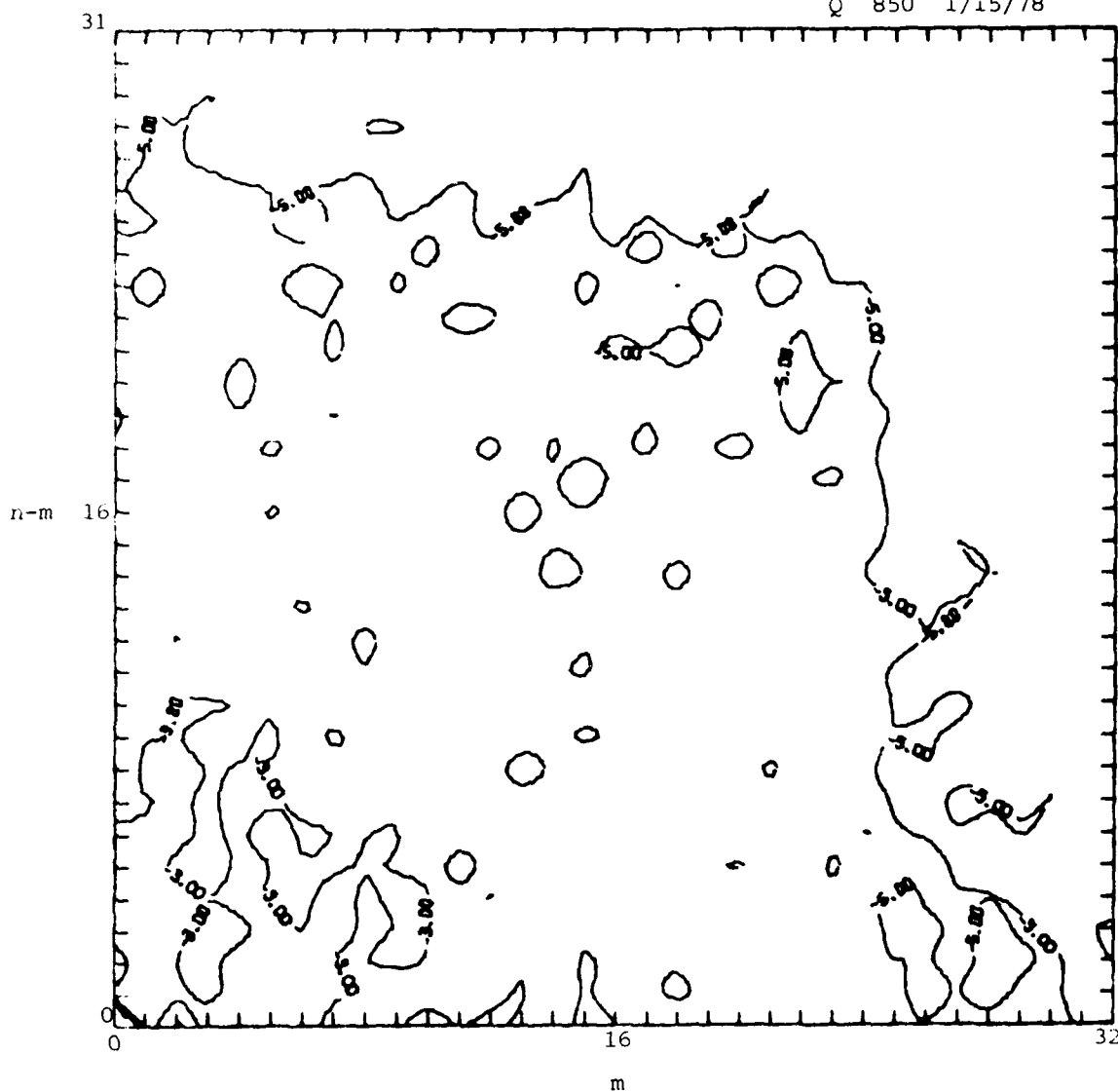


Fig. 9a. Spherical harmonic analysis for the departures from the global average. Contour values represent powers of 10 which are the fractional contribution to the total power by each wave number combination.

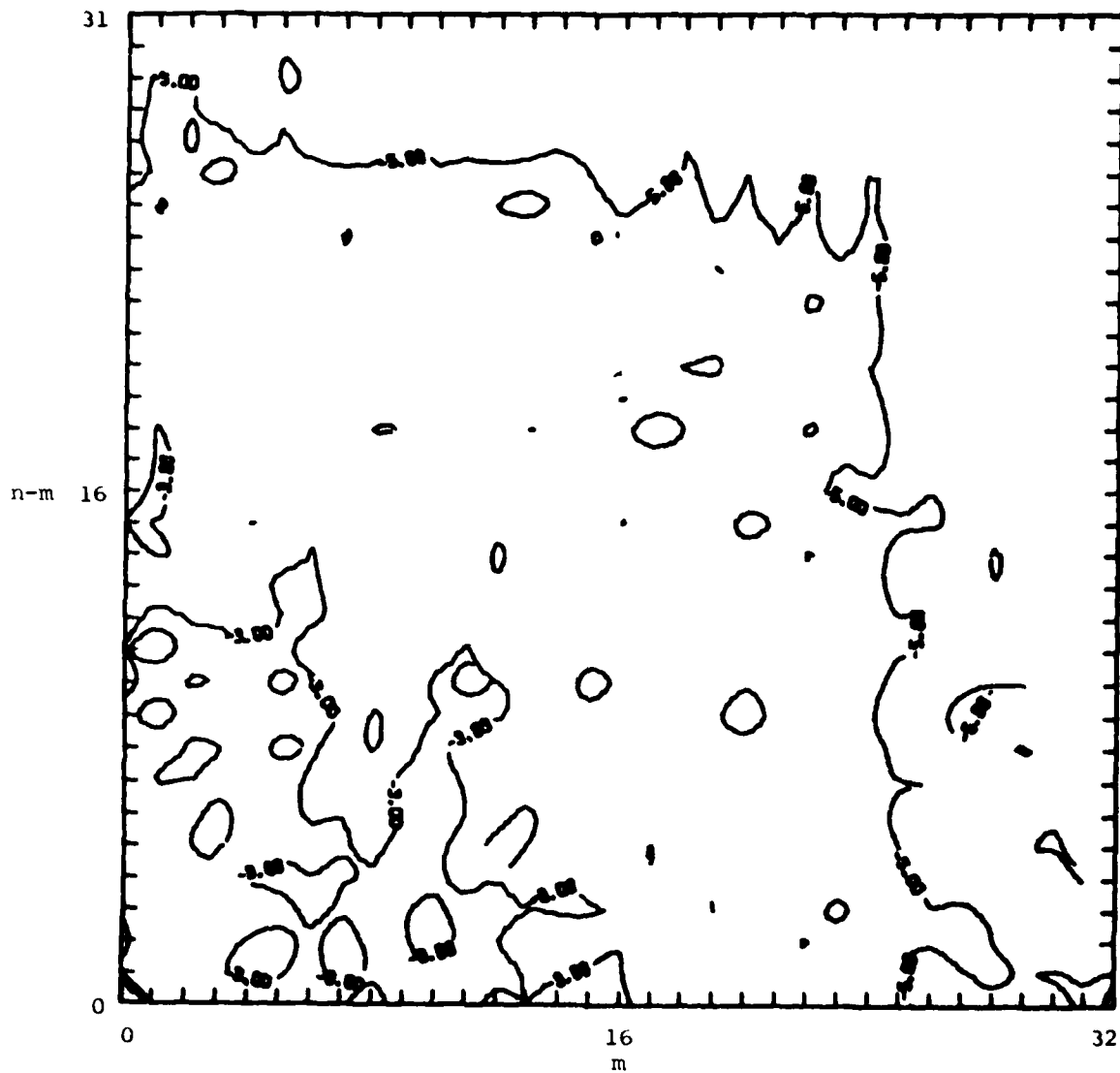


Fig. 9b. Spherical harmonic analysis for the departures from the global average. Contour values represent powers of 10 which are the fractional contribution to the total power by each wave number combination.

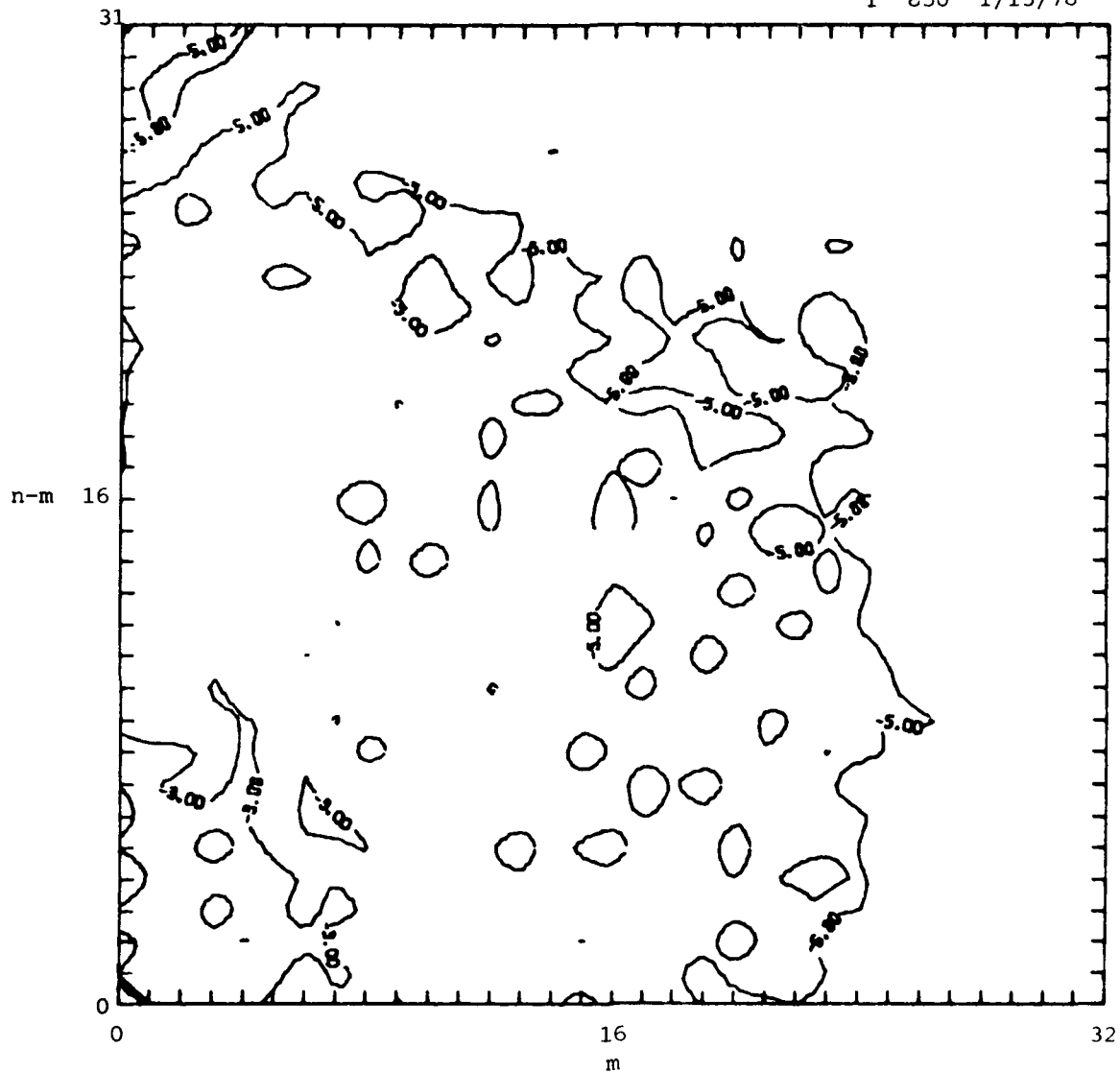


Fig. 9c. Spherical harmonic analysis for the departures from the global average. Contour values represent powers of 10 which are the fractional contribution to the total power by each wave number combination.

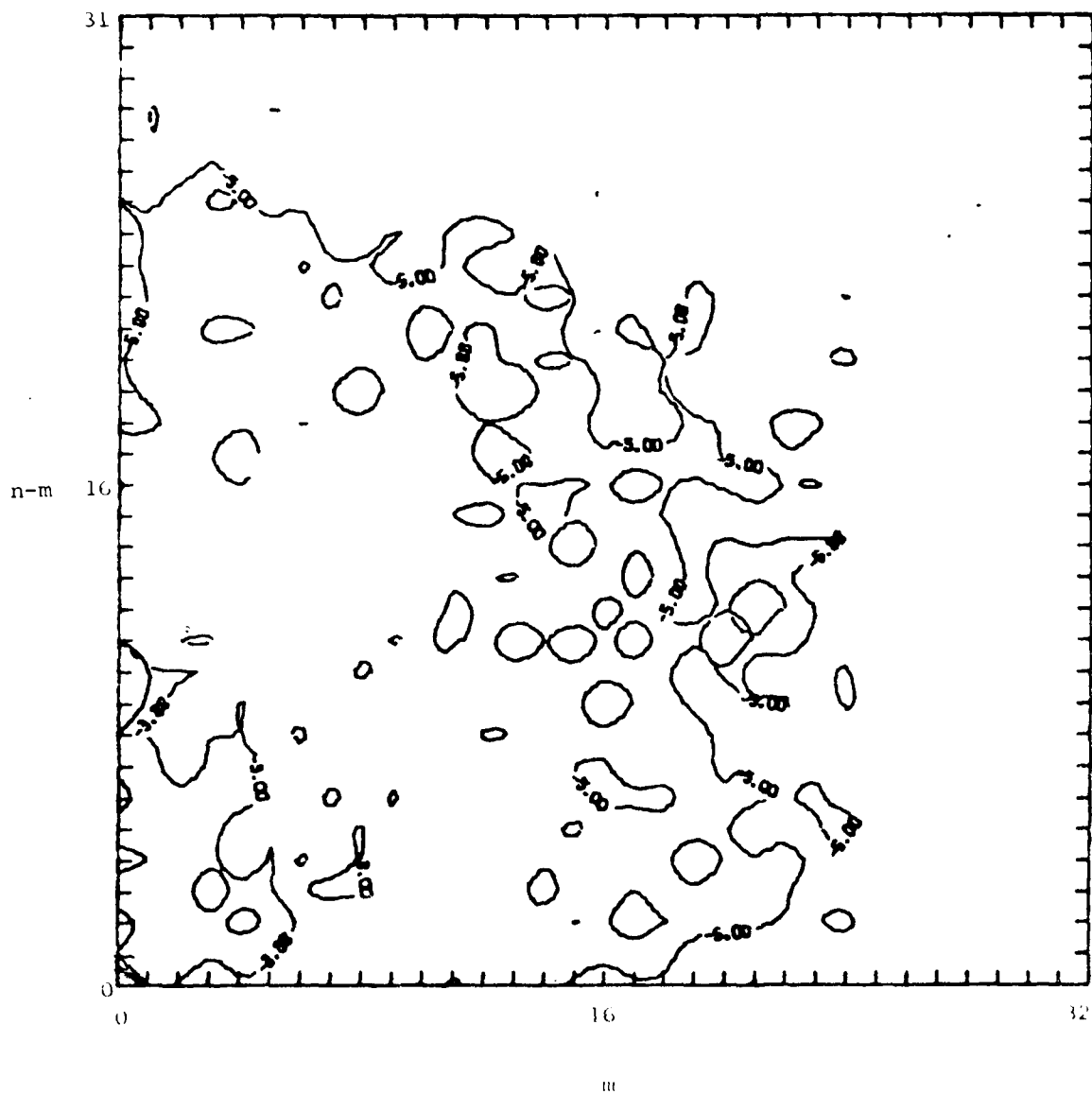


Fig. 9d. Spherical harmonic analysis for the departures from the global average. Contour values represent powers of 10 which are the fractional contribution to the total power by each wave number combination.

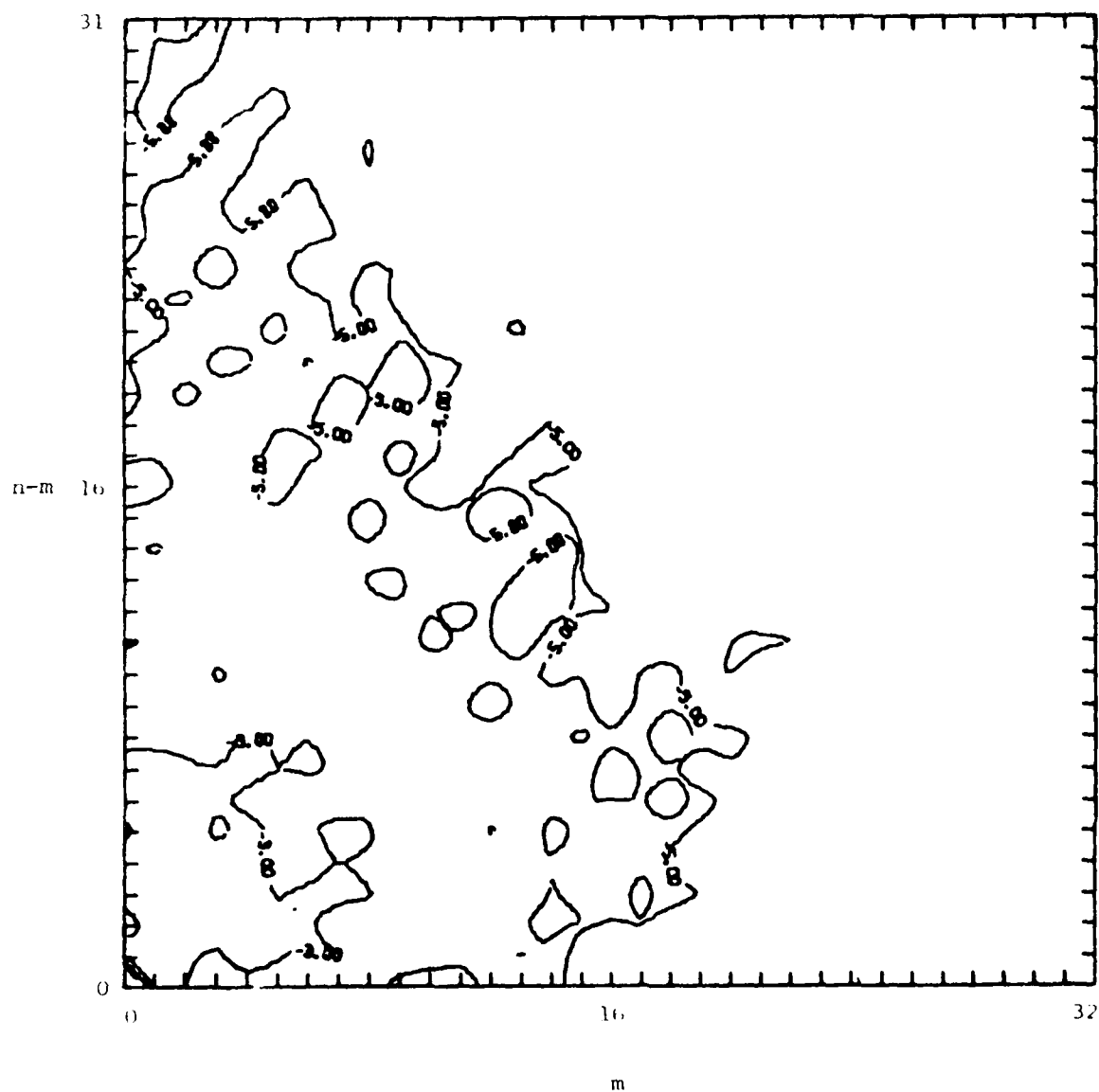


Fig. 9e. Spherical harmonic analysis for the departures from the global average. Contour values represent powers of 10 which are the fractional contribution to the total power by each wave number combination.

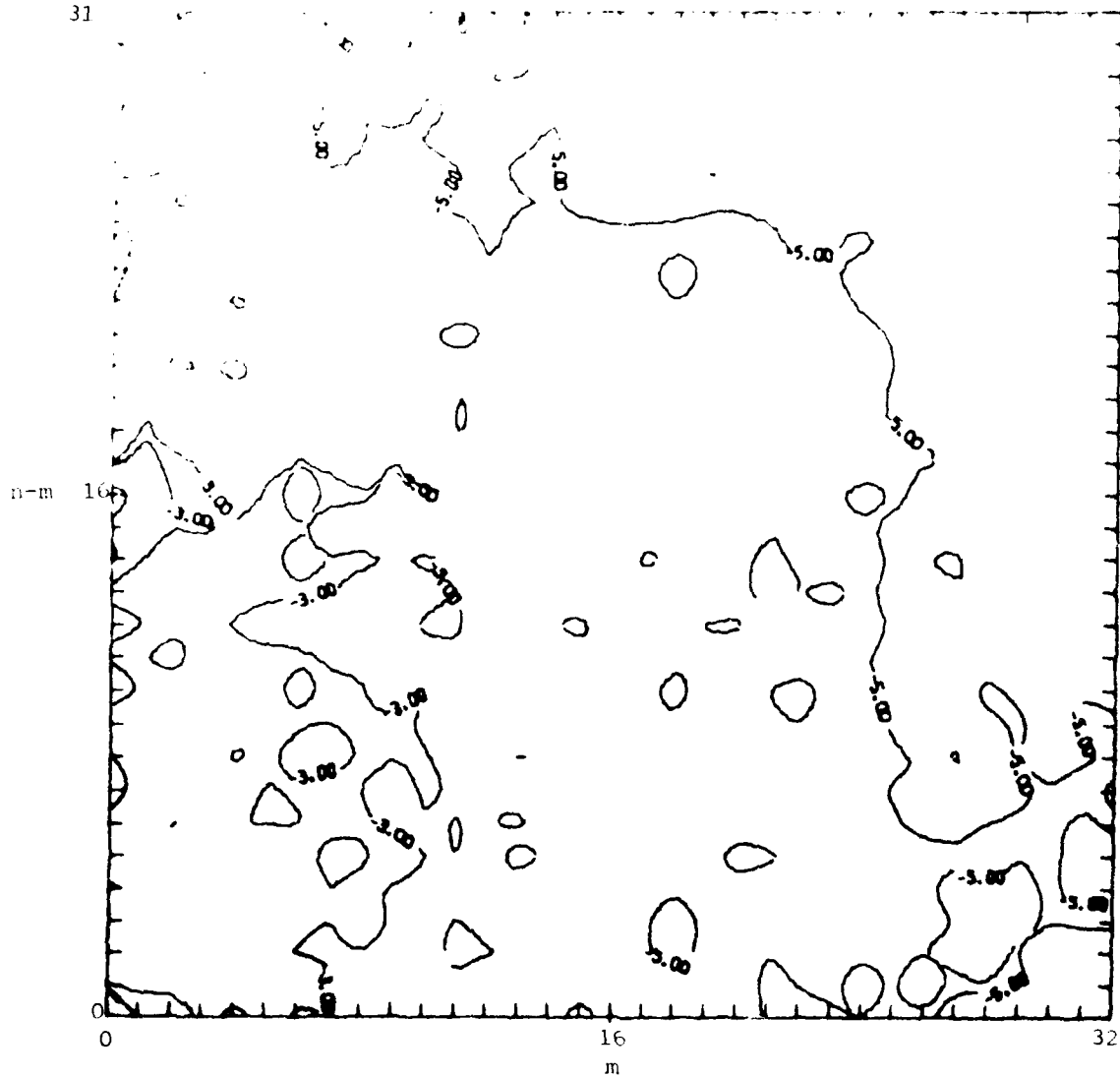


Fig. 9f. Spherical harmonic analysis for the departures from the global average. Contour values represent powers of 10 which are the fractional contribution to the total power by each wave number combination.

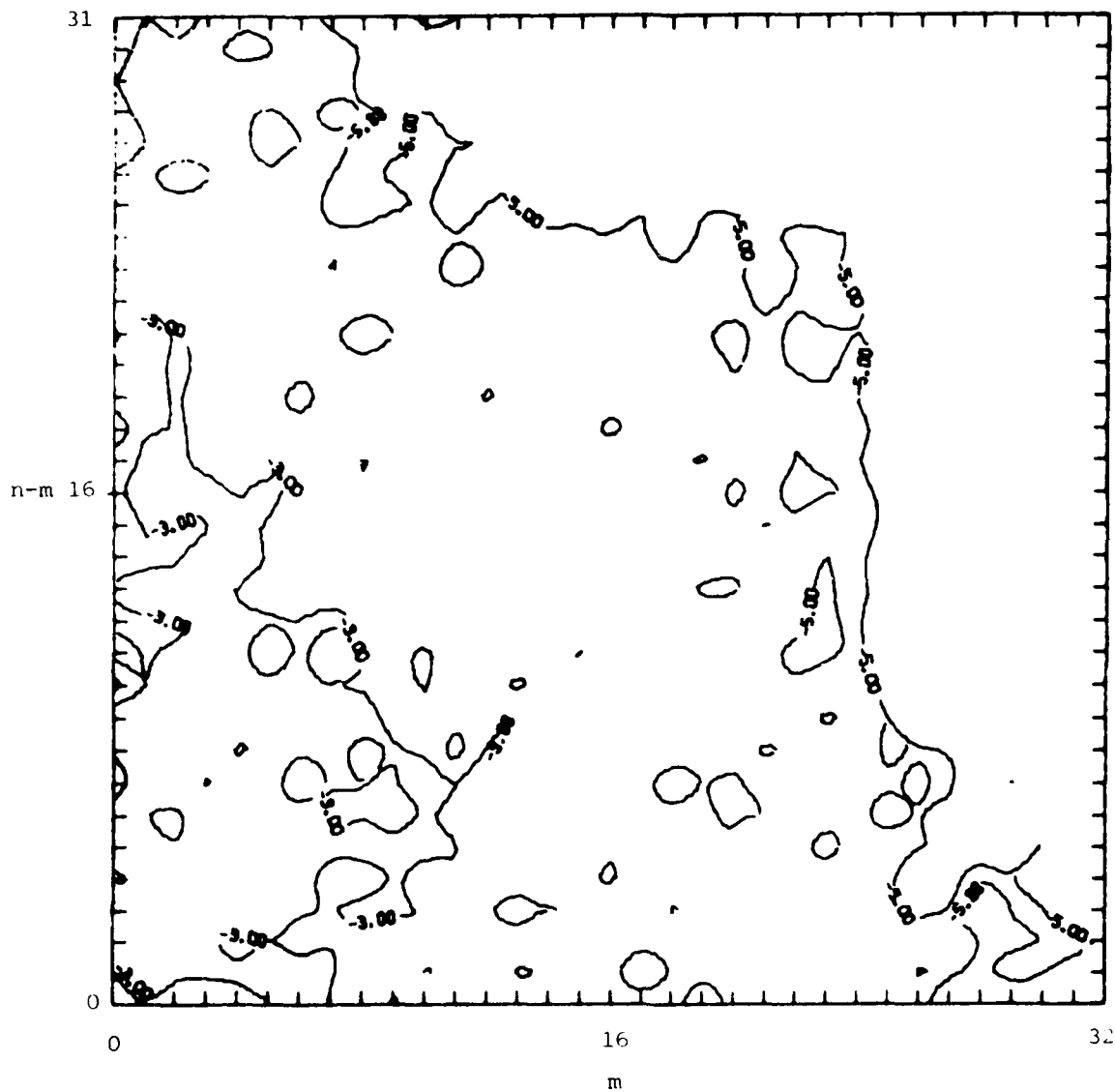


Fig. 9g. Spherical harmonic analysis for the departures from the global average. Contour values represent powers of 10 which are the fractional contribution to the total power by each wave number combination.

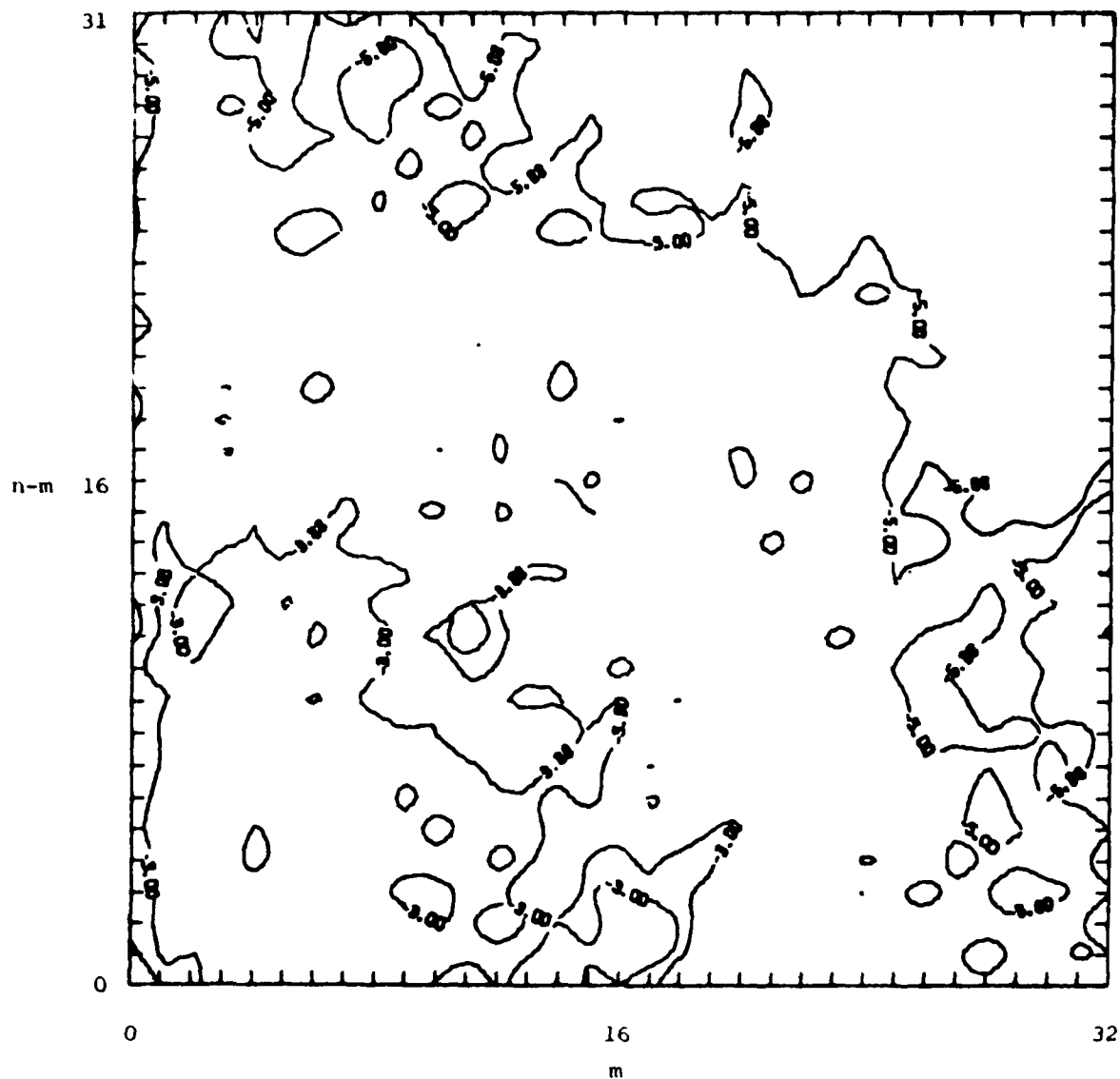


Fig. 9h. Spherical harmonic analysis for the departures from the global average. Contour values represent powers of 10 which are the fractional contribution to the total power by each wave number combination.

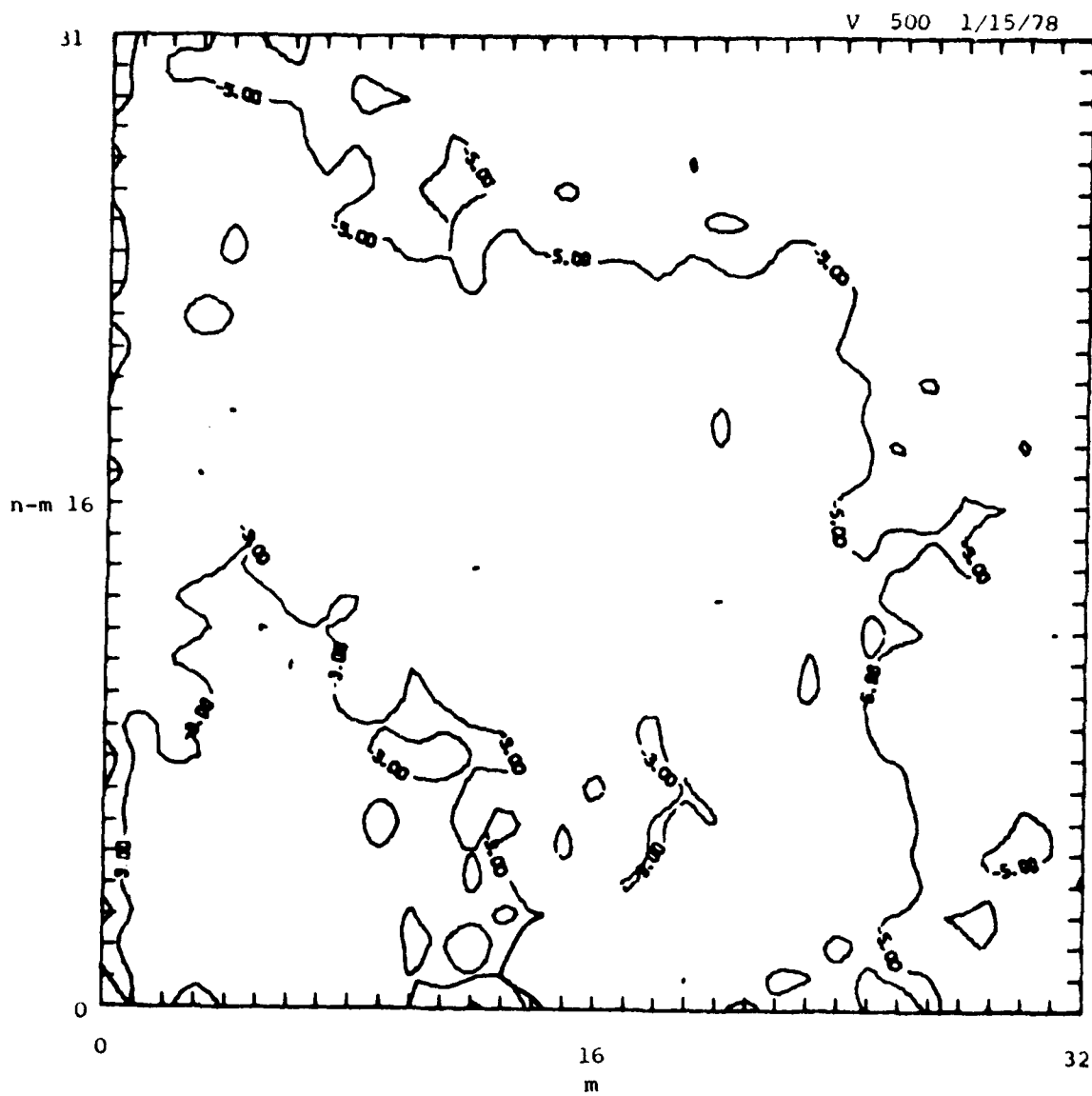


Fig. 9i. Spherical harmonic analysis for the departures from the global average. Contour values represent powers of 10 which are the fractional contribution to the total power by each wave number combination.

wave numbers and greater concentration of power in low zonal wave numbers. The v diagrams indicate a somewhat greater spectral spreading in both directions than q , although less meridionally than u . Also, because of the very small magnitudes of the zonal average of v , the power contribution from the $m = 0$, $n - m = 1, 2, 3, 4, \dots$ wave numbers is very small.

The greater concentration of power in long waves for temperature as compared with specific humidity is shown graphically in Figs. 10a-d. Here, the cumulative fraction of the power contributed by all the components that have both $n-m$ and m less than or equal to the value of "wave number" on the abscissa is plotted against wave number. Thus, for example, the value plotted on the figure at wave number 2 represents the sum of the fractional power contributions from all wave number combinations such that both m and $n-m$ are less than or equal to 2. The difference between values for consecutive wave numbers indicates the fraction contributed by the larger wave number. Since the analysis was performed on departures from the global average, there is no wave number zero contribution.

From the diagrams it is evident that while there is little seasonal or height variation in the power distribution for temperature, there is a distinct variation with height in the q curves. Wave numbers 1 and 2 together contribute some 60 - 65 percent of the total power at 850 mb, but less than 40 percent at 500 mb for both dates. In all cases, it is clear that a greater portion of power is accounted for in the first two wave numbers for temperature than for q . These graphs demonstrate the error incurred in a rhomboidal truncation at a given wave number. For example, choosing a wave number 10 truncation in an analysis would be quite satisfactory for temperature since in all cases well over 90 percent of the variance would be accounted for. However, this would not be a satisfactory choice for q , since a lesser portion of the variance would be included. In all cases for both q and T , the wave number 2 contribution is greatest. The cumulative fractional power curves for u and v (Figs. 11a-d) reveal a significantly different picture. The larger contributions are at higher wave numbers and no single wave number is so clearly dominant as is the case in the q and T curves.

Because the fields analyzed spectrally in this study are corrected Flattery analyses, it is conceivable that some characteristics of the Flattery analysis procedure may be evident in the fields. One feature of

850 MB 1/15/78

T —————

Q x—x—x—x—x

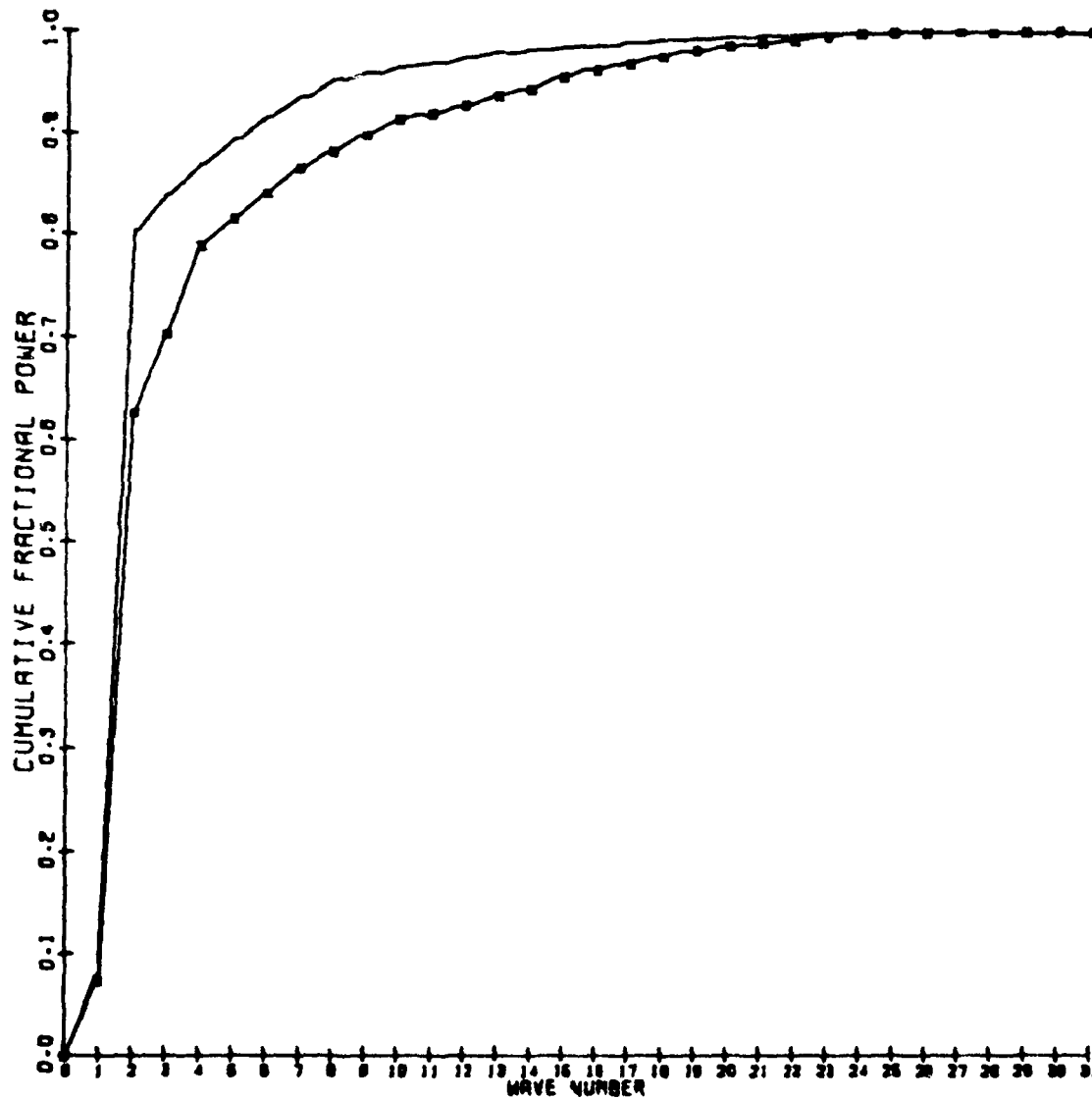


Fig. 10a. Cumulative fractional power for the spherical harmonic analyses. Wave numbers refer to equal values of m and $n-m$, and fractional amount plotted refers to contribution by all wave numbers less than or equal to the indicated wave number

300 MB 1/15/78

I —————
 2 x x x x x x x x

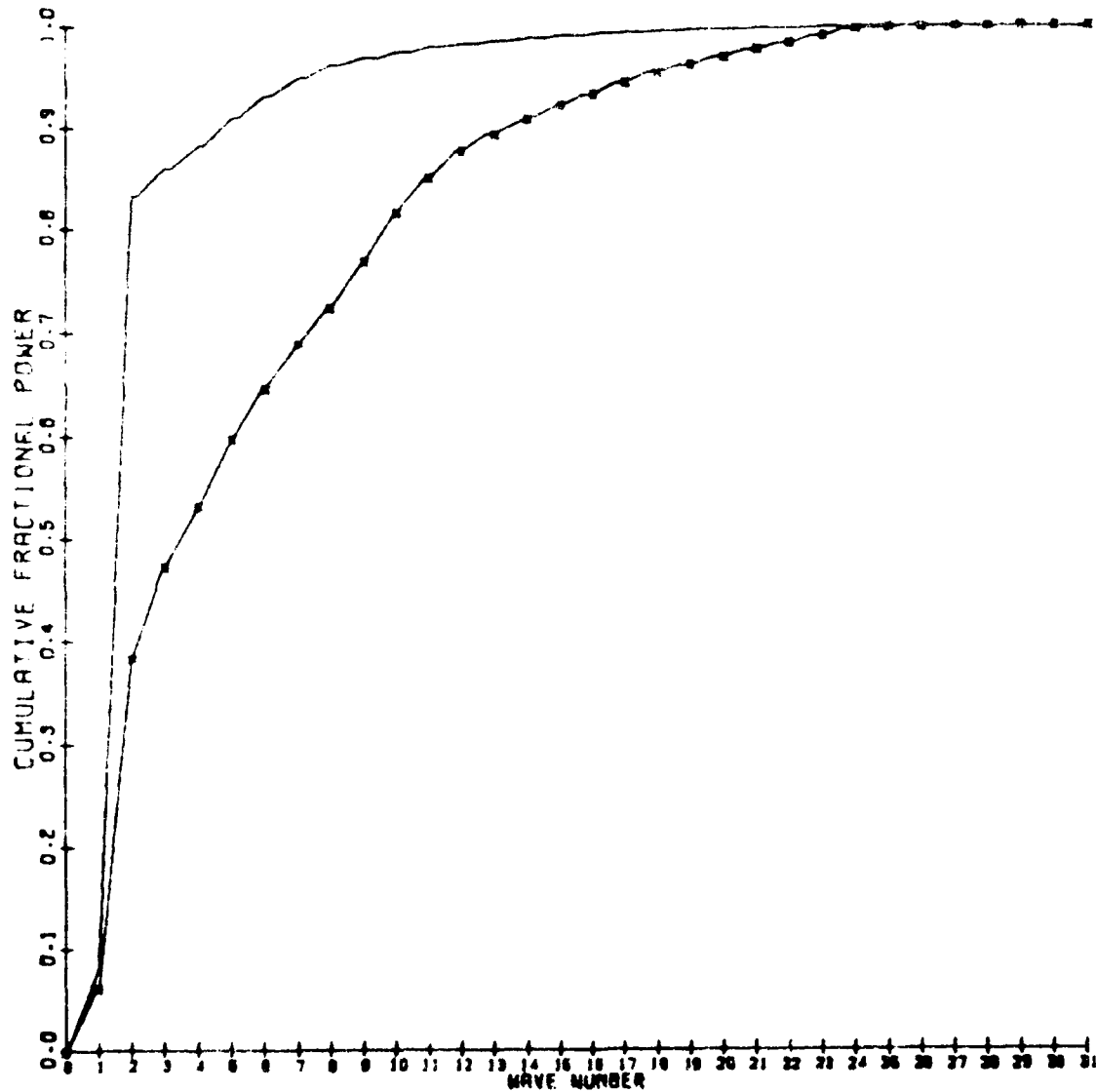


Figure 4. Cumulative fractional power for the spherical harmonic analysis. Wave numbers refer to equal values of n and $n-m$, and fractional amount plotted refers to contribution by all wave numbers less than or equal to the indicated wave number.

850 MB 7/20/78

T —————
Q x—x—x—x—x

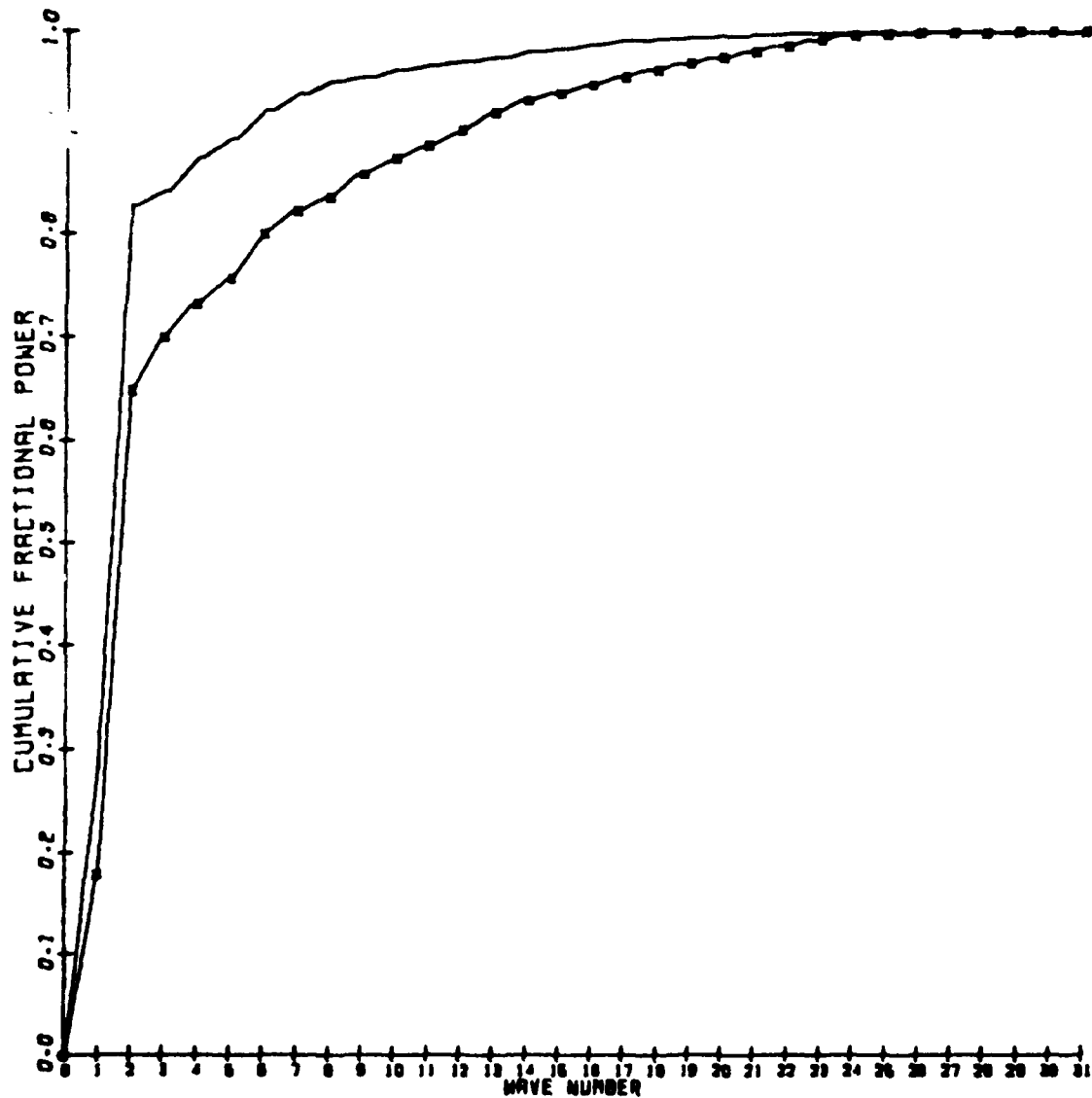


Fig. 10c. Cumulative fractional power for the spherical harmonic analyses. Wave numbers refer to equal values of m and $n-m$, and fractional amount plotted refers to contribution by all wave numbers less than or equal to the indicated wave number.

500 MB 7/20/78

T —————
Q x—x—x—x—x

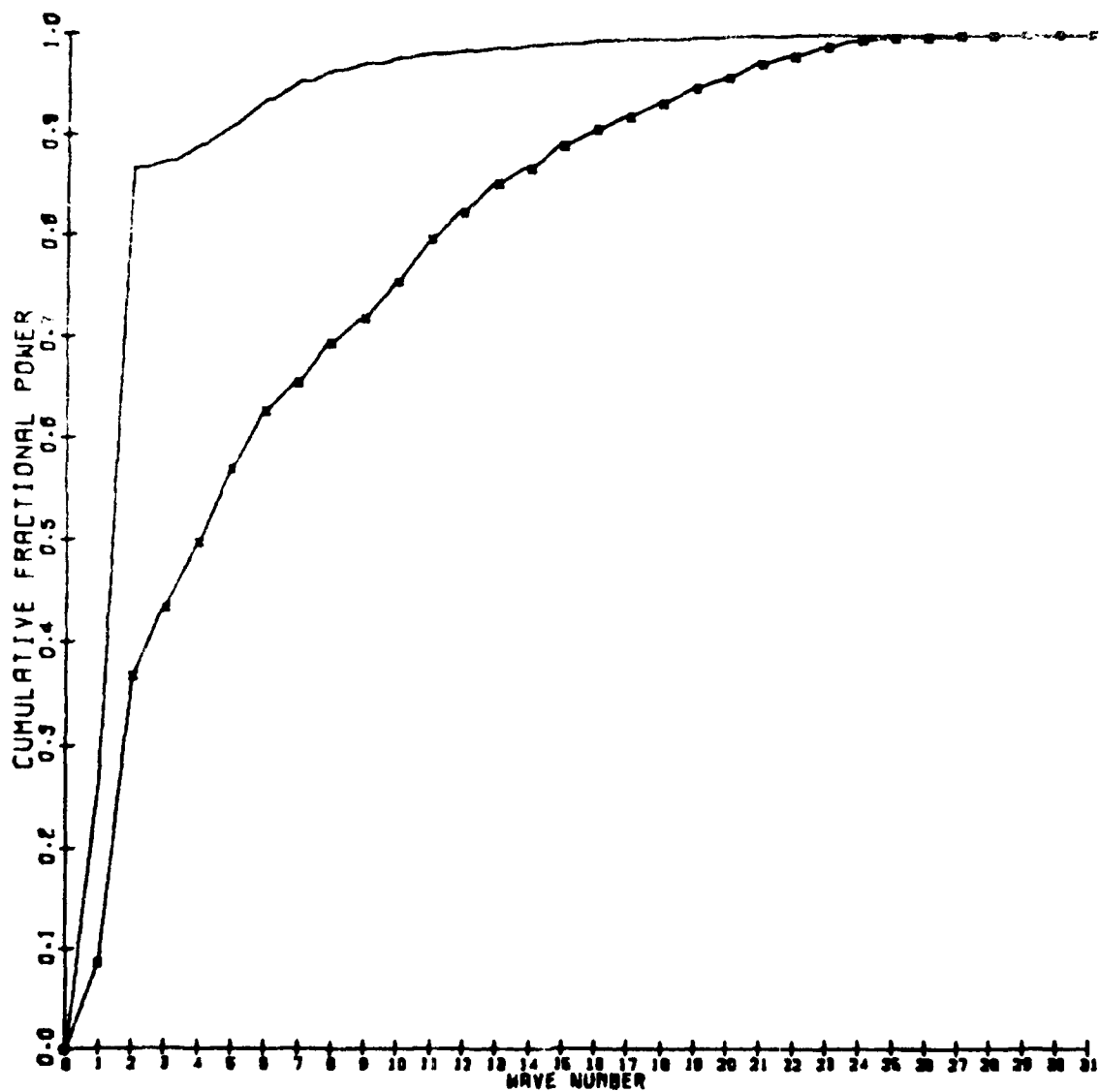


Fig. 10d. Cumulative fractional power for the spherical harmonic analyses. Wave numbers refer to equal values of m and $n-m$, and fractional amount plotted refers to contribution by all wave numbers less than or equal to the indicated wave number.

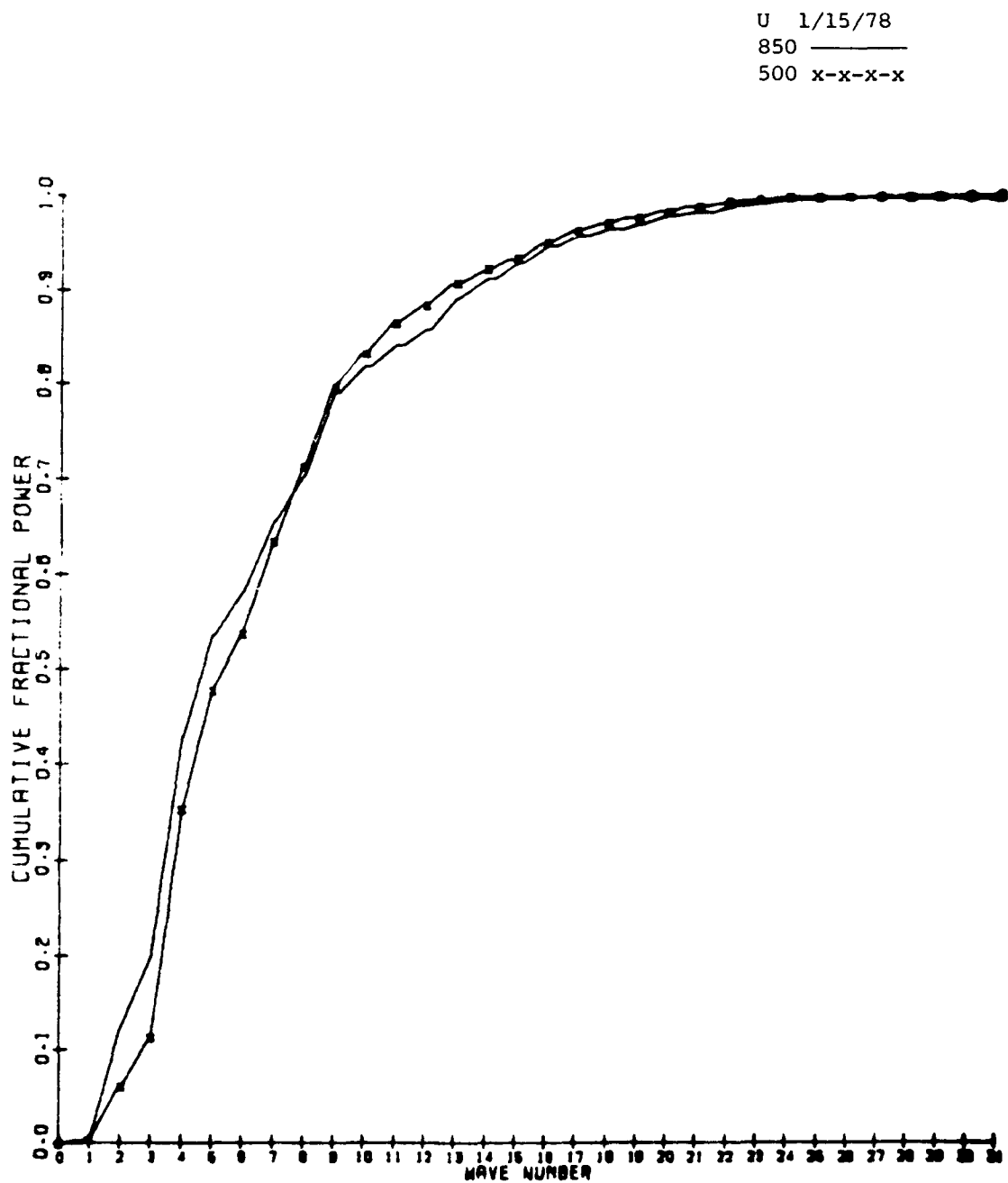


Fig. 11a. Cumulative fractional power for the spherical harmonic analyses of the wind components.

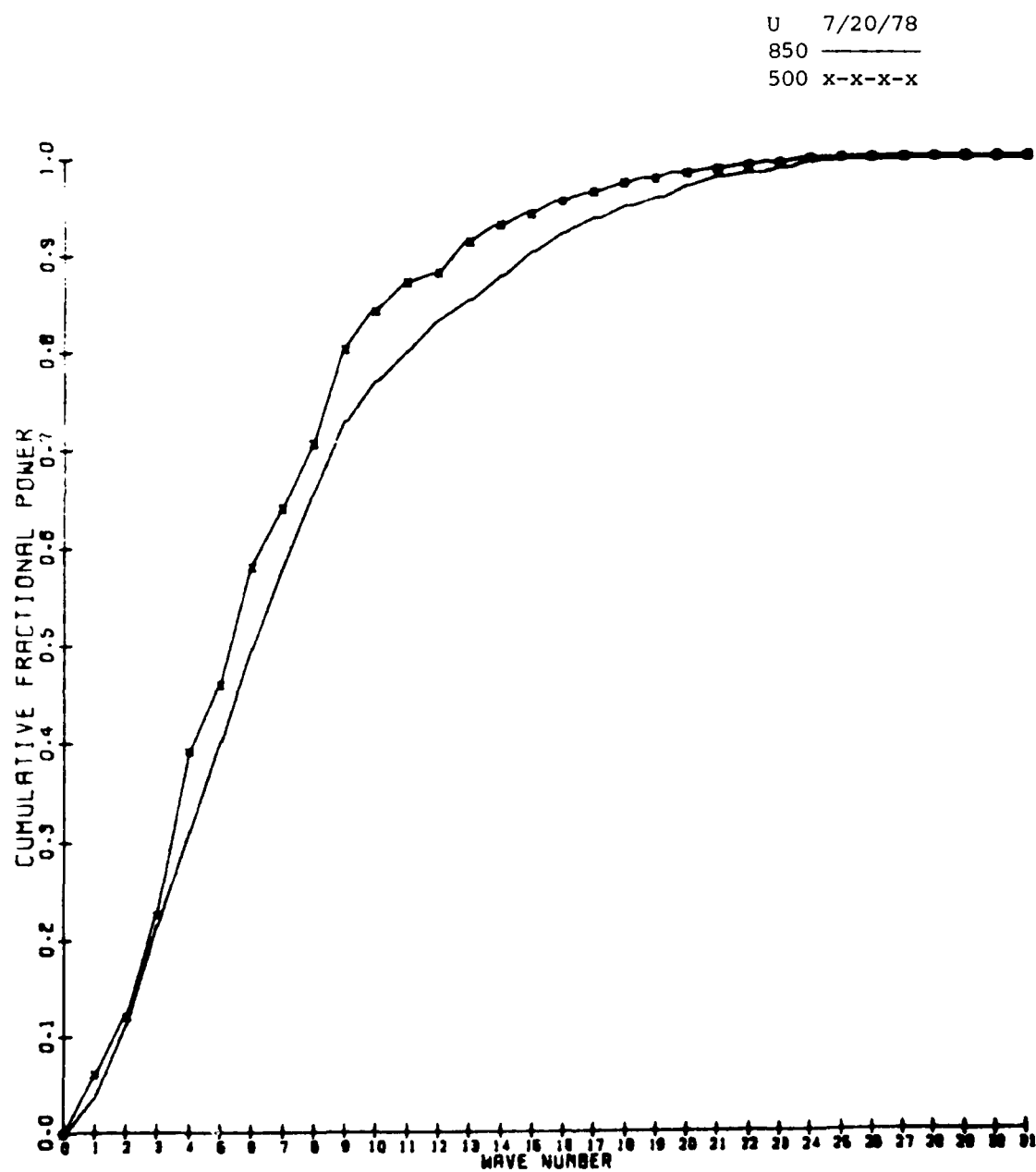


Fig. 11b. Cumulative fractional power for the spherical harmonic analyses of the wind components.

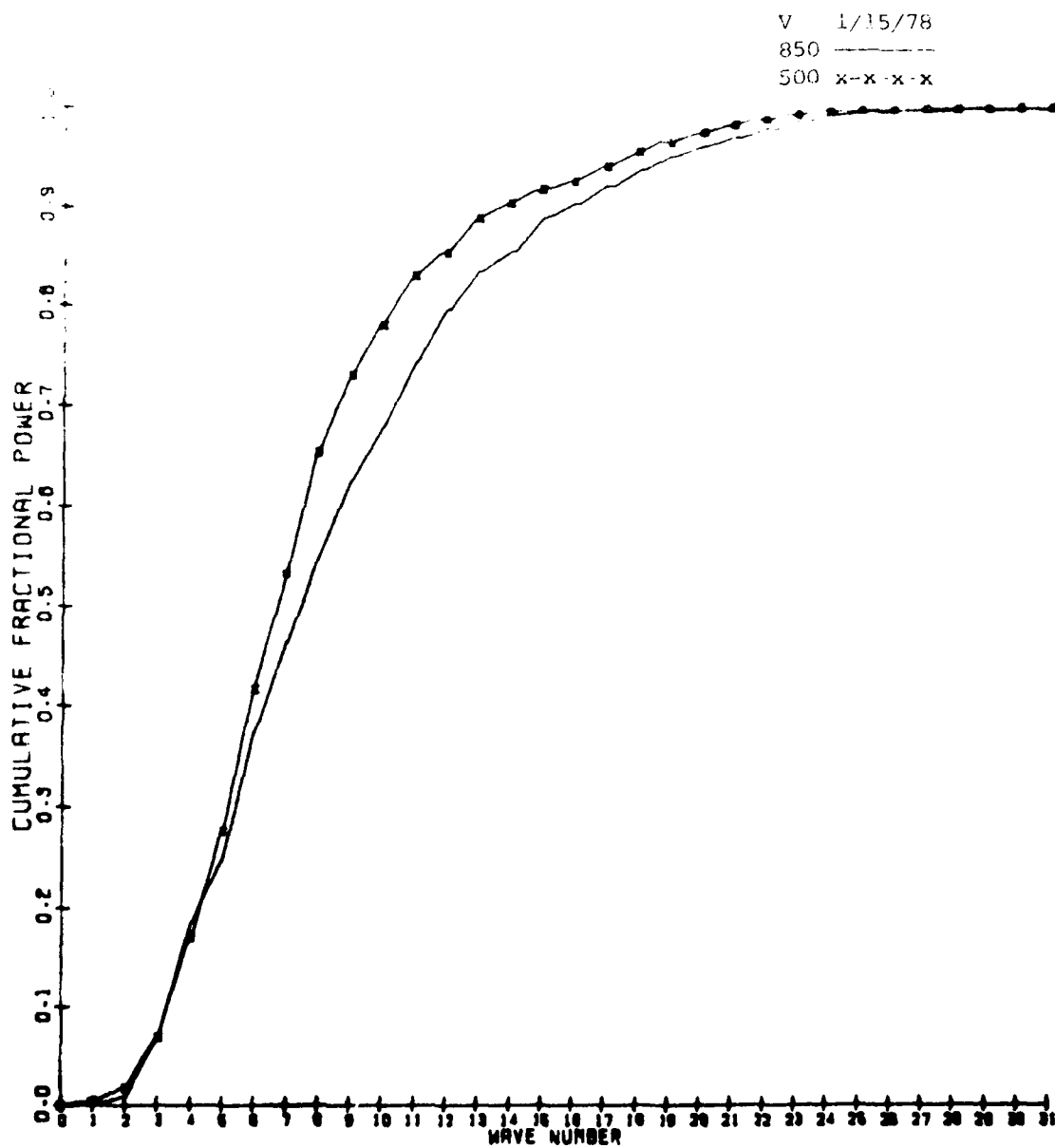


Fig. 11c. Cumulative fractional power for the spherical harmonic analyses of the wind components.

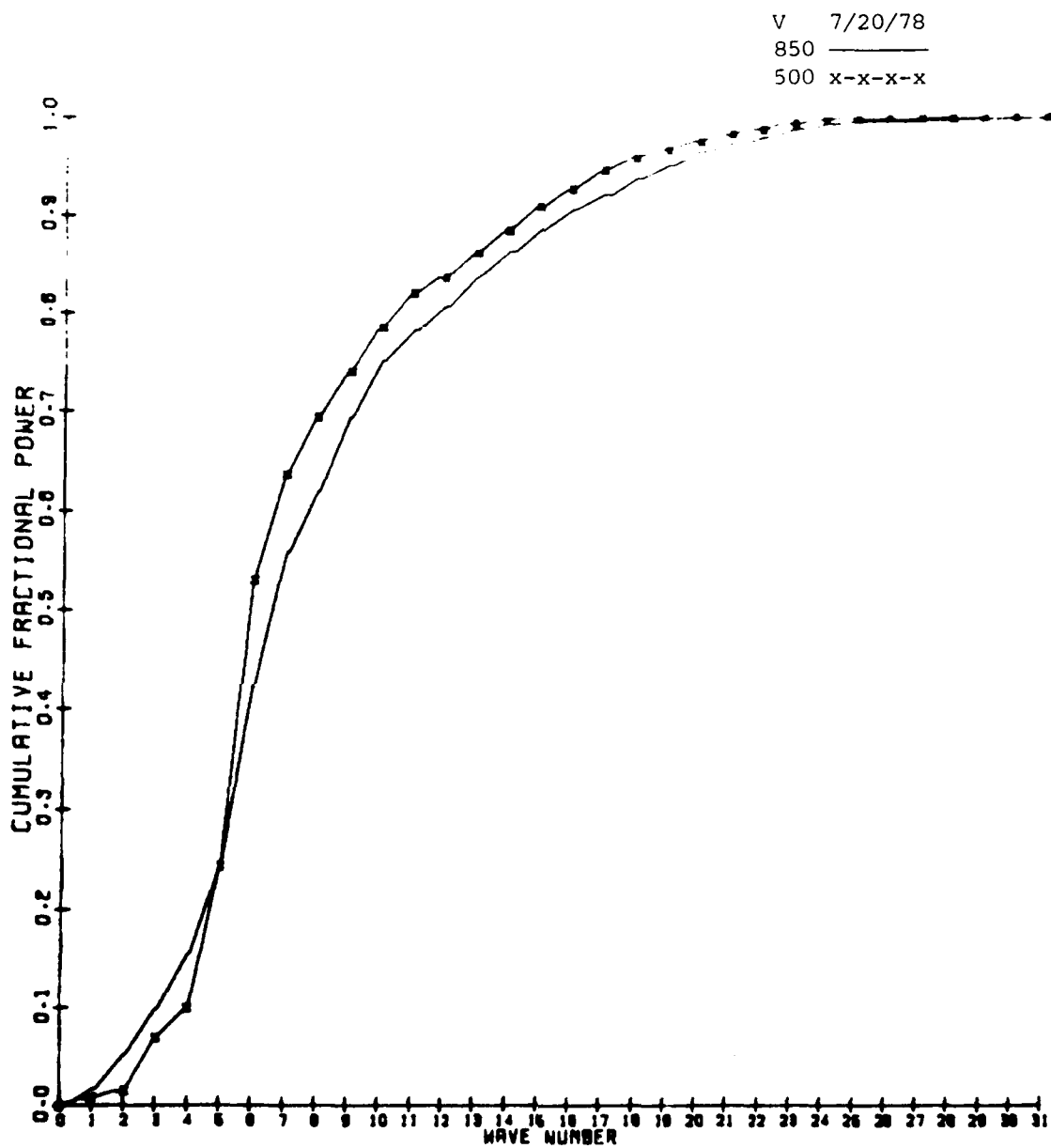


Fig. 1ld. Cumulative fractional power for the spherical harmonic analyses of the wind components.

the Flattery analysis of relative humidity is the use of only the first three modes of the vertical part of the variation of the quantity, as compared to the use of seven modes for the other quantities. For $s(\lambda, \phi)$ defined as the departure from the global mean for the quantity $s(\lambda, \phi, p)$, the horizontal coefficient, $s_k(\lambda, \phi)$ of the expansion

$$s(\lambda, \phi, p) = \sum_{k=1}^K s_k(\lambda, \phi) \psi_k(p) \quad (15)$$

can be obtained for each vertical level p if $\psi_k(p)$ is a specified vertical function (EOF) values $\psi_k(p)$ are obtained at each vertical level. Holmström (1963)¹⁰ has developed an iterative method to obtain both s_k and ψ_k values for all K modes from global simultaneous observation of the quantity s under consideration. The mode limit K cannot exceed the number of radioonde pressure levels included in the calculations, but the Flattery relative humidity analysis requires $K=3$ even for three radioonde pressure levels are available. To determine whether or not this truncation can account for the unexplained variation of the horizontal spectrum of q in the Freeman-corrected fields (where Flattery analyzed the fields were used to form the first guess q field), ratios of observed q for both JAN and JUL were processed under Holmström's method. The quantity

$$r_k = \left[\frac{s_k^2(\lambda, \phi)}{\sum_{k=1}^K s_k^2(\lambda, \phi)} \right] \quad (16)$$

was computed from the results, where the bracket refers to a time-weighted average over all sounding. This averaged normalized power of the horizontal spectrum r_k is then summed for increasing values of k to a cumulative sum, with $\sum_{k=1}^K r_k = 1$. Results show that between 90 and 99 percent of the variance can be computed only by the first three modes. This indicates that the choice of only the first three modes for the relative humidity analysis probably has very little impact on the vertical distribution of the horizontal spectral characteristics of humidity.

10. Holmström, L., 1963: On a method for parametric representation of the state of the atmosphere. Tellus, 15, 127-149.

Table 4 gives the fractional contributions from several wave number bands for the four quantities q , T , u , v . For the lowest wave number band, the power contribution for u and v is very small compared to T and q 850, and somewhat smaller than the q 500 cases. However, the tables are turned in the 3-10 wave number band, where the contributions for u and v are substantially larger. The contributions for q , u , and v are closer in the highest wave number band. In summary, q is unique in showing much more variation with height than the other three parameters. There are no great changes in any of the quantities with season, and q stands quite alone in its distribution of power with wave number, lying somewhere between the high concentration in low numbers for T and the greater distribution of power from shorter waves for the wind components.

TABLE 4. FRACTIONAL CONTRIBUTIONS TO TOTAL POWER IN SPHERICAL HARMONICS SPECTRUM FROM SEVERAL WAVE NUMBER BANDS.

<u>DATE</u>	<u>LEVEL</u>	<u>WAVE NUMBER BAND</u>	<u>q</u>	<u>T</u>	<u>u</u>	<u>v</u>
1/15/78	850	1-2	.63	.80	.12	.01
		3-10	.28	.16	.70	.67
		11-20	.07	.03	.16	.28
	500	1-2	.38	.83	.06	.02
		3-10	.43	.15	.77	.76
		11-20	.16	.02	.15	.19
7/20/78	850	1-2	.65	.83	.11	.05
		3-10	.22	.13	.66	.70
		11-20	.10	.04	.20	.21
	500	1-2	.37	.87	.12	.01
		3-10	.38	.11	.72	.77
		11-20	.21	.02	.14	.19

The preceding discussion lumped zonal and meridional wave numbers together in discussing spectral composition. It is also of interest to determine the largest contribution from a single wave number combination. Table 5 shows the fractional contribution from the $n = 2$, $m = 0$

wave for each of the quantities. In addition, the maximum values for any single wave number combination for u and v are given. For q , T , and Z , these contributions stood out as by far the largest of any wave number combination. This is expected since it represents the maximum at the equator and minimum at the poles displayed by the zonal mean of these quantities. The zonal wind component shows its maximum power in the $n = 4$, $m = 0$ harmonic, reflecting the dominance of the zonal mean in its variation between westerlies at mid-latitudes and easterlies in the tropics. Because the zonal mean is so small, v shows its largest power at zonal wave number 4 for JAN and 6 for JUL, and for the variation passing through two zeros between the poles.

TABLE 5. FRACTIONAL CONTRIBUTION OF $n = 2$, $m = 0$ HARMONIC TO TOTAL POWER.

Level	Date	q	T	Z	u	v
850	1/15/78	.54238	.66164	—	.10771(.11622)*	.00014(.06318)
500	1/15/78	.29926	.72589	.75830	.04684(.14380)	.00036(.06103)
850	7/20/78	.40235	.52509	—	.05337(.06181)	.00084(.04251)
500	7/20/78	.24650	.59242	.52723	.05083(.12871)	.00001(.10358)

* Values in parentheses for u , v represent the largest contribution from a single harmonic: for u , in all cases the $n = 4$, $m = 0$ harmonic; for v , the $n = m = 2$, $m = 4$ harmonic for 1/15 and the $n = m = 2$, $m = 6$ harmonic for 7/20.

The correlation coefficient given in Eq. (4) was evaluated between the fractional spherical harmonic power spectrum values of q and those of T , u , and v . The results are given in Table 6. The large values for T relative to those of u and v come about directly from the fact that both q and T have relatively large fractional contributions at common harmonics (especially $n = 2$, $m = 0$) compared to those of u and v . However, the danger of drawing conclusions on the basis of correlations alone is seen when one recalls the differences between power distribution of q and T in the cumulative fractional power curves. What is surprising is that the greater difference in power distribution between q and T at 500 mb than at 850 mb is not indicated at all in the correlation coefficient values. It appears that the two-dimensional correlation coefficient values are heavily influenced by the coincidence of large values at just a very few components.

TABLE 6. CORRELATION OF T, u, AND v WITH q FOR SPHERICAL HARMONIC SPECTRA.

Level	Date	T	u	v
850	1/15/78	.99	.62	.62
500	1/15/78	.97	.36	.64
850	7/20/78	.97	.46	.65
500	7/20/78	.92	.38	.68

For completeness, the values for total power for the spherical harmonic analyses are given in Table 7. Here, q seems to be more similar to the lack of change of total power with season which is evident in the other four parameters. In all four cases, the greater variance occurs in the Northern Hemisphere winter. This may result from the greater number of observations and therefore greater corrections to a relatively smooth Flattery-analyzed field. While there are more observations for q in the Northern Hemisphere also, this may be partially offset by the lower variance of q in the winter hemisphere as seen from the zonal spectrum analyses.

TABLE 7. TOTAL POWER FOR SPHERICAL HARMONICS.

Level	Date	q (G/KG) ²	T (°K) ²	u (M) ²	v (M) ²	v (M/S) ²
850	1/15/78	41.26866	358.15657	---	204.15673	128.61541
500	1/15/78	6.17996	297.63161	181255.28491	533.97243	291.94008
850	7/20/78	43.22954	249.25719	---	149.16504	107.41301
500	7/20/78	5.77466	233.86061	127382.00693	380.12735	217.46096

IV. Summary and Conclusions

The following is a summary of the similarities and differences noted when comparing observed and analyzed global specific humidity fields with those of temperature, zonal wind component, and meridional wind component:

1. In physical space on the synoptic scale there is good correlation between the q perturbations and T, u, and v perturbations. Warm, moist air is transported poleward and cold, dry air equatorward by the large-scale eddies.
2. The zonal harmonic spectra for q are more similar to those of T than they are for u and v in that most of the power is contributed by low wave number (large scale) waves. The zonal wind appears to be even more re-

stricted to long waves in its power distribution, while the v power seems to be more spread out over shorter waves.

3. While the total power of the departures from the zonal mean for q exhibits a broad maximum in a band of latitudes about the equator, the T total power shows a minimum at the equator and the poles and relative maxima at mid-latitudes. Zonal eddy power curves for u and v are decidedly more monotonic with latitude. In addition, the total zonal perturbation power for q is somewhat less in the winter hemisphere than in the summer hemisphere, in direct contrast to T , u , and v . However, total eddy power for relative humidity in the two hemispheres is about the same.

4. The spherical harmonic spectra for q are similar to those for temperature in having most of their power contributed by the zonal mean that has a single wave length between the poles (minima at the poles, maxima at the equator). The u , v spectra showed maximum power contributed by shorter waves in both directions.

5. However, the spherical harmonic power spectrum for q is less concentrated in low wave numbers than is that for T , but is not as spread out in higher wave numbers in either direction as are u and v .

6. For a single wave number representing an equal number of zonal waves as zeros between the poles, the q spectra show a significantly greater concentration of power in the 1-2 wave number band at 350 mb than at 500 mb. This height difference was not evident in T , u , or v . None of the quantities shows much variation in the power distribution with season.

In general, the temperature and geopotential height spectra have their power too highly concentrated in the low wave numbers to be good representations for q . The wind components seem to have too much power in high wave numbers to be representative for q . As a result, it appears that neither the mass field nor the wind components analyses will adequately portray the moisture field.

The results of this study seem to indicate that a separate moisture analysis scheme is required in order to generate a satisfactory moisture representation for a forecast model input. Because of the unique spectral character of specific humidity, it seems inadvisable to use a multivariate analysis for moisture using any of the other parameters considered in this study.

B. THE GENERATION OF HARMONICS FOR ANALYSIS OF METEOROLOGICAL DATA IN THE VERTICAL AND HORIZONTAL

To prepare meteorological observations as initial conditions for the proposed AFGL spectral model, sets of orthogonal functions were generated to act as bases in the analysis and initialization of the data. The functions are solutions of the Laplace tidal equations which are linearized versions of the equations governing the behavior of a fluid in a basic state of rest but subject to coriolis forces and linear pressure gradients. The functions used in the meridional and zonal directions are the Hough harmonics which yield Fourier components zonally and Hough functions meridionally. The vertical direction is handled by a set of empirical orthogonal functions (EOF) according to the method of Holmström (1963).

The Hough functions are derived according to the method discussed by Kasahara (1976, 1978)¹¹. Three functions are defined relating to the velocity potential, stream function, and geopotential height, respectively:

$$\begin{aligned} \text{a. } \psi_s &= \sum_{n=0}^{\infty} i A_n^s P_n^s(\mu) \\ \text{b. } \phi_s &= \sum_{n=0}^{\infty} B_n^s P_n^s(\mu) \\ \text{c. } Z_s &= \sum_{n=0}^{\infty} C_n^s P_n^s(\mu) \end{aligned} \quad (1)$$

where $i = \sqrt{-1}$ and P_n^s are the Legendre functions of $\mu = \sin \phi$, where ϕ is latitude, s is the zonal index and n is the meridional index. By using (1) in the basic equations of motion, one can derive expressions for the set of coefficients $\{A_n^s\}$, $\{B_n^s\}$, and $\{C_n^s\}$. These solutions divide into two categories - symmetric and anti-symmetric. The symmetric mode contains only even values of $n - s$ for A_n^s and C_n^s and odd values for B_n^s . The anti-

11. Kasahara, A., 1976: Normal modes of ultralong waves in the atmosphere. Mon. Wea. Rev., 104, 669-690.

_____, 1978: Further studies on a spectral model of the global barotropic primitive equations with Hough harmonic expansions. J. Atmos. Sci., 35, 2043-2051.

symmetric solution has odd values of $n + 1$ for A_n^S and C_n^S and even values for B_n^S . The symmetric solutions imply $\hat{U}_s^0 = \hat{U}_s^0(-a)$, $\hat{V}_s^0 = \hat{V}_s^0(-a)$, and $\hat{Z}_s^0 = \hat{Z}_s^0(-a)$. The antisymmetric solutions require $\hat{U}_a^0 = -\hat{U}_a^0(-a)$, $\hat{V}_a^0 = -\hat{V}_a^0(-a)$, and $\hat{Z}_a^0 = -\hat{Z}_a^0(-a)$. The velocity and stream function are defined as:

$$\begin{aligned} \text{a. } \hat{U}_s^0 &= -\epsilon^{-1/2} (\text{is } \hat{\Phi}_s^0 = D\hat{V}_s^0) = -\epsilon^{1/2} \hat{V}_s^0 \\ \text{b. } \hat{V}_s^0 &= -\epsilon^{-1/2} (\text{is } \hat{\Phi}_s^0 = D\hat{U}_s^0) = -\epsilon^{1/2} \hat{U}_s^0 \end{aligned} \quad (2)$$

where ϵ is a constant and the operator $D = (d - \frac{\partial}{\partial a}) \frac{\partial}{\partial a}$. The stream vector $\hat{V}_s^0 = (\hat{U}_s^0, \hat{V}_s^0, \hat{Z}_s^0)$ can be shown to be orthogonal with respect to the inner product, which is the inner product to the vector space (i.e., the complete set of coefficients A_n^S, B_n^S, C_n^S that are derived from the boundary conditions, by a suitable choice of ϵ and a , the stream vectors can be made orthonormal), giving

$$\int_{-1}^1 \hat{V}_s^0 \cdot \hat{V}_s^0 da = \int_{-1}^1 (\hat{U}_s^0 \hat{U}_s^0 + \hat{V}_s^0 \hat{V}_s^0 + \hat{Z}_s^0 \hat{Z}_s^0) da = \delta_{k,l} \quad (3)$$

where $\delta_{k,l} = 0$ when $k \neq l$ and $\delta_{k,l} = 1$ when $k = l$.

When $\epsilon = 0$, many of the solutions (those corresponding to the rotational or kinetic modes) degenerate to give zero values for the coefficients when the streamvector solutions are sought. Hence, a different approach is undertaken whereby the original equations are rewritten for $\epsilon = 0$ and the non-dimensional period, $\sigma = 0$. Under these conditions $\hat{V} = 0$, while \hat{U} is governed by a geostrophic relationship. The coefficients B_n^0 and C_n^0 are then related by substituting into the reduced equations. The ensuing relationship involves only each B_k^0 with C_{k+1}^0 and C_{k-1}^0 , leaving the other coefficients arbitrary. Their selection is made so as to render the entire set orthonormal. By choosing a specific $B_k^0 = 1$, and all others zero, a set of N vectors can be generated, then orthonormalized to give \hat{U}_0^0 and \hat{Z}_0^0 . The lowest order gives $\hat{U}_0^0 = 0$ for all a , while \hat{Z}_0^0 must become $1/\sqrt{2}$ for all a in order to satisfy orthonormality. Solution for the non-rotational modes (i.e., the gravitational modes) is straightforward. The resulting expressions for \hat{U}_0^0 and \hat{V}_0^0 can be simplified to give

AD-A118 744 SYSTEMS AND APPLIED SCIENCES CORP RIVERDALE MD
TECHNIQUE DEVELOPMENT FOR WEATHER FORECASTING. (U)
NOV 81 A M GERLACH

SYSTEMS AND APPLIED SCIENCES CORP RIVERDALE MD
TECHNIQUE DEVELOPMENT FOR WEATHER FORECASTING.(U)
NOV 81 A M GERLACH F

F/G 4/2

UNCLASSIFIED

AFGL-TR-82-0020

F19628-81-C-0039
NL

2 of 2
AQ 4
11/8/94

END
DATE
FILMED
09-82
DTIC

$$\begin{aligned}\hat{U} &= -\epsilon^{-\frac{1}{2}} \sum_{n=1}^N B_{n,n}^{0,1} \\ \hat{V} &= -\epsilon^{-\frac{1}{2}} \sum_{n=1}^N A_{n,n}^{0,1}\end{aligned}\quad (4)$$

where the first order associated Legendre polynomial is introduced because of the identity $D P_n^0 (1-\mu^2)^{-\frac{1}{2}} = P_n^1$.

The poles present special problems for the computation of \hat{U}_s^ℓ and \hat{V}_s^ℓ because Eq. (2) seems to indicate a singularity when $\mu = \pm 1$. At close inspection, however, Eq. (2) presents no problems when $s > 1$, because the Legendre functions starting with P_n^2 are polynomials at least of order 2 in μ , while the denominator, $(1-\mu^2)^{-\frac{1}{2}}$, is only first order in μ . Since $P_n^s(\pm 1) = 0$ for all $s > 0$, there is no question that $\hat{U}_s^\ell(\pm 1) = \hat{V}_s^\ell(\pm 1) = 0$ for all $s > 1$. When $s = 1$, the formula

$$P_n^2 - 2\mu(1-\mu^2)^{-\frac{1}{2}} P_n^1 + n(n+1) P_n^0 = 0$$

may be used to derive the limit of $P_n^1(1-\mu^2)^{-\frac{1}{2}}$ as $\mu \rightarrow \pm 1$ and hence the values of $\hat{U}_1^\ell(\pm 1)$, $\hat{V}_1^\ell(\pm 1)$, which will not be zero at the poles. For $s = 0$, Eq. (4) indicates that $\hat{U}_0^\ell(\pm 1) = \hat{V}_0^\ell(\pm 1) = P_n^1(\pm 1) = 0$, while Eq. (1) indicates that $\hat{Z}_0^\ell(\pm 1) \neq 0$, because $P_n^0(\pm 1) \neq 0$.

Truncation of the sums for the generation of the Hough functions was always at $s = 39$. The number of modes calculated was 40: 25 rotational modes, 8 westward-travelling gravity modes and 7 eastward-travelling modes. The functions can be calculated for any latitude and stored on disc or tape for use in the analysis of data. To date, the Hough functions have been generated for every 2.5° latitude and for 64 Gaussian latitudes. The latter have been used to test the orthonormality of the Hough vectors, which has been verified to an order of approximately 10^{-9} .

The 2.5° latitude values have also been used in a computer program which was developed to take wind and height values on a 2.5° latitude-longitude grid at any number of pressure surfaces in the vertical and calculate the coefficients $\alpha_{\ell,k}^s$ and $\beta_{\ell,k}^s$ in the expansions

$$\begin{aligned}\tilde{u}(\lambda, \theta, p) &= \sum_{s=0}^{24} \sum_{\ell=1}^{40} \sum_{k=1}^{12} [\alpha_{\ell,k}^s \cos(s\lambda) + \beta_{\ell,k}^s \sin(s\lambda)] \hat{U}_s^\ell(\sin\theta) F_k(p) \\ \tilde{v}(\lambda, \theta, p) &= \sum_{s=0}^{24} \sum_{\ell=1}^{40} \sum_{k=1}^{12} [\alpha_{\ell,k}^s \sin(s\lambda) - \beta_{\ell,k}^s \cos(s\lambda)] \hat{V}_s^\ell(\sin\theta) F_k(p)\end{aligned}\quad (5)$$

$$\tilde{z}(\lambda, \theta, p) = \sum_{s=0}^{24} \sum_{\ell=1}^{40} \sum_{k=1}^{12} [\alpha_{\ell,k}^s \cos(s\lambda) + \beta_{\ell,k}^s \sin(s\lambda)] \hat{z}_s^{\ell}(\sin\theta) F_k(p)$$

in which \tilde{u} , \tilde{v} , and \tilde{z} are the non-dimensionalized wind and height values related to the actual grid point values u , v , h by

$$\tilde{u} = u/C_q, \quad \tilde{v} = v/C_q, \quad \tilde{z} = h/h_0$$

where $C_q = (gh_0)^{1/2}$ and h_0 is the equivalent height. A value of 10 km was used for h_0 . The $F_k(p)$ are the EOF's which will be discussed shortly. Details on how $\alpha_{\ell,k}^s$ and $\beta_{\ell,k}^s$ were obtained are given in Kasahara (1976) and his method was followed exactly except the $s = 0$ case was included, as was the vertical dimension. Once the coefficient values were obtained, they were used in the expansions Eq. (5) to retrieve the values \tilde{u} , \tilde{v} , and \tilde{z} and subsequently u , v , h . This analysis procedure was performed on PGGE Level III (analyzed) data for July 20, 1978 at 00 GMT. The results showed good agreement with the Level III data; however, no examination of the nature of the difference in values between the Level III analysis and our analysis has yet been conducted.

Assimilations with the Hough functions are being tested. Some tests have already been made using known analytic functions of μ . Initial results are disappointing. The fact that Hough functions are orthogonal does not guarantee that they will necessarily define or represent an arbitrary function. Obviously, functions which are not identically zero at the poles will not be accurately portrayed by Hough functions of higher order. In fact, there are probably many classes of functions which cannot be represented by even the associated Legendre functions of higher order. Even for those functions which can be represented, truncation can become a serious matter, especially for higher values of zonal wavenumber s .

The functions used in the tests included polynomials in μ of various order, exponential functions of μ , and sines and cosines of $2\pi\mu$. Some were forced to equal zero at the poles, while some were not. Several were symmetric with respect to the equator, while others were antisymmetric and yet others were asymmetric. When these functions were expanded in associated Legendre functions, the representation grew worse as s increased. Also, results were inevitably worse for odd s than for even s , probably due to the fact that P_n^s is a pure polynomial in μ if s is even but contains a fac-

tor of $(1-\mu^2)^{1/2}$ if s is odd. When expanding in Hough harmonics, similar test functions were employed for $u(\mu)$, $v(\mu)$, and $h(\mu)$ and the resulting expansions compared with the original values. The errors, in general, were at least of the same order as the expansions in associated Legendre polynomials with odd s , and usually even higher. With variables normalized to 1, errors were of the order 10^{-2} - 10^{-1} . Thus expansions in Hough functions could engender severe errors in portraying "true" meteorological fields.

As an example of Hough analyses, Figs. 12a-d and 13a-d show the height fields and their approximation by Hough series for a symmetric and anti-symmetric function, respectively. The symmetric function was chosen to give $h = 3\mu^8 - 4\mu^6 + 2\mu^4 - 5\mu^2 + 4$, $u = -e^{-1/2} (24\mu^7 - 24\mu^5 + 8\mu^3 - 10\mu) r(\mu)$, and $v = 3\mu^5 - 4\mu^3 + \mu$, where

$$r(\mu) = \begin{cases} (1-\mu^2)^{1/2} \mu^{-1}, & |\mu| > 0.3 \\ -(1-\mu^2)^{1/2} / 0.3, & |\mu| \leq 0.3 \end{cases}$$

The representation for u was taken as a geostrophic relationship for extra-tropical regions. Notice that the functions satisfy the requirement that they be zero at the poles. Figs. 12a, b, c, and d are for $s = 0, 3, 5$, and 6, respectively. Agreement is acceptable, with decreasing accuracy for increasing s . Regions most affected are near the poles and the equator. The anti-symmetric functions are given by:

$$h = \sin^3 2\pi\mu + 4 \sin 2\pi\mu, \quad u = -e^{-1/2} \{6\pi \sin^2 2\pi\mu \cos 2\pi\mu + 8\pi \cos 2\pi\mu\} r(\mu), \\ v = \frac{1}{2} \cos 2\pi\mu - \frac{1}{2}.$$

Hough expansions are shown in Figs. 13a, b, c, and d for $s = 0, 3, 5$, and 6, respectively. Here, the errors are larger than for the previous case and the deterioration with increasing s is quite noticeable. In fact, besides an increase in error there is also a phase shift, with the analyzed ridges being displaced to the right and the troughs to the left. The reason for these errors is unclear. It could be a factor of truncation, inaccurate integration, or disassociation of the windfield from the height field. Representation of the same h functions by Legendre functions leads to much closer approximation even for higher s values. This would seem to indict not so much the truncation, which was the same for both the Legendre and Hough functions, but the difficulty in balancing waves of different frequencies with the Hough functions.

The vertical harmonics, based on EOFs, are calculated separately for

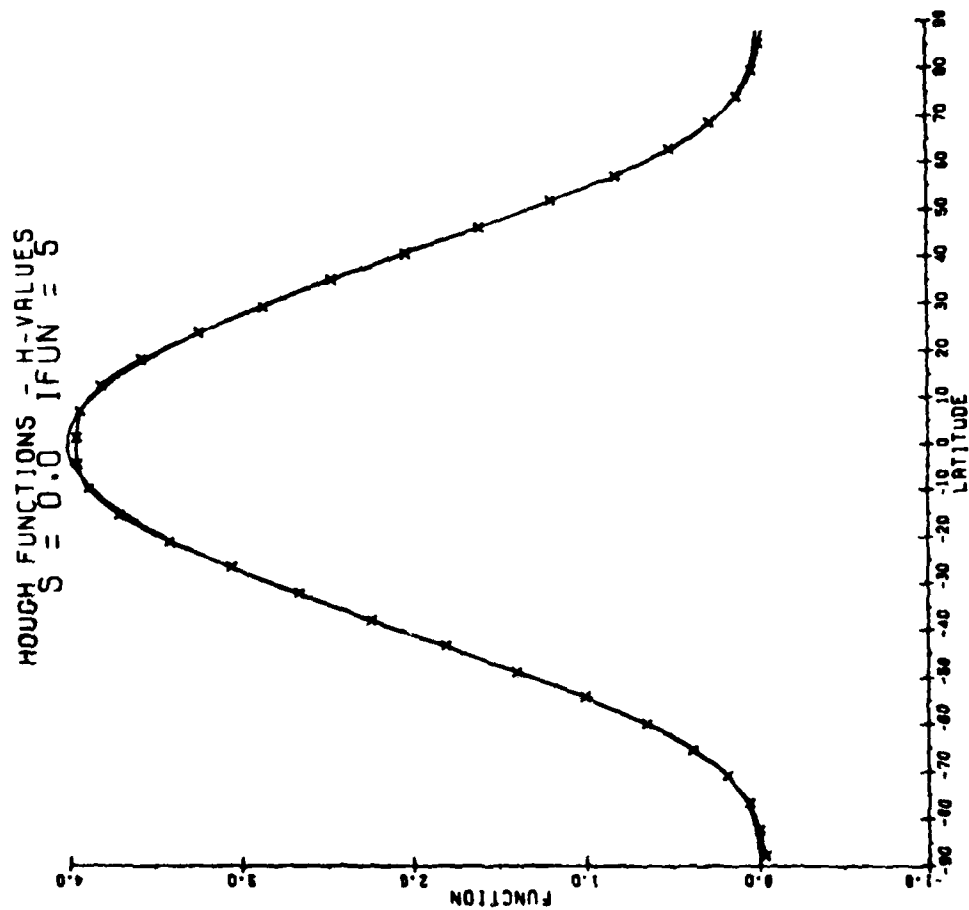


Fig. 12a. Symmetric function versus latitude and Hough analysis of the function for $S = 0$.

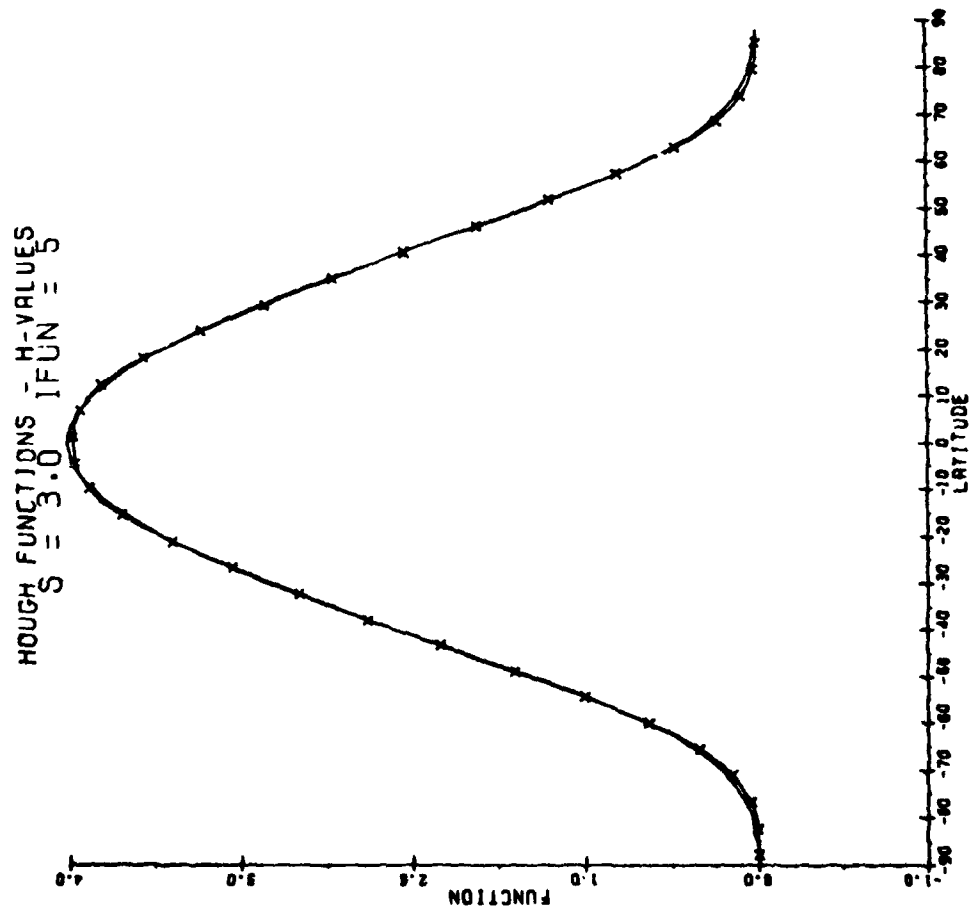


Fig. 12b. Symmetric function versus latitude and Hough analysis of the function for $S = 3$.

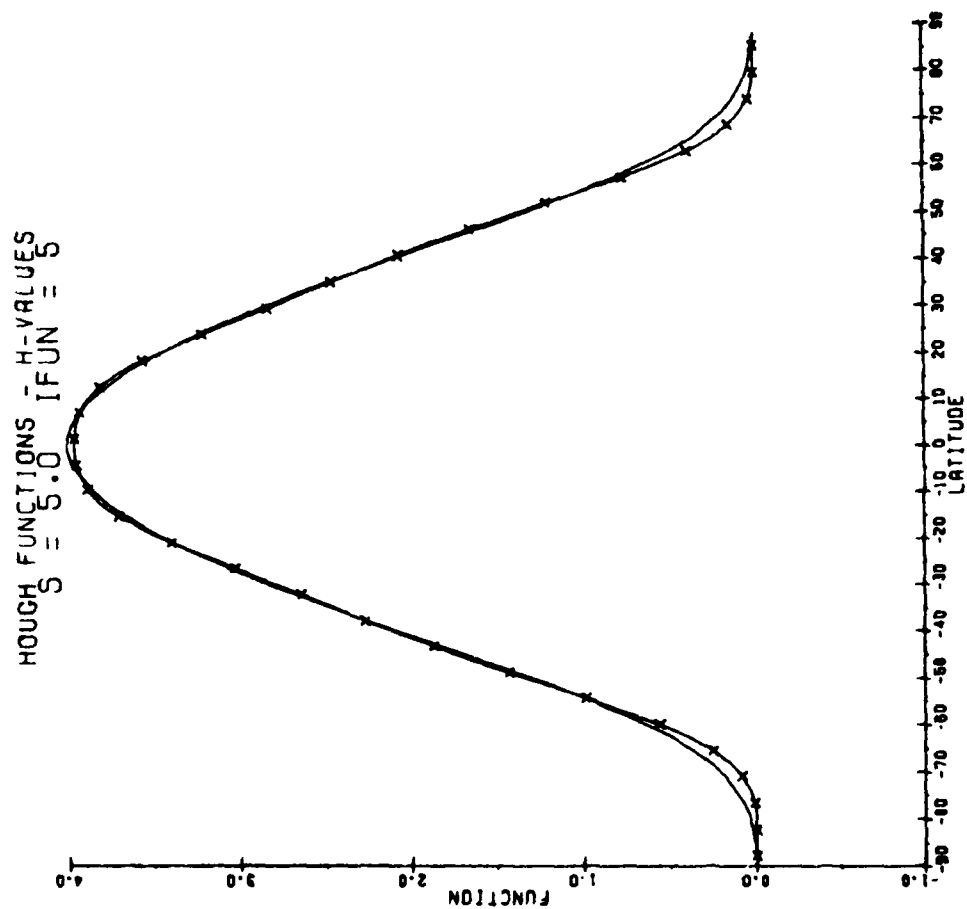


Fig. 12c, Symmetric function versus latitude and Hough analysis of the function for $S = 5$.

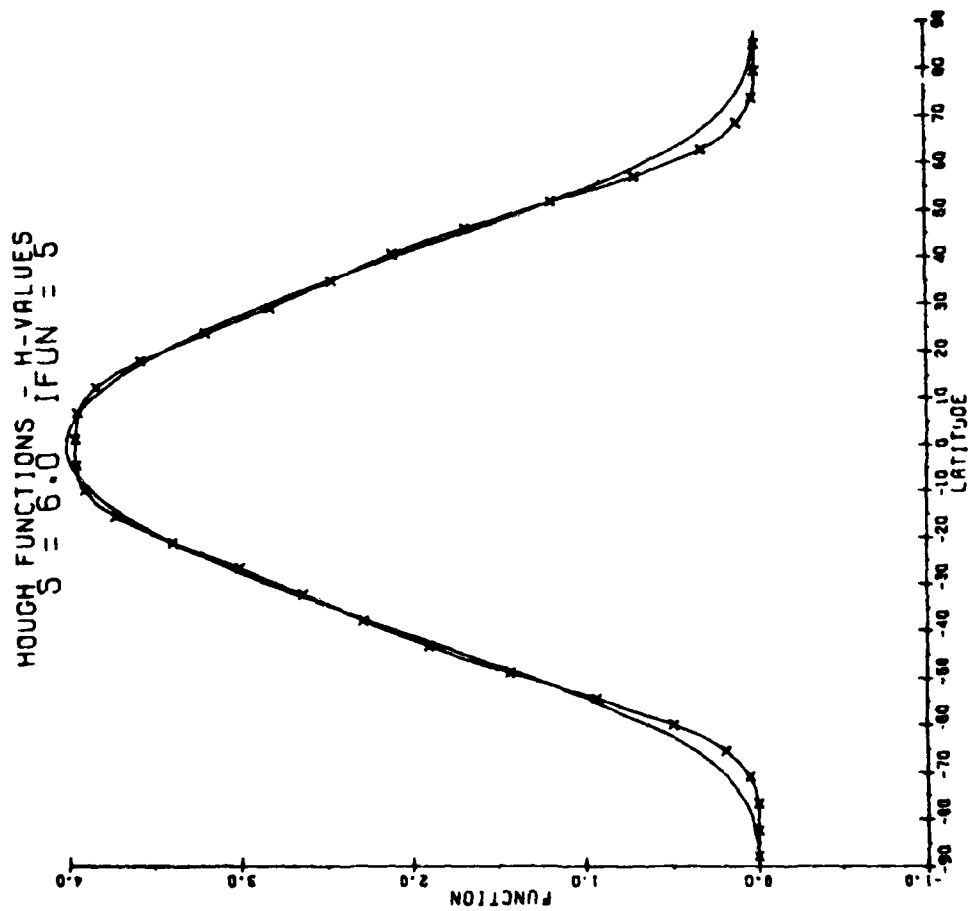


Fig. 12d. Symmetric function versus latitude and Hough analysis of the function for $S = 6$.

HOUGH FUNCTIONS - H-VALUES
 $S = 0.0$ IFUN = 4

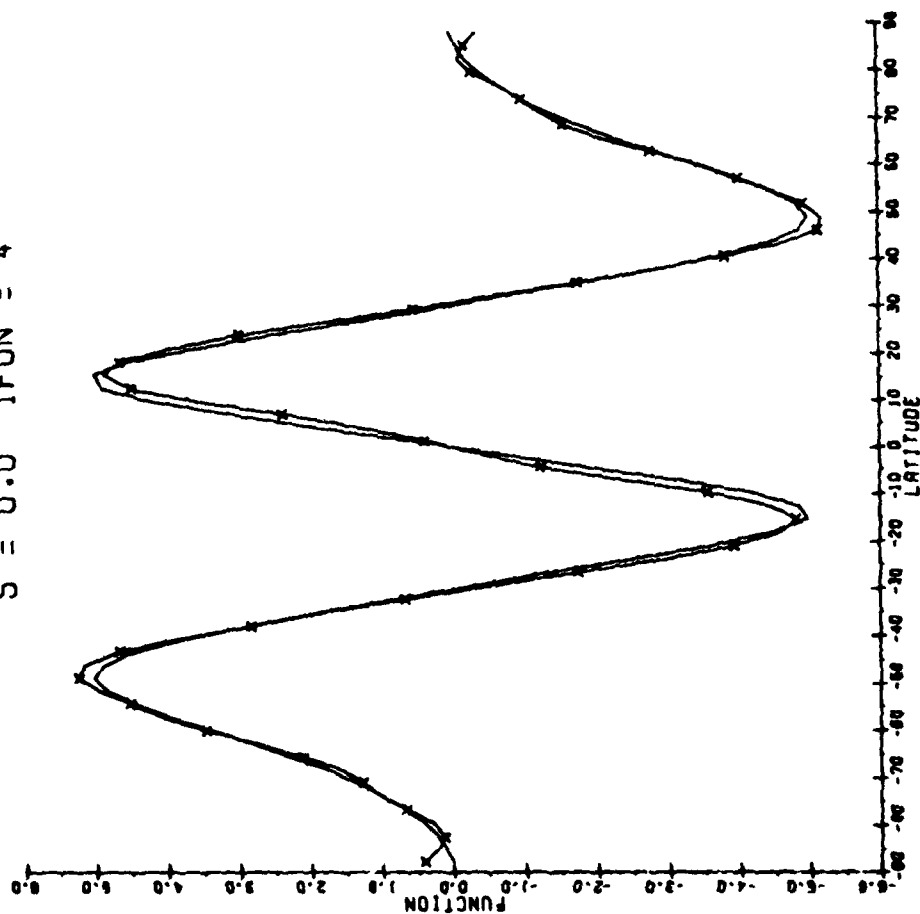


Fig. 13a. Anti-symmetric function versus latitude and Hough analysis of the function for $S = 0$.

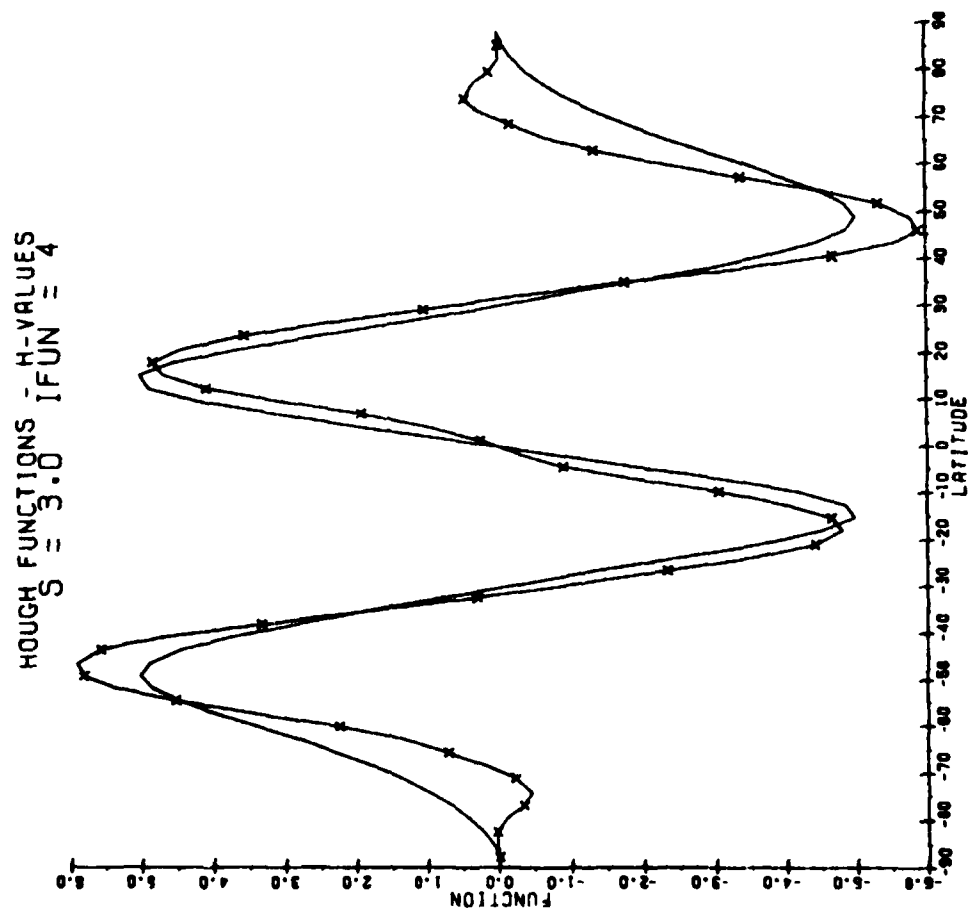


Fig. 13b. Anti-symmetric function versus latitude and Hough analysis of the function for $S = 3$.

HOUGH FUNCTIONS - H-VALUES
 $S = 5.0$ IFUN = 4

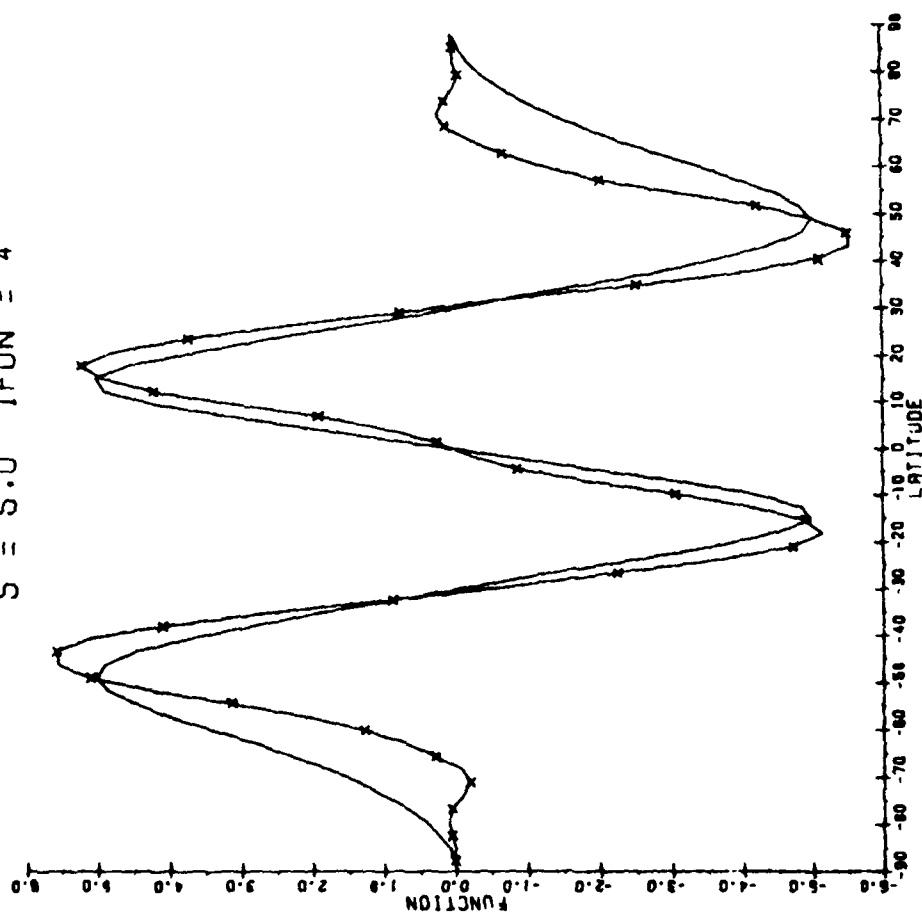


Fig. 13c. Anti-symmetric function versus latitude and Hough analysis of the function for $S = 5$.

HOUGH FUNCTIONS - H-VALUES
 $S = 6.0$ IFUN = 4

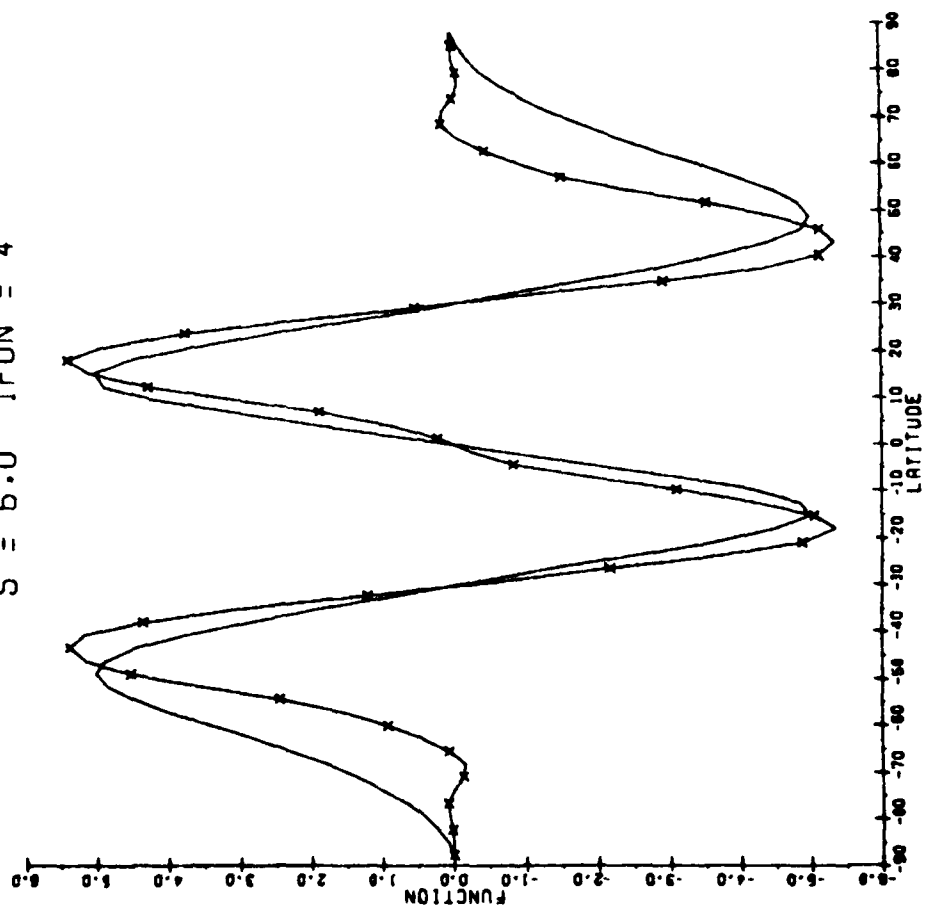


Fig. 13d. Anti-symmetric functions of latitude and Hough analysis of the function for $S = 6$.

each set of data. Given any set of data defining $Z(x, y, p)$, where x and y are the horizontal variables and p is pressure, it is possible to obtain a set of EOFs, $F_n(p)$, using the calculus of variations. The first order EOF, $F_0(p)$, is simply the average over x and y for a particular p . That is,

$$F_0(p) = \frac{1}{S} \int_S Z(x, y, p) dS,$$

where S indicates the surface area over the entire field of x and y . It is now necessary to consider only the departure from the mean, $z(x, y, p) = Z(x, y, p) - F_0(p)$. By expanding z such that

$$z(x, y, p) = \sum_{k=1}^N z_k(x, y) F_k(p) + r(x, y, p),$$

and minimizing the residual r , we arrive at conditions governing z_k and F_k . By requiring that these conditions be applied sequentially, and that F_k be normalized so that $\int_p F_k^2 dp = 1$, we get the following system of equations,

$$\frac{1}{p} \int_p z F_1 dp = z_1, \quad \int_S z z_1 dS = F_1 \int_S z_1^2 dS \quad (6)$$

$$1/p \int_p (z - z_1 F_1) F_2 dp = z_2, \quad \int_S (z - z_1 F_1) z_2 dS = F_2 \int_S z_2^2 dS$$

.

.

.

.

$$1/p \int_p (z - \sum_{k=1}^{n-1} z_k F_k) F_n dp = z_n, \quad \int_S (z - \sum_{k=1}^{n-1} z_k F_k) z_n dS$$

$$= F_n \int_S z_n^2 dS.$$

The sequential nature of the calculation guarantees that the low order values z_k and F_k carry the major portion of the variable $z(x, y, p)$ and higher values of z_k and F_k will eventually become minimal. The Eqs. (6) also guarantee that the sets $\{F_k\}$ and $\{z_k\}$ are orthogonal in the sense that

$$\frac{1}{p} \int_p F_k F_j dp = \delta_k^j \quad \text{and} \quad \int_S z_k z_j dS = 0 \text{ if } k \neq j.$$

The components $\{z_k\}$ and $\{F_k\}$ can be theoretically solved using Eq. (6), since for each pair of unknowns F_k and z_k there are two equations. Practically, the equations can only be solved through iteration once an appropriate quadrature is chosen to represent the integrals. For the surface integral a simple sum of all points is substituted as an approximation to the double integral. This means that distribution plays no role in the computation. Areas which are data void will receive very little weight in this sort of approximation. The vertical integration is approximated using the trapezoidal rule so that

$$\int_p F_n(p) dp \approx \frac{1}{2p} \sum_{j=1}^{J-1} (F_n(p_{j+1}) + F_n(p_j)) (p_{j+1} - p_j).$$

The actual procedure, then, is to first calculate $Z(x, y, p)$ at all mandatory pressure levels by taking all observations of $Z(x, y, p)$, determining $F_0(p_k) = \frac{1}{M} \sum_{j=1}^M Z(x_j, y_j, p_k)$, and subtracting F_0 from Z . An initial guess for $F_1(p)$ is then evaluated. In practice, the expression

$$F_1^{(1)}(p_k) = 1 - \frac{p_k - p_t}{p_B - p_t}$$

was used, where p_B is the pressure at the lowest level and p_t is the pressure at the topmost level. This first guess was chosen only on the basis of varying monotonically with height; no consideration was given to its orthonormality since the subsequent iterations for F_1 are always normalized. The first integral in Eq. (6) is now approximated to give $z_1^{(1)}$,

where the superscript indicates the iteration step. The integral $\int_S \{z_1^{(1)}\}^2 dS$ is approximated by $\sum_{j=1}^M \{z_1^{(1)}(x_j, y_j)\}^2$ and similarly $\int_S z z_1^{(1)} dS \approx \sum_{j=1}^M z(x_j, y_j, p_k) z_1^{(1)}(x_j, y_j)$. The ratio of these will yield $F_1^{(2)}(p_k)$ for each k . $\alpha = \int_p \{F_1^{(2)}\}^2 dp$ is evaluated by the trape-

zoidal rule and each $F_1^{(2)}(p_k)$ divided by $\alpha^{1/2}$ in order to achieve the required normalization. The new $F_1^{(2)}(p_k)$ are now re-inserted into the first

integral and the process repeated. Convergence is usually very swift depending, of course, on the convergence criterion.

The drawback with this method is that the vertical modes must be recalculated for each data set. Also, there is little theoretical support for the calculation of EOFs, but alternate methods such as the numerical methods recommended by Kasahara (1981)¹² may not be worth the effort. One possible alternative may be the calculation of vertical EOFs which are functions of the mandatory levels only and need not be updated at each analysis time. Such a method was attempted by Dixon et al. (1972)¹³ for all three dimensions with limited success¹⁴.

The status of the current analysis method may thus be classified as encouraging but subject to cautious evaluation. The Hough analysis does not represent an arbitrary field of variables with great accuracy. But Hough functions are not chosen as bases because of their accuracy. Their primary use is in damping the growth of unwanted gravity waves. The question is whether the loss of accuracy in the initial conditions will depreciate the forecast more than the gravity noise. Also, a problem arises when interpolating data onto a fixed grid system in order to prepare an analysis. But this is a problem related to data distribution and is com-

12. Kasahara, A. and K. Puri, 1981: Spectral representation of three-dimensional global data by expansion in normal mode functions. Mon. Wea. Rev., 109, 37-51.
13. Dixon, E., A. Spackman, J. Jones, and A. Francis, 1972: The global analysis of meteorological data using orthogonal polynomial base functions. J. Atmos. Sci., 29, 609-622.
14. A comparison of EOF generation using fixed levels with a sequential derivation of coefficients of a given function, similar to Holmström's method, is presented in a report by Halberstam ("An Investigation of Three Methods for Spectral Representation of Randomly Distributed Data," Scientific Report No. 1, 1981, issued under this contract). Results show that although EOF generally produce more accurate approximations than sequential derivation, they are very sensitive to spatial distribution of data points. In fact, results from EOF were identical to those produced from a straightforward matrix inversion where the known quantities were given at the observation levels. A matrix of this form is known to be ill-conditioned because of its dependency on spatial distribution, and when the matrix solution fails, the EOF method will fail also.

mon to all analysis schemes. The vertical analysis has been used operationally for some time but still has shortcomings. Despite its quick convergence, the scheme requires updating at each analysis time. This could become a costly procedure. It also fails to weigh data from data-poor areas more heavily than data from data-rich areas. Some of these problems can be overcome by adopting certain features from other analysis schemes such as optimal interpolation. Future research will be geared to investigating techniques used by other analysis procedures to overcome some of the current problems.

SECTION 2.

MESOSCALE FORECASTING

A. MESOSCALE FORECAST EXPERIMENT

I. Introduction

The need for developing interactive aids for formulating short-range forecasts led to SASC participation in the AFGL Mesoscale Forecast Experiment (MFE). Development of a menu-driven Mesoscale Forecast Facility (MFF)¹ and the forecast experiment conducted with it² constituted Phase I of the MFE. This section reports on the follow-on program which continued research into the kinds of data, displays, and capabilities to be supplied to interactive facilities (MFE Phase II). More rigorous forecasting sessions lasting an entire working day were conducted and only two predictands, wind and cloud amounts, were forecast. Participation was limited to six forecasters. Results of the experiment were expected to lead to development of techniques and software to enhance interactive forecast facilities.

II. Software Modifications

Software changes were required to modify the MFF (Phase I) program prior to the start of Phase II forecasting activities. The data file used to store forecast and skill score information, FCSFIL, had to be restructured to accommodate changes in the numbers of forecasters, forecast periods, and predictands. Most of the MFF menu was eliminated in compliance with the Phase I conclusion that displays of conventional and satellite data could be generated more easily using regular McIDAS commands. The chief forecaster position was eliminated, leading to deletion of another branch of the menu. Predictand selection and review was also eliminated in the Phase II format. All that remained of the MFF menu were the forecast entry and interrogation modules, both of which required rewriting because of changes in the file structure of FCSFIL. Modifications were also made to the output formats of past forecast and skill score reviews.

1. Gerlach, A. M., (ed), 1980a: Computer-based weather research, AFGL-TR-80-0069, pp. 49-73.
2. Gerlach, A. M., (ed), 1980b: Development of automated objective meteorological techniques. AFGL-TR-81-0017, pp. 48-51.

Fig. 1 shows examples of the format used in listing forecasts. The primary changes involved computation of vector errors for wind forecasts and the inclusion of the variable forecast length N. Examples of skill score reviews for the first two forecast lengths are presented in Fig. 2. Changes for Phase II included elimination of three types of skill scores which had proved uninformative during Phase I and addition of two new scores. Percent correct, AWS (Air Weather Service) skill score, and bias were replaced by RMS (root mean square) error and the Heidke score. P-score, cumulative P-score, and mean absolute error were retained from Phase I.

III. Forecast Procedure

During April - May, 1981, six significant weather situations, ranging from an advancing cloud deck to developing sea breezes, were designated forecast days. Two shifts (morning, afternoon), of three forecasters each, were responsible for monitoring and preparing hourly forecasts for each situation. At their disposal were the entire McIDAS now-casting capability, half-hourly one-mile resolution GOES imagery, the full McIDAS display and enhancement capability, 0Z and 12Z LFM Model Output Statistics (MOS) forecasts, and 0Z and 12Z LFM products. One-, two-, and four-hour forecasts of total cloud amount and wind speed and direction were formulated and entered for Boston and a second station in the northeast U.S. chosen according to prevailing conditions. A forecast was also prepared and entered for a period chosen so as to verify on the nearest MOS forecast valid time. Forecasters were responsible for their individual forecasts but group discussions were encouraged during the analysis period. The 0Z and 12Z MOS forecasts and forecasts based on morning and afternoon climatology for Boston were entered as controls. An automated procedure was used the next day to verify the forecasts and calculate skill scores.

Each forecaster selected a specific facet of the interactive forecast facility for concentrated study throughout the experiment. Satellite imagery utilization, new data sources, improved analyses and displays, and forecast aids were the technical areas chosen, based on individual expertise and system capabilities. Advantages and disadvantages of the current facility were examined, and potential improvements were considered.

PREDICTAND: WIND

FORECAST OBSERVED
VALUE VALUE/ERROR

		INITIAL VALUE	MOS 1107	JFK 910				
		1 HOUR FORECAST (VALID 21000)						
		PROBABLE ERROR:	(0.0-3.5)	(3.6-6.5)	(6.6-10.5)	(>10.5)		
1208	704/ 6.2	MOS FORECAST :	50	40	10	0		
		PROBABLE ERROR:	(0.0-3.5)	(3.6-6.5)	(6.6-10.5)	(>10.5)		
811	1004/ 4.4	JFK FORECAST :	50	35	15	0		
		2 HOUR FORECAST (VALID 21000)						
		PROBABLE ERROR:	(0.0-3.5)	(3.6-6.5)	(6.6-10.5)	(>10.5)		
1210	1206/ 4.0	MOS FORECAST :	45	35	10	10		
		PROBABLE ERROR:	(0.0-3.5)	(3.6-6.5)	(6.6-10.5)	(>10.5)		
812	1008/ 5.3	JFK FORECAST :	40	35	15	10		
		4 HOUR FORECAST (VALID 22100)						
		PROBABLE ERROR:	(0.0-3.5)	(3.6-6.5)	(6.6-10.5)	(>10.5)		
1408	1702/ 4.5	MOS FORECAST :	35	40	15	10		
		PROBABLE ERROR:	(0.0-3.5)	(3.6-6.5)	(6.6-10.5)	(>10.5)		
1210	1007/ 4.2	JFK FORECAST :	40	30	15	15		
		4 HOUR FORECAST (VALID 30000)						
		PROBABLE ERROR:	(0.0-3.5)	(2.6-6.5)	(6.6-10.5)	(>10.5)		
1808	1739/ 1.8	MOS FORECAST :	30	35	20	15		
		PROBABLE ERROR:	(0.0-3.5)	(3.6-6.5)	(6.6-10.5)	(>10.5)		
1509	1004/ 9.8	JFK FORECAST :	30	35	25	10		

PREDICTAND: TOTAL CLOUD AMOUNT

FORECAST OBSERVED
CATEGORY CATEGORY

		INITIAL CATEGORY	MOS	4	JFK	4		
		1 HOUR FORECAST (VALID 21000)						
		CATEGORIES	1	CLEAR	SCATTERED	BROKEN	OVERCAST	
4	4	MOS FORECAST	1	0	0	0	100	
		CATEGORIES	1	CLEAR	SCATTERED	BROKEN	OVERCAST	
4	4	JFK FORECAST	1	0	0	0	100	
		2 HOUR FORECAST (VALID 21000)						
		CATEGORIES	1	CLEAR	SCATTERED	BROKEN	OVERCAST	
4	4	MOS FORECAST	1	0	0	0	100	
		CATEGORIES	1	CLEAR	SCATTERED	BROKEN	OVERCAST	
4	4	JFK FORECAST	1	0	0	0	100	
		4 HOUR FORECAST (VALID 22100)						
		CATEGORIES	1	CLEAR	SCATTERED	BROKEN	OVERCAST	
4	4	MOS FORECAST	1	0	0	0	100	
		CATEGORIES	1	CLEAR	SCATTERED	BROKEN	OVERCAST	
4	4	JFK FORECAST	1	0	0	0	100	
		4 HOUR FORECAST (VALID 30000)						
		CATEGORIES	1	CLEAR	SCATTERED	BROKEN	OVERCAST	
4	2	MOS FORECAST	1	0	0	10	90	
		CATEGORIES	1	CLEAR	SCATTERED	BROKEN	OVERCAST	
4	4	JFK FORECAST	1	0	0	20	80	

Fig. 1. Past Forecast Review.

PREDICTAND

1 HOUR FORECAST

2 HOUR FORECAST

WIND

NUMBER OF FORECASTS:	41
PRIMARY	20
SECONDARY	21
MEAN ABS. ERROR:	5.38
PRIMARY	4.77
SECONDARY	6.00
RMS ERROR:	6.20
PRIMARY	5.37
SECONDARY	6.93
P-SCORE:	.78
PRIMARY	.73
SECONDARY	.84
CUMULATIVE P-SCORE:	.19
PRIMARY	.18
SECONDARY	.21
HEIDKE SCORE:	-.10
PRIMARY	-.01
SECONDARY	-.18

NUMBER OF FORECASTS:	41
PRIMARY	20
SECONDARY	21
MEAN ABS. ERROR:	7.77
PRIMARY	5.41
SECONDARY	10.13
RMS ERROR:	9.13
PRIMARY	5.87
SECONDARY	11.51
P-SCORE:	.88
PRIMARY	.73
SECONDARY	1.03
CUMULATIVE P-SCORE:	.25
PRIMARY	.15
SECONDARY	.35
HEIDKE SCORE:	-.38
PRIMARY	-.06
SECONDARY	-.71

CLOUD AMOUNT

NUMBER OF FORECASTS:	41
PRIMARY	20
SECONDARY	21
MEAN ABS. ERROR:	.19
PRIMARY	.10
SECONDARY	.29
RMS ERROR:	.49
PRIMARY	.32
SECONDARY	.62
P-SCORE:	.22
PRIMARY	.13
SECONDARY	.31
CUMULATIVE P-SCORE:	.04
PRIMARY	.02
SECONDARY	.06
HEIDKE SCORE:	.47
PRIMARY	.35
SECONDARY	.58

NUMBER OF FORECASTS:	41
PRIMARY	20
SECONDARY	21
MEAN ABS. ERROR:	.24
PRIMARY	.15
SECONDARY	.33
RMS ERROR:	.49
PRIMARY	.39
SECONDARY	.58
P-SCORE:	.30
PRIMARY	.21
SECONDARY	.40
CUMULATIVE P-SCORE:	.05
PRIMARY	.03
SECONDARY	.07
HEIDKE SCORE:	.27
PRIMARY	.00
SECONDARY	.55

Fig. 2. Skill Score Review.

IV. Resulting Improvements

a. Satellite Imagery Utilization

One area of interest was the application of real-time geostationary satellite imagery to mesoscale forecasting of cloud cover and winds. Loops of high resolution images were found to be invaluable in predicting the motion of cloud systems and in timing the arrival of breaks and cloud bands at the forecast site. Cumulus growth on several occasions signaled the development of a sea breeze front in coastal regions where surface reports were not available. However, two problems with the satellite display capability became immediately evident.

The more serious difficulty was inadequate navigation, or earth location, of images. Without highly accurate navigation it was impossible, for example, to judge precisely the distance between the forecast station and an advancing cloud edge. Inadequate navigation also resulted in apparent motion of land beneath the clouds. Problems were encountered in attempting to separate actual cloud motion from false motions induced by navigation error, particularly in cases where no land features were visible in the images.

To improve navigational accuracy, copies of navigation software (both library and load modules) were obtained from the Space Science and Engineering Center, University of Wisconsin, developers of the McIDAS system. These programs were modified to make them compatible with the AFGL McIDAS and entered into the system. The new navigation technique is fully automated, requiring a single key-in and a maximum of 25 seconds of execution time. This replaces a process which required approximately four hours. Imagery loops of clearly identifiable land features remain motionless even at full resolution, indicating the marked improvement in navigational accuracy.

The second problem noted in using satellite imagery was the occasional degradation in picture contrast. Programs for enhancing the imagery to produce greater black and white contrast were available, but tended to be time-consuming and awkward to use. A new enhancement program was written which scans the image, determines the maximum and minimum brightness values present, and applies a contrast stretch that optimizes use of the full gray scale of the video system. The dramatic difference made by the optimum enhancement program is illustrated in Figs. 3

and 4. Fig. 3 shows an unenhanced infrared image. Fig. 4 shows the same image after enhancement. Contrast between different cloud types is sharpened as well as the cloud/land and land/ocean interfaces. The enhanced image even reveals variation in the sea surface temperature in the vicinity of the Gulf Stream. The speed and simplicity of the program make it a very useful aid to the forecaster in sharpening details of cloud features.

b. Increased McIDAS Data Base

(1) FOUS Bulletins

Another area of interest during MFE Phase II was evaluation of the current McIDAS non-satellite meteorological data display. One goal of this evaluation was to develop a series of routines which archive and display new types of meteorological data. Initially, only surface and upper air (RAOB) reports were available to forecasters using McIDAS for plotting and analysis purposes. Software was therefore developed to access and display new non-satellite data types available through land base telephone lines.

To provide the mesoscale forecast group with reliable station-specific forecast guidance, software routines were written which decode, store and display the LFM-II derived United States Forecast (FOUS) bulletins. These bulletins are available via the McIDAS conventional data port (weather band line 604).

Three series of FOUS bulletins are available for display:

FOUS12	Model Output Statistics (MOS)
FOUS50-57	Trajectory Model Output
FOUS60-78	Initial LFM Guidance Output.

Forecasts contained in the FOUS12 bulletin are highly dependent on output from the LFM-II model. All forecasts are produced by using the MOS technique which determines a statistical relationship between the predictand and variables from the numerical model at some prediction time. Forecasts being saved include probability of precipitation, categorical probability of quantitative precipitation, thunderstorm probability, conditional probability of precipitation type, probability of heavy snow, maximum/minimum temperature, 3-hourly surface temperature and dew point, surface wind speed and direction, categorical probability of cloud amount, categorical probability of ceiling height and visibility, and categorical



Fig. 4. Unenhanced IR image.



Fig. 4. Enhanced IR image.

probability of non-precipitating obstructions to visibility.

The bulletins designated as FOUS50-57 contain 24-hour forecasts of temperature, dewpoint, and George's K-index for each station. They also contain the positions (latitude, longitude, pressure level), at 6 hour intervals, for air parcels that will be located at a station (surface, 850 mb, and 700 mb) at the end of the 24-hour forecast period. These positions, which define three air parcel trajectories, are computed from smoothed wind forecasts generated by the LFM model. Knowledge of air parcel movement along with the subsequent evolution of the temperature and moisture fields provides necessary clues to the development of convective activity and precipitation.

The FOUS60-78 bulletins contain the numerical model analysis and forecasts for stations in the U. S. and adjacent waters. Forecasts are provided in 6-hourly intervals from 6-48 hours after the model run time (either 0 or 12 GMT). The forecasts are relative humidity, vertical velocity at 700 mb level, lifted index, 1000-500 mb thickness, direction and speed of the boundary layer wind, mean potential boundary layer temperature, sea level pressure, and the 6-hourly accumulated precipitation. Figs. 5 through 7 illustrate station distribution for each bulletin.

The FOUS decoder package was designed to be as transparent to the McIDAS user as possible. Much of the software is activated through internal branching from the McIDAS data line handler (SVCARX) to the main FOUS decoder program SVCFOS. A detailed flow chart of the decoder package is given in Fig. 8.

The primary function of SVCFOS is to identify the test received from SVCARX by type (either FOUS12, 50-57, or 60-78) and transfer processing to the appropriate subroutine. Each of these subroutines contains code specific to the format of its intended bulletin. It is designed to sense text length as well as forecast time(s) and file storage locations.

Because of the variety in formats among these bulletins, information decoded from the test is stored in one of three disk data files. Data files contain station 3-letter identifiers, latitudes, and longitudes, plus a file directory and blocked storage for up to four days of forecasts. The files continually update themselves, discarding the oldest information to provide space for new forecasts as they are decoded.

The display program FOSLIS allows users access to information



Fig. 5. FOUS12 Station Distribution.

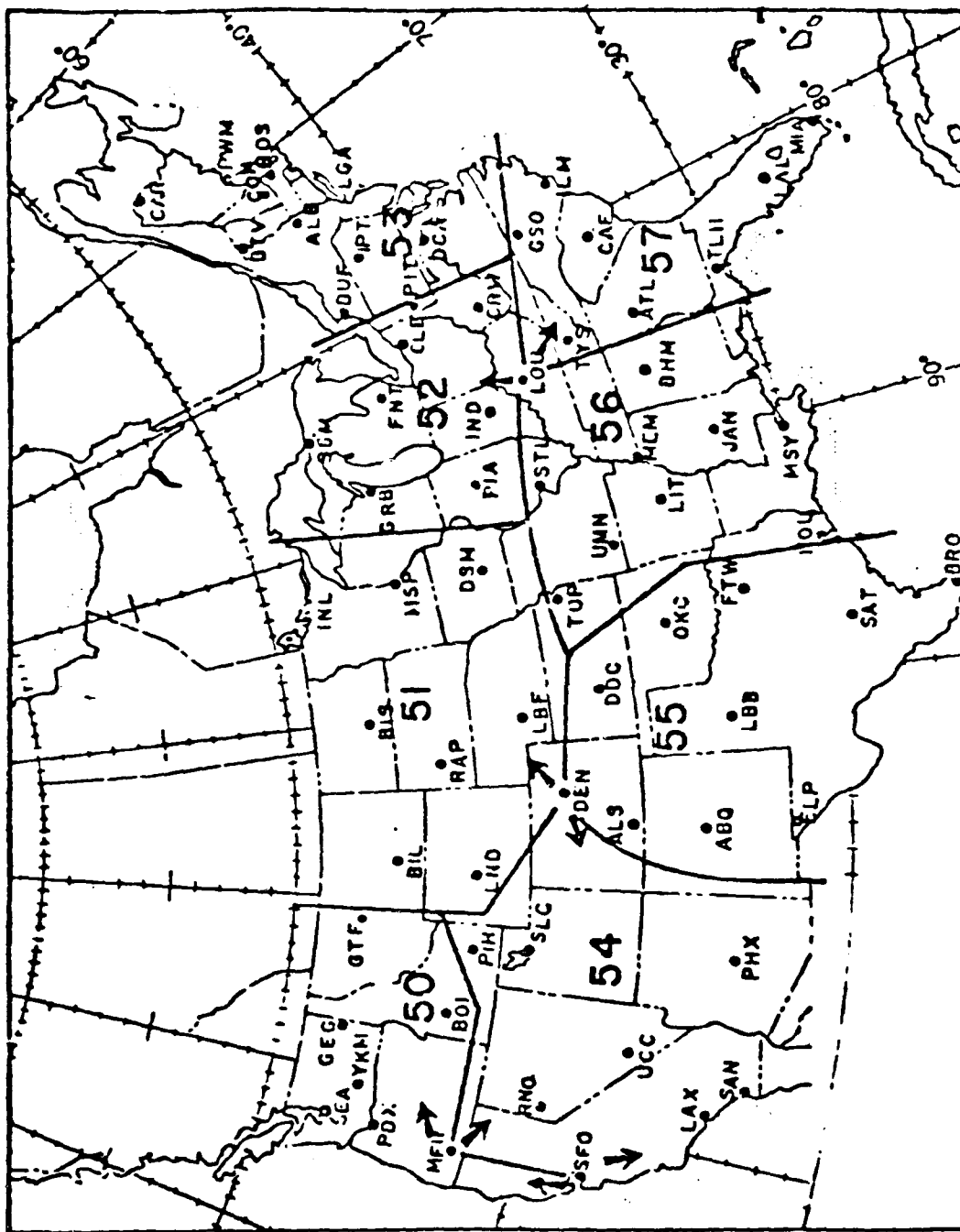


Fig. 6. FOCUS 50-57 Station Distribution.

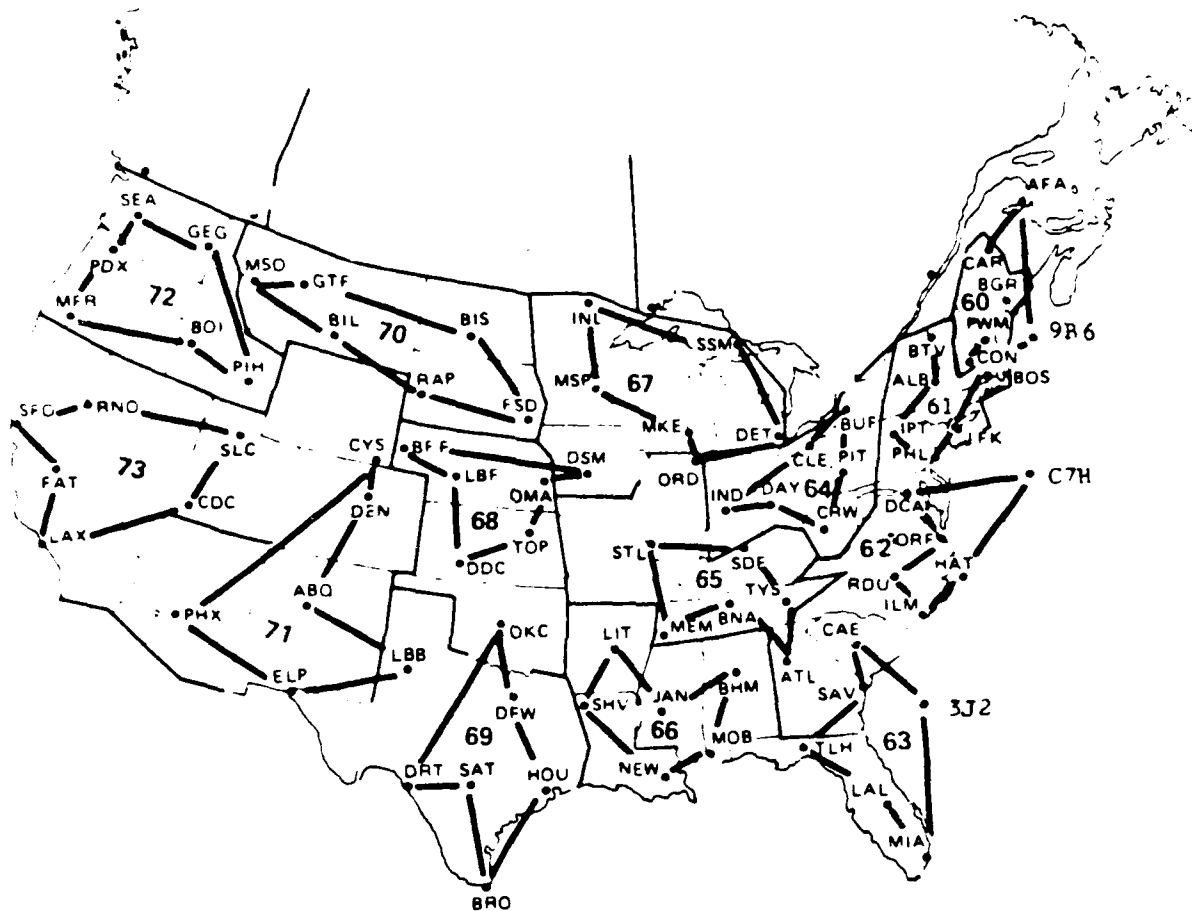


Fig. 7. FOUS60-78 Station Distribution.

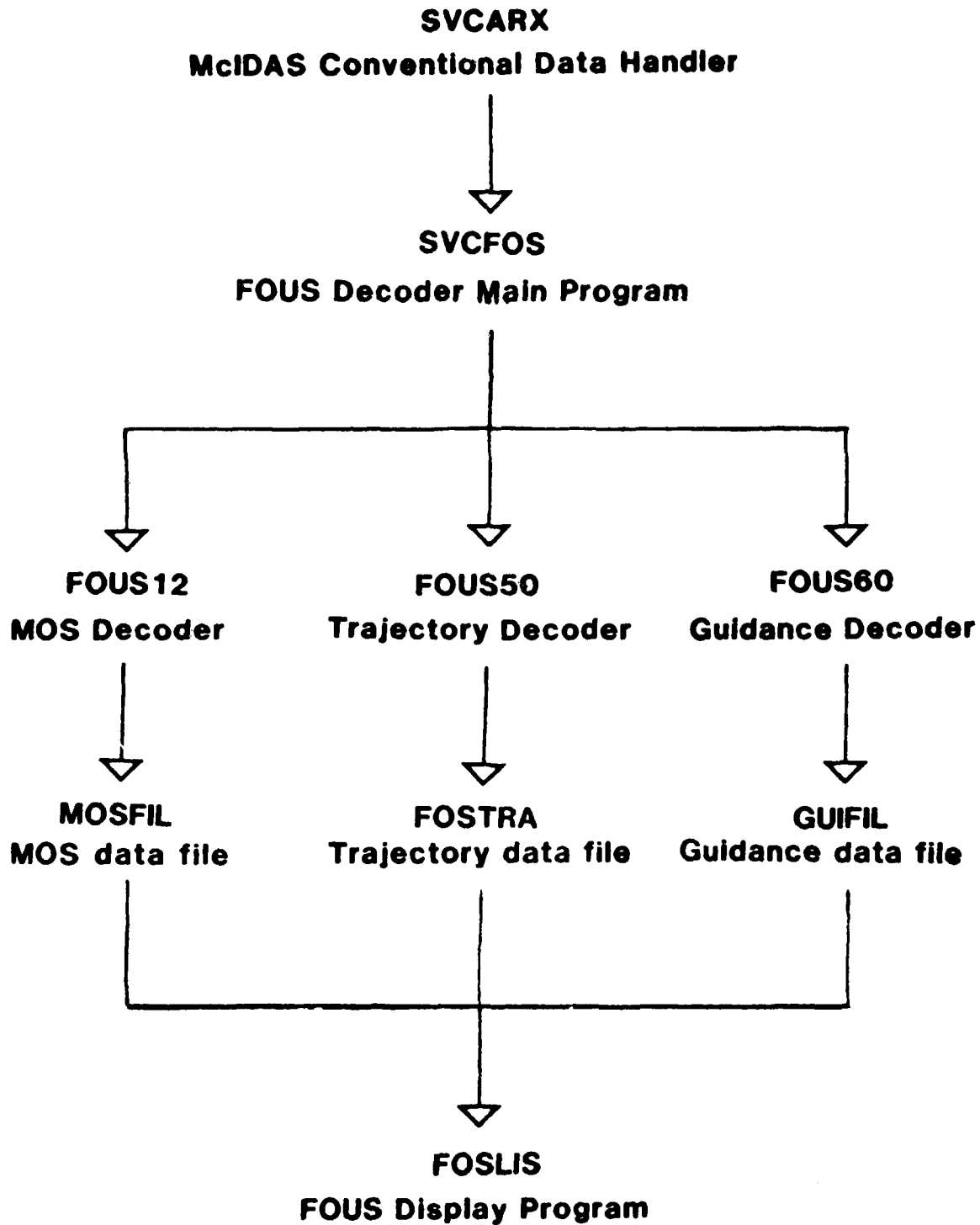


Fig. 8. FOUS Decoder Flow Chart.

stored in any of the FOUS data files. Listings of forecasts for any data period in the files are presented in the NWS format on the CRT. FCSLIS also displays file directory information such as forecast times in the file and the number of stations available for each forecast time. Examples of bulletin display formats are given in Figs. 9 and 10.

(2) Manually Digitized Radar (MDR) Data

SASC meteorologists modified and implemented a McIDAS program set partially developed by the University of Wisconsin, which decodes, stores, and displays Manually Digitized Radar (MDR) code. The code, which is issued hourly by NWS radar sites, is available to McIDAS via the FAA high speed data link (WB-604).

The radar code is made up of two major sections: an SD section which gives radar data in an azimuth-range format and the digital section which contains echo locations and intensities in digitized form. It is the digital section of the radar code which is processed by McIDAS.

The digital section is based upon a grid system. Maximum observed Digital Video Integrator and Processor (DVIP) levels are reported for each grid box containing echoes of moderate or greater intensity. DVIP levels and their corresponding intensities are listed in Table 1.

Data entered in the digital section are encoded in one or more groups. Each group starts with the two-letter identifier of the grid box in the row containing the most westerly echo. The first number following the box identifier is the DVIP level in that box. Subsequent numbers are intensities in the sequentially adjacent boxes in that row. This process is repeated until there are no more rows containing echoes to be encoded. The digital section is limited to a 125 nm range. Any echo outside this limit will not be encoded.

Fig. 11 illustrates echoes on a radar scope over which the 125 nm sweep and the station grid system have been laid. The complete radar code report for this situation is listed below it. The start of the digital section is marked by the upward turned arrow. Fig. 12 illustrates the encoded DVIP levels as they would appear in their grid box positions.

The grid used with the digital code is a subgrid of the LFM-11 model grid. It has 1/4 the mesh length of the LFM model (boxes are approximately 22 nm on a side and have an area of 484 sq nm). Grid boxes

A. For the 0000 GMT forecast cycle:

HDNG	FOUS12	MOS	FCSTS	LFM	GUIDANCE	10/15/80	0000 GMT		
DATE/GMT	15/06	15/12	15/18	16/00	16/06	16/12	16/18	17/00	
ABE	POP06	10	10	10	5	5	10	10	
	POP12			20		10		20	
	QPF06	000/1	000/1	000/1	000/1	000/1	000/1		
	QPF12			0000/1		0000/1		1000/1	
	TSTM			1		3		2	
	POPT	0000/3	0000/3	0000/3	0000/3	0100/3	0000/3	0000/3	
	POSH			99 99/0					
	MX/MN			59		46		65	
	TEMP	48 46	46 52	57 58	54 51	49 49	49 57	63 63	59 56
	DEWPT	35 36	37 39	41 42	43 46	46 46	46 50	52 53	52 53
	WIND	0000	1001	2005	1402	0000	0000	2406	1501
	CLDS	1117/4	1126/4	1225/3	4213/1	3224/3	2225/4	2223/3	3223/3
	CIG	000163	000135	001235	000118	010117	110125	000127	000028
	VIS	000009	000117	001117	000019	000009	101116	001117	000118
	C/V	5/6	5/6	5/6	6/6	6/6	5/6	6/6	6/6
	OBVIS	9000/1	8002/1	9101/1	9001/1	8002/1	6004/4	8101/1	9002/1

B. For the 1200 GMT forecast cycle:

HDNG	FOUS12	MOS	FCSTS	LFM	GUIDANCE	10/15/80	1200 GMT		
DATE/GMT	15/18	16/00	16/06	16/12	16/18	17/00	17/06	17/12	
ABE	POP06	20	5	20	5	5	0	10	
	POP12			20		10		10	
	QPF06	000/1	000/1	000/1	000/1	000/1			
	QPF12			0000/1		0000/1		0000/1	
	TSTM			2		2		4	
	POPT	0000/3	0000/3	0000/3	0000/3	0000/3	0000/3	0100/3	
	POSH			99 99/0					
	MX/MN			46		64		48	
	TEMP	52 54	52 50	49 48	49 56	52 63	59 56	53 52	52 61
	DEWPT	42 43	44 45	45 45	46 48	49 50	50 51	50 49	50 54
	WIND	0904	1202	0000	0000	2505	0000	0000	0000
	CLDS	0136/4	0117/4	2016/4	4113/1	4322/1	4322/2	5113/1	3222/2
	CIG	000154	011234	011224	011126	000117	000118	000117	010017
	VIS	000009	001108	001118	001115	000019	000009	001117	101115
	C/V	5/6	5/6	5/6	6/5	6/6	6/6	6/6	6/5
	OBVIS	9001/1	9002/1	7003/1	6003/2	8102/1	8002/1	7003/1	6004/4

Fig. 9. FOUS12 Display Format.

FOUS57 KWBC 030000

TRAJECTORY FCST

		030000Z LATLONPPP	030600Z LATLONPPP	031200Z LATLONPPP	031800Z LATLONPPP	MTP	040000Z TEMP	DEWPT	K
MIA	700	207836702	216837724	229833729	243822717		7.6	-5.3	22
	850	208812857	217820868	228822872	244818863		15.7	9.4	
	SFC	220790980	226795993	231800003	242804007	008	25.7	21.4	
LAL	700	223914766	236902760	249885745	262856725		4.0	1.5	35
	850	227881891	244880895	259871888	270849871		13.9	12.1	
	SFC	230817987	241822999	250823009	266826012	011	26.4	23.1	
TLH	700	314012698	302972703	294930708	294889710		-5.8	-20.8	3
	850	328935897	321918882	313896867	308872855		3.0	1.8	
	SFC	333904984	333899988	328882994	318862000	009	14.0	9.7	

FOUS72 KWBC 191844
 TO CIRCUITS 30 33 34
 OUTPUT FROM 12Z NOV 19 80
 STA RH R1R2R3 VVLI HHDDFF TBPSFTT
 SEA 87 998120 //12 492407 8921///
 06073 987320 -1312 442513 8720000
 12061 976819 -1011 402821 8518001
 18055 965228 00811 372927 8419001
 24064 954678 00519 332729 8316001
 30073 935595 02309 302629 8317001
 36084 927598 01807 262731 8114001
 42092 939192 02708 212629 7914002
 48091 929092 02606 152524 7711004

Fig. 10. FOUS50-57 Display Format (top); FOUS60-78 Display Format (bottom).

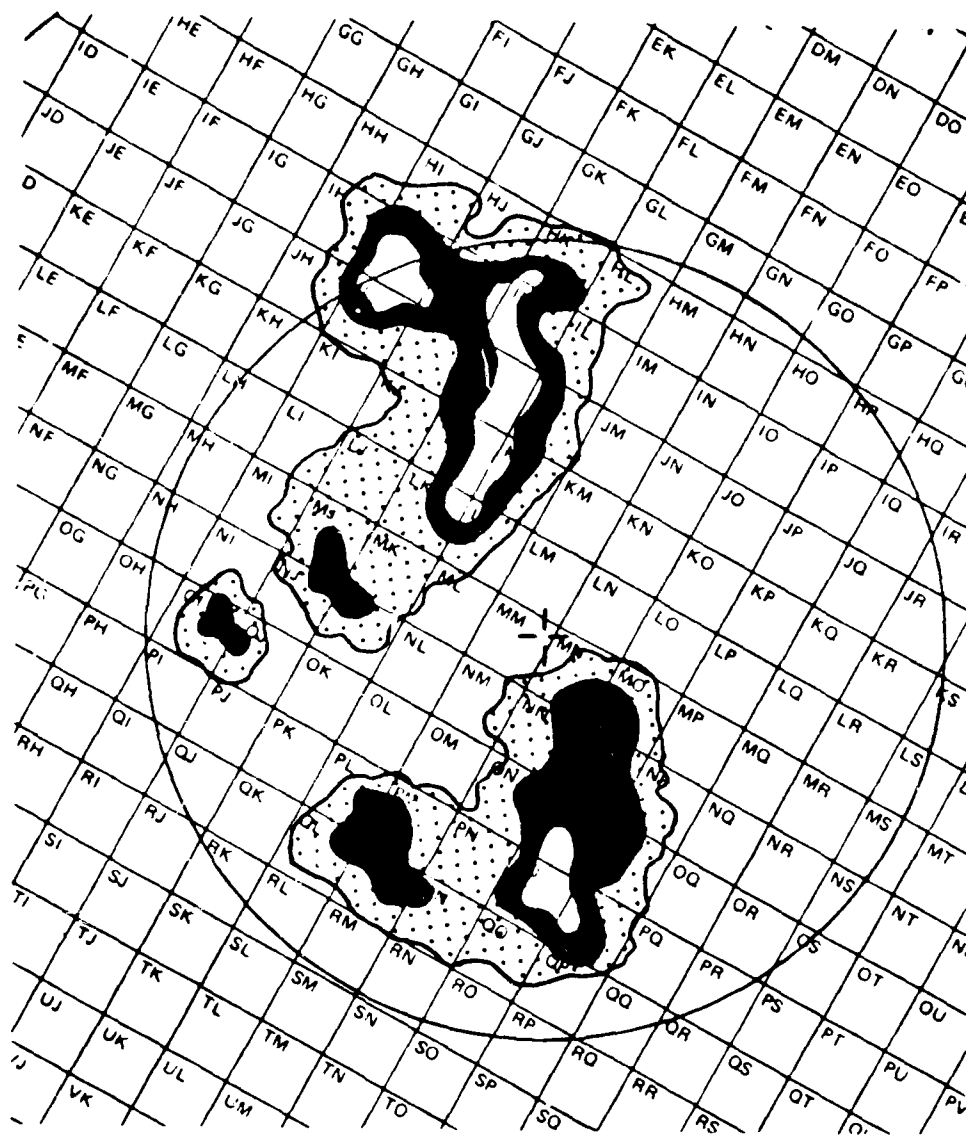
TABLE 1. RAINFALL RATE ECHO INTENSITIES

DVIP Level	Symbol	Echo Intensity	Precipitation Intensity	dBZ [#]	Rainfall Rate (In/Hr) Stratiform*	Convective**
1	-	Weak	Light	< 30	< 0.1	< 0.2
2		Moderate	Moderate	30-41	0.1-0.5	0.2-1.1
3	+	Strong	Heavy	41-46	0.5-1.0	1.1-2.2
4	++	Very Strong	Very Heavy	46-50		2.2-4.5
5	X	Intense	Intense	50-57		4.5-7.1
6	XX	Extreme	Extreme	> 57		> 7.1

*Based on $Z = 200R^{1.6}$. Stratiform rain of DVIP levels 4, 5, and 6 does not occur.

**Based on $Z = 55R^{1.6}$, except that levels 5 and 6 are empirically determined. Hail is likely at these levels.

[#]dBZ = $10 \log_{10} Z_e \text{ mm}^6 \text{ m}^{-3}$, where Z_e is the equivalent radar reflectivity.



ABC 1933 AREA 6TRW+/NC 339/165 15/125 159/130 215/115
 269/115 A2325 MT 370 AT 351/75 TOP 340 AT 179/80
 †HJ231 II3332 JH23333 KJ233 LI1133 MI1220022 NI22201222
 O122000232 PL22133 QL222120

Fig. 11. Example of Radar Display and Radar Code.

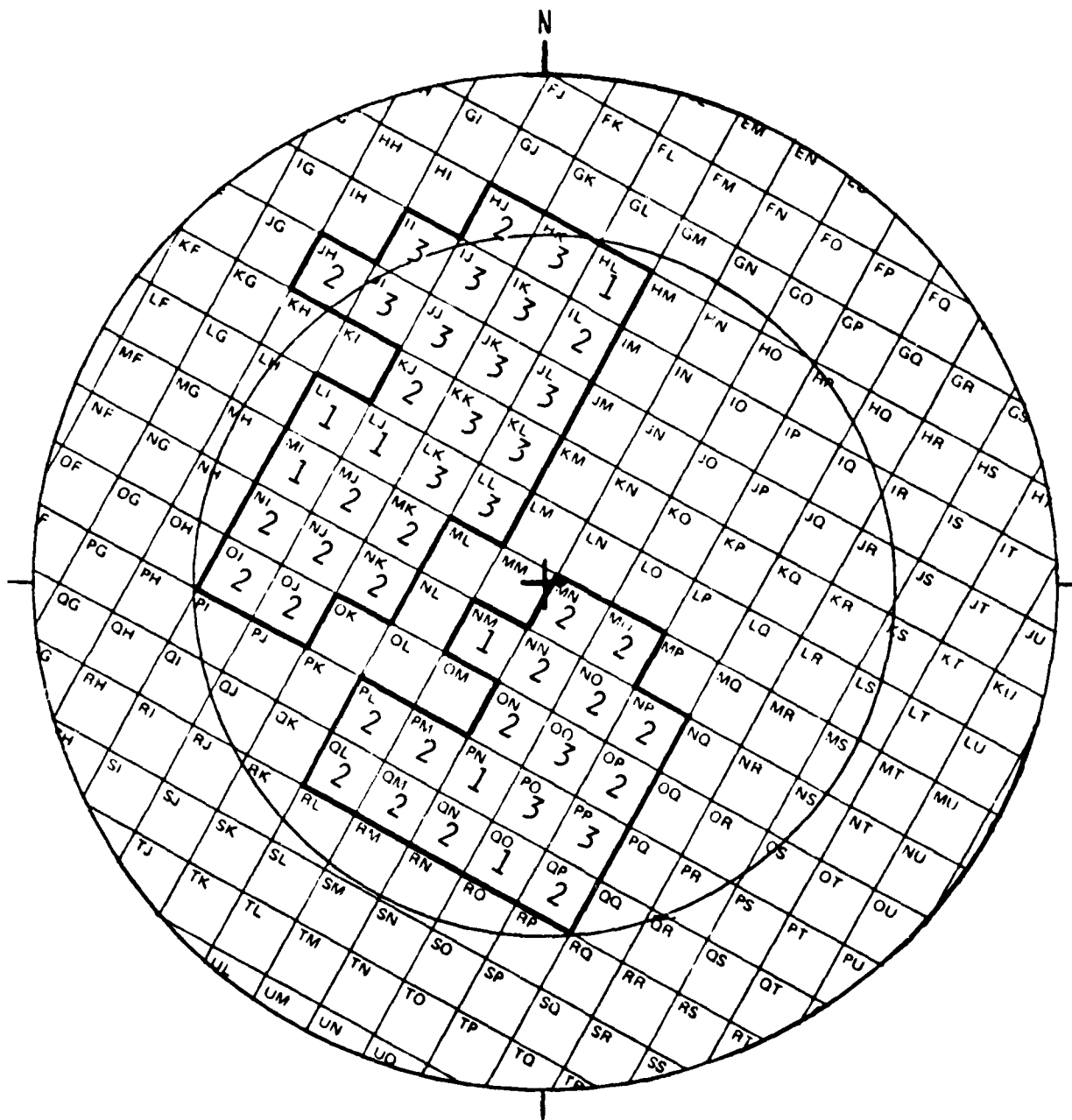


Fig. 12. Grid Box Location for Sample Radar Code.

are located with respect to the radar site such that box MM will always contain the radar antenna.

Fig. 13 shows the digital radar code grid for Worcester, MA (the skew of the grid is due to the curvature of the earth). Table 2 lists the National Weather Service network radars, FAA/ARTC radars, U.S. Air Force radars, and NWS local warning radars from which McIDAS receives digital data.

MDR software is designed to run almost independently of McIDAS users. All the processing routines (decoding and store programs) are initiated by internal cues from one program to the next. Fig. 14 gives a detailed flow chart of the MDR decoder.

Initialization occurs when SVCARX detects an ASCII coded string containing MDR information. The data handler sends all necessary information to the main MDR routine SVCMDR, which searches each radar report for digitized code. If found, the digitized report is stored within the MDR recovery file (MDRFIL). When the end of a MDR text string is sensed, the final processing program MDRMAP retrieves the code stored in MDRFIL, transforms the digitized field to earth latitude and longitude coordinates, and calculates the McIDAS MDR display grid point field, which is then stored in disk grid file GRID00.

The display program MOVMDR allows McIDAS users access to the MDR grid point fields. The operator simply specifies the time and location of the data to be displayed. McIDAS then determines map specifications and projections for the specified location (map specifications include regional, state, city, center point, and satellite overlay options) and generates a contoured MDR field using the MDR grid point data. Figs. 15-17 illustrate the ways data may be displayed using various map specifications.

c. Improvements In Conventional Data Displays

In preparing short-range terminal forecasts, regional plots of weather parameters are valuable aids. Precise tracking of dry lines, wind shifts, and precipitation areas, for example, can keep the forecaster abreast of rapidly changing situations. However, the density of data plotted by McIDAS routines IASVCA and WISPLT was significantly less than the density of stations reporting data. Figs. 18a and 19a show that this reduction was done to prevent overlapping of reports on the map projections

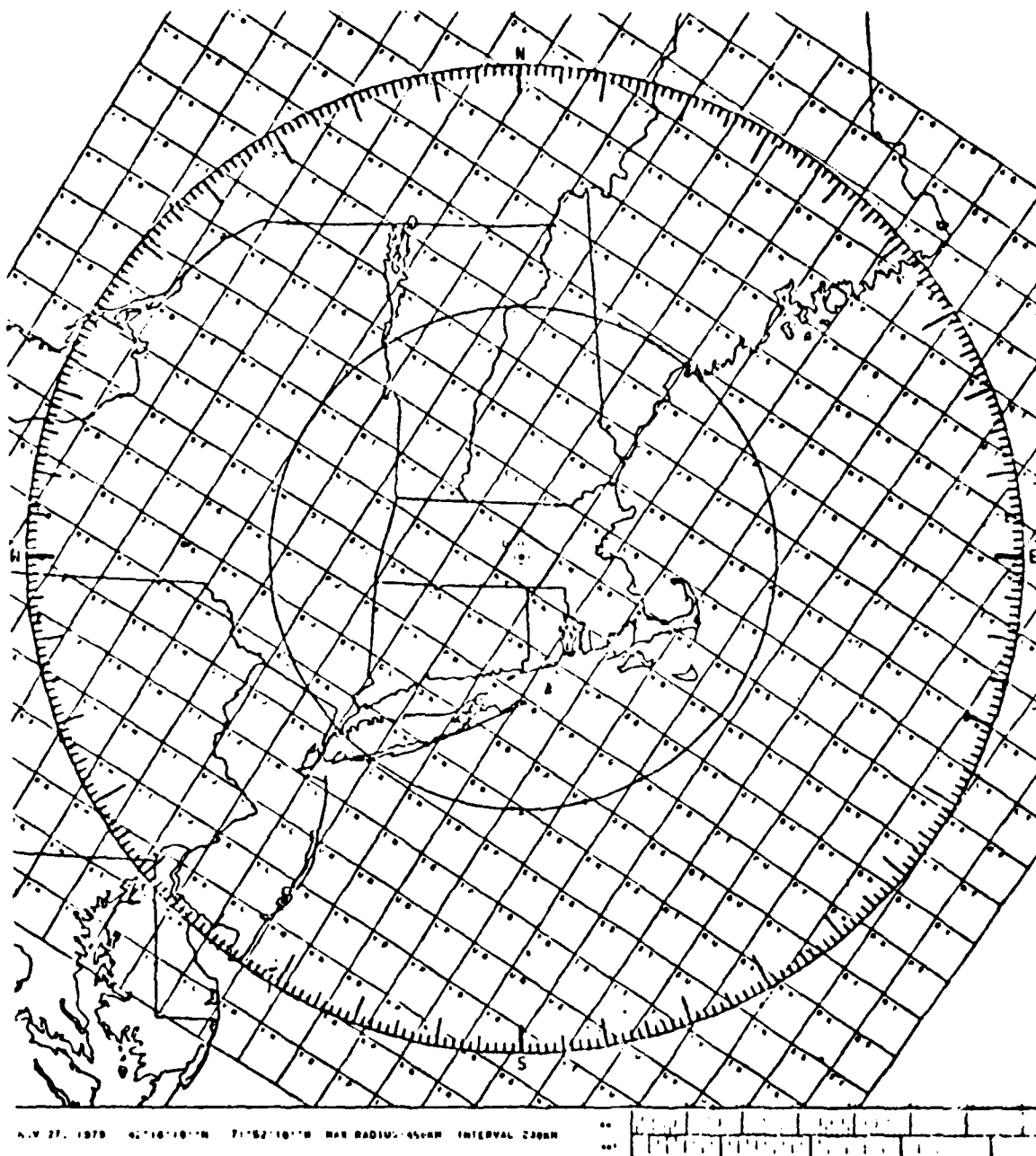


Fig. 13. MDR Grid Box System for Worcester, MA.

TABLE 2. SOURCES OF DIGITAL RADAR DATA FOR MCIDAS.

NATIONAL WEATHER SERVICE NETWORK RADARS

Alliance, Nebraska	Lake Charles, Louisiana
Amarillo, Texas	Limon, Colorado
Apalachicola, Florida	Little Rock, Arkansas
Athens, Georgia	Longview, Texas
Atlantic City, New Jersey	Marseilles, Illinois
Binghamton, New York	Medford, Oregon
Bristol, Tennessee	Memphis, Tennessee
Brownsville, Texas	Miami, Florida
Brunswick, Maine	Midland, Texas
Buffalo, New York	Minneapolis, Minnesota
Cape Hatteras, North Carolina	Missoula, Montana
Centreville, Alabama	Monett, Missouri
Charleston, South Carolina	Nashville, Tennessee
Chatham, Massachusetts	Neenah, Wisconsin
Cincinnati, Ohio	New York City, New York
Daytona Beach, Florida	Oklahoma City, Oklahoma
Des Moines, Iowa	Patuxent River, Maryland
Detroit, Michigan	Pensacola, Florida
Evansville, Indiana	Pittsburgh, Pennsylvania
Fargo, North Dakota	Sacramento, California
Galveston, Texas	Slidell, Louisiana
Garden City, Kansas	Stephenville, Texas
Grand Island, Nebraska	St. Louis, Missouri
Hondo, Texas	Tampa, Florida
Huron, South Dakota	Volens, Virginia
Jackson, Mississippi	Waycross, Georgia
Kansas City, Missouri	Wichita, Kansas
Key West, Florida	Wilmington, North Carolina

FAA/ARTC RADARS

Albuquerque, New Mexico	Mesa Rica, New Mexico
Amarillo, Texas	Mt. Laguna, California
Ashton, Idaho	Paso Robles, California
Battle Mountain, Nevada	Phoenix, Arizona
Boise, Idaho	Rock Springs, Wyoming
Boron, California	Salem, Oregon
Cedar City, Utah	Salt Lake City, Utah
El Paso, Texas	San Pedro, California
Klamath Falls, Oregon	Seattle, Washington
Las Vegas, Nevada	Silver City, New Mexico
Lovell, Wyoming	Spokane, Washington

U.S. AIR FORCE RADARS

Laughlin AFB, Texas	Loring AFB, Maine
---------------------	-------------------

TABLE 2 (cont.)

NATIONAL WEATHER SERVICE LOCAL WARNING RADARS

Abilene, Texas	Los Angeles, California
Akron, Ohio	Louisville, Kentucky
Albany, New York	Lubbock, Texas
Alpena, Michigan	Macon, Georgia
Atlanta, Georgia	Madison, Wisconsin
Augusta, Georgia	Marquette, Michigan
Austin, Texas	Meridian, Mississippi
Baton Rouge, Louisiana	Mobile, Alabama
Beckley, West Virginia	Moline, Illinois
Billings, Montana	Montgomery, Alabama
Bismarck, North Dakota	Muskegon, Michigan
Burlington, Vermont	Norfolk, Nebraska
Charleston, West Virginia	North Platte, Nebraska
Charlotte, North Carolina	Omaha, Nebraska
Cheyenne, Wyoming	Phoenix, Arizona
Cleveland, Ohio	Portland, Oregon
Columbia, Missouri	Raleigh, North Carolina
Columbia, South Carolina	Rapid City, South Dakota
Columbus, Georgia	Rochester, Minnesota
Columbus, Ohio	San Angelo, Texas
Concordia, Kansas	San Juan, Puerto Rico
Corpus Christi, Texas	Shreveport, Louisiana
Duluth, Minnesota	Sioux Falls, South Dakota
Erie, Pennsylvania	Springfield, Illinois
Fort Smith, Arkansas	Topeka, Kansas
Fort Wayne, Indiana	Tulsa, Oklahoma
Goodland, Kansas	Victoria, Texas
Harrisburg, Pennsylvania	Waco, Texas
Hartford, Connecticut	Waterloo, Iowa
Houghton Lake, Michigan	West Palm Beach, Florida
Huntsville, Alabama	Wichita Falls, Texas
Indianapolis, Indiana	Williston, North Dakota
Jackson, Kentucky	Worcester, Massachusetts
Las Vegas, Nevada	

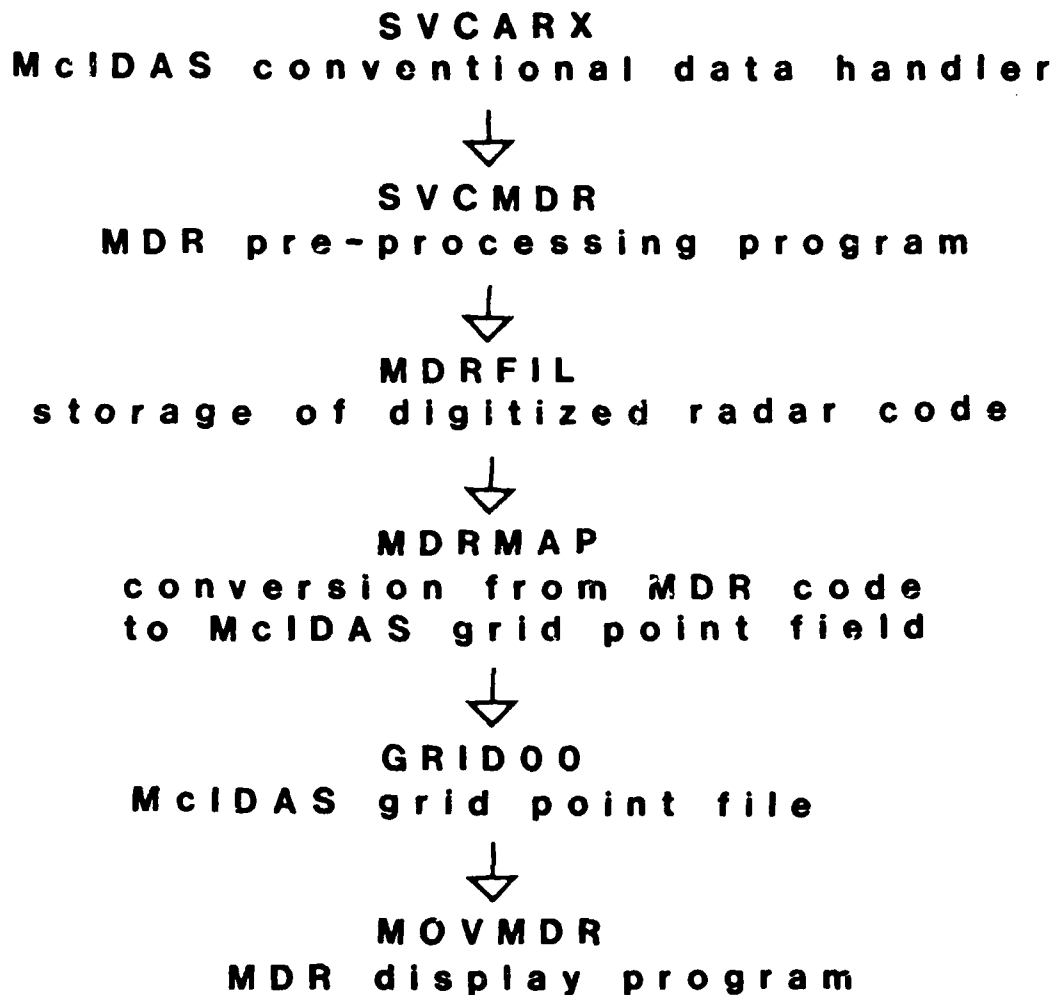
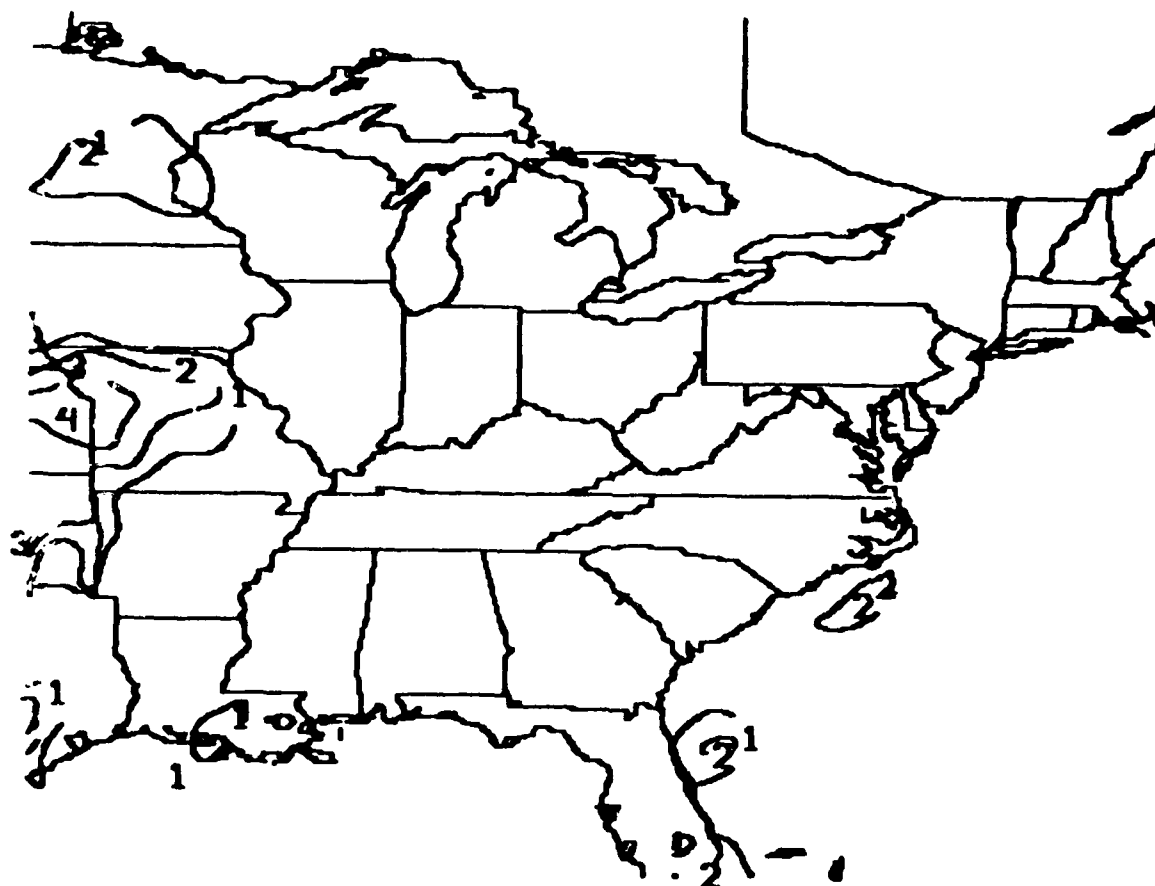
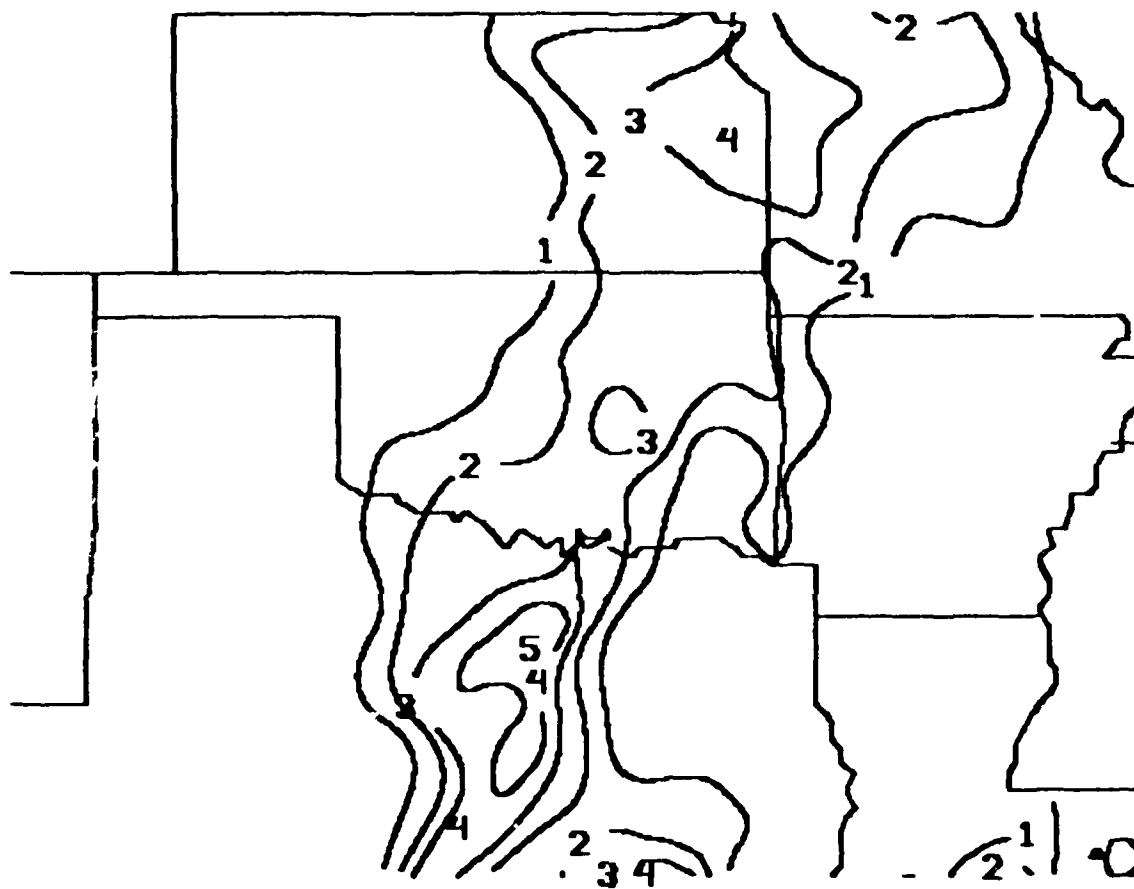


Fig. 14. MDR Decoder Flow Chart.



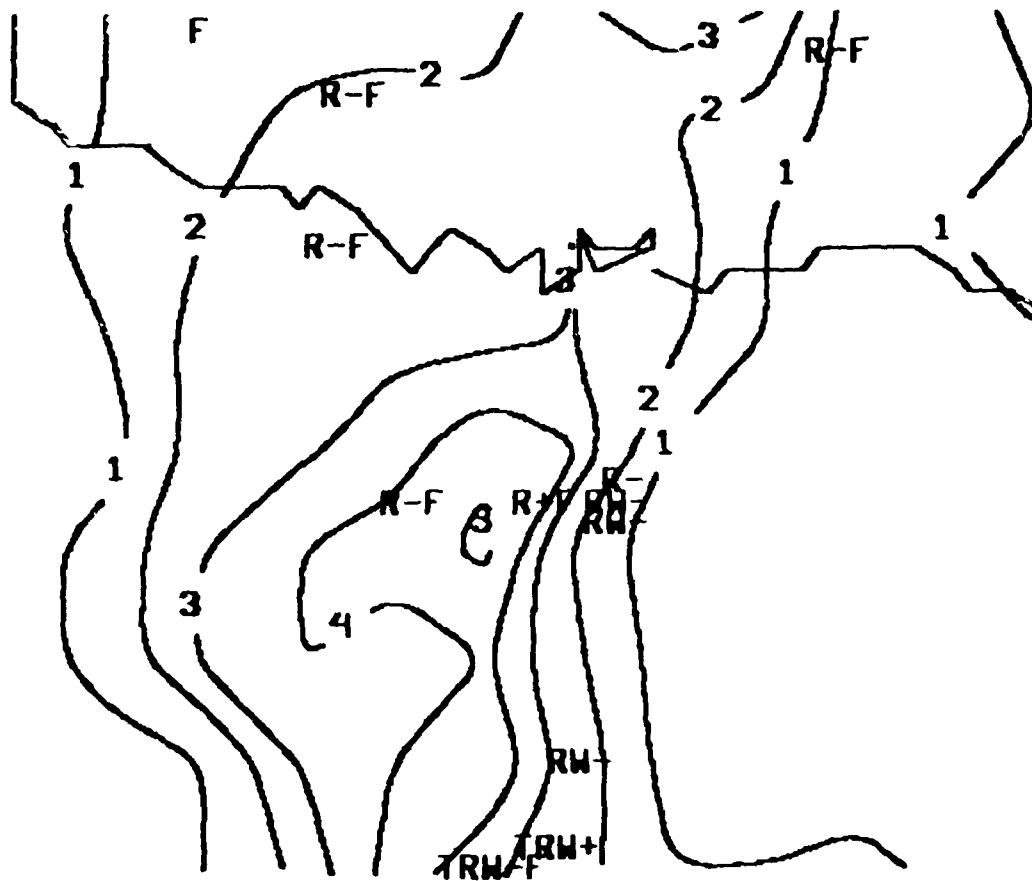
MDR SFC 131700

Fig. 15. MDR Regional Display for Eastern United States.



MDR SFC 131700

Fig. 16. MDR State Display Centered on Oklahoma.



MDR SFC 131700

Fig. 17. MDR City Display Centered on Fort Worth, TX
with Overlaid Weather Symbols.

provided. In order to plot all available data, a smaller map projection was devised, to be centered on any of the 1103 stations in the McIDAS surface data file. Figs. 18b and 19b illustrate the resultant increase in plotted data, approximately threefold, which allows more precise location of discontinuities.

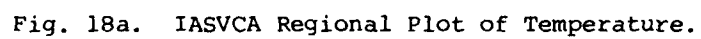
The capability to display four analyses, one in each quadrant of the CRT monitor, was recognized as an important feature of interactive forecast systems. Four-panel analysis of various parameters, such as data from various levels in the atmosphere or data from various time periods, facilitates rapid visual integration of pertinent data. To provide data plotting overlay compatibility as well as four-panel plotting capability, the graphics plotting routines IASVCA and IARAOB were rewritten to include that option (see Fig. 20).

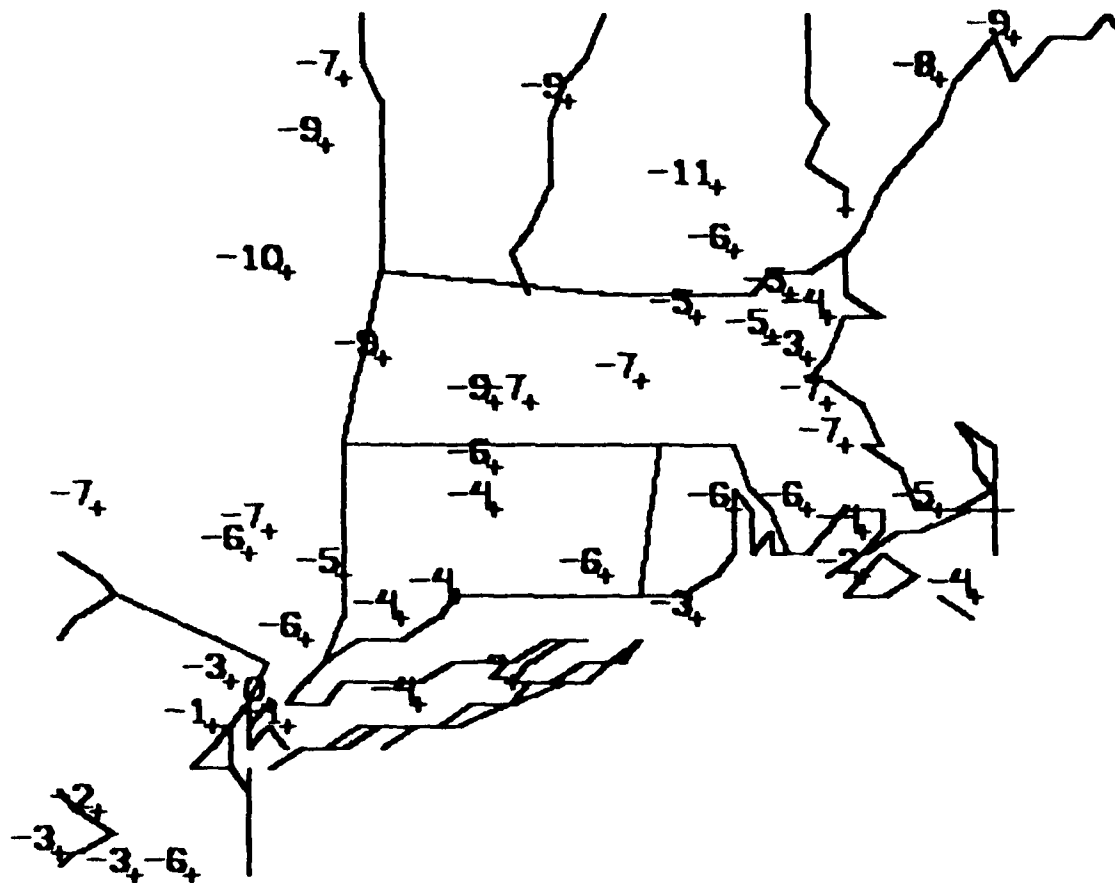
When these plotting capabilities were used operationally it was noted that stations with incomplete reports, i.e., temperature, dew point temperature, or pressure reported as missing, would not be plotted at all. The missing data checks in the plotting routines were revised to permit plotting of reported data in such incomplete reports. The data listing routine SVCADI was also revised to list incomplete station reports which were previously left blank (see Fig. 21).

d. Interactive Forecast Aids

In response to the need for forecast aids noted during the experiment, two menu-driven guidance routines were added to the MFF: a cloud band movement decision tree algorithm developed at Pennsylvania State University³ and an automated version of the severe weather checklist developed by the National Weather Service Forecast Office at Portland, Maine.⁴ Both routines ask a series of yes/no questions designed to guide the forecaster through an analysis of the current weather situation. The cloud band decision tree helps isolate the key factor governing the motion of the cloud band, i.e., confluence zones or vorticity patterns.

3. Cahir, J., J. Norman and D. Lowry, 1981: Use of a real-time computer graphics system in analysis and forecasting. Monthly Weather Review, 109, 486-488.
4. Gulezian, D., 1980: Severe weather checklist used at National Weather Service Forecast Office, Portland, Maine. Bulletin of the American Meteorological Society, 61, 1592-1599.





11200

Fig. 18b. IASVCA Detailed Regional Plot of Temperature.

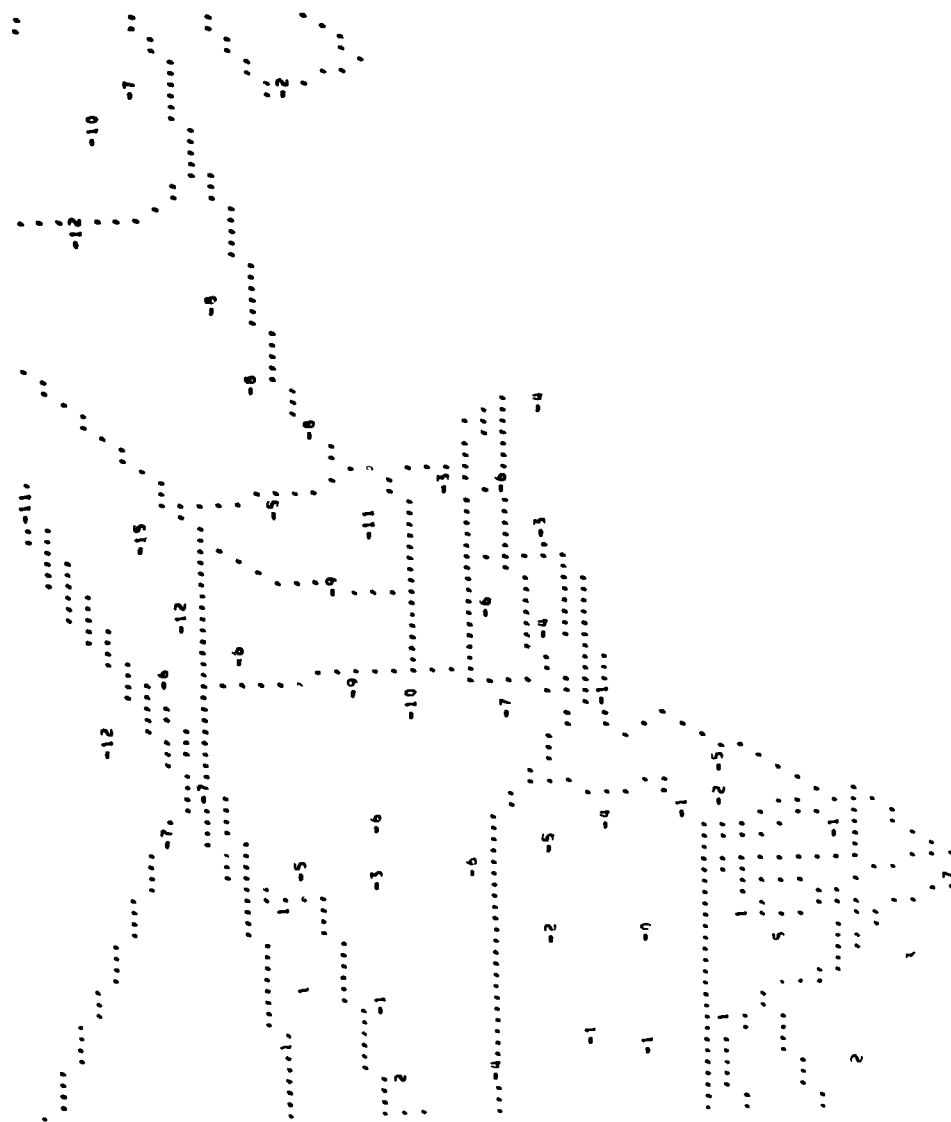


Fig. 19a. WISPLT Regional Plot of Temperature.

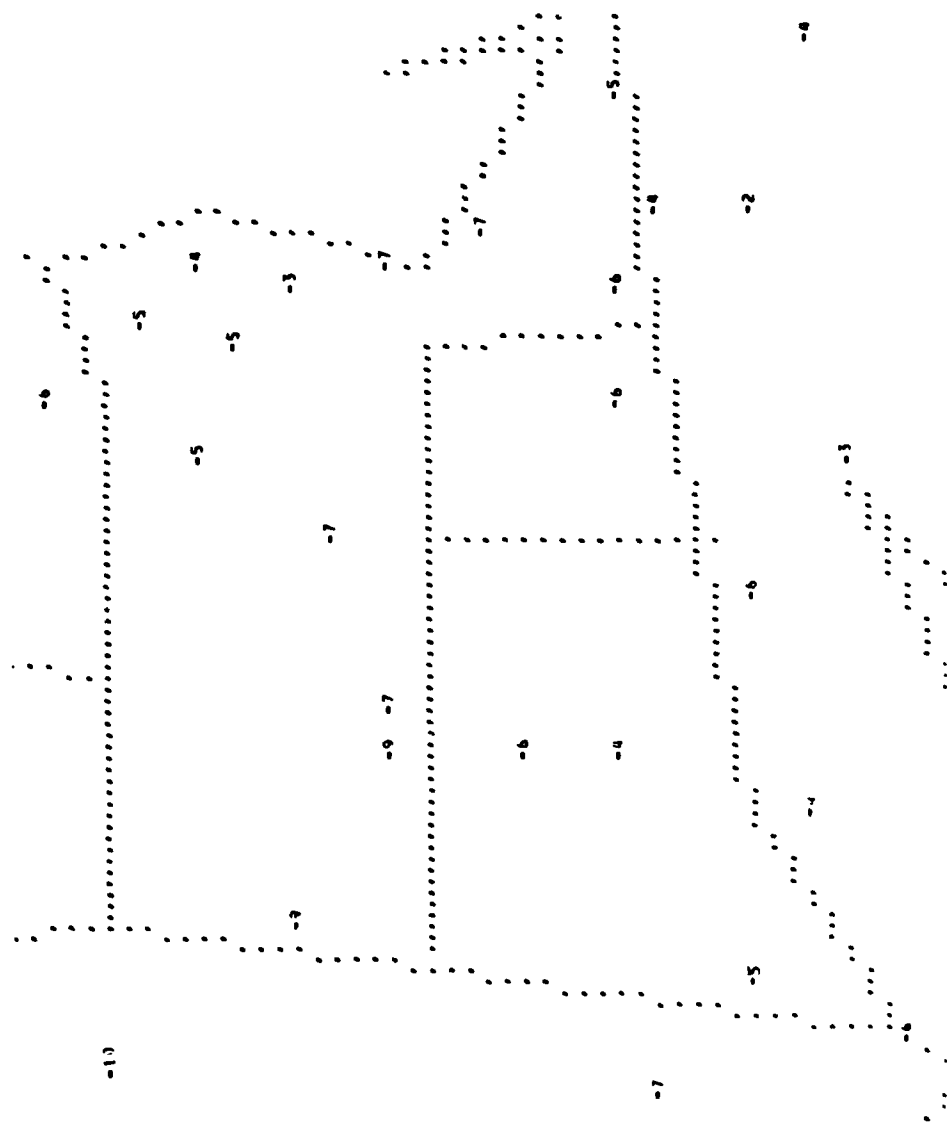


Fig. 19b. WISPLT Detailed Regional Plot of Temperature.

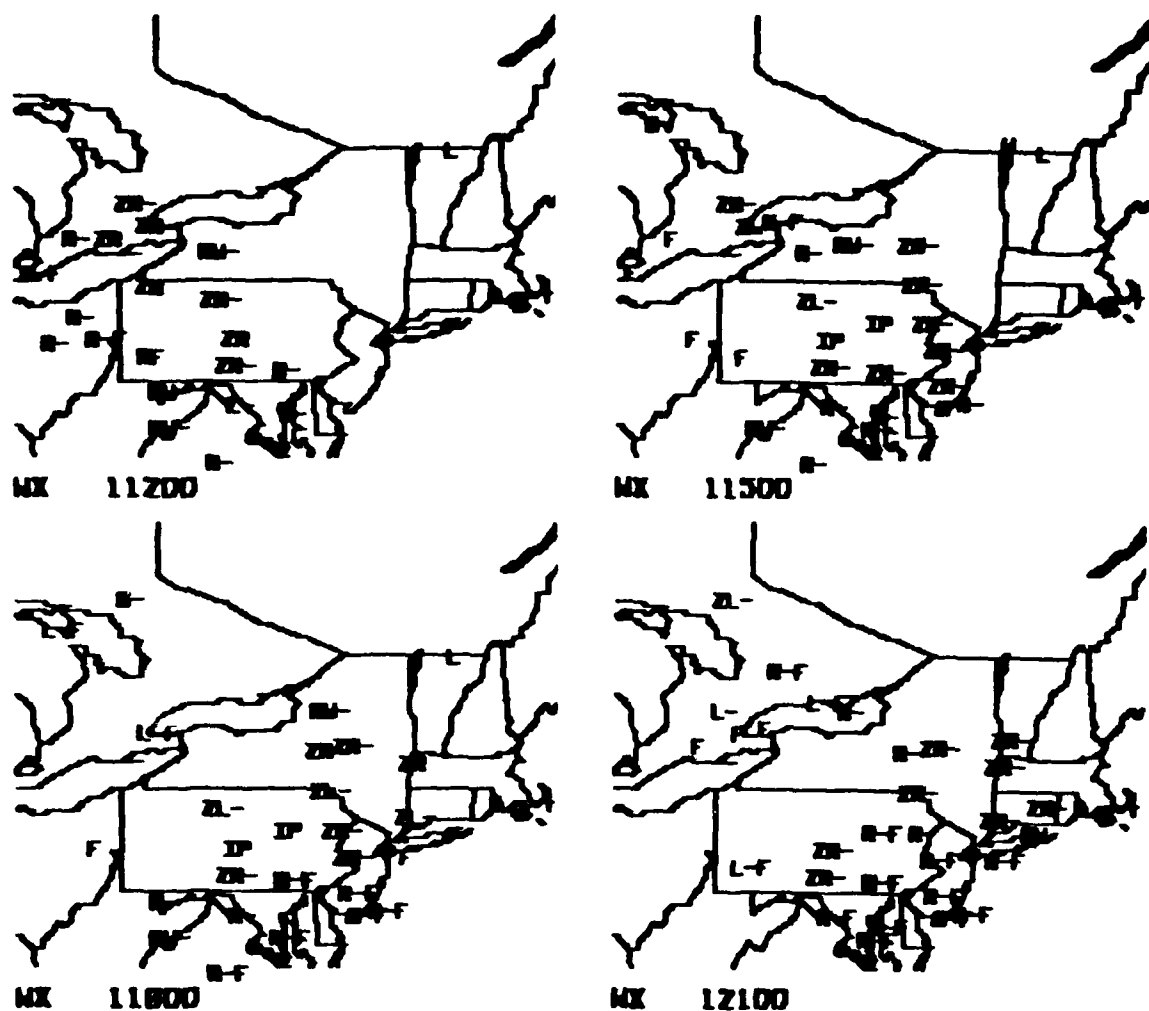


Fig. 20. Four-Panel Plot of Current Weather.

```

***
A F G L V C I D A S          PROGRAM: SVCADI          TERMINAL: 021
T ID AID          PRES LD MID HI VIS AX          LOW MDL HGM          PCPN
021200 000 13 13 2308          1005.0 3 0 0 2.5 RF          003
021300 000
021400 000
021500 000 14 14 1605          1004.0 3 0 0 5 R-F          008

```

```

***
A F G L V C I D A S          PROGRAM: SVCADI          TERMINAL: 021
T ID AID          PRES LD MID HI VIS AX          LOW MDL HGM          PCPN
021200 000 13 13 2308          1005.0 3 0 0 2.5 RF          003
021300 000 14-52 1906          1005.0 3 0 0 2.5 RF          008
021400 000 13-52 2210          1005.0 3 0 0 3 RF          015
021500 000 14 14 1605          1004.0 3 0 0 5 R-F          008

```

Fig. 21. Surface Data Listing with Old Missing Data Check Routine (top) and New Missing Data Check Routine (bottom).

When this key factor is determined, a brief message advising forecast procedure is displayed. The checklist tabulates yes answers provided by the forecaster and predicts whether convective weather will occur and indicates whether or not it will reach severe levels. Both routines are area forecasting aids that can be applied to a particular station.

e. Automated Analysis and Forecast Routines

When a previously calculated analysis was redisplayed on the WRRRM graphics, AFGL surface and upper air analyzing routines SACONT and RBCONX had to collect the raw data, re-interpolate them to grid points and then contour those re-gridded data. To speed up this redisplay process, grid files were added to the McIDAS data base to store interpolated data. Software developed at the University of Wisconsin to write gridded data into these files and to display saved analyses was modified and added to the nowcasting capability.

With gridded data saved in this manner, processing and use of the grids not previously possible could now be accomplished. A bilinear interpolation technique to return the field value at any point in the analysis was developed and added to PLTMAP. This option, when used with a two-dimensional approximation of the LFM-derived Trajectory Model Forecast, provided a means to forecast any conservative property of the atmosphere at the surface, 850, and 700 millibar levels for 12- and 24-hour time periods.

Program GRIDWK, developed at the University of Wisconsin, was modified and added to McIDAS to manage and manipulate the grids within each file. Options to change extreme values within the grid permit crude data editing and changes to the analysis without affecting the original raw data. The ability to transfer grids from the file of one terminal to another provides common access to any analysis. In response to a need to archive MDR data, which must be transferred to a terminal's grid file to be displayed, save and restore options were developed for GRIDWK. Up to 28 eastern U.S. 0.5° resolution grids of MDR data can be saved or restored by these routines.

Access to gridded data also allowed the combination of surface and upper air data in a more accurate 1000-500 millibar thickness analysis. Since a 1000 mb level report is not received from a RAOB station if its uncorrected surface pressure is less than 1000 mb, previous analysis

routines which were limited to upper air data only contained large regions with missing data. By using a 0Z or 12Z surface pressure analysis and converting it to a 1000 mb height grid, a quick and reasonable approximation to the thickness field can be calculated.

Writing gridded data to a file permitted the addition to McIDAS of two routines developed at the University of Wisconsin to aid the short-range forecaster. PRERAB, a trajectory model forecast routine, and SETRAB, a vertically averaging wind field analysis routine, were modified for compatibility with the AFGL McIDAS. A vertically-averaged, density-weighted wind field using any or all mandatory level data is calculated to produce u and v component wind field grids. Using these grids and an initial field grid, point or station forecasts and area forecasts based on either advection or trajectory methods can be computed for any time period.

V. Conclusion

The speed and flexibility of McIDAS in analyzing and displaying the data base available have only begun to be exploited. The addition of LFM forecast products, simple forecast techniques, and menu-driven guidance programs allows the terminal forecaster to assess the regional impact of weather systems. Expansion of the McIDAS data base to include MDR data and improvements in GOES imagery navigation provide important data to the mesoscale forecaster for modifying this regional picture and tailoring it to his local area. While modification of McIDAS may not yield the ideal terminal forecast system, the changes made do point out the direction in which the development of such a system should proceed.

B. AFGL WEATHER TEST FACILITY SUPPORT

I. Introduction

The Weather Test Facility (WTF) at Otis AFB of the Air Force Geophysics Laboratory includes towers equipped with weather instruments at selected heights which, along with ground based instruments, sample wind, temperature, visibility, precipitation, cloud base height and other weather parameters.

To facilitate data collection, the Modular Automated Weather System (MAWS) was installed at Otis to accept signals from the various sensors, create one-minute mean digital values and send these values over tele-

phone long lines to AFGL where they are recorded onto magnetic tape.

II. Data for Sensor Evaluation

Under the contract SASC was involved in computerized data processing and evaluation of new or improved sensors from MAWS data tapes. The sensors included Rosemount wind sets and such visibility meters as a modified Fumosens, Wright forward scatter visibility meter, an AFGL-developed side-looking forward scatter meter referred to as a "lookaway," and a Wright Fog 15 visibility sensor.

The processing was accomplished by various versions of a CDC computer program, MAWSE, which displays outputs of the sensors in convenient form for analysis. Statistical correlation between the data from the instrument being tested and those from one of known reliability was computed and printed along with simple statistical measures of the two. Additional statistical information was displayed on graphical representations used to highlight similarities and differences between instruments.

Another effort in sensor evaluation involved examining periods of significant wind shear. A wind shear event was defined as a period of time when the wind shear between the 200 ft level and the ground was greater than four meters per second for a period of more than four minutes' duration. Episodes of wind shear were isolated from the minute to minute wind data. The shear magnitude of a given event was examined in relation to the surface wind during that event and in relation to the temperature differences occurring between the two heights during the event.

III. Verification of Prediction Techniques

A further Air Force concern was short-term prediction techniques for weather parameters critical to aviation. Computer program VERIFY, designed to be the final software module in AFGL's low cloud observation and prediction system, was completed. The program performed a thorough analysis of all probability and categorical forecasts based on cloud ceiling data retrieved from three rotating beam ceilometers (RBC) and wind and visibility data as processed by the MAWSE program. Forty episodes during which clouds were reported below 6000 ft for at least three hours were selected. Approximately 20,000 one-minute observations were processed.

Verification statistics were calculated for 15 prediction techniques, which fell into two groups. The first group consisted of probability forecasts, based on REEP equations. REEP (Regression Estimation of Event Probabilities) calculates probabilities of being within certain categories. The model employed placed cloud data into five categories: <200 ft, 200-500 ft, 500-1000 ft, 1000-3000 ft, and >3000 ft or no ceiling; or into two categories, <1000 ft or \geq 1000 ft. Exceedance probabilities were produced based on three sets of REEP equations: REEP5 using only cloud observations, REEP.01 using the predictor set in which the last predictor selected reduced the total variance by at least one percent, and REEP11 where wind and visibility data were added to the cloud observations. Also, an equivalent Markov technique and persistence were used.

The second group included thresholding techniques such as maximum probability, iterative, using REEP, and unit bias, climatology, and persistence.

All the exceedance probabilities and categorical forecasts generated were supplied to SASC to be used in program VERIFY for four forecast lengths: 30, 60, 120 and 180 minutes. Statistical tests applied to these data included bias, threat score, percent correct, Brier score, t-statistic, and chi-square. For each successive episode of the 40 selected, these statistics were compiled and stored in a random access data file (RADF). The RADF retained data for each of the 15 forecast techniques, stratified by forecast length, episode number, and eventually for all episodes combined. The RADF required less storage than a sequential file, and provided faster and more efficient retrieval for several persons desiring access to the information, whether for analysis, or print or plot display.

VERIFY provided a summary listing of all statistics calculated and became the critical module which provided the initial forecast processing and subsequent display of verification data.

IV. Fog Model Display

A program was written to produce a three-dimensional display of the temporal variability of the drop size distribution during the life cycle of a fog episode. As part of an AFGL effort to develop improved numerical techniques for the short-range prediction of fog, the drop size distribution data were obtained at the WTF with a FMS forward scatter

spectrometer system. A graphics display package developed by the National Center for Atmospheric Research (NCAR) was extensively revised to achieve the proper angles for displaying the data and to label the axes. With additional routines, displays were produced which demonstrated the variation of the droplet concentration (N) with drop size and time.

Fig. 23 shows two displays of data, collected at 3 m and 5 m above ground, during a five-hour fog episode at Otis AFB.

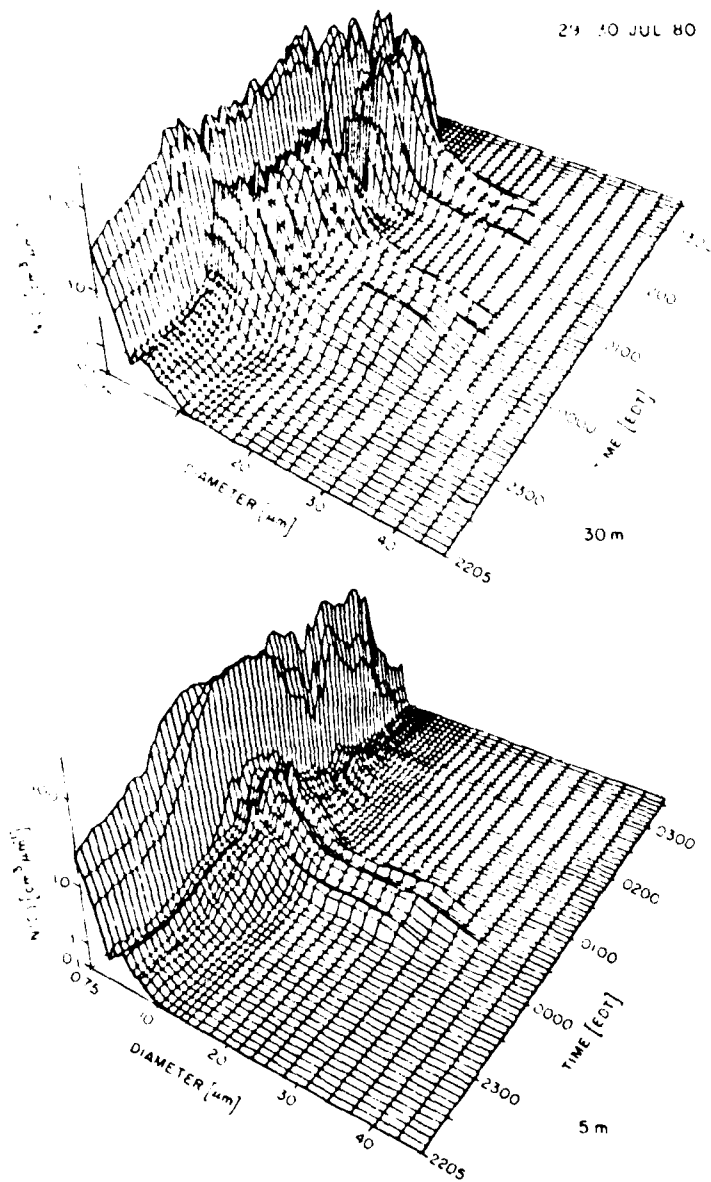


Fig. 22. Drop-Size Distributions From Spectrometer Probes.

SECTION 3.

SATELLITE METEOROLOGY

A. CLUSTERING TECHNIQUE FOR SATELLITE IMAGERY ANALYSIS

As one step in developing an automated satellite imagery analysis scheme, AFGL developed a technique using infrared radiative count values for analyzing data samples into sub-regions representing various cloud types.¹ Manual classification was performed, assigning to each sub-region, or cluster, a cloud type based on the scheme in Table 1.

Texture and gradient calculations were performed on the data in each cluster. It was expected that, with a sufficiently large number of samples from each of the eighteen cloud categories, distinctive attributes or combinations of attributes could be isolated by which each cloud type could be identified in a fully automated system. All data selection and analysis were performed on the AFGL CDC 6600 computer using recorded satellite imagery from the ODIS (Offline Data Ingest System) archive.

TABLE 1. CLOUD CLASSIFICATION SYSTEM.

<u>Cirrus</u>	<u>Cumulus</u>	<u>Other</u>
1. Thin	8. Small scattered	12. Stratus
2. Moderate	9. Small	13. Stratocumulus
3. Thick	10. Moderate	14. Altocumulus
4. Thin over Cu	11. Large	15. Altostratus
5. Moderate over Cu		16. Nimbostratus
6. Thin over St		17. Cumulonimbus
7. Moderate over St		18. Clear

SASC developed an interactive adaptation of the clustering algorithm, called CLUSTR, for use on McIDAS. Documentation of the command options is provided in Appendix A to this section. The interactive approach was selected to facilitate quick and easy sample selection. Analysis and display options were later incorporated, followed by file editing and management capabilities.

A stepwise procedure was established for data collection. Visible and infrared satellite images were loaded on television frames and examined for suitable cloud formations. After a sample was visually selected, the box cursor under joystick control was positioned over it, and the command CL was entered. This command initiated CLUSTR, which extracted

1. Hawkins, R. S., 1980: A clustering technique for satellite imagery analysis. Preprints, 8th Conference on Weather Forecasting and Analysis, AMS, Boston; pp. 115-118.

the visible and infrared data arrays corresponding to the region within the cursor, executed the clustering algorithm, computed histograms of texture and gradient at each of three spatial scales, and entered the results in a disk file called CLSFIL. Documentation of the structure of CLSFIL is provided in Appendix B.

A message was sent to the operator's console indicating where the sample was stored in the file. CLSFIL has a maximum capacity of ten sample entries. Samples were displayed on the television monitor by the LOAD option of CLUSTER. Fig. 1 is an example of the type of display resulting from this command. The visible imagery sample, blown up by a factor of three, appears in the upper left quadrant of the picture. The corresponding infrared sample is shown in the lower left. In the upper right quadrant is a representation of the results of clustering. Each of the four clusters derived from the infrared data is depicted in a different gray shade.

Based on the information provided in displays like Fig. 1, manual cloud classification was performed and entered in the TYPE option of CLUSTER. Texture and gradient histograms were drawn using the option HIS. Each curve could be displayed individually or in combination with up to five others. Fig. 2 shows an example of histograms of the three scales of texture for the third cluster of an imagery sample. On the McIDAS graphics display the TEX 1 curve and annotation appeared in red, TEX 2 in green, and TEX 3 in yellow. Additional curves were added in dashed lines up to a maximum of six curves per display, as in Fig. 3. Labels, not present on McIDAS, have been added in Figs. 2 and 3 to identify each curve.

Summaries of data collected for individual samples or for all entries in the file were available through the SUM option of CLUSTER. Listings were directed either to the operator's console or to the line printer for hard copies, like the example in Fig. 4. The entry number in these listings refers to position within CLSFIL, and the sample number refers to location on a particular visible/infrared picture pair identified by SSYYDDD (satellite-year-date code) and HHMMSS (hour-minute-second of picture start time). Cut levels and Mean IR and VIS are given in radiative count values. Cloud type assignments correspond to the numbers given in Table 1.



Figure 1. Sample Display Produced by CLUSTER.

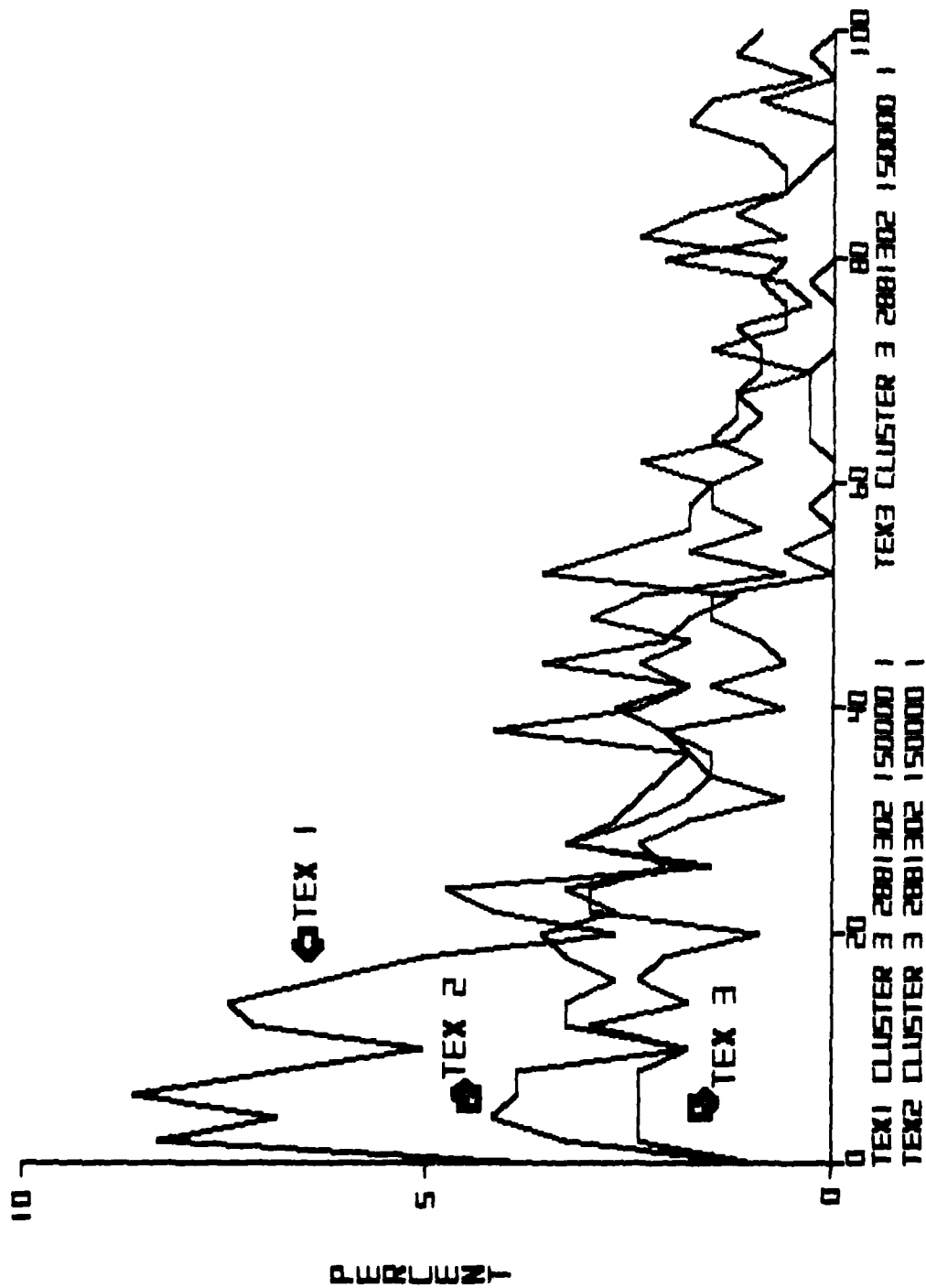


Fig. 2. Histogram Results for Three Scales of Texture.

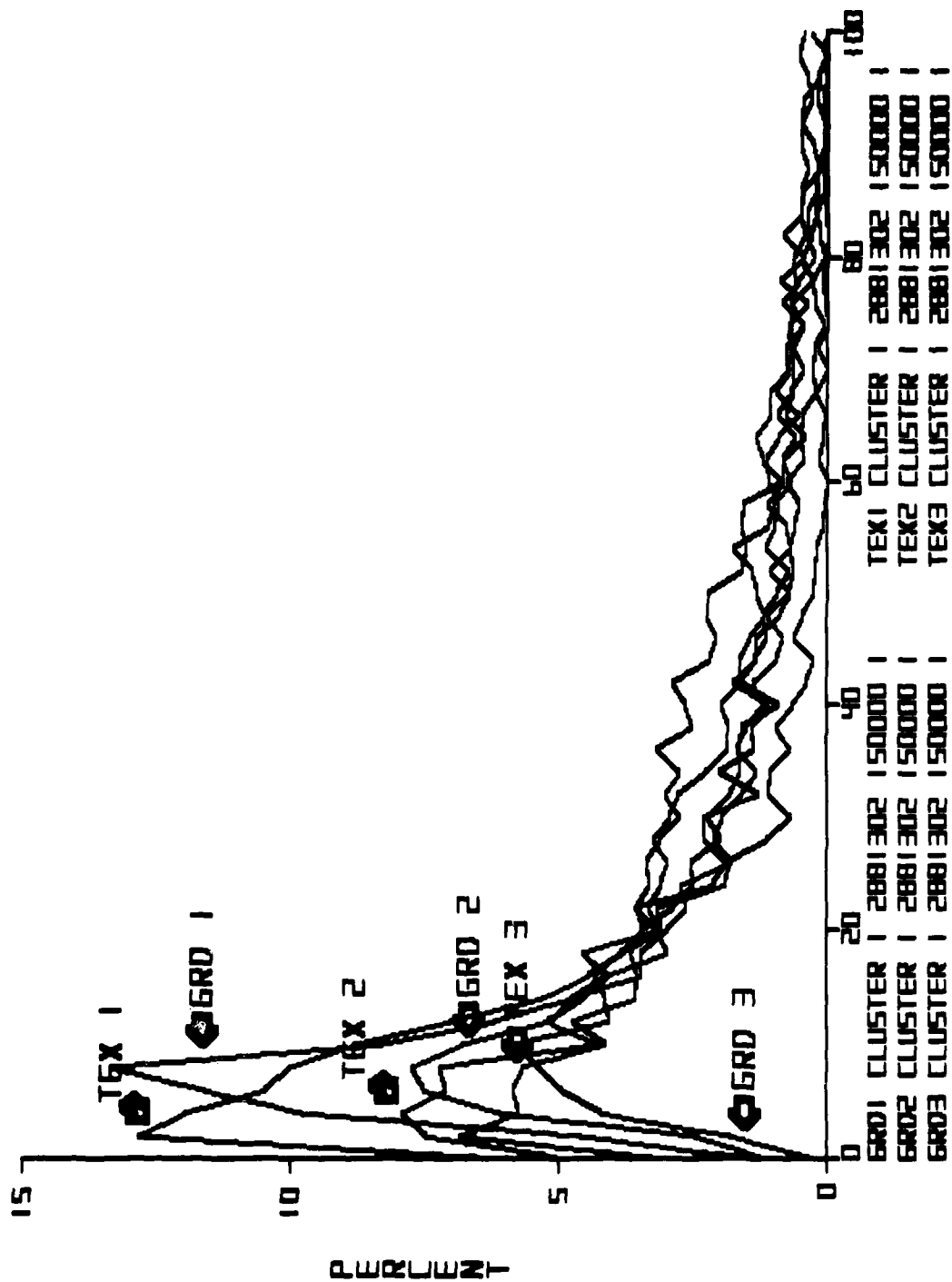


Fig. 3. Histogram Results for Texture and Gradient Calculations.

*** A F G L M C I D A S *** PROGRAM: CLUSTER

CONTENTS OF CLUSTER FILE

ENTRY 1 SAMPLE 2 SSYYDDD=2881252 HHMMSS=130000

CLUSTER	1	2	3	4
CUT LEVEL		115	155	205
NO OF POINTS	38	42	119	57
MEAN IR	103.0	131.6	188.6	211.1
MEAN VIS	73.4	100.9	149.0	179.9
CLOUD TYPE	18	1	4	17

ENTRY 2 SAMPLE 1 SSYYDDD=2881254 HHMMSS=130000

CLUSTER	1	2	3
CUT LEVEL		105	115
NO OF POINTS	76	51	129
MEAN IR	95.6	109.2	124.0
MEAN VIS	82.3	107.9	132.3
CLOUD TYPE	18	13	14

ENTRY 3 SAMPLE 2 SSYYDDD=2881254 HHMMSS=130000

CLUSTER	1	2
CUT LEVEL		95
NO OF POINTS	239	17
MEAN IR	80.9	101.5
MEAN VIS	66.5	96.0
CLOUD TYPE	18	15

ENTRY 4 SAMPLE 3 SSYYDDD=2881254 HHMMSS=130000

CLUSTER	1	2
CUT LEVEL		95
NO OF POINTS	38	218
MEAN IR	92.8	104.4
MEAN VIS	69.3	123.1
CLOUD TYPE	18	13

ENTRY 5 SAMPLE 4 SSYYDDD=2881254 HHMMSS=130000

CLUSTER	1
NO OF POINTS	256
MEAN IR	91.4
MEAN VIS	96.8
CLOUD TYPE	12

Fig. 4. Summary Listing of Contents of CLSFIL.

The final CLUSTR display option, BOX, was used to identify all samples selected from an image. Figs. 5 and 6 show boxes over visible and infrared satellite images respectively with labels corresponding to sample numbers in entries 2-5 of Fig. 4.

When CLSFIL was full or sample selection was completed, file contents were saved on magnetic tape using the SAVE option of CLUSTR. The converse function, that of restoring data from tape to disk file, was performed by the RES option. File editing functions consisted of INI, which initialized or cleared the contents of CLSFIL, and DEL, which was used to delete any single entry from the file.

B. BRIGHTNESS VARIATION ANALYSIS

In an effort to utilize geostationary satellite data for determining cloud cover amounts, SASC scientists developed software to reduce and analyze archived GOES and SMS imagery (Gerlach, 1980a)². The conclusions reached in the first phase of the effort — calculation of curves relating cloud cover and average reflectivity (Method 1) — were reported in Keegan and Niedzielski (1981)³.

This follow-on study entailed the testing of these relationships on the dependent data sample (1977-1978 data) to assess their effectiveness.

Results showed an overall 67 percent correct classification rate (see Table 2). Weather station reports of cloud amounts were used as cloudtruth. Detailed study showed this rate to be heavily weighted by the clear and overcast categories, which account for 31 percent and 24 percent of the sample, respectively. Both categories were classified correctly nearly 80 percent of the time. Categories of scattered and broken cloud cover had correct classification rates ranging from 20 percent for three-tenths coverage to 57 percent for seven-tenths coverage. Testing with an independent data sample (1979 data) yielded essentially the same results.

2. Gerlach, A. M. (ed), 1980a: Computer-based weather research. AFGL-TR-80-0069, pp. 74-81.
3. Keegan, T. J., and M. E. Niedzielski, 1981: Specification of cloud amount over local areas from GOES visual imagery. Environmental Research Papers No. 743, AFGL-TR-81-0153.

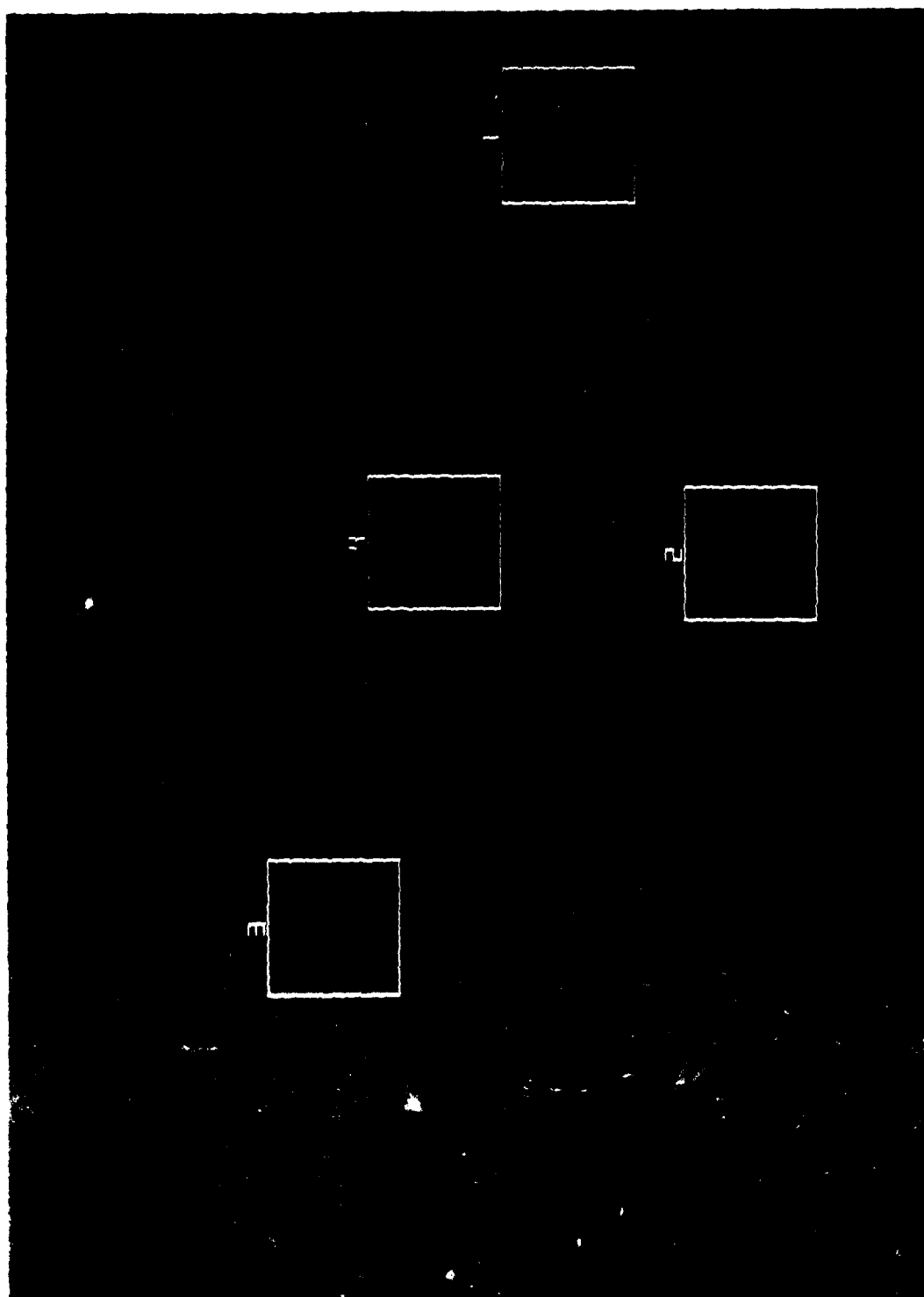


Figure 1. Boxes Showing Samples Selected over Visible Image.

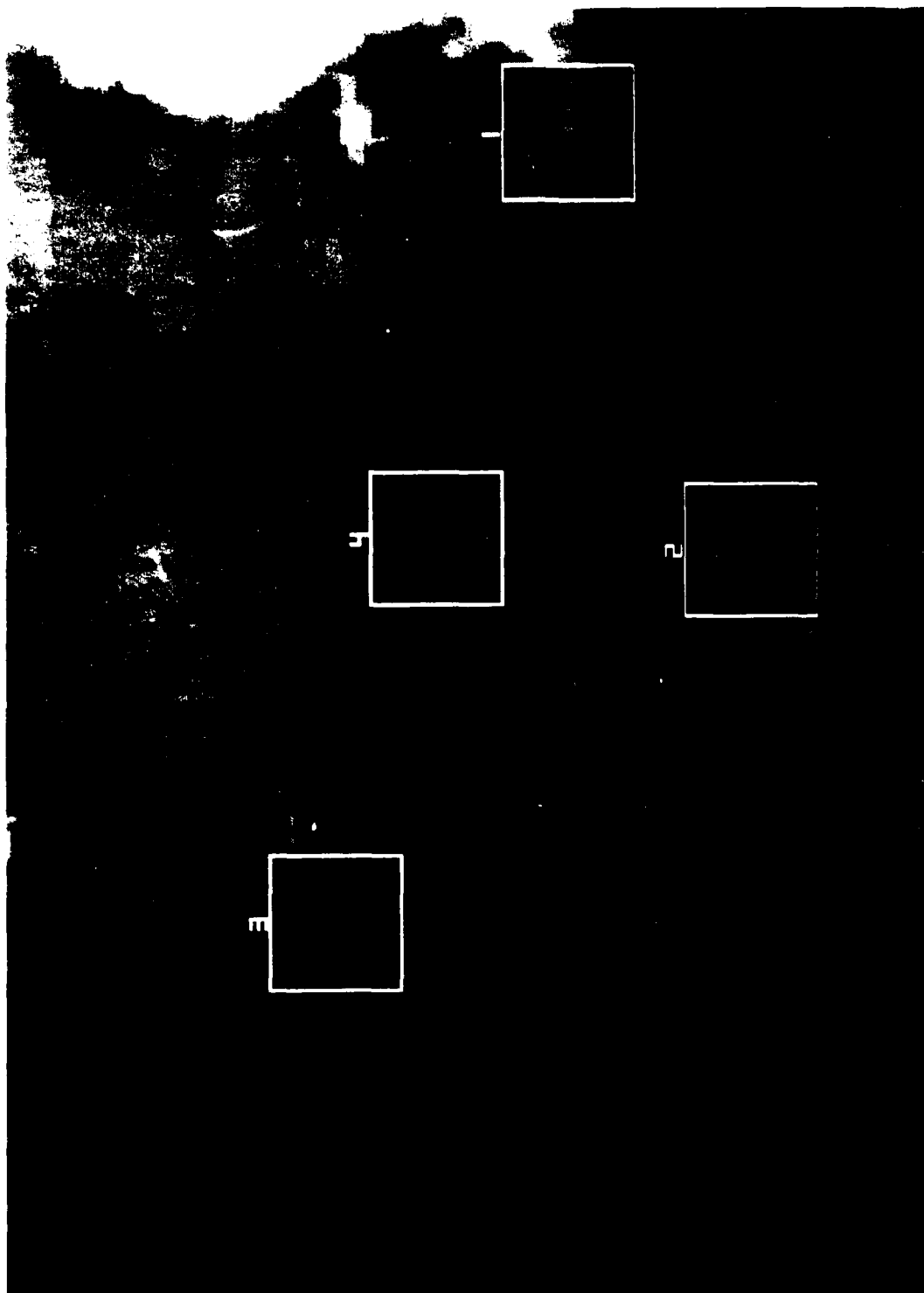


Fig. 1. 10 x 6 cm. 10 x 6 cm. 10 x 6 cm. 10 x 6 cm.

TABLE 2. COMPARISON OF CLOUD AMOUNT TECHNIQUES

METHOD	1	2	3	4
All Cloud Amounts	67	64	75	77
Clear	80	79	85	92
Overcast	80	78	91	91

Correct Classification Rates in Percent

Method 1 is Average Reflectivity; Method 2 is Average Reflectivity, Texture, and Maximum Reflectivity; Method 3 is Simple Threshold (fixed threshold); and Method 4 is Variable Threshold (decision tree algorithm).

Two important conclusions were reached as a result of these tests. First, average reflectivity could generally distinguish cloud-free and cloud-filled fields of view but was a poor parameter for determining scattered and broken cloud amounts. Second, the data remained stable enough from several satellites (GOES 1, GOES 2, SMS 2) to yield nearly constant results.

The addition of other reflectivity characteristics for multivariate analysis was the next phase of the study. Relationships between cloud amount and average reflectivity, sample texture (standard deviation), and maximum reflectivity were calculated (Method 2) and the testing repeated on both dependent and independent data. Overall results of classification rates decreased slightly to 64 percent correct. This led to the subjective conclusion that the variability of reflectivity characteristics within each cloud cover category was too large to allow regression techniques to define the relationships clearly.

As a result of the indifferent ability of regression curves to specify cloud cover, a different method, a threshold technique, was implemented (Method 3). This approach is similar to the Air Force Global Weather Central cloud analysis program 3DNEPH, which uses location-dependent thresholds for cloud detection in visible data on polar-orbiting satellites.⁴

4. Fye, F. K., 1978: The AFGWC automated cloud analysis model. AFGWC Technical Memorandum 78-002, pp. 26-31.

Using information deduced from analysis of all clear and overcast cases, a cloud/no cloud threshold reflectivity of 18 percent was selected. A simple addition was made to program CENTER to count the number of pixels within the 9 x 9 pixel analysis box that were above the threshold value and to compute a percent cloud cover. This straightforward technique resulted in a 75 percent correct classification rate of cases with no tenuous cirrus clouds. Clear and overcast conditions were classified correctly 85 percent and 91 percent of the time, respectively. Closer analysis of misclassified clear cases showed that sample texture could help distinguish cases with clouds whose areal extent was somewhat below image resolution. If the sample texture exceeded 2.5 percent, a cloud/no cloud threshold of 16.0 percent was indicated. Incorporating this information into a simple decision tree algorithm in CENTER (Method 4) resulted in a 92 percent correct classification rate for clear conditions.

As a first attempt to deal with the problem of tenuous cirrus clouds, collocated IR data were added to the data sample. A variable threshold for cirrus/no cirrus IR count was selected and case studies begun to determine if detection of cirrus would be a straightforward procedure. Analysis revealed that these clouds are not blackbody radiators and varying amounts of background radiation leaks through. Therefore, no specific IR threshold can be considered appropriate for even a majority of the cases. This threshold value must be interactively determined and entered into the cloud amount algorithm for each case. High cloud studies brought to light the need to vary the size of the analysis box with varying cloud heights so as to keep the satellite field of view in agreement with that of a surface-based observer. An option to vary the size of the analysis box has been added to CENTER but remains an interactive procedure.

Threshold techniques for specifying cloud cover amounts (Methods 3 and 4) are a more accurate method than average brightness techniques, as is shown in Table 1.

By properly choosing a cloud/no cloud threshold, with a decision-tree or similar algorithm, clear and overcast conditions can be classified to a high degree of accuracy. Sophistication of these techniques can help to enhance the results achieved by the simplistic methods tested to date.

APPENDIX A. COMMAND DOCUMENTATION FOR PROGRAM CLUSTER.

COMMAND: CLUSTER

KEY IN: CL

PROGRAMMER: G. DENGEL

DATE: 3 SEPT 81

CHAPTER: AFGL

COMMAND FORMAT:

CL OPT P1 P2 P3 P4 P5 P6 P7

COMMAND DEFAULT PARAMETERS: CL_{cr}

Unless an option is specified, CL will extract the VIS and IR imagery samples within the cursor, cluster, compute histograms of texture and gradient for each cluster, and write the results into CLSFIL.

PARAMETER DESCRIPTION:

OPT Program Options

1. CL LOAD Area Frame Entry

Area = digital area in which to store data
Frame = TV frame on which to display data
Entry = entry number in CLSFIL (≤ 10)

2. CL TYPE Entry C1 C2 C3 C4

Assign cloud types C1-C4 to clusters in Entry

3. CL HIS Entry Cluster Function Inc Color Max X Max Y

Draw histogram of data from Entry and Cluster specified.

Function = TEX or GRD

Inc = 1, 3, or 5

*Color = 1 (red), 2 (green), 3 (yellow)

Negative for dashed lines
(default = green)

Max X = maximum value of abscissa
(default = 100)

Max Y = maximum value of ordinate
(default = 50)

* Axes will only be drawn when green is requested, otherwise an overlay is assumed.

4. CL SUM E1 E2... (PRI)

CL SUM ALL (PRI)

Print data summaries for entries

E1, E2, etc. or ALL entries in file on CRT. For line printer output, last parameter should be "PRI."

5. CL BOX

Draws boxes around all samples in file taken from currently displayed frame.

6. CL SAVE Tape (NEW)
Write contents of file to magnetic tape.
Tape = Tape number (type 96)
NEW indicates new tape
7. CL RES Tape File
Restore contents of tape to CLSFIL
Tape = Tape number (type 96)
File = Tape file to be restored
8. CL INI
 nitialize CLSFIL
9. CL DEL Entry
 Delete entry from CLSFIL

APPENDIX B. DOCUMENTATION OF THE CLSFIL FILE STRUCTURE.

Type Disk File
 (Disk File, Savetape, COMMON block, etc.)

NAME CLSFIL
 (If applicable)

DOCUMENTER G. Dengel Date 3 Sept 81

Description of Structure:

Type: Data file (binary)
Size: 1380 sectors
Use: Store data samples and results for program CLUSTR. Holds a maximum of 10 samples.

Initialization: Key in "CL INI"

Allocation: 138 sectors per entry

Imagery samples and cluster information:

<u>Sectors</u>	<u>Words</u>	
0-15	1-112	VIS data, packed
16	1-34	VIS data, packed
	35	SSYYDDD
	36	HHMMSS
	37	Upper left corner line coordinate
	38	Upper left corner element coordinate
	39	Sample number
	40	Number of clusters
	41-43	Cut levels
	44-47	Number of points in each cluster
	48-51	Mean VIS count for each cluster
	52-55	Mean IR count for each cluster
	56-59	Cloud type assigned to each cluster
	60-81	Cluster frequency table, packed
	82-111	Unused
	112	Number of entries in file (sector 16 only)
17	1-86	IR data, packed
	87-112	Unused

Histogram data, half-words:

<u>Sectors</u>	<u>Cluster</u>	<u>Function</u>
18-22	1	TEX 1
23-27	1	TEX 3
28-32	1	TEX 5
33-37	1	GRD 1
38-42	1	GRD 3
43-47	1	GRD 5
48-77	2	
78-107	3	
108-137	4	

SECTION 4.

MCIDAS OPERATION AND ENHANCEMENT

A. SUPPORT TO RESEARCH PROJECTS

The McIDAS Facility supports on a daily basis various research projects of the AFGL Meteorology Division. The Mesoscale Forecast Experiment described in Section 2A, for example, depends wholly on the McIDAS ability to display meteorological data. Studies in satellite meteorology are particularly dependent on McIDAS.

In addition, McIDAS is used to support field programs. During 1981 eighteen aircraft flights were made for two AFGL research projects: the Large Scale Cloud System (LSCS) and Icing studies. Both studies used a specially instrumented C-130 aircraft based at Wright-Patterson AFB, OH.

The LSCS study sampled large homogeneous cloud masses as they progressed from west to east across the U.S. The objective was to obtain a better understanding of the microphysics of clouds in large winter storms. The hydrometeor data collected by the aircraft included particle size, number, type, distribution, and liquid water content. The Icing study was conducted in a similar manner since it involved observing and measuring the accumulation of ice on aircraft control surfaces. The C-130 gathered data on intensity (light, moderate, heavy) and type of icing (glaze, mixed, rime).

McIDAS satellite imagery loops (both visible and infrared) depicting cloud growth, and decay, cloud top temperatures, and objective analyses and plots of radiosonde data (see Fig. 1) provided the ground support team information on the best sampling locations and altitudes. Additional information examined prior to and in real-time during the flights included: surface observation plots, analyses of pressure fields, streamlines, dew-point temperatures, wind vectors, precipitation amounts, current weather, cloud cover, upper air cross-sections, icing probability (see Table 1), and radar observations (see Fig. 2). Data for both studies were archived to help document the synoptic situation for post analysis.

The McIDAS facility was also used to collect one-half mile resolution visible satellite imagery last winter and spring over North America for a study of cloud brightness related to development of Tactical Decision Aids. Times for the imagery ranged from 1530 to 1830 GMT when the sun's declination angle was at its highest for that time of year. Real-time as well as Sony archived imagery were used. A software program specifically written for the project provided printouts of various cloud

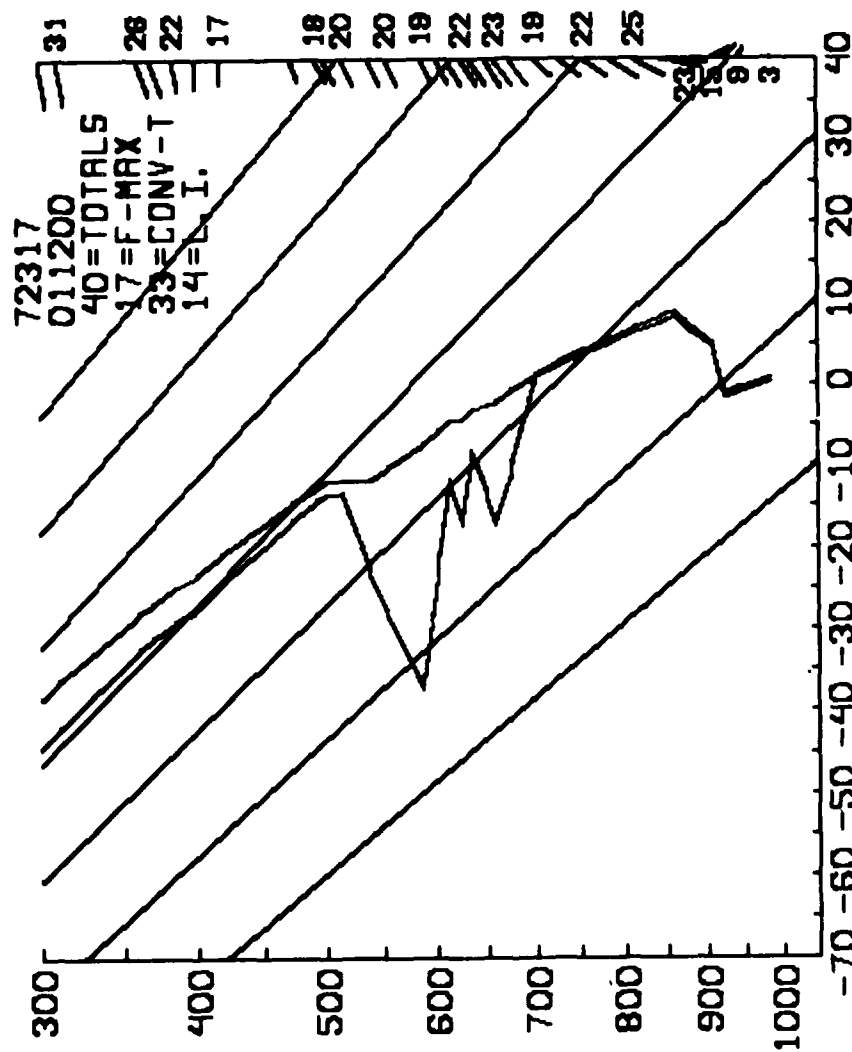


Fig. 1. Stüve Plot Based on Radiosonde Data.

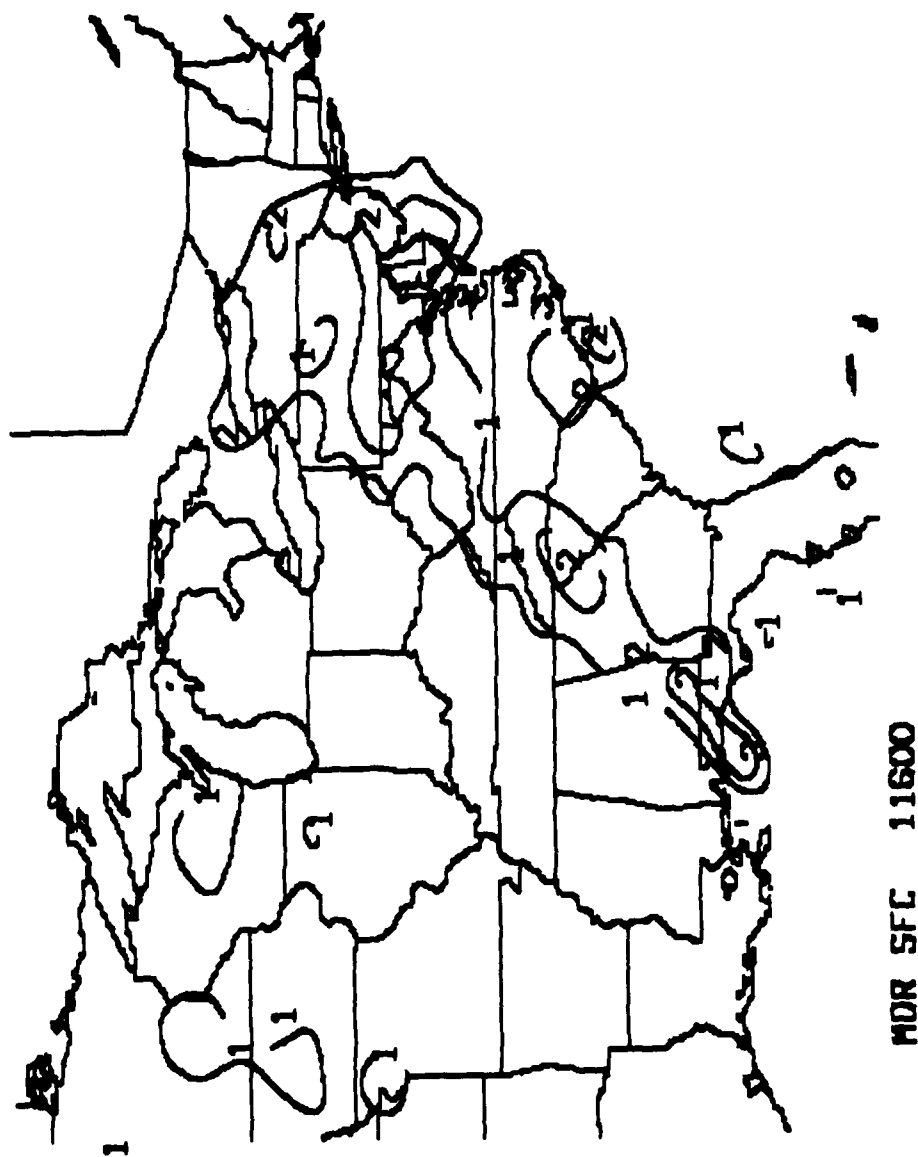


Fig. 2. Radar Analysis for Eastern U.S.

brightness thresholds found in the imagery. These data were saved on magnetic tape for later analysis.

TABLE 1. ICING PROBABILITY LISTING.

* * * * A F G L M C I D A S * * * * PROGRAM: ICING						
ICING PROBABILITY ESTIMATES FOR 72429 AT 10000						
Z(FT)	T(0)	TD(0)	T-TD	TYPE	INTENSITY	PROBABILITY
1004	.8	-4.2	5.0			0
* 1641	0.0	-4.8	4.8			0
1880	-.3	-5.0	4.7			0
1919	0.0	-5.3	5.3			0
2389	4.0	-9.0	13.0			0
3622	3.8	-10.2	14.0			0
4731	5.6	-24.4	30.0			0
5791	5.6	-24.4	30.0			0
6890	2.8	-17.2	20.0			0
7438	2.6	-7.4	10.0			0
9289	.6	-29.4	30.0			0
* 9526	0.0	-22.4	22.4			0
9882	-.9	-11.9	11.0			0
10905	-3.9	-12.9	9.0			0
11526	-5.3	-8.2	2.9	RIME	LIGHT	33
11723	-3.1	-4.1	1.0	RIME	MODERATE	51
13072	-4.1	-5.5	1.4	RIME	MODERATE	33
14958	-8.1	-9.0	.9	MIXED	MODERATE	41
18502	-12.5	-13.7	1.2	RIME	MODERATE	19
23968	-24.1	-27.2	3.1	RIME	LIGHT	11

* INTERPOLATED FREEZING LEVEL

McIDAS provided verification data for a project by the Rome Air Development Center (RADC/ET). This study examined the anomalous propagation of microwave signals due to atmospheric refractive gradients. A modified McIDAS software program, using upper air data from the Albany, NY and Chatham, MA radiosonde stations, provided the verification data (Fig. 3 and Table 2).

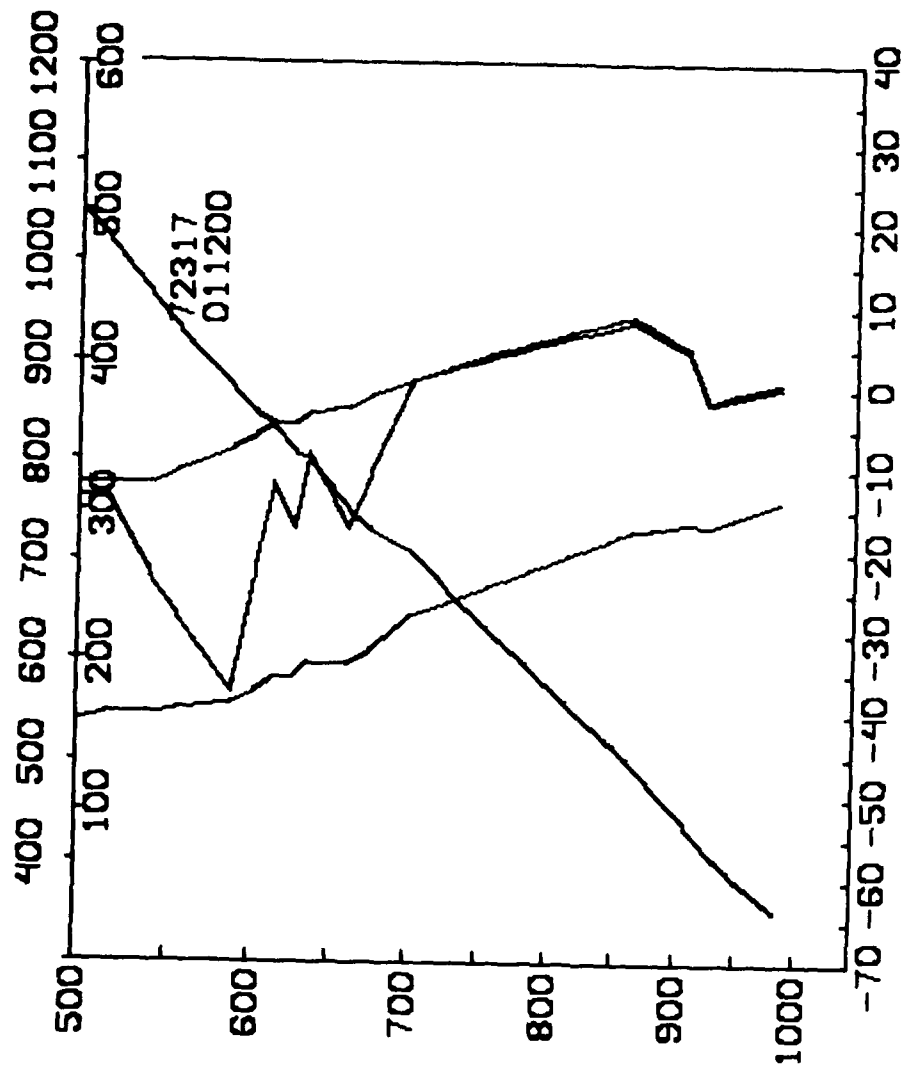


Fig. 3. Refractive Index Plot.

TABLE 2. RADIOSONDE DATA LISTING.

	72317	011200		
984	1.0	.4	070003	281
944	-.4	-.8	115009	609
922	-1.3	-1.6	135013	802
908	5.0	4.7	148015	926
876	7.6	7.1	180023	1219
861	9.0	8.4	188024	1364
850	8.8	8.0	195025	1471
844	8.6	7.8	190025	1524
814	7.2	6.5	210025	1829
784	5.8	5.2	215024	2134
755	4.3	3.9	215022	2439
727	2.8	2.5	220020	2743
700	1.2	1.0	225019	3058
674	-.9	-10.4	235023	3353
660	-2.3	-17.3	237023	3529
649	-2.6	-13.6	240023	3658
634	-3.1	-8.1	241022	3848
626	-4.3	-17.3	241022	3948
612	-4.5	-11.5	243021	4126
601	-5.8	-22.7	245019	4268
587	-7.5	-37.5	245019	4453
555	-10.3	-28.1	245020	4878
539	-11.9	-22.9	245020	5111
515	-11.7	-13.3	245020	5460
500	-11.9	-13.5	245019	5687
493	-12.6	-14.3	245018	5792
473	-14.6	-16.8	250017	6097
419	-20.9	-24.4	275017	7012
400	-23.3	-27.4	270020	7357
385	-24.9	-29.2	260022	7621
369	-26.9	-31.2	250026	7926
361	-28.1	-32.5	251026	8101
311	-36.4	-42.1	260031	9146
300	-38.5	-44.5	260033	9400
250	-48.9		260048	10624
200	-59.3		255051	12054
159	-69.1		263049	13456
150	-70.5		265048	13803
132	-70.9		270042	14561
127	-66.9		271040	14792
117	-67.4		275036	15243
100	-68.7		270030	16229

The GOES Research Rapid Scan Winter Storm project was initiated by AFGL in November. It calls for five winter storm research days during the period November 1981 - January 1982. During the first storm research day the eastern GOES satellite went into a seven-minute scan mode; that

is, it transmitted eight images in one hour instead of the normal two. Areal coverage of the imagery ranged from 10° N to 80° N latitude, roughly the North American continent.

The rapid scan satellite transmissions were recorded on the McIDAS archive system. The area of interest was then stripped off and stored on magnetic tape for future display and analysis.

B. HARDWARE ACQUISITION AND ENHANCEMENT

The process for storing TV images in McIDAS used to display satellite imagery was changed in 1981. In the previous system, the image data flowed from the host computer to a fast storage system where the digital picture was converted into an analog signal and sent to the analog disk for storage. When played back for display, the picture left the video disk as an analog signal, entered a high speed analog to digital converter where it was converted back to a digital image. The digital data were then sent to the red, green and blue enhancement drawers. After enhancement the signal was converted to a standard RGB analog signal and sent to the video monitors for display. The conversions from digital to analog and back again contributed to picture degradation.

The new system, installed in June, is the Digital Video Storage System (DVSS) manufactured by Idetik Corporation of Wisconsin. This system stores the image as sent by the satellite, in digital format, thus eliminating the digital to analog conversion. The system is composed of: a Harris channel interface card, two V ram cards, two timing and control cards, two DVSS cards, two 86/12 processor cards with on-board memory, two XY logic disk controller cards, and two CDC 80 megabyte Winchester disks.

The DVSS has not only enhanced picture quality but has also increased the picture storage volume from 260 frames per terminal to 400 frames per terminal. The DVSS was installed in parallel configuration with the old analog system as a back-up. Because of the different timing outputs of the DVSS, a channel interface circuit was designed to accommodate the signal going into the timing drawer for Terminal 21. Also designed into this circuit was an interlacing capability; that is, displaying two channels simultaneously.

Another component purchased from and installed by Idetik Corporation was a VAS frame synchronizer. This unit is a sophisticated satellite in-

formation processing device used in systems receiving Mode A and Mode AA transmission formats. It is designed to perform major and minor frame synchronization on stretched visible and infrared (VISSR on Mode A) and VISSR atmospheric sounder (VAS, or Mode AA) data from the new GOES satellites. The following circuitry cards are in the system: Mode A frame synchronizer, Mode AA frame synchronizer, bit error rate and line count card, GOES satellite data simulator card, Intel 86/12 single board computer, average and ingest card, and a Multibus/Harris channel interface card. When the McIDAS data ingest and handling software is revised, the frame synchronizer will be fully operational.

To increase McIDAS operational reliability two new electronic circuits were designed and installed. A Texas Instruments Silent 700 electronic data terminal was integrated into the system for use as back-up for the McIDAS teletype terminal. This terminal is essential for communication between the McIDAS operating system and the user. The interface circuit, designed by Richard Lynch (AFGL), can accommodate any standard RS232 terminal with a 110 baud rate. The other circuit installed is a relay switching panel designed to reverse the controls of the two interactive consoles. Using coaxial relays, the switching panel reverses all RS232 lines and cables to and from the joysticks and color monitors. This permits what is displayed on one terminal to be viewed on the other. Again, this is a back-up measure should either of the terminals fail.

During the year the elevation motor for the McIDAS antenna malfunctioned. When the motor was sent to the manufacturer's maintenance center for repairs, it was decided to overhaul both the antenna elevation and azimuth drive assemblies. A new motor was installed in the azimuth axis, all drive and tachometer belts were replaced, and all gears were lubricated. The overhaul was performed by personnel from Scientific-Atlanta.

The Data Products line printer was replaced in May with a new printer that is quieter and faster (300 lpm as opposed to 200 lpm) than its predecessor.

C. SOFTWARE DOCUMENTATION

Most programs written for the AFGL McIDAS facility rely heavily on pre-existing subroutines and functions that are on disk in the form of library modules. A main library and seven specialized libraries exist in

the system. The main library, LL, contains a wide variety of support routines for functions ranging from input/output to number conversions. The specialized libraries deal with the areas of graphics, nowcasting, navigation, WINDCO, real-time radar, manually digitized radar, and general data management. Documentation of the subprograms within these libraries was at best sparse, consisting of occasional comment cards in a small percentage of the routines.

SASC completed documentation of the graphics library, GRALIB. For each of the 58 modules within GRALIB, the type of subprogram, calling sequence, and description of the arguments were documented. Any additional insights into use of the routines were also noted, such as files accessed, variable types, and other statements that may be helpful. A major index of all graphics library modules was also compiled, giving the name of each routine and a short description of its purpose.

SECTION 5.
RADAR METEOROLOGY

A. WIND RETRIEVAL

I. Introduction

Several methods for retrieving winds from single-Doppler radar have been proposed. Browning and Wexler (1968)¹ and Waldteufel and Corbin (1979)² presented several such techniques which depend upon linearity of the wind velocity components and resolve the wind over large areas. Various storm and echo tracking schemes have also been presented (e.g., Crane, 1979³, and Bjerkaas and Forsyth, 1979⁴). Rinehart (1979)⁵ and Smythe (1981)⁶ presented techniques which give local estimates of the wind over much smaller areas by seeking smaller-scale patterns in reflectivity fields using correlation. Smythe (1981) also investigated the feasibility of tracking small-scale perturbations in Doppler radial velocity fields to estimate the horizontal wind and produced favorable results when these winds were compared with winds synthesized from two Doppler radars. This report is a continuation of the study of Smythe (1981).

II. Discussion

The algorithm of Smythe (1981) was modified to increase its efficiency in an attempt to meet AFGL requirements for real-time applications. Correlation coefficients were computed using the equation

1. Browning, K. A., and R. Wexler, 1968: The determination of kinematic properties of a wind field using Doppler radar. J. Appl. Meteor., 7, 105-113.
2. Waldteufel, P., and H. Corbin, 1979: On the analysis of single Doppler radar data. J. Appl. Meteor., 18, 532-542.
3. Crane, R. K., 1979: Automatic cell detection and tracking. IEEE Trans. Geoscience Electronics, GE-17, 250-262.
4. Bjerkaas, C. L., and D. E. Forsyth, 1979: Operational test of a three-dimensional echo tracking program. Preprints, 19th Conference on Radar Meteorology (Miami Beach), AMS, Boston, 244-247.
5. Rinehart, R. E., 1979: Internal storm motions from a single non-Doppler weather radar. NCAR/TN-146+STR.
6. Smythe, G. R., 1981: Correlation of Doppler-radar velocities and reflectivities with application to retrieving the transverse wind. Cooperative Institute for Mesoscale Meteorological Studies, Report No. 4, 72 pp. (Available from Cooperative Institute for Mesoscale Meteorological Studies, 815 Jenkins St., Norman, OK 73019.)

$$r = \frac{N \sum_{i=1}^N x_i y_i - \left(\sum_{i=1}^N x_i \right) \left(\sum_{i=1}^N y_i \right)}{\left\{ \left[N \sum_{i=1}^N x_i^2 - \left(\sum_{i=1}^N x_i \right)^2 \right] \left[N \sum_{i=1}^N y_i^2 - \left(\sum_{i=1}^N y_i \right)^2 \right] \right\}^{1/2}}$$

where r is the coefficient of cross-correlation, the x_i 's and y_i 's are either reflectivity or pulse pair velocity estimates for each pulse volume in the regions correlated, and N is the number of samples available, as some data might have been removed due to various editing criteria. Doppler velocities were averaged over the correlation region (array) of the first scan. This average was used to find a first-guess approximation of the radial displacement of the region at a later time. Data (reflectivity or velocity) were then lagged azimuthally to search for a correlation maximum. Fig. 1 shows an example of the first-guess displacement (D), the array of the first scan (hatched area), and the region of the second scan (between dashed curves) over which the initial array was lagged and correlated.

Several software versions of the wind retrieval algorithm were written, two of which were hybrids consisting of both Assembler and Fortran statements. Portions of the programs were timed and the tightest loops were recoded from Fortran to Assembler. In these loops floating point arithmetic was changed to halfword arithmetic. Also, register operations were used extensively. Excessive iterations through unnecessary time-consuming code were thus avoided.

Using the hybrids it was found that the time required to analyze an area of dimensions $40 \text{ km} \times 40^\circ$ (which is large enough to cover a thunderstorm) was approximately 140 s on the Interdata 7/32 minicomputer. Although the software was not tested on the Perkin-Elmer (P-E) 3242, run-time should be less than one-third of the present run-time. This would then allow a real-time analysis of six levels within the volume of the storm.

Features not coded in the original programs were added. Those features included the flagging, before processing, of arrays containing high percentages of low signal data, thus distinguishing areas of storm (strong echo return) from weak signal. The code was also modified to accommodate reflectivity and velocity data staggered at different range gate intervals

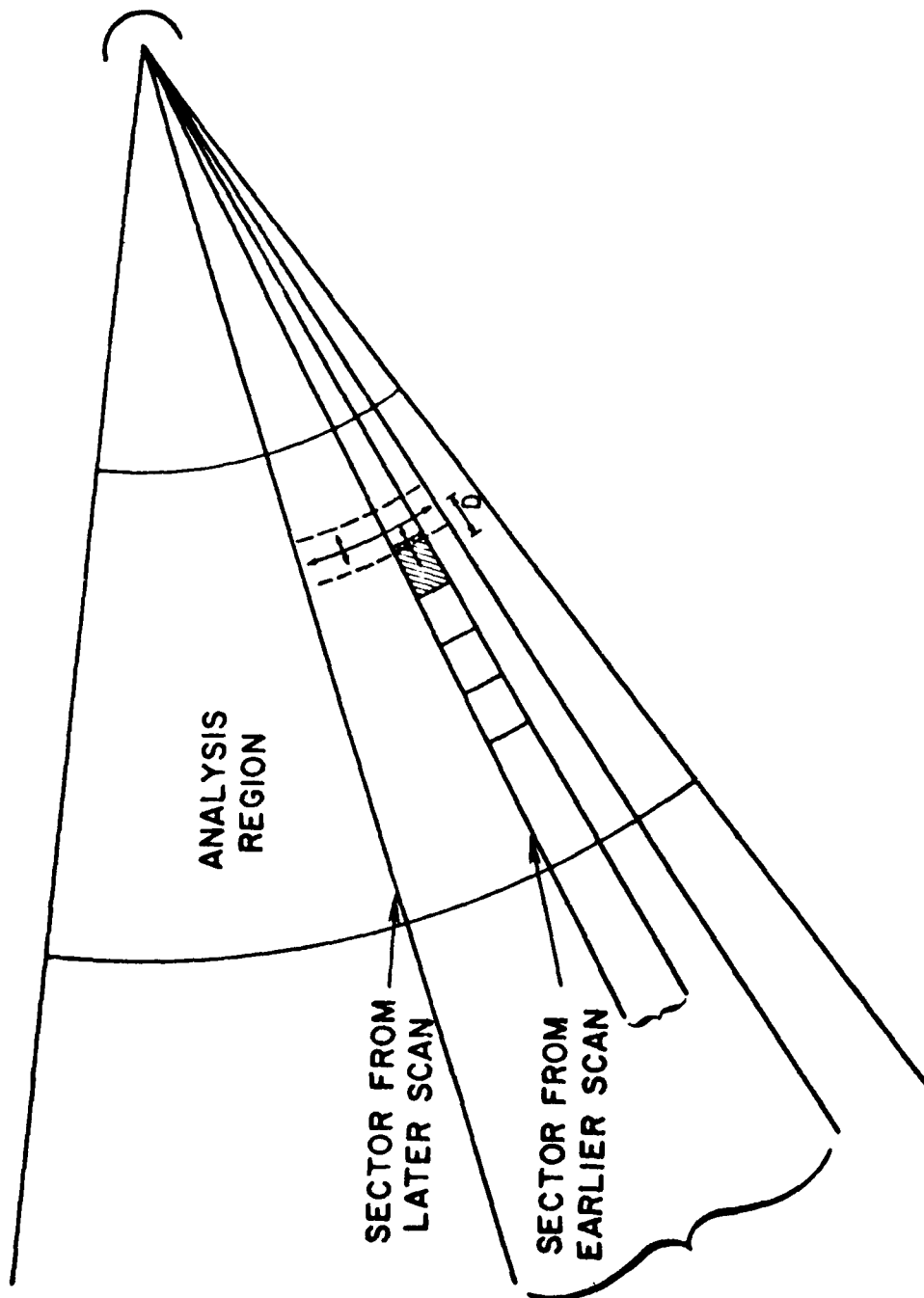


Fig. 1. Wind Retrieval Technique Geometry.

Δs (e.g., $\Delta s_{\text{velocity}} = 150\text{m}$, $\Delta s_{\text{reflectivity}} = 300\text{m}$).

Shown in Fig. 2 are correlation coefficients computed from data collected May 2, 1978, at 0.6° elevation in Oklahoma. The coefficients were obtained from correlating reflectivity and lagging in intervals of 0.6° azimuthally and 300m radially about the first-guess approximation of the radial displacement. The temporal lag was about $6\frac{1}{2}$ min. Comparable maxima in correlation coefficients are at lags -8 and +6. In this example the structure of the field appears to be wave-like. Fig. 3 illustrates this wave structure also. Smythe (1981) showed that this type of structure can obscure the true maximum and produce spurious results. Further investigation is required to identify these features and determine causal mechanisms.

Fig. 4 depicts a wind field reconstructed from May 2, 1978 data collected at 0.7° elevation, for which $3\text{ km} \times 4^\circ$ correlation arrays were used. Light ends of arrows correspond to arrowheads. Shown is a gust front marking the leading edge of cold air outflow ahead of a storm advancing toward the radar. Convergence is clearly evident.

An algorithm for reducing effects of range ambiguities in velocity data was also added. If the pulse width of reflectivity were expanded to double the width of velocity sampling, then velocity values can be assigned to their respective trips. Reflectivity (power) values at range R were compared with values at range 2R. If the difference in power was greater than 7 dB the range with the larger power was assigned the velocity value, the other was flagged. If the difference was less than 7 dB neither range was assigned a velocity value.

Another approach to the problem is to use two elevations in the analysis. It was thought that by this approach a data volume might be recognized more readily than if only one level were used. This could also lead to reconstructing three-dimensional winds. A program to do this analysis was coded but not tested.

At the end of the contract period cases of April 28, 1978 and April 10, 1979 were being examined. In the 1978 case data were collected in volume scan mode with full plan position indicators (PPI's), so scans at the same level were about six minutes apart. However, in the 1979 case data were

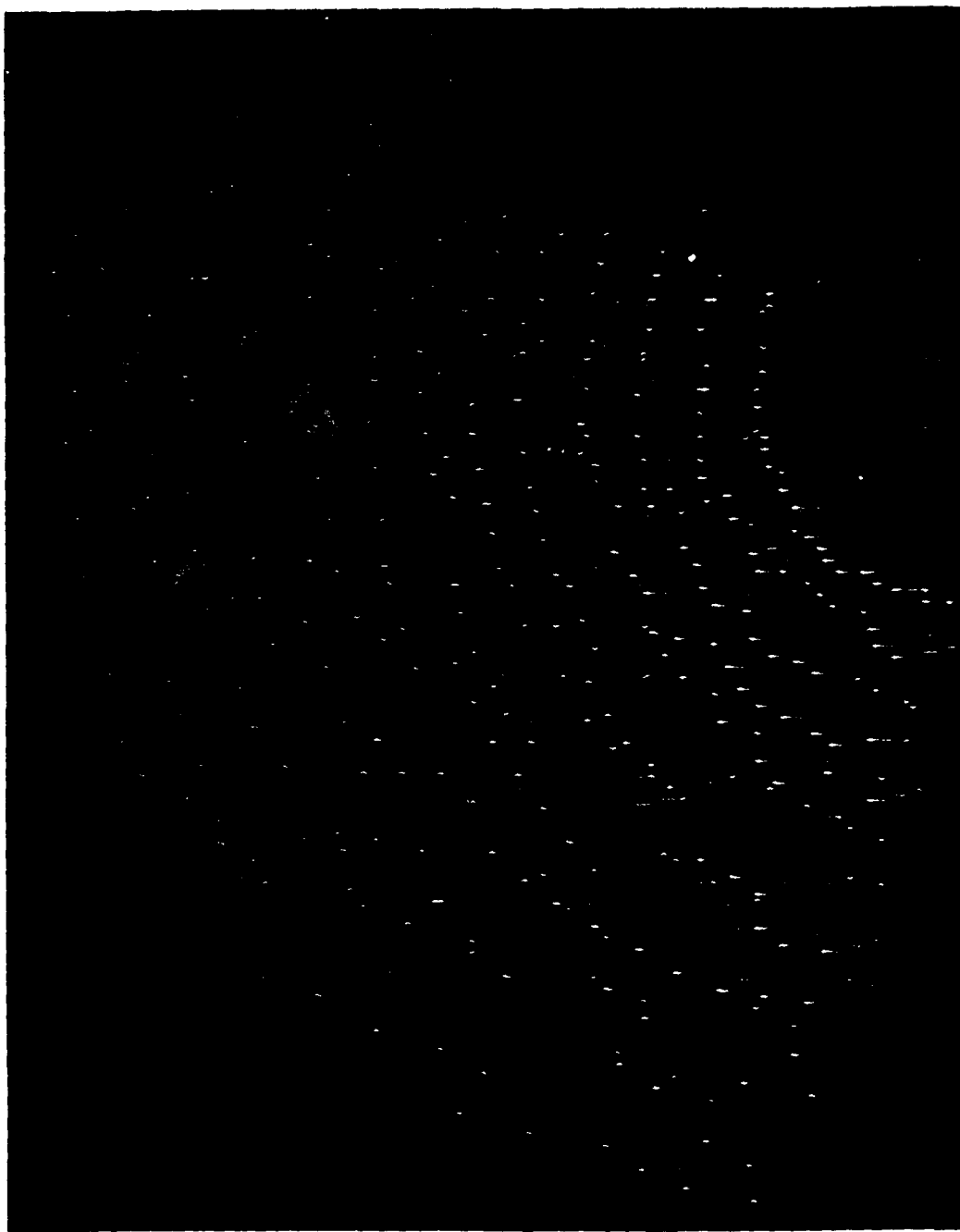


Fig. 4. Resolution of Gust Front Winds.

collected at 0.5° , so scans were approximately one minute apart. The 1979 data, collected by the National Severe Storms Laboratory (NSSL) but obtained through the courtesy of the National Center for Atmospheric Research, include dual-Doppler data. For the other cases no dual radar data were available for comparisons.

Since the NSSL data were packed into six-bit words, it was necessary to write software to unpack these data so that they would conform to the 32-bit word format of the AFGL P-E computers. This software was combined with editing software.

For analyses of the April 28, 1978 and April 10, 1979 data the algorithm of Smythe (1981) was changed so the the range of uncertainty about the first-guess range displacement was not fixed for each correlation array but instead was allowed to vary according to the standard deviation of level of confidence limits about the mean velocity. Preliminary results of testing were encouraging.

B. REAL-TIME STORM CELL DETECTION AND TRACKING

SASC continued its efforts to develop a real-time software technique for the detection and tracking of significant storm cells by reducing the running time of the processing algorithm originally developed by Crane (1979). It extracts the essential information required to describe the organization, development, and motion of the storm system. This information includes the characteristics of the active cells within the storm system, the clusters of cells, the fixed-threshold contours or echo regions that encompass the cells, and the complexes of echo regions that comprise the storm system. The algorithm was modified in 1979 for use on the Interdata 7/32 on-site computer at AFGL.

The original software includes one main program, nine subroutines, and one data block. The main program and the data acquisition subroutine are written in a mixed mode of Fortran and assembler; other subroutines are written in Fortran. The software is designed to collect raw weather radar data, decode, perform the necessary data extraction, and provide these data for later analysis. To make this system real-time the data must be gathered, processed, and stored quickly enough to receive the next set of input.

The data processing scheme is shown in Fig. 5. The data decoding and conversion processing routine in the data acquisition subroutine is

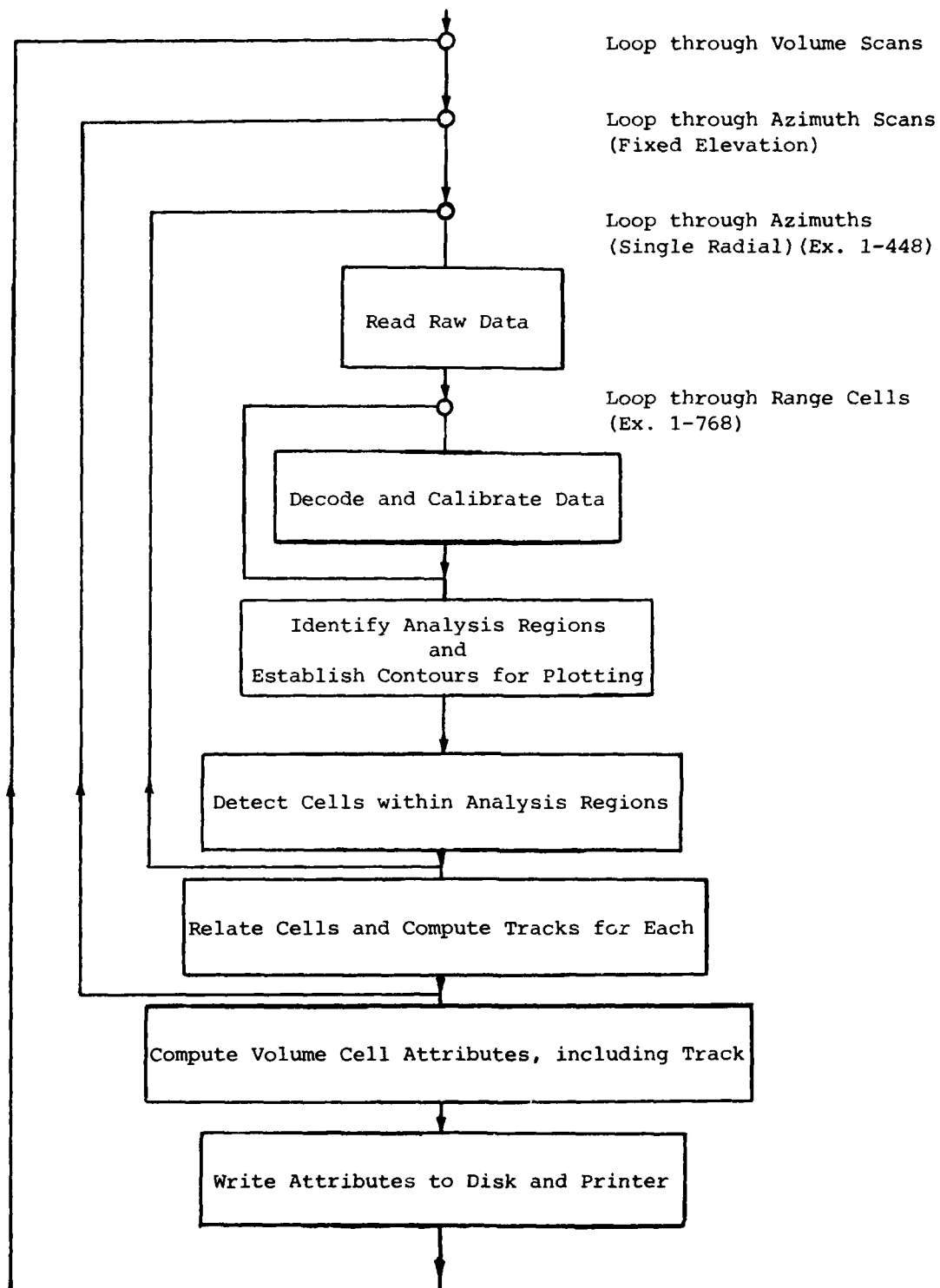


Fig. 5. Overall Processing Scheme.

the most time-critical process. For instance, if there are 768 range cells per radial and the azimuthal difference ($\Delta\theta$) is 0.8 degree, this routine needs to be iterated more than 300,000 times. Event calculation and referenced peak calculation routines are next most pressing in the time constraint problem. They have to be run over 400 times per azimuth scan if the azimuthal difference is 0.8 degree.

Since assembly language is capable of using registers directly for central processor unit (CPU) execution, it is more efficient in bit manipulation and addressing calculation, which are the important steps in reducing CPU execution time. The conversion and decoding processing routine and event calculation routine were therefore rewritten into assembly language. In addition, the conversion algorithm from bit-count to dBZ was optimized. These modifications saved more than 50 sec per azimuth scan.

On the other hand, assembler is hard to maintain and needs more debugging time. Also, a mixed mode of Fortran and assembler needs extra housekeeping time for interchange between the two different languages. Therefore the Fortran code was optimized in the referenced peak calculation subroutine.

April 30, 1978 data were employed to test these modifications. The output of the post mission (1979) program was used as the standard. Timing analysis of the modified version of the tracking program showed that the average processing time for each azimuth scan on the Interdata 7/32 is about 47 sec, which is close to the requirement for real-time operation (40 sec).

However, a problem was detected with the post mission output: the same program, using identical input data, on successive runs on the Interdata 7/32 minicomputer produced two different outputs. Results for one run are shown in Fig. 6, which is a plan view of the centroids of the cells detected by the software. On a subsequent run the four cells identified by arrows were not detected at those locations. Instead, four cells were detected at large distances north or south (off-scale on the plot), where none had been previously detected. The source of this problem has not been identified. As a consequence, use of the post mission program as a standard must be questioned. There is, however, agreement among the the results shown in Fig. 6, the results from an earlier run made with

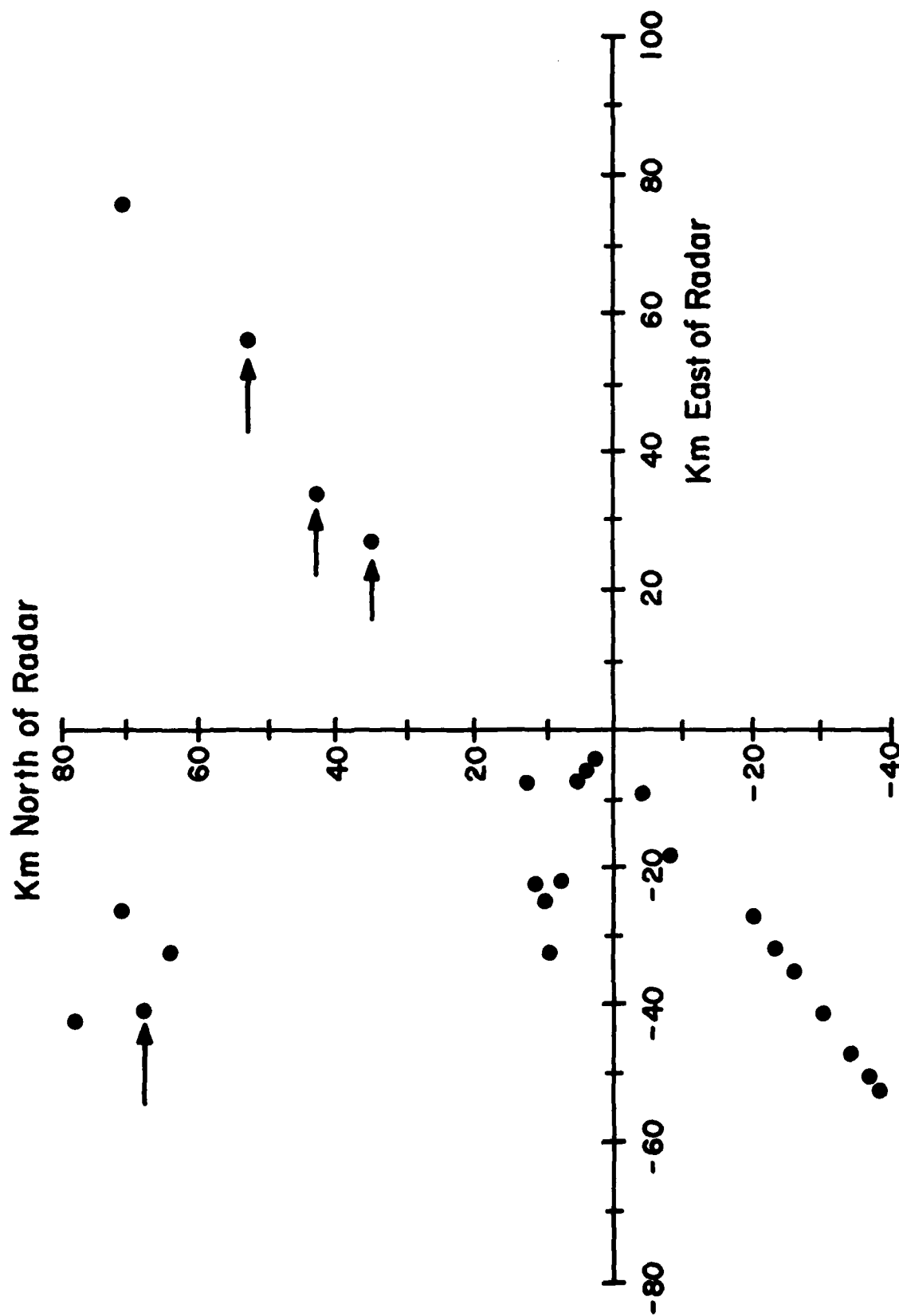


Fig. 6 Output of Volume Cell Location for April 30, 1976.

the same program, and the results from the current modified program. This consistency suggests that the changes incorporated in the modified version are valid but that the two programs may share a common problem.

C. TURBULENCE MEASUREMENTS

Several tasks were undertaken in support of AFGL's Wallops Island turbulence project. A program was written to read data from fourteen-track tape via the pulse-pair recorder interface and write the data to nine-track tape. Several nine-track data tapes were prepared for future use in non-real-time analyses. Coding of software for unpacking raw data into 16-bit halfwords was begun. Also, writing of a program to produce B-scans of data was begun.

A study based on techniques proposed by Atlas and Srivastava (1969)⁷ and Serafin (1972)⁸ was initiated. Implementation of these techniques would permit estimation of eddy dissipation rates by incoherent (non-Doppler) radar.

7. Atlas, D., and R. C. Srivastava, 1969: A method for radar turbulence detection. Laboratory for Atmospheric Probing, Tech. Report No. 15, University of Chicago.
8. Serafin, R. J., 1972: Radar measurement of the atmospheric turbulence structure function. Laboratory for Atmospheric Probing, Tech. Report No. 26, University of Chicago.

DATE
FILMED
9-8